PHYSICS AND CHEMISTRY OF SILICON SURFACE PASSIVATION

Thesis by

David J. Michalak

In Partial Fulfillment of the Requirements for the

Degree of

Doctor of Philosophy

CALIFORNIA INSTITUTE OF TECHNOLOGY

Pasadena, California

2006

(Defended December 15, 2005)

Acknowledgements

Caltech is truly an amazing place. The source of Caltech's greatness really stems from the truly diverse and amazingly talented people here. I have had the pleasure to interact with countless colleagues who are not only excellent at science, but in other dimensions as well. Because so many of these people have been instrumental in my development, both scientifically and personally, I will attempt to mention and thank as many of them as possible in the next few pages.

First and foremost is my academic advisor Nate Lewis. Nate is truly an amazing scientist and advisor. He has allowed me the intellectual freedom to pursue those scientific directions that piqued my curiosity. In lab, I was also allowed the freedom to hypothesize, try, fail, reconsider, and iterate all on my own: a usual sequence of events that practiced my scientific development and developed my confidence. Yet at the same time, Nate could always identify within 5 minutes the source of a problem that had me occupied beyond my means. In addition to being an excellent academic advisor, Nate has been a good friend through many adventures, whether mountain biking, windsurfing, jet skiing, or killing horses.

Many of my close friends have been fellow Lewis groupies. I met Elizabeth "Libby" Mayo as a prospective graduate student at Caltech some weekend in early March 1999. Since then, we have gotten ourselves involved in countless wild ideas, pranks, and ridiculous experiences. Shawn "Sean" Briglin idealizes the perfect friend. Our discovery of mountain boards, master plans, and the San Gabriel Mountains has sent us on numerous, and occasionally near-death, adventures. Libby, Sean and I were co-founders of the "<u>Skate Squad</u>" TV show, which served as an excellent source of distraction from the intellectual stresses of grad school. Florian Gstrein has been an excellent friend and scientific colleague over the past several years. Florian and I collaborated on several projects, and I can fondly remember the countless hours we'd spend together working in the lab or trying to understand the data we had just collected. Lauren Webb and I have braved trips to Brookhaven, Rutgers, Stanford, and probably some other places I've since forgotten. Dr. Pat Hurley, David Knapp, and Matt Traub have been great friends and scientific colleagues; I wish we could have spent more time together. During my first couple years at Caltech, Rob Rossi and Will Royea were extremely helpful at introducing me to the field of semiconductor surface science. Bruce Brunschwig, the director of the Molecular Materials Research Center (MMRC), has been a wonderful academic resource, knowledgeable on countless subjects, and he has also been a great friend with an excellent personality. The Lewis group is blessed with an administrative staff that flawlessly runs all behind-the-scenes activities making payment reimbursements, travel arrangements, and grant submissions easy. Outside her usual duties, Nannette Pettis invited the group to her house for numerous Calzone nights and even let a bunch of us, wielding sledge hammers and axes, bring down a large shed in her back yard. In addition to running everything perfectly, Sherry Feick has increased the morale of the whole group by spoiling us with various baked goods, her caring attitude, and her ceaseless sense of good humor. Sherry has been a great friend and colleague I will miss. From Thai Elvis, to brick oven pizza, to wild parties, all the Lewis group members have made the lab an enjoyable place to be.

I am also grateful for mentorship and friendships outside the Lewis group. Not only have I learned from a wide range of great classes, but the members of my committee have been excellent as well. Rudy Marcus represents an ideal role model on a scientific and personal level; it has been a joy to learn from him. I have also benefited from both the scientific rigor and friendship of Pat Collier, the latter of which was developed over a margarita (or two) at Amigos and during the re-creation of ZZ Top songs. Harry Gray, the most recent addition to my committee, has been a great source of guidance and support for academics as well as life. He, Jonas Peters, and David Goodstein took the time to chat with me and my dad about science policy. All of these professors exemplify the caring and interdisciplinary nature that makes Caltech one of a kind.

A good friend is one who will selflessly spend many hours helping you overcome your own research problems, and for this reason I am in great debt to Robert Strittmatter, who spent countless hours helping me to understand and repair a broken contactless photoconductivity decay apparatus. Tom Dunn has also been very helpful whenever I was confronted with equipment no longer working. I am also thankful for the excellent work of Lillian Kremar in the purchase department, who flawlessly sent various chemicals to various cities around the country at short notice. Dian Buchness has been a great co-conspirator in Holiday party planning. And I also have to thank Joe Drew for not getting too upset when Julie and I, caught by security, almost dumped his cart in Millikan pond one fortuitous Holiday-party evening.

Outside of lab, I have been extremely lucky to live in the same city as my best friend from home (the Lancaster, PA, ‘hood). As my closest and oldest friend, Jay Olin has always been there to provide the necessary mix of keeping it real, experiencing new things, and mixing with the Caltech crowd. From music, to games, to filming, to mountain boarding, to just chilling, Jay has been a great part of my life and social group at Caltech. Thanks buddy!

I have enjoyed a closer relationship with my sister, Sarah, over the past several years; her visits over holidays and other breaks have always been fun. My mom has been a great support over the past several years, and it’s been wonderful to share beach holidays with her in California. I have also really enjoyed playing jazz with my dad when he and Bev come for visits. I look forward to seeing more of my parents while I’m on the East Coast for the next couple months.

Lastly, and most importantly, is Juliane Fry. She has been a never-ending, and much-needed, source of optimism, hope, and love. It has been truly wonderful to spend the last several years with her talking science, relaxing with friends, and escaping on diverse mini-breaks. We have battled several moves, day-to-day grad school life, and most recently the thesis process together. She has provided an endless source of support and also the necessary dose of distraction. I look forward to experiencing the next stages in life together. I love you, Jules!

This acknowledgement would be incomplete without a listing of the many other people who have meant more to me than such a simple list can justify. I have been really lucky to live, as roommates, with so many easy-going yet vivacious people such as Theofilos Strinopoulos, Jamie Lindfors, Brett Maune, and, more recently and for a longer time, Juliane Fry, Wendy Belliston Bittner, Garrett Bittner, Christine Ueda, and fellow honorary housie Robert Dirks. Other honorary housemates that have provided much joy and entertainment are Maria Campa, David Knapp, and Donna, Oded, and Charlie Aharonson. It has been great sharing life with all of these creative and fun individuals.

Music is a great hobby of mine and it has been a joy to play with such talented musicians as long-time friend and excellent musician, Jay Olin, with whom we wrote the

"Skate Squad" soundtrack and formed the death metal band, "Toxic Waste." With fellow Toxic Waste-er and Donkey Show-er Colin Cameron, I discovered the joys of weird time signatures. Andrew Spakowitz and I have been playing music together since I first arrived at Caltech, and we've shared a fun evolution of various types of music (on various instruments) over the years: Andrew Spakowitz, Colin Cameron, Nicholas Wisniewski, and I as "The Donkey Show"; Andrew Spakowitz, Brendan Kayes, Francis, Lady Lo, and I as the unnamed Hip-Hop, Reggae fusion band; and many other bands with too many guitarists.

In this last hour, I'm sure I've missed many people very important and dear to me. While my foggy head missed thanking you on paper, know that, at moments of higher clarity, I have not forgotten your help, support, and love.

Lastly, I want to thank all of the people who have spent several hours with a nut who thinks making a TV show about cops on skateboards is a good idea. While the premise for "Skate Squad" is quite abstract, all of the dedicated help from numerous friends has made it something far better than I could have ever hoped for. Thanks!

Abstract

Low interfacial electron-hole recombination rates are essential for low-noise electronic devices and high-efficiency solar energy converters. This recombination rate is dependent on both the surface electrical trap state density, $N_{T,s}$, and the surface concentrations of electrons, n_s, and holes, p_s. A reduction in $N_{T,s}$ is often accomplished through surface chemistry, and lower recombination rates, through lower $N_{T,s}$ values, have been demonstrated in this work for surfaces chemically treated to produce methoxylated, $Si-O-CH_3$, overlayers. The H−Si(111) surfaces can react with methanol quickly in the presence of an oxidant or slowly in neat anhydrous methanol. Mechanisms have been proposed for both reactions.

Low recombination rates can also be achieved through control of the surface physics; a large n_s or p_s can lower recombination rates. To date, low recombination rates have often been attributed only to a reduction in $N_{T,s}$, without a direct measurement of n_s and p_s, partly because the importance of n_s and p_s has not been fully recognized and partly because an accurate evaluation of n_s and p_s can be very difficult. Surface recombination rates of silicon immersed in liquids containing various redox species (*e.g.*, $Fc^{+/0}$, I_2, $Me_{10}Fc^{+/0}$, or $CoCp_2^{+/0}$) were studied using an rf photoconductivity decay apparatus and compared with n_s and p_s values obtained from Mott-Schottky and other analysis techniques. The results demonstrate that the observed recombination rates can only be correlated with $N_{T,s}$ values when $n_s \approx p_s$. In all other cases, the recombination rate was low due to a large n_s or p_s even for surfaces with large $N_{T,s}$ values.

The full impact of this work was further realized through a study of the recombination rates of H−Si immersed in solutions of 48% HF, 40% NH_4F, and buffered HF (BHF), because such measurements are often performed for *in situ* monitoring of the surface quality during wafer processing steps. Our results demonstrate that only HF contacts can be used for *in situ* monitoring because $n_s \approx p_s$. For NH_4F or BHF contacts, low recombination rates were observed only because $n_s >> p_s$, and $N_{T,s}$ cannot be inferred from these measurements.

Table of Contents

List of Figures

List of Tables

1 Introduction

1.1 Motivation

Since their discovery in 1947,[1] semiconductors have played a prominent role in the development of electronic devices. The operation of computer and solar energy devices all rely on the intricate workings of semiconductor devices. With serious demands on energy looming in the near future, low power electronics and high-efficiency solar energy devices are being sought as solutions. The performance of these devices depends critically on the electrical perfection of the device as a whole. Electrical traps within the bulk of the semiconductor or at its surface can lead to losses in the electrical current, which can deleteriously affect either the power consumption of electronic devices or limit the efficiency of solar cells. Thus, understanding the mechanisms by which these electrical traps cause current loss is of fundamental importance towards making devices well-suited for the future.

1.2 Background

1.2.1 Semiconductor Fundamentals

Semiconductors have the unique ability to generate electrical power from sunlight. Their ability to do this is due to the presence of a bandgap, a range of forbidden electronic states separating the conduction band from the valence band. The bandgap prevents the rapid thermalization of photo-excited electrons and provides an energetic driving force that can be harnessed as electrical energy or spent to generate chemical fuels. Electrical current within a semiconductor is carried by the transport of either electrons in the conduction band or holes in the valence band, and they are referred to, generally, as charge carriers. Use of a semiconductor device demands a departure from equilibrium, which means that either an excess or a scarcity of the charge carriers will be imposed. Whether the sample is illuminated (which creates equal numbers of excess electrons and holes) or biased (which enhances or depletes only the majority carrier concentration), the recombination-generation mechanism is nature's way to restore equilibrium.

Of the many recombination mechanisms that are possible, the most prominent recombination mechanism for silicon devices is through electrical "trap" states. Trap states are electronic (impurity) states that exist within the bandgap and they can occur for various reasons: chemical impurities either in the bulk or at the surface that have an atomic energy level within the band gap, or strain or other lattice defects containing silicon dangling bonds that introduce electronic states within the band gap. Trap-mediated recombination dynamics are expressed in the Shockley-Read-Hall expression[2, 3] shown in equation 1, and its derivation is demonstrated in the first Appendix.

$$U = N_T \frac{k_n k_p \left(np - n_i^2\right)}{k_n\left(n + n_1\right) + k_p\left(p + p_1\right)} \tag{1}$$

In the SRH equation, U is the rate at which excess carriers recombine, N_T is the number of electrical traps per unit volume, k_n and k_p are the rate constants for electron and hole capture by this electrical trap respectively, n is the concentration of electrons per unit volume (n is the sum of both the equilibrium electron concentration, n_0, and any excess electron concentration, Δn), p is the concentration of holes per unit volume (p is similarly the sum of both the equilibrium hole concentration, p_0, and any excess hole concentration, Δp), n_i is the intrinsic free carrier concentration, and n_1 and p_1 are constants for a given trap that relate its energetic position to either the conduction band or valence band respectively.

The Shockley-Read-Hall rate expression applies for trap-mediate recombination at any position, either within the bulk or at the surface of the semiconductor, but the specific values of the various terms may vary between the bulk and surface. For example, the bulk of the semiconductor may have a different trap state density, N_T, or it may have different electron and hole concentrations than the surface. For these reasons it is important to specify different bulk, U_b, and surface, U_s, recombination rates as shown below.

$$U_b = N_{T,b}\frac{k_{n,b}k_{p,b}\left(n_b p_b - n_i^2\right)}{k_{n,b}\left(n_b + n_1\right) + k_{p,b}\left(p_b + p_1\right)} \tag{2}$$

$$U_s = N_{T,s}\frac{k_{n,s}k_{p,s}\left(n_s p_s - n_i^2\right)}{k_{n,s}\left(n_s + n_1\right) + k_{p,s}\left(p_s + p_1\right)} \tag{3}$$

Semiconductor manufacturing has become so technologically advanced that silicon can be made so pure (*i.e.*, really low $N_{T,b}$) that bulk recombination is often negligible compared with other recombination mechanism. Electrically passive surfaces and interfaces are in general much harder to create for two reasons. First, achieving a low surface recombination rate may require an electrical defect density as low as 1 defect per million surface atoms, and this can only be performed using the best procedures with the purest of chemical. Second, there is a large thermodynamic driving force for silicon to grow an oxide layer, which is often formed uncontrollably, introducing electrically defective lattice mismatches or dangling bonds, even if the initial surface was defect free.

Surface recombination, which is often the dominant recombination mechanism for silicon devices, can be reduced in two ways. First, a reduction in the number of surface electrical traps, $N_{T,s}$, will reduce the recombination rate. Throughout this thesis, this will be called *chemical passivation* because the number of electrical trap states at the surface can often be minimized through adequate chemical control of the surface. This passivation mechanism will require a chemically bound surface species that is not only defect-free but also stable towards oxidation for extended periods of time in air.

Another method to reduce the surface recombination rate is through the formation of a great imbalance in the charge carrier concentrations at the surface. It can be seen in equation 3 that the surface recombination rate can be lowered by either a large surface electron concentration, n_s, or a large surface hole concentration, p_s. This can be understood mathematically because n_s and p_s are additive in the denominator; if either is large, the whole denominator becomes large, and the rate is reduced. Kinetically, this can be understood because both electrons and holes are needed for a recombination event; a large excess of one carrier implies a scarcity of the other ($n_{s,0}p_{s,0} = n_i^2$) that limits the recombination rate. For example, the surface could have a large hole concentration, but if there are only a few electrons at the surface, recombination will be slow and limited by the electron concentration even if the surface has a high defect density. Similarly a highly defective surface could have a high surface electron concentration, but the recombination rate will be slow because there are no holes for those electrons to recombine into. This passivation mechanism will be called *electrochemical passivation* since n_s and p_s are determined by the charge transfer equilibrium that occurs during the formation of a particular semiconductor interface.

The surface concentrations of electrons, n_s, and holes, p_s, are determined by the barrier height, ϕ_b, (or built-in voltage, V_{bi}) of a given semiconductor junction that forms during the initial contact. The expressions relating the equilibrium charge carrier concentrations at the surface, $n_{s,0}$ and $p_{s,0}$, *for an n-type semiconductor* to ϕ_b and V_{bi} are given below, where N_C is the density of states in the conduction band, $n_{b,0}$ and $p_{b,0}$ are the equilibrium bulk electron and hole concentrations respectively, q is charge on an electron, and kT is the thermal energy. (In these expressions, a negative V_{bi} value correspond to situation where bands bend up towards the surface on an energy level diagram since the energy, E, is defined as $E = -qV$ for an electron)

$$n_{s,0} = N_C \exp\left(\frac{q\phi_b}{kT}\right) = n_{b,0} \exp\left(\frac{qV_{bi}}{kT}\right) \tag{4}$$

$$p_{s,0} = \frac{n_i^2}{n_{s,0}} = p_{b,0} \exp\left(-\frac{qV_{bi}}{kT}\right) \tag{5}$$

These expressions demonstrate the exponential dependence of the surface carriers on built-in voltage or barrier height. It can be seen through these expressions that a large $n_{s,0}$ or a large $p_{s,0}$ (and therefore a large n_s or a large p_s), necessary for electrochemical passivation, can be accomplished either with a very small or a very large barrier height respectively. More moderate barrier heights will lead to nearly equal surface electron and hole concentrations; the condition where $n_s \approx p_s$ will yield the maximum possible recombination rate for a given $N_{T,s}$. For this reason, the barrier heights of semiconductor interfaces can hold important implications on the recombination rates observed at those interfaces.

To date, the observation of low recombination rates has often been ascribed to chemical passivation through a reduction in N_T,s, without a direct measure of $n_{s,0}$ and $p_{s,0}$; the possibility of electrochemical passivation is often neglected for a number of possible reasons. First, perhaps the importance of n_s and p_s has not been fully recognized in the field. Second, an accurate evaluation of n_s and p_s is often very difficult to perform. Third, the assignment of a reduced trap state density as responsible for lower observed recombination rates seems a bit more intuitive and, conveniently, surfaces with lower trap state density are imagined to be more technologically relevant.

Both passivation mechanisms, however, can be of extreme importance to the semiconductor industry. It is not doubt that chemical passivation provides the highest quality and most robust mechanism for increasing device performance, but such passivation techniques can also be expensive or not currently achievable in some cases. Electrochemical passivation, on the other hand, can be performed relatively easily through the formation of interfaces with either large or small barrier heights. This method for electrical passivation, however, dictates the necessity for either a large rectification (diodic behavior) or an Ohmic behavior at these interfaces which may not be desired. Furthermore, the electrochemical passivation may not retain under the application of significantly large biases, or significantly large illumination intensities because, under these extreme injection conditions, the total electron and hole concentrations may become equal ($\mathrm{n} \approx \mathrm{p} \approx \Delta n$ or Δp) and therefore engage in the maximum recombination rate for the given N_T value of that interface. Understanding the chemistry and physics of silicon interfaces and their influence on recombination comprises the major focus of this thesis.

1.3 Summary

Surfaces can be passivated either using a chemical passivation technique that is accomplished through the elimination of electrical defects, or through an electrochemical mechanism that involves the formation of either a large surface electron concentration or a large surface hole concentration. In order to distinguish which mechanism is responsible for an overall recombination rate, barrier height measurements for a given silicon/liquid or silicon/solid contact is necessary.

The correlation between the barrier height and electrochemical passivation is demonstrated in Chapter 2. The techniques of Chapter 2 are applied in Chapter 3 to study the mechanism of silicon passivation in contact with aqueous fluoride and acidic solutions. It was also observed in Chapter 2 that contact of silicon to a solution of ferrocenium in methanol resulted in a *chemically* passivated surface and, thus, the study of the methoxylated surface is the focus of Chapter 4.

1.4 Collaborators

I have had the opportunity to work with numerous talented researchers during the completion of the work presented in this thesis. This section describes the collaborative nature of the work.

The initial surface recombination velocities measured in redox solutions were performed mostly by me under the guidance of Will Royea, who helped me learn how to use the rf photoconductivity system. Tom Vaid and Rob Rossi were helpful for discussions in how to perform and analyze the Mott-Schottky data for methoxylated surfaces described in Chapter 4. Rob Rossi spent a lot of time teaching me and others in the Lewis group about semiconductor electrochemistry.

Florian Gstrein performed finite element modeling of the recombination rates, which complemented the experimental lifetime study that I had performed and the results of his work are published elsewhere.[4] Much of the work presented in this thesis was done in collaboration with Florian, and it was extremely enjoyable as well as scientifically invigorating to work with him.

The first studies involving the channel conductance technique were performed by me in methanolic or THF solutions of Fc^+, $Me_{10}Fc^+$, or I_2 using p^+-n-Si(100)-p^+ devices that were manufactured by Paul Laibinis in 1993. Since only a few of the devices were still working, it was clear that more devices needed to be made. In addition, the study of solution contacts that formed a large surface electron concentration (*e.g.*, $CoCp_2^{+/0}$, NH_4F, and buffered HF) demanded the fabrication of devices with the opposite, n^+-p-n^+ , polarity. These additional devices were fabricated solely by Florian Gstrein. The initial measurements made with these devices were performed by both of us, but I carried on with several of the measurements after he left.

The study of silicon immersed in etching solutions was initiated by me and Florian Gstrein. This project encountered several experimental and mathematical difficulties, and overcoming these stumbling blocks required a true collaborative effort.

The electrical and Mott-Schottky measurements of silicon in acetonitrile solutions of decamethylferrocene and cobaltocene were performed in collaboration with David Knapp. David synthesized and purified the redox couples and supporting electrolytes used in these studies. He has also helped with the deposition of sputtered Al on the backside of *p*-Si(111) samples used for various studies. The acquisition of data was performed by both of us, while I performed all of the analysis presented here. These studies often produced unexpected results and together, David and I would spend numerous hours checking this and that in order to fully understand our system.

I am grateful for the help of Robert Strittmatter, who, in addition to being a great friend, spent numerous hours teaching me the principles of rf electronics and helping me apply them towards understanding, and fixing, the contactless rf photoconductivity decay apparatus. Without his help, many of the recombination rates presented in this thesis could not have been performed.

The infrared spectra of methoxylated species were collected by me in the laboratory of Yves Chabal at Rutgers. I am very grateful for the help of Yves Chabal and Dr. Sandrine Rivillion who were instrumental in helping me quickly acquire all the data. They also provided critical comments, suggestions, and other scientific guidance.

Quantum mechanical modeling of the methoxyl functionalities on silicon surface, although not included in this thesis, was performed by Santiago Solares in the Goddard group and recently published.[5] Santiago was an excellent colleague, and we had many enjoyable discussions.

I have also had the opportunity to enjoy fruitful discussions about my or related projects with a number of great scientists including Dr. Pat Hurley, Lauren Webb, E. Joseph Nemanick, Matthew Traub, Brendan Kayes, Julie Biteen, Tom Hamann, and many others.

2 Electrochemical Passivation

2.1 Observation of Chemical and Electrochemical Passivation Mechanisms Using RF Photoconductivity Decays

ABSTRACT

Recombination rates have been obtained for atomically smooth H−Si(111) and for air-oxidized Si(111) surfaces in contact with solutions of methanol, tetrahydrofuran (THF), or acetonitrile containing either ferrocene$^{+/0}$ (Fc$^{+/0}$), [bis(pentamethylcyclopentadienyl)iron]$^{+/0}$ (Me$_{10}$Fc$^{+/0}$), iodine (I_2), or cobaltocene$^{+/0}$ (CoCp$_2^{+/0}$). These measurements were made under both low-level and high-level injection conditions using a contactless rf photoconductivity decay apparatus. When in contact with electrolyte solutions having either relatively positive (Fc$^{+/0}$, I_2/I^-) or very negative (CoCp$_2^{+/0}$) Nernstian redox potentials with respect to a saturated calomel electrode (SCE), low recombination rates were observed independent of the level of surface electrical perfection. Surfaces that were exposed only to N_2(g) or to electrolyte solutions that contained a mild oxidant (such as Me$_{10}$Fc$^{+/0}$) showed differing recombination rates depending on their different surface chemistry. Specifically, surfaces terminated with Si−OCH_3 bonds, produced by the reaction of H−Si(111) with CH_3OH−Fc$^{+/0}$, showed lower recombination rates in contact with N_2(g) or in contact with CH_3OH−Me$_{10}$Fc$^{+/0}$ solutions than did H−Si(111) surfaces in contact with the same

ambients. Additionally, the Si−OCH_3 surface, formed by reaction of H−Si(111) with CH_3OH−$Fc^{+/0}$, displayed lower recombination rates than did similar surfaces also containing Si-I bonds, formed by the reaction of H−Si(111) with CH_3OH−I_2, or for those surfaces formed by reaction of H−Si(111) with THF−I_2 solutions. These results can all be consistently explained through chemical and electrochemical passivation mechanisms presented in Chapter 1. The data reveal that formation of an inversion layer (*i.e.*, a large surface hole concentration) on *n*-type Si, and not a reduced density of surface electrical trap sites, is primarily responsible for the low recombination rates observed for silicon in contact with CH_3OH or THF electrolytes containing I_2 or $Fc^{+/0}$. Similarly, the formation of an accumulation layer (*i.e.*, a large surface electron concentration) explains the low recombination rates observed for silicon in contact with CH_3OH-$CoCp_2$ or CH_3CN-$CoCp_2$ solutions. Digital simulations of the photoconductivity decay dynamics for semiconductors in contact with redox-active electrolytes that form either inversion or depletion conditions support these conclusions but are presented elsewhere.[4]

I. INTRODUCTION

The chemical modification of semiconductor surface is performed in order to improve the electrical properties of such surfaces and move away from high temperature, typically oxide forming procedures. The electrical performance of a surface is quantified by the surface recombination velocity, S (described in cm s^{-1}), which can be viewed as the speed at which carrier recombine at the surface. In photovoltaics or low power devices recombination currents are undesirable and surfaces with low S values are being sought.[1, 6, 7] While most surfaces and interfaces typically involve solid/solid junctions, low *S* values of Si/liquid interfaces are also of importance for silicon-based photoelectrochemical energy conversion devices.[8]

H-terminated Si(111) surface exhibits a low surface recombination velocity in contact with aqueous acids,[9] although the electrical properties of this surface rapidly degrade upon exposure to an air ambient.[10] Silicon surfaces also exhibit low recombination rates when in contact with methanolic solutions of one-electron oxidants such as 1,1'-dimethylferrocenium ($Me_2Fc^{+/0}$),[11-13] as do Si surfaces in contact with I_2 or Br_2 in methanol, ethanol, or tetrahydrofuran (THF).[14-18] Such systems have been proposed for pre-treatments in the formation of Si-based metal-insulator-semiconductor devices that have improved electrical properties.[19-22] The recombination rates of Si in contact with iodine-containing electrolytes has been ascribed to passivation of the Si surface resulting from Si-I bonding[16] or in some cases ascribed to passivation due to formation of surface Si-alkoxide bonds.[14] The data presented in this section indicate, however, that another effect is important in producing the behavior observed in this system, and that the observed carrier recombination dynamics reflect low *effective* surface recombination velocities. These low effective *S* values are the result of electrochemical passivation through charge-transfer induced band-bending formed at various Si/liquid contacts.[23-26] Specifically, Fermi-level equilibration with the cell potential of the liquid induces a net charge transfer between the two phases such that an inversion layer (high surface hole concentration) forms on *n*-type Si samples contacting solutions that have sufficiently positive electrochemical potentials.[23-26] This high surface holes concentration produces recombination rates (via the electrochemical passivation mechanism) even if the surface actually has a significant number of electrically active defect sites. The existence of this charge-equilibration process explains the rapid and reversible changes in recombination rates that are observed upon removal of Si surfaces from these electrolytes. The recombination rates observed in this work correlate well with the charge transfer based equilibrium model of electrochemical passivation as well as with the electrochemical potentials of the various solutions that have been reported to yield low *S* values for Si/liquid contacts to date.[11, 12, 26]

In the present study, we describe measurements of the recombination rates of (111)-oriented crystalline Si surfaces under both low- and high-level injection conditions in contact with solutions with various electrochemical cell potentials. Different carrier injection levels can provide information on the relative contributions of electrochemical and chemical recombination mechanisms on the observed surface recombination velocity. Changes in the redox potential of the contacting electrolyte provide additional information on the possibility of electrochemical passivation mechanism because such changes in the redox potential are presumed to change the surface electron and hole concentrations considerably. Variation of these parameters is especially useful for Si/alcohol contacts, for which a variety of measurements have revealed well-defined values of the band-edge energies and hence known equilibrium band-bending values which determine the surface electron and hole concentrations.[24, 27-30]

II. EXPERIMENTAL

Surfaces and Electrolyte Solutions

Long bulk lifetime (> 200 μs), (111)-oriented float-zone Si wafers were obtained from Virginia Semiconductor, Inc. The wafers were double side polished, were 190–200 μm thick, and were lightly *n*-type (phosphorous) doped with resistivities of 3817–3826 Ω cm, implying a free carrier concentration of 1×10^{12} cm^{-3}.[1] The wafers were cut into squares ≈1 cm^{2} in size for use in photoconductivity decay measurements. An atomically smooth H−Si(111) surface was prepared by immersion of the samples into 40% NH_4F(aq) (Transene Co.) for 15-20 min, rinsed with distilled H_2O (18.2 MΩ cm resistivity), and dried under a stream of N_2(g) prior to use.

Methanol was obtained from EM Science and was distilled over magnesium turnings. Concentrated (18 M) H_2SO_4 was obtained from EM Science. Anhydrous THF and I_2(s) were purchased from Aldrich and were used without further purification. Anhydrous CH_3CN was purchased from Aldrich and was further dried by distillation over CaH_2. Ferrocene (Fc^0) and bis(pentamethylcyclopentadienyl) iron ($Me_{10}Fc^0$) were obtained from Strem Chemicals Inc. and were sublimed under N_2(g) before use. Ferrocenium tetrafluoroborate (Fc^+)(BF_4^-) was obtained from Aldrich and was recrystallized from a mixture of THF and CH_3CN. Bis(pentamethylcyclopentadienyl) iron tetrafluoroborate ($Me_{10}Fc^+$)(BF_4^-) was synthesized from sublimed $Me_{10}Fc^0$ according to published methods.[31] Cobaltocene ($CoCp_2^0$) was purchased from Aldrich and was purified by sublimation at 45 °C under N_2(g). Cobaltocenium hexafluorophosphate ($CoCp_2^+$)$(PF_6)^-$ was purchased from Aldrich and was recrystallized from a mixture of CH_3CN and diethyl ether. All nonaqueous solutions were prepared and stored in a N_2(g)-purged flushbox that contained less than 10 ppm of O_2(g) as indicated by the absence of visible fumes from diethyl zinc. All solutions were chemically stable on the time scale of the photoconductivity decay measurements.

Redox potentials were referenced to $Fc^{+/0}$ in each solvent. The $Fc^{+/0}$ potential was in turn referenced in a given solvent with respect to a methanolic saturated calomel electrode (SCE). The formal reduction potential of $Fc^{+/0}$ measured by cyclic voltammetry in CH_3CN, CH_3OH, and THF was 0.48, 0.44, and 0.66 V, respectively vs. a methanolic SCE. The formal reduction potential of $Me_{10}Fc^{+/0}$ was −0.52, −0.49, and −0.41 V vs. $Fc^{+/0}$ in CH_3CN, CH_3OH, and THF, respectively. The formal reduction potential of $CoCp_2^{+/0}$ was −1.36, −1.34, and −1.37 V vs. $Fc^{+/0}$ in CH_3CN, CH_3OH, and THF, respectively. The cell potential of 0.05 M I_2 in CH_3CN, CH_3OH, and THF was 0.32, 0.05, and 0.20 V vs. $Fc^{+/0}$, respectively. The redox potentials of solutions used in rf decay measurements corresponded closely to the formal reduction potentials with the appropriate Nernstian correction incorporating the actual concentrations of reduced and oxidized electroactive species in such cells.

Photoconductivity Decay Measurements

The recombination rates of the various silicon/liquid contacts were measured using the contactless rf photoconductivity decay apparatus described in the Appendix. Silicon sample were enclosed in sealed glass vessels that enabled collection of rf conductivity decays for the sample in contact with either $N_2(g)$, air, or various liquid solutions. Prior to the measurement of each silicon contact, the LC circuit needed to be tuned to account for changes due to the presence of an electrolyte solution or due to samples of slightly different geometry. Tuning was performed for each silicon contact in the dark by adjusting the variable capacitors and output frequency until the amplitude of the reflected rf signal was minimized. Samples were illuminated with 10 ns pulses from a 10 Hz Nd:YAG laser. The beam was expanded to approximately 2 cm^2 in diameter, and the power density of the beam was attenuated to either 7×10^{-4} mJ cm^{-2} pulse^{-1} for high-level injection conditions or to 1.3×10^{-6} mJ cm^{-2} pulse^{-1} for low-level injection conditions, which would produce injected carrier concentrations of 2.8×10^{14} carriers cm^{-3} pulse^{-1} and 5.2×10^{11} carriers cm^{-3} pulse^{-1} respectively.

Data were recorded within 20 min of exposure to the ambient of interest, and the photoconductivity decays were stable over a 30 min time period. Both sides of the semiconductor sample were exposed during etching and during contact with the various electrolyte solutions or gas ambients and both sides were active surfaces for recombination. Data for each silicon contact were obtained by averaging 128 signal photoconductivity decays. All rf decay signals were well-fitted by single exponential decays; three representative rf decay curves are shown in Figure 1. The mean lifetimes reported for each surface treatment were determined by averaging the lifetimes of at least 3 samples that had been subjected to nominally identical surface treatments.

Data Analysis

Photoconductivity decay data were well-fitted by single exponential functions using a standard-least-square-fitting method (Sigma Plot 5.0) with no weighting applied to the residuals. The observed single exponential decay lifetime, τ, extracted from the fit, can be related to the bulk lifetime, τ_b, and to the surface recombination velocity, S, through the following expression:[32-34]

$$S = \frac{d}{2}\left(\frac{1}{\tau} - \frac{1}{\tau_b}\right) \tag{6}$$

In the expression above, *d* is the sample thickness and factor of 2 arises because both surfaces are electrically active during charge carrier recombination.

For the samples measured using this setup, the surface recombination velocities can only be measured within a certain range of conditions. Specifically, if the surface is sufficiently passivated, the total observed photoconductivity decay lifetime will be limited by the bulk recombination rate, and hence only the calculation of an upper limit on *S* can be performed. If the surface is sufficiently electrically defective, carrier diffusion from the bulk of the crystal can be the rate limiting process, and this case only the calculation of a lower limit on *S* can be performed.

Measurements of silicon in contact with 18 M H_2SO_4 have previously been used to estimate, or at least provide lower bounds on, the bulk lifetime, which will allow the calculation of S values from observed photoconductivity decay lifetimes. For many of the surfaces measured in this work, however, the measured lifetimes approached, or in some cases exceeded, the values of the lifetimes obtained for the same wafer in 18 M H_2SO_4. This implies that contacts to 18 M H_2SO_4 do not provide a useful value of the bulk lifetime and unless otherwise specified, *S* values are reported assuming $\tau_b = \infty$. The reported *S* values therefore represent upper limits to the true value of *S*.

To estimate the carrier diffusion-controlled lifetime for a sample with an infinite surface recombination velocity, an ambipolar carrier diffusion coefficient, $D_{n,p}$, of 10 cm^2 s^{-1} is used, and the characteristic time is approximated by $\tau = L^2/D_{n,p}$. For a 200 μm thick sample, the diffusion length, L, is 100 μm and the diffusion-limited carrier decay lifetime is ≈5 μs. Hence for such samples, only lower bounds on *S* ($S > 2\times10^3$ cm s^{-1}) can be established when the experimentally observed decay time is < 6 μs.

X-ray Photoelectron Spectroscopy Measurements

X-ray photoelectron (XP) spectra were acquired with an M-Probe surface spectrometer (Surface Science Instruments) operating at a base pressure of $< 6\times10^{-10}$ torr. Monochromatic, focused Al K$\alpha_{1,2}$ (1486.6 eV) irradiation was directed at the surface in a 300 μm circular spot at an incident angle of 35° from the surface plane. Photoejected electrons were collected using a hemispherical analyzer also positioned at an angle of 35° from the surface plane but 90° degrees from the x-ray source. Spectra in the Si 2p region were recorded in an unscanned mode with a 15 min accumulation and oxide coverages were determined by use of an overlayer model that has been described previously.[35]

III. RESULTS

Photoconductivity Decay Measurements of Atomically smooth H−Si(111) in Contact with Aqueous Acids and in Contact with Air

Photoconductivity decays for (111)-oriented, H-terminated Si in contact with 18 M H_2SO_4 were long and were well-fit by a single exponential function. The mean decay lifetime for samples from this wafer was 490±50 μs under low-level injection (Table 1: **1a**). As described above, this value is consistent with the manufacturer's specification that the minority carrier lifetime within the bulk of these samples, τ_b, is > 200 μs. If this observed lifetime were due to surface recombination only, then the surface recombination velocity, *S*, would be $S = 19\pm2$ cm s^{-1}. Of course, this value is an upper bound on the true surface recombination velocity since it assumes no contribution from charge carrier recombination in the bulk of the sample.

Subsequent immersion of these samples into 48% HF produced slightly shorter lifetimes of 180±60 μs under low-level injection and 460±90 μs under high-level injection (Table 1: **1b**). These data are in accord with the observations of Yablonovitch *et al.*, which indicate that S for H-terminated, (111)-oriented Si surfaces is a function of the acidity of the electrolyte.[33] However, in contrast to the results of Yablonovitch, the measured surface recombination velocity was not as low as the 0.25 cm sec^{-1} value. This is not unexpected since such a low value of S could only be measured with bulk lifetimes in excess of several millisecond, which were not available to us, however, the lifetimes measured in HF should have at least been as long as those in contact with H_2SO_4. Personal communication with Yablonovitch indicates that the lower values we observed in 48% HF are due to surface contaminations that could be removed by cycling various oxidizing and etching steps to reveal a clean surface.

Re-exposure of the silicon sample to 18 M H_2SO_4 solutions yielded higher lifetimes again (data not shown). Exposure of a H_2SO_4-treated Si surface to air produced a rapid decrease in the carrier lifetime, and lifetimes as short as 10 μs were observed immediately upon exposure to air (Table 1: **1c**). The small τ value was stable in air for lengths of time, and a long lifetime could only be recovered by re-etching the Si surface and/or by re-immersing the crystal into a highly acidic aqueous electrolyte. These effects were observed under both low-level and high-level injection conditions.

B. Photoconductivity Decay Measurements of H−Si(111) in Contact with CH_3OH or THF Solutions of I_2 or $Fc^{+/0}$

Because the comparison of Nernstian cell potential to the recombination rates is of interest in this work, the $Fc^{+/0}$- and I_2-containing solutions of CH_3OH and THF are considered together in this section since they form solutions with similar Nernstain redox potentials that are relatively positive with respect to a methanolic SCE (mSCE) reference potential; all solutions are approximately within 200 mV of 0.6 V vs. mSCE.

The mean decay time for atomically smooth H−Si(111) surface in contact with CH_3OH−0.05 M I_2 was very long, displaying lifetimes for both low-level and high-level injection conditions near 550 μs (Table 1, **2a**). Using equation 6, the measured sample thickness, $d = 195$ μm, and assuming an infinite bulk lifetime, the surface recombination velocity, S, can be calculated to be near 18 cm s^{-1} for both high-level and low-level injection conditions. Once the samples were removed from the I_2-CH_3OH solution, rinsed with CH_3OH, and measured under an inert N_2(g) atmosphere, however, the lifetimes dropped to approximately 10 μs yielding S values near 1000 cm s^{-1} (Table 1: **2b**). The long lifetimes observed under I_2-CH_3OH solution were completely reversible in that re-immersion of the Si surface into the CH_3OH−0.05 M I_2 solution resulted in lifetimes values within error to those initially observed those sample in contact with that solution (Table 1: **2c**). Subsequent removal, rinsing, and measurement under N_2(g) again produced very short lifetimes (data not shown).

Similarly, long lifetimes around 600 μs (Table 1: **3a** and Figure 1a) were observed for H−Si(111) surfaces in contact with a CH_3OH−0.05 M $Fc^{+/0}$ solution, however different decay characteristics were measured under N_2(g). In contrast to the short lifetimes observed under N_2(g) after contact to CH_3OH−0.05 M I_2 solutions, silicon samples measured under N_2(g) after contact to the $Fc^{+/0}$-MeOH solution displayed S values only slightly larger then those obtained when in contact with the solution (Table 1: **3b** and Figure 1c). Similar to the I_2-MeOH case, however, re-immersion of the silicon sample back into the $Fc^{+/0}$-MeOH solution produced the longer lifetimes values that were within error of those measured previously in that solution (Table 1: **3c**). The long lifetimes observed for silicon in contact with the I_2-CH_3OH and $Fc^{+/0}$-CH_3OH solutions are in accord with earlier measurements of low surface recombination velocity for silicon in contact with a $Me_2Fc^{+/0}$-CH_3OH solution, which has a Nernstian potential within 100 mV of the $Fc^{+/0}$-CH_3OH solution and with 150 mV of the I_2-CH_3OH solution.[11, 12]

Infrared spectroscopic data indicate that Si−OCH_3 bonds are formed on the surface when H−Si surfaces are immersed into methanolic solutions of either I_2 or Fc^+, although immersion into CH_3OH-I_2 also produces some surficial Si−I bonds.[14-16, 35] To address the role of the Si−OCH_3 and/or Si−I bonds in producing low surface recombination velocities, photoconductivity decay data were collected for Si surfaces in contact with THF as the solvent. In contact with a THF−0.05 M I_2 solution, the effective surface recombination velocity of an H−Si surface under high-level injection conditions was 40±10 cm s^{-1} (Table 1: **4a**). These data are in qualitative accord with prior observations on this system[14] and indicate that surface alkoxylation is not necessary to yield low recombination rates for Si in contact with certain electrolyte solutions. The observed charge carrier lifetime for H−Si samples in contact with THF−0.05 M Fc^0−0.005 M Fc^+ solutions was also quite long, corresponding to *S* values under high-level injection of 50±30 cm s^{-1} (Table 1: **5a**). Rinsing of the silicon samples previously contacted to either solution produced high *S* values when measured under an inert $N_2(g)$ ambient (Table 1: **4b**, **5b**), and this effect was reversible in that re-immersion of those samples back into either a THF–0.05 M I_2 solution (Table 1: **4c**) or into a THF−0.05 M Fc^0–0.005 M Fc^+ solution (Table 1: **5c**) produced a long lifetime again.

C. Photoconductivity Decay Measurements of H−Si(111) in Contact with CH_3OH or THF Solutions Containing $Me_{10}Fc^{+/0}$

Solutions containing the $Me_{10}Fc^{+/0}$ redox couple were studied because the Nernstian cell potentials of this compound were approximately 500 mV more negative than either the $Fc^{+/0}$- or I_2-containing solutions; cell potentials were near 0 V vs. mSCE. These solutions were used to study what influence a significantly more negative cell potential has on the recombination lifetimes of silicon immersed in these solutions. Indeed, silicon contacts to the $Me_{10}Fc^{+/0}$-containing solutions produced significantly shorter lifetimes around 3 μs, indicative of a diffusion limited rate and a high surface trap state density, regardless of whether a H−Si(111) sample had been directly immersed into the $Me_{10}Fc^{+/0}$-THF solution (Table 1: **6a**) or if it had been first contacted to a $Fc^{+/0}$-THF solution (observed to give a long lifetimes) prior to contact with the THF-$Me_{10}Fc^{+/0}$ solution (Table 1: **5d**). Furthermore, removal of the samples from solution, rinsing with CH_3OH, and subsequent measurement under $N_2(g)$ exhibited lifetime values within error of those observed in solution (Table 1: **6b**). This demonstrate that, unlike the $Fc^{+/0}$ and I_2-containing solutions, the $Me_{10}Fc^{+/0}$-containing solutions do not significantly alter the recombination statistics from those measured under $N_2(g)$. Again this effect is reversible in that the sample could be placed back into the $Me_{10}Fc^{+/0}$ solutions to recover similar lifetimes (Table 1: **6c**). However, subsequent removal of these samples from the THF-$Me_{10}Fc^{+/0}$ solution and immersion into the THF-$Fc^{+/0}$ solution restored long lifetimes with

S values near 40 cm s^{-1} (Table 1: **6d**) that are within the error of those previously observed for fresh H−Si(111) samples contacted directly to a $Fc^{+/0}$-THF solution (Table 1: **5a**). This strongly suggests that it is the electrochemical potential of the electrolyte solution, and not a pretreatment history or a unique chemical state of the surface, that is the dominant factor in producing the observed recombination lifetimes for these silicon/liquid contacts.

The presence of Si−OCH_3 bonds, formed through the immersion of a H−Si(111) surface into a CH_3OH-$Fc^{+/0}$ solution, did however produce a longer lifetime when in contact the $Me_{10}Fc^{+/0}$-THF solution (Table 1: **3d**) than did a bare H−Si(111) surfaces in contact with the same $Me_{10}Fc^{+/0}$-THF solution (Table 1: **6a** and **6c**). Because long and similar lifetimes of Si−OCH_3-terminated surfaces were observed in both N_2(g) and the $Me_{10}Fc^{+/0}$-containing solutions, and because both short and similar lifetimes for the H−Si(111) surfaces were also observed in these two contacts, it seems reasonable that these contacts yield recombination rates according to the surface electrical defect density. These results imply that the surface electron and hole concentrations are roughly equal when in contact with these two surface.

D. Photoconductivity Decay Measurements of H−Si(111) in Contact with CH_3OH or CH_3CN Solutions Containing $CoCp_2^{+/0}$

Photoconductivity decay data were also collected for Si surfaces in contact with CH_3OH-$CoCp_2^{+/0}$ and CH_3CN-$CoCp_2^{+/0}$ electrolytes. These redox systems produce very negative Nernstian cell potentials around −0.9 V vs.mSCE and are expected to produce an accumulation layer with a high surface electron concentration. The $CoCp_2^{+/0}$

electrolyte was chosen because a high surface electron concentration should also impart a similar electrochemical passivation mechanism as the inversion layers (high surface hole concentrations) that are formed for silicon in contact with $Fc^{+/0}$- or I_2-containing solutions.

The photoconductivity decay lifetime for H−Si surfaces in contact with a solution of CH_3OH–0.01 M $CoCp_2^{+/0}$ was approximately 740 μs under either high-level or low-level injection conditions, which corresponds to *S* values near 20 cm s^{-1} (Table 1: **7a**). Similar to the case of the $Fc^{+/0}$- and I_2-THF contacted samples, the subsequent exposure of these samples to an N_2(g) environment produced low decay lifetimes near 10 μs and *S* values near 1800 cm s^{-1} (Table 1: **7b**). Re-immersion of the silicon samples into the CH_3OH–0.01 M $CoCp_2^{+/0}$ solution produced decay lifetimes of about 200 μs (*S* values near 70 cm s^{-1}) that were not nearly as long as those previously measured in those solutions. However, after cleaning with solvent, re-etching in NH_4F, and subsequent re-immersion of these same samples into the CH_3OH–0.01 M $CoCp_2^{+/0}$ solution, the lifetimes increased to about 750 μs with *S* values near 20 cm s^{-1} as previously observed (Table 1: **7c**). Silicon samples in contact with CH_3CN–0.01 M $CoCp_2^{+/0}$ displayed similar behavior although the specific lifetimes in contact with CH_3CN were not as long as those measured in CH_3OH and that re-immersion into the $CoCp_2^{+/0}$-CH_3CN solution after N_2(g) contact displayed very short lifetimes (data not shown) prior to re-etching and re-immersion (Table 1: **8c**).

E. Photoconductivity Decay Measurements of Air-Oxidized (111)-Oriented Silicon in Contact with CH_3OH- or THF-Containing Redox Solutions

To further elucidate the role of the electrochemical cell potential on the recombination rate, photoconductivity decay measurements were collected for Si surfaces that had been deliberately oxidized. Due to the thermodynamic stability of silicon oxide (SiO_x), oxidized silicon surfaces constitute systems in which chemical reactions are not feasible between the electrolyte and the surface states at the Si/SiO_x interface. This is because the surface states are presumed to reside at the Si/SiO_x interface and the remaining oxide overlayer physically obstructs chemical passivation by any species larger than atomic hydrogen which can diffuse through the oxide lattice.

Oxidized silicon samples were created by etching and then allowing a native oxide to grow onto the surface by exposure to air for five days prior to measurement. Si/SiO_x surface grown in this manner are relatively thin, x-ray photoelectron analysis of the Si 2p region of these interfaces indicated the presence of approximately 4 Å of silicon oxide, and are very electrically defective. Oxide layers this thin are desirable so that only a small potential drop occurs across the oxide layer, so that the band structure within the near-surface region of the unoxidized silicon is similar to oxide-free, H-term surface. If a significant fraction of the built-in voltage of the Si-liquid contact drops across a thicker oxide layer, lower V_{bi} values will result which will change both the $n_{s,0}$ and $p_{s,0}$ values and the extent of electrochemical passivation.

The time-resolved rf conductivity decays for Si/SiO_x samples are shown in Table 2. The S value (and low lifetimes) for such a sample in contact with $N_2(g)$ are expected for an electrically defective Si/silicon oxide interface. Despite the absence of any possible chemical passivation mechanisms, immersion of such a sample into CH_3OH−0.05 M I_2 (Table 2: **9a** and **9c**) or into CH_3OH−0.05 M $Fc^{+/0}$ (Table 2: **10a** and

10c) produced a long photoconductivity decay time and a low effective *S* value. This effect was fully reversible in that removal from the solution produced a high effective *S* value in contact with the N_2(g) ambient (Table 2: **9b** and **10b**). The XP spectra of the sample after removal from the electrolyte still showed a significant amount of surface oxidation, which eliminates the possibility that these solutions can etch away an oxide layer and passivate the silicon surface. High *S* values were observed again upon immersion of these samples into a THF−0.05 M $Me_{10}Fc^0$−0.01 M $Me_{10}Fc^+$ solution (Table 2: **9d** and **10d**), again demonstrating the critical role of the redox potential of the electrolyte in producing the low recombination rates for Si in contact with CH_3OH−0.05 M I_2 or with CH_3OH−0.05 M $Fc^{+/0}$ solutions.

Another striking difference can be observed by comparing the results of oxidized sample, Table 2: **10a-d**, to the same sequence of contacts for the H−Si(111) sample, Table 1: **3a-d**. In these two cases, only the NH_4F-etched H−Si(111) samples exhibited relatively long lifetimes when in contact with either N_2(g) or $Me_{10}Fc^{+/0}$-containing solutions, while the Si/SiO_x-terminated sample did not. These results confirm that the Si/SiO_x-terminated surface cannot be chemically passivated by contact to these electrolytes and they also provide further evidence for the chemical passivation imparted by the Si−OCH_3 termination, as formed by immersion of the H−Si(111) surface into $Fc^{+/0}$-CH_3OH solutions. The fact that both the chemically passivated Si−OCH_3 surface and the electrically active Si/SiOx surface display significantly longer lifetimes upon re-immersion into the $Fc^{+/0}$- or I_2-containing solutions demonstrates that the electrochemical passivation technique is relatively insensitive to the chemical passivation, *i.e.*, trap state density, of these surface.

IV. DISCUSSION

A. Electrochemical Passivation of Si Surfaces: Correlation of Recombination with the Electrochemical Potential of the Solution

The electrolytes that produced low effective Si surface recombination velocities all had either relatively positive, or very negative, redox potentials relative to the standard calomel electrode (SCE).[36] THF- or CH_3OH-containing solutions of I_2 or $Fc^{+/0}$ all have redox potentials, $E(A/A^-)$, near 0.45 V vs. SCE, and each of these silicon/liquid contacts always produced low recombination rates (Table 1, **3-5** and Table 2: **9-10**). Electrochemical data have located the conduction band edge of alkoxylated Si surfaces at ≈ -0.83 V vs.the standard calomel electrode, SCE, in CH_3OH solutions,[24] and, in the absence of Fermi-level pinning, contacts to solutions with cell potentials near 0.4 V vs. SCE should produce barrier heights in excess of the band gap. This will lead to the formation of an inversion layer, characterized by a very high surface hole concentration, that reduces the overall recombination rate through the electrochemical passivation method.

Similarly, long recombination rates were observed for the $CoCp_2^{+/0}$ electrolytes(Table 1, **7** and **8**), which have a very negative redox potential near −0.9 V vs.SCE which, based on the conduction band edge position of −0.83 V, should lead to the formation an accumulation layer at these interfaces. Similar to the case of $Fc^{+/0}$ and I_2-containing solutions, these solution contacts consistently displayed low recombination rates (lifetimes were always large and effective *S* values were always low) independent of the various chemical state of the Si surface.

In contrast to the solutions mentioned above, a large range of both low and high S values was observed for Si surfaces in contact with N_2(g) or in contact with either CH_3OH-$Me_{10}Fc^{+/0}$ or THF-$Me_{10}Fc^{+/0}$ solutions. This strongly suggests that surface recombination rates observed for such contacts are sensitive to the chemical state of the surface and hence can be used to estimate the trap state density, $N_{T,s}$.

This behavior can be understood in the context of the Shockley-Read-Hall treatment for surface recombination, provided that the different effects of interfacial charge transfer in producing band bending at the semiconductor/liquid contact are considered for each contact of interest.[2, 3, 37] The recombination rate for a surface with traps at a single energy involves the carrier capture rate constants, $k_{\mathrm{n,s}}$ and $k_{\mathrm{p,s}}$, the electron and hole concentrations at the surface of the semiconductor in the dark, $n_{\mathrm{s,o}}$ and $p_{\mathrm{s,o}}$, respectively, and the injected electron and hole concentrations, Δn_{s} and Δp_{s}, respectively (note: $\Delta n_{\mathrm{s}} = \Delta p_{\mathrm{s}}$):

$$U_S = N_{T,s} \frac{k_{n,s} k_{p,s} \Delta p_s \left(p_{s,0} + n_{s,0} + \Delta p_s \right)}{k_{n,s}\left(n_s + \Delta n_s + n_{1,s} \right) + k_{n,s}\left(p_s + \Delta p_s + p_{1,s} \right)}. \qquad (7)$$

In equation 7, $N_{\mathrm{T,s}}$ is the surface trap density, and $n_{1,\mathrm{s}}$ and $p_{1,\mathrm{s}}$ are the electron and hole concentrations, respectively, when the Fermi-level is located at the energy of the surface trap.[37, 38]

The electron and hole concentrations in equation 7 refer to the values at the solid/liquid interface and are strong functions of any electric potential drops in the near-surface region of the semiconductor. Qualitatively, it is clear that redox couples that have very positive redox potentials are capable of extensive charge transfer from the Si into the electrolyte, allowing for the formation of an inversion layer (and a large concentration of holes) at the surface of *n*-type Si.[23, 24, 26] Similarly, charge-transfer equilibration with redox couples that have very negative redox potentials will produce an accumulation layer (and a large concentration of electrons) at the Si surface if Fermi-level pinning at these interfaces is not a problem. In either case, the lack of one carrier type or the other for participation in steady-state surface recombination kinetics will produce a low effective surface recombination velocity even for significant values of $N_{T,s}$.

Electrochemical data have located the conduction-band edge of alkoxylated Si surfaces at ≈ –0.83 V vs. SCE in CH_3OH.[24] This band-edge position is consistent with the observation that in contact with air, $N_2(g)$, or electrolytes having moderately negative redox potentials, such as THF-$Me_{10}Fc^{+/0}$, surfaces with significant $N_{T,s}$ values exhibit a higher effective surface recombination velocity than they do under conditions that produce an inversion or accumulation layer at the Si surface. The effect should be rapid and reversible because only electron transfer between the liquid and solid is required to produce the inversion or accumulation layers necessary for the observation of low S values. Removal of the sample from the electrolyte will generally change the surface potential in a direction that minimizes the band bending. This should lead to an increase in the observed value of S and the variations in $N_{T,s}$ can be reflected in the measurements of S under these conditions. This expectation is in accord with the experimental observations that the low S values for silicon contacts to either the oxidizing or the strongly reducing electrolyte solutions exhibited higher S values when subsequently measured in contact with $N_2(g)$ or $Me_{10}Fc^{+/0}$ solution.

Further evidence for the effect of electrochemical passivation is demonstrated by the results in Table 2, where native oxide terminated surfaces, known to have a high surface electrical defect density, display high *S* values when in contact with either $N_2(g)$ or $Me_{10}Fc^{+/0}$ solutions as expected, but reversibly and reproducibly display low *S* values when in contact with either CH_3OH-I_2 or CH_3OH-$Fc^{+/0}$ solutions, which are known to create inversion layers. In these cases, it is a good assumption that the high electrical defect density remains throughout each measurement; the reversible chemical passivation of the trap states associated with the native oxide surface is not expected because the electrical defects are presumed to be in close proximity to the silicon of the Si/SiO_x interface, and not near the SiO_x/liquid interface, and any chemical interactions by these solutions with the trap states are inhibited by the physical thickness of the oxide layer.

Further evidence for the correlation between low surface recombination rates and surface charge carrier density can be obtained through reference to prior electrical and electrochemical measurements on Si/liquid contacts.[23, 24, 26, 36, 39] Near-surface channel conductance measurements of p^+-n-p^+ Si structures have clearly demonstrated the formation of an inversion layer at the *n*-Si channel region when it is in contact with CH_3OH–5.4 mM Me_2Fc–2.9 mM Me_2Fc^+ contacts but not for CH_3OH-$Me_{10}Fc^{+/0}$ contacts.[23] In addition, Mott-Schottky measurements of the *n*-Si/CH_3OH-$Me_2Fc^{+/0}$ system have indicated an equilibrium barrier height of $\approx$ 1.03 V,[24, 29, 39] which is sufficient to drive the system into carrier inversion. The surface recombination velocities of *n*-Si/CH_3OH contacts, after the formation of a Si–OCH_3 surface by contact with CH_3OH-$Me_2Fc^{+/0}$, is < 100 cm s^{-1}, as deduced from current density vs. potential data. Higher *S* values were deduced for similar *n*-Si samples in contact with redox systems, such as CH_3OH-$Me_{10}Fc^{+/0}$, that cannot produce an inversion layer at the *n*-Si surface.[36] Direct measurements of the surface recombination velocity of the alkoxylated *n*-

Si/CH_3OH interface as a function of the electrode potential have shown that at positive (or negative) potentials, where the surface is in inversion (or accumulation), the recombination rates are very low, whereas for surface potentials that produce moderate band bending in the semiconductor, much higher recombination rates are obtained.[36] These results are all in excellent agreement of the predictions based on the Shockley-Read-Hall formulation (equation 7) and with the experimental observations reported herein.

B. Chemical Passivation Due to Si Surface Chemistry as Observed for Silicon in Contact with Inert, Gaseous Ambients

In the work described herein, only H−Si(111) surfaces that had been contacted with CH_3OH-0.05 M $Fc^{+/0}$ solutions showed low surface recombination velocities (or long lifetimes) in N_2, as shown in Figure 1**b**. Thus, only these surfaces had low values of $N_{T,s}$, because only these surfaces displayed low surface recombination rates when in contact with an ambient (*e.g.*, $N_2(g)$ Table 1-3**b**, or CH_3OH-$Me_{10}Fc^{+/0}$ Table 1-3**d**) that did not produce a charge-transfer-derived inversion or accumulation layer at the Si surface.

Exposure of H−Si(111) surfaces to CH_3OH-$Fc^{+/0}$ solutions has been shown previously by infrared and XP spectroscopy to produce an alkoxylated, Si−OCH_3-terminated Si surface,[14, 35] and work reported in Chapter 4 of this thesis demonstrates evidence for Si−OCH_3 formation with extensive FTIR analysis. The recombination data presented here indicate that this alkoxylated Si(111) surface also has a lower electrically active defect density than the water-rinsed atomically smooth H-terminated Si(111) surface also measured under N_2(g) or in contact with THF-$Me_{10}Fc^{+/0}$ or CH_3OH-$Me_{10}Fc^{+/0}$ solutions (Table 1). Exposure of H−Si(111) surfaces to methanolic solutions that do not contain oxidizing agents, or to THF solutions of $Fc^{+/0}$ or $Me_{10}Fc^{+/0}$, results in surface chemistries that do not exhibit chemical passivation, as evidenced by high S values and low lifetimes, when measured under an N_2(g) ambient. Immersion of Si into CH_3OH-I_2 solutions produces Si-OCH_3 bonds as well as a measurable surface coverage of iodine.[35] The data of Table 1 therefore indicate that I_2 is not needed to obtain a low effective S value for (111)-oriented Si in contact with a methanol electrolyte and in fact is deleterious to the electrical properties of such surfaces when their recombination properties are subsequently measured in contact with a N_2(g) ambient. In general, the S values measured herein can therefore be understood using a combination of electrochemical and chemical passivation mechanisms for the various silicon contacts studied in this work.

C. The Effect of the Injection Level on the Photoconductivity Decay Data

Different injection levels were used in this study to sort out the implications of electrochemical and chemical passivation techniques. High-level injection conditions exist when the photoinjected carrier concentrations are larger than the bulk concentration of majority carriers, and these conditions are used to minimize the effects of small amounts of band bending on the observed surface recombination velocities. For sufficiently large amounts of band-bending, *e.g.*, inversion, the minority carrier concentration at the surface exceeds the majority carrier concentration in the dark and hence also exceeds the photoinjected carrier concentration. Under such conditions, the minority carrier concentration at the surface also exceeds the photoinjected carrier concentration and the bands are not sufficiently unbent. Significantly higher light intensities, compared to those calculated from the conventional definition of high-level injection, would be needed in order to flatten the bands and thereby minimize the effects of the equilibrium built-in voltages on the recombination rates. For the inversion and accumulation conditions examined in the work, the recombination rates observed at high-level injection conditions ought to be similar to those observed in low-level injection. This is also in accord with the experimental behavior observed in our studies. It should eventually, of course, be possible to flatten the bands at sufficiently high carrier injection levels, but such conditions were not accessible during the course of this study due to a reduction in the bulk lifetime at higher injected carrier concentrations resulting from Auger recombination processes in such samples.

D. Implications of these Results on Other Studies

The reduction in surface recombination velocity at solid/liquid contacts studied herein that produce an accumulation region in *n*-type Si, *i.e.*, *n*-Si/CH_3OH-$CoCp_2^{+/0}$ contacts, is of interest with respect to the behavior of interfaces formed between acidic aqueous electrolytes and H-terminated Si surfaces. These systems have attracted widespread attention for its low surface recombination velocity and for its high apparent degree of electrical passivation,[33, 34] which has been ascribed to the high degree of structural perfection of the H−Si bonding on such surfaces. Interestingly, infrared spectroscopy indicates that the most well-ordered, H−Si-terminated surfaces are obtained when the Si is exposed to mildly basic NH_4F solutions.[40-42] Etching in acidic media produces an increase in the intensity of infrared vibrational peaks ascribable to -SiH_2 and -SiH_3 species and also produces a broadening of the H−Si monohydride stretching peak.[40, 41, 43, 44] However, the conditions that produce the most structurally ordered monohydride-terminated Si surfaces do not produce the lowest measured surface recombination velocity values once removed from these solutions. Instead, the *S* values measured after contact with neutral or slightly basic aqueous media are in excess of 10^3 cm s^{-1}, whereas the experimentally measured *S* values decrease as the acidity of the electrolyte increases, with *S* becoming less than 100 cm s^{-1} only at $[H^+] > 1.0$ M.[33] Furthermore, the observed *S* values for such contacts are rapidly reversible as the pH of the electrolyte is varied.

This behavior has been ascribed to the reversible protonation of weakly basic defect sites, such that the defect state density is almost completely eliminated (and *S* minimized) only in the most strongly acidic aqueous solutions. The Pourbaix-Ellingham diagram for Si suggests that Si is stabilized with respect to oxidation in aqueous solutions at low pH and open-circuit conditions.[45] The observations described herein suggest another explanation for the observed trend in *S* with variations in pH. In this alternate mechanism, the change in effective *S* values is primarily due to charge-transfer equilibration processes between the Si and the various aqueous electrolytes. Allongue *et al.* have shown that n-type Si surfaces are under accumulation in contact with acidic aqueous media,[46] and they claim that the degree of band bending at the Si/H_2O contact is a function of the acidity of the solution, due to the variation in the electrochemical potential of the electrolyte according to the Nernst equation.

An accumulation of electrons at the Si surface will lead to a low effective S value even for high values of $N_{T,s}$, as has been shown above. The change in band bending as the pH is varied is expected to be rapid and reversible, which is consistent with the observed surface recombination behavior. For these reasons the surface recombination rates and the passivation mechanisms responsible for such rates are the focus of Chapter 3 of this thesis.

V. CONCLUSIONS

The experimentally observed recombination rates for a variety of chemically treated Si surfaces can be explained in the context of both electrochemical and chemical passivation techniques. Low recombination rates, via the electrochemical passivation mechanism, were observed for Si in contact with electrolyte solutions capable of forming either inversion layers or accumulation layers as the Si surface. Except for the CH_3OH−0.050 M $Fc^{+/0}$ solution, these types of Si/liquid contacts are therefore only potentially useful for use in photoelectrochemical energy conversion systems, but do not at present appear to provide routes to the effective passivation of Si surfaces for use in applications outside of these specific media. Surfaces that possess Si-OCH_3 bonds, formed through the reaction of H−Si(111) surfaces with a CH_3OH-$Fc^{+/0}$ solution, are potentially useful in electronic devices since they display show much lower surface recombination velocities in contact with N_2(g) or in contact with CH_3OH-$Me_{10}Fc^{+/0}$ solutions than do H-terminated Si(111) surfaces or similar surfaces that have been exposed to CH_3OH-I_2 or to THF-I_2 solutions. In conjunction with prior measurements of the near-surface channel conductance for p^+-n-p^+ Si structures in contact with CH_3OH-$Fc^{+/0}$ solutions, the data reveal that formation of an accumulation of holes, and not a reduced density of electrical trap sites on the surface, is primarily responsible for the long charge carrier lifetimes observed for Si surfaces in contact with CH_3OH or THF electrolytes containing I_2 or $Fc^{+/0}$. Similarly, the data suggest that an accumulation layer, formed at the surface of Si samples contacted to $CoCp_2^{+/0}$-containing solutions, is primarily responsible for the long lifetimes observed for these contacts. The data also suggest that an analogous electrochemical passivation effect may play a significant role in producing the low recombination rates that are observed for H-terminated Si(111) surfaces in contact with highly acidic aqueous solutions.

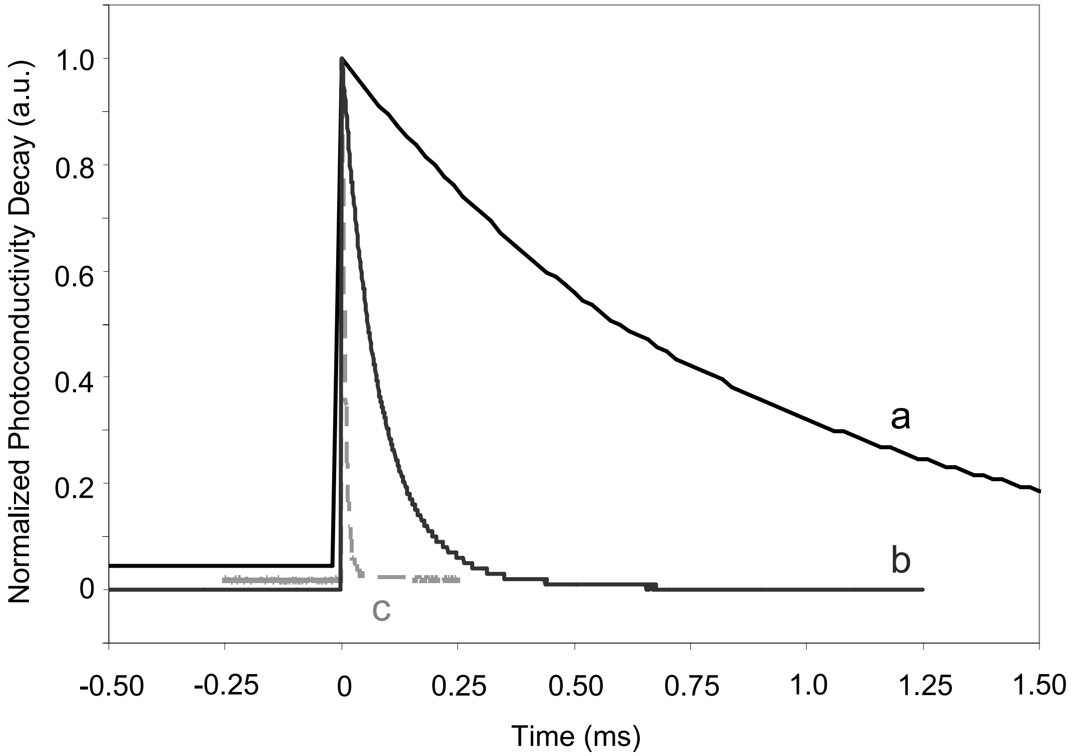

Figure 1: Photoconductivity decays for various silicon contacts.

Time-resolved photoconductivity decays for **a**) (dark solid line) H−Si(111) surfaces in contact with a CH_3OH−0.05 M Fc^0−0.005 M Fc^+ solution, **b**) (gray solid line) the CH_3OH−0.05 M Fc^0−0.005 M Fc^+ contacted sample removed from solution and measured under N_2(g), or **c**) (light gray broken line) freshly etched H−Si(111) measured under N_2(g). The data were well-fitted by single exponential curves (not shown) with time constants of 818 μs, 83.9 μs, and 3.2 μs for **a**, **b** and **c**, respectively. The very long lifetime observed for the sample immersed in CH_3OH-$Fc^{+/0}$ solution, **a**, is bulk recombination limited due to electrochemical passivation of the surface. The Si−OCH_3 terminated sample, **b**, measured in contact with N_2(g) has a distinctly larger lifetime than the H-terminated silicon sample, **c**, demonstrating the chemical passivation imparted by the Si−OCH_3 group under N_2(g).

Table 1: Measured lifetimes for various silicon surface treatments.

		Low Injection		High Injection	
		τ (μs)	S (cm s^{-1})	τ (μs)	S (cm s^{-1})
1a	18 M H_2SO_4	490±50	21±2	-	-
1b	48 % $HF_{(aq)}$	180±60	60±20	460±90	20±4
1c	18 M H_2SO_4-treated, in air	10±1	1000±100	-	-
1d	NH_4F-etched, in air	-	-	16±0.3	625±12
2a	CH_3OH-0.05 M I_2	520±90	19±3	600±300	16±8
2b	N_2	7.8±0.8	1300±100	12±1	810±70
2c	CH_3OH-0.05 M I_2	500±100	20±4	700±200	14±4
3a	CH_3OH-0.05 M Fc^0-0.05 M Fc^+	500±100	20±4	700±200	14±4
3b	N_2	150±60	70±30	140±40	70±20
3c	CH_3OH-0.05 M Fc^0-0.05 M Fc^+	470±40	21±2	600±20	16±1
3d	THF-0.05 M $Me_{10}Fc^0$-0.01 M $Me_{10}Fc^+$	120±20	80±10	101±8	98±8
4a	THF-0.05 M I_2	280±90	30±10	270±90	40±10
4b	N_2	3.7±0.2	$>2\times10^3$	3.8±0.2	2×10^3
4c	THF-0.05 M I_2	300±100	30±10	300±100	30±10
5a	THF-0.05 M Fc^0-0.005 M Fc^+	280±90	30±10	180±90	50±30
5b	N_2	2.7±0.3	$>2\times10^3$	2.9±0.3	$>2\times10^3$
5c	THF-0.05 M Fc^0-0.005 M Fc^+	300±100	30±10	220±160	40±30
5d	THF-0.05 M $Me_{10}Fc^0$-0.01 M $Me_{10}Fc^+$	2.6±0.3	$>2\times10^3$	3.0±0.2	$>2\times10^3$
6a	THF-0.05 M $Me_{10}Fc^0$-0.01 M $Me_{10}Fc^+$	3.0±0.7	$>2\times10^3$	4.0±1.0	$>2\times10^3$
6b	N_2	2.7±0.3	$>2\times10^3$	3.4±0.1	$>2\times10^3$
6c	THF-0.05 M $Me_{10}Fc^0$-0.01 M $Me_{10}Fc^+$	2.8±0.3	$>2\times10^3$	3.0±0.4	$>2\times10^3$
6d	THF-0.05 M Fc^0-0.005 M Fc^+	290±90	30±10	250±60	40±10
7a	CH_3OH-0.01 M $CoCp_2^0$-0.01 M $CoCp_2^+$	730±180	22±5	745±20	21±1
7b	N_2	8±0.6	1920±150	9±0.7	1660±130
7c	CH_3OH-0.01 M $CoCp_2^0$- 0.01 M $CoCp_2^{+a}$	760±110	20±3	750±50	21±1
8a	CH_3CN-0.01 M $CoCp_2^0$- 0.01 M $CoCp_2^+$	375±210	55±35	375±180	50±25
8b	N_2	6±0.1	$>2\times10^3$	6±0.3	$>2\times10^3$
8c	CH_3CN-0.01 M $CoCp_2^0$- 0.01 M $CoCp_2^{+a}$	420±100	40±10	390±70	40±10

[a] Samples have been rinsed with solvent and re-etched

Table 2: Measured lifetimes for air-oxidized silicon samples.

		Low Injection		High Injection	
		τ (μs)	S (cm sec^{-1})	τ (μs)	S (cm sec^{-1})
9a	CH_3OH-0.05 M I_2	400 ± 100	24 ± 6	500 ± 200	19 ± 8
9b	N_2(g)	16 ± 5	600 ± 200	12 ± 1	800 ± 100
9c	CH_3OH-0.05 M I_2	400 ± 200	20 ± 10	500 ± 200	19 ± 8
9d	THF-0.05 M $Me_{10}Fc^0$-0.01M $Me_{10}Fc^+$	30 ± 10	300 ± 100	23 ± 5	420 ± 90
10a	CH_3OH-0.05 M Fc^0-0.05 M Fc^+	300 ± 100	30 ± 10	30 ± 100	30 ± 10
10b	N_2(g)	7 ± 2	1400 ± 400	9 ± 2	1100 ± 200
10c	CH_3OH-0.05 M Fc^0-0.05 M Fc^+	150 ± 50	60 ± 20	220 ± 40	44 ± 8
10d	THF-0.05 M $Me_{10}Fc^0$-0.01M $Me_{10}Fc^+$	7 ± 2	1400 ± 400	8 ± 1	12 ± 200

2.2 Measurement of the Barrier Heights for Contacts that Form High Surface Hole Concentrations

ABSTRACT

Near-surface channel conductance measurements, differential capacitance vs. potential measurements, and surface recombination velocity measurements have been performed on (111)- and (100)-oriented *n*-type Si samples in contact with nitrogen and or liquid electrolyte solutions containing I_2, I_2/I^-, ferrocene$^{+/0}$, or decamethylferrocene$^{+/0}$ in either methanol or tetrahydrofuran. Si/liquid contacts that displayed a low effective surface recombination velocity, *S*, corresponded to those that formed an inversion layer at the solid/liquid contact as indicated by channel conductance measurements or by differential capacitance vs. potential measurements. Contacts that did not produce an inversion layer at the Si surface did not produce low effective *S* values. The observed behavior is consistent with the known energetics of Si/liquid contacts and provides an explanation for the low effective *S* values observed in these systems.

I. INTRODUCTION

We have previously demonstrated that immersion of H-terminated (111)-oriented Si surfaces into alcoholic solutions that contain mild oxidants, including ferrocenium (Fc^+), I_2, and Br_2, produces a common surface chemistry involving formation of surficial Si alkoxyl (Si-OR) groups.[35, 47] The effective surface recombination velocity, *S*, of all of these Si/liquid interfaces is $<1\times10^2$ cm s^{-1}.[4, 15, 16, 25, 48] The effective surface recombination velocity of Si in contact with tetrahydrofuran (THF) solutions containing either I_2 or $Fc^{+/0}$ is also quite low,[4, 16, 25, 48] even though these electrolytes do not produce surficial Si-alkoxide groups. [35, 47] This behavior was previously ascribed to the formation of an inversion layer at the n-type Si surface that produces low effective surface recombination velocities for a wide range of actual carrier trap densities at the n-Si/liquid interface.[4, 25] This hypothesis was supported by the rapid, reversible increase in *S* that was observed when these surfaces were removed from contact with the electrolytes and measured in inert N_2(g) ambients, and by the observation of high *S* values when such surfaces were placed in contact with electrolytes that were not expected to produce a high charge carrier concentration at the Si/liquid contact. [4, 25] In this work, we report the results of near-surface channel conductance measurements and differential capacitance vs. potential measurements that directly confirm the formation of an inversion layer when n-type Si is placed in contact with these electrolyte solutions. These measurements also show that the disappearance of the inversion layer is reversible when these surfaces are put in contact with other types of ambients. Finally, the formation of an inversion layer is completely correlated with an observed low effective *S* value for these systems.

II. EXPERIMENTAL

Using conventional Si device fabrication processes, two regions of p^+-Si (each 0.25 cm × 0.84 cm separated by 0.1 cm along the long axis) were formed in 40 Ω-cm resistivity, (100)-oriented, 525-μm thick n-type Si substrates. Ohmic contacts of Al were then formed on top of the p^+-Si regions, producing a structure that allowed measurement of the conductance in the near-surface channel between the two p^+-Si regions. Details of the fabrication process have been described previously.[23] A significant dark dc conductance between the implanted p^+-Si regions can only be observed when an inversion layer has been formed in the near-surface region of the n-type Si sample. Otherwise, high-impedance rectifying behavior should be observed for the blocking p^+-n-p^+ current path.

To insure the uninterrupted formation of any inversion layer in the n-Si sample, the full area of the n-Si surface between the two p^+ regions, along with a small portion of the p^+-Si regions, was exposed to the ambients of interest. Contact of redox-active electrolytes to portions of the exposed p^+-Si regions and to their Ohmic contacts will produce a component of the measured conductance that arises from Faradaic current flow through the electrolyte solution.[23] This undesirable but unavoidable component of the signal is minimized by using relatively low concentrations of redox species and can be readily separated from the component that corresponds to the current path through the solid by analyzing the impedance data as a function of frequency.[23]

III. RESULTS AND DISCUSSION

Figure 2 displays the impedance vs. frequency data for a Si channel structure in contact with N_2(g), CH_3OH−0.1 M $LiClO_4$, CH_3OH−0.1 M $LiClO_4$−0.5 mM decamethylferrocene ($Me_{10}Fc$) −0.5 mM $Me_{10}Fc^+$, CH_3OH−0.1 M $LiClO_4$−0.5 mM I_2, and CH_3OH−0.1 M $LiClO_4$−0.5 mM Fc−0.5 mM Fc^+, respectively. The Si/CH_3OH-$Fc^{+/0}$ and Si/CH_3OH-$Me_{10}Fc^{+/0}$ data are in accord with prior work[23] and demonstrate that the measured channel impedance is much lower, and has a significantly different dependence on frequency, when the n-type Si is in contact with the CH_3OH−0.1 M $LiClO_4$−$Fc^{+/0}$

redox system than when it is in contact with either $N_2(g)$ or $CH_3OH-0.1$ M $LiClO_4$. Analysis of these data to extract the low frequency channel conductance yields an equilibrium barrier height of ≈ 1.0 V for the *n*-Si/CH_3OH-$Fc^{+/0}$ contact[23] and provides direct evidence for formation of an inversion layer at this solid/liquid contact. However, the redox potential of the CH_3OH-$Me_{10}Fc^{+/0}$ solution is not positive enough to produce an inversion layer on n-type Si,[36, 49] so the impedance spectrum of this contact primarily represents the residual Faradaic conductance between the p^+ regions facilitated by interfacial charge carrier exchange with the redox-active electrolyte solution. Similar to the case of $CH_3OH-0.1$M $LiClO_4-0.5$ mM $Fc^{+/0}$, the low frequency channel conductance increased substantially when the sample was in contact with the $CH_3OH-0.1$ M $LiClO_4-0.5$ mM I_2 solution, but not when the sample was in contact with either $N_2(g)$ or $CH_3OH-0.1$ M $LiClO_4$.

Table 3 summarizes the analysis of the impedance data and also presents *S* values measured for these same Si/ambient contacts using photoconductivity decay methods[4, 25] on long lifetime, float-zone, double-side polished, (111)-oriented n-Si samples. The Si/liquid contacts that showed a low effective *S* value as probed by photoconductivity decay measurements also formed an inversion layer in contact with the electrolyte solutions. Although the near-surface channel conductance experiments reported herein were performed using (100)-oriented Si surfaces, the flat-band potentials of (100)- and (111)-oriented Si surfaces are sufficiently similar[24] that the general conclusions derived from these measurements regarding the electrochemical potentials of the electrolyte solutions required to form an inversion layer are expected to be applicable, with only minor changes, to (111)-oriented Si surfaces.

Differential capacitance (C^{-2}) vs. potential (E) data were also collected to independently confirm the formation of an inversion layer for (111)-oriented Si surfaces in contact with the electrolyte solutions of interest (Table 4). The slopes of plots of C^{-2} vs. E yielded values in agreement with those calculated from the known dopant density of the sample and the calculated C^{-2} values at each potential were independent of frequency, with a phase angle of >87°, over the frequency range 5-100 kHz. The barrier heights calculated from the x-intercepts of such C^{-2} vs. E plots for all of the (111)-oriented n-Si/liquid contacts clearly confirmed that an inversion layer had been formed as a result of charge transfer equilibration between the Si and the I_2/I^- and $Fc^{+/0}$ systems in either THF or CH_3OH. Higher concentrations of redox-active reagents were required in these experiments to insure negligible concentration polarization in the C^{-2} vs. E experiments, but low effective S values were also measured under these conditions for contacts that formed inversion layers at the n-Si surface (Table 4).

From the steady-state Shockley-Read-Hall (SRH) treatment, the surface recombination rate, U_s, for a surface with traps at a single midgap energy is a function of the surface electron-capture and hole-capture rate constants, $k_{n,s}$ and $k_{p,s}$, respectively, the electron and hole concentrations at the surface of the semiconductor in the dark, $n_{s,0}$ and $p_{s,0}$, respectively, and the injected electron and hole densities, Δn_s and Δp_s, respectively. This equation was presented in the previous section but is reproduced here for clarity.

$$U_s = N_{T,s}\frac{k_{n,s}k_{p,s}(n_{so}\Delta p_s + p_{so}\Delta n_s + \Delta n_s \Delta p_s)}{k_{n,s}(n_{so} + \Delta n_s + n_{1,s}) + k_{p,s}(p_{so} + \Delta p_s + p_{1,s})} \tag{7}$$

In equation (7), $N_{T,s}$ is the surface trap density and $n_{1,s}$ and $p_{1,s}$ are the electron and hole concentrations, respectively, when the Fermi level is located at the energy of the surface trap. A generalized SRH model, including effects of band bending and/or carrier inversion at Si surfaces, has been described recently.[4, 39] According to this generalized SRH model, low effective *S* values can either be produced by an inherently small value of the surface trapping velocity, or by a higher, and potentially variable, value of $N_{T,s}$ accompanied by a high value of p_{so} (or n_{so}) in the denominator of equation 7.[2, 4] The experiments described herein clearly indicate that the latter situation, as a result of inversion, is occurring at the n-Si/CH_3OH-$Fc^{+/0}$, *n*-Si/CH_3OH-I_2, *n*-Si/THF-I_2, and *n*-Si/THF-$Fc^{+/0}$ contacts.

This inversion effect accounts for the similar surface recombination velocity behavior observed for silicon samples in contact with these solutions, even though the surface chemistries are known to be quite different. Exposure of Si to solutions of $Fc^{+/0}$ in alcohols produces Si-alkoxide bonds,[35, 47] whereas exposure to CH_3OH-I_2 solutions produces partial alkoxylation and partial Si-I bonding.[35, 47] In contrast, no significant Si methoxylation is formed as a result of exposure of crystalline Si to THF-$Fc^{+/0}$ solutions.[47] The chemical differences between these surfaces are manifested by the differing *S* values obtained for these systems only when in contact with N_2(g) or in contact with pure THF or CH_3OH. Such chemical differences do not significantly change the effective *S* values measured in contact with the oxidizing electrolytes ($Fc^{+/0}$, Br_2, I_2) due to the inversion layer that is formed under such conditions. The results described herein also indicate that the Si surfaces studied in this work do not display low *S* values in contact with N_2(g) or in contact with room air. Such surfaces will therefore have limited use for passivation of Si-based electrical devices. This stands in contrast to the passivation of Si through formation of surficial Si-alkyl bonding, which has recently been demonstrated to produce persistent, low *S* values in contact with either N_2(g) or air.[10]

IV. CONCLUSIONS

In summary, near-surface channel conductance measurements and differential capacitance vs. potential measurements have provided direct evidence for the formation of an inversion layer in *n*-type Si surfaces in contact with a variety of electrolytes of interest. This behavior is consistent with the known energetics of Si/liquid contacts[36] and explains the low effective surface recombination velocity values measured for these *n*-type Si/liquid contacts using photoconductivity charge carrier decay methods.[4, 15, 16, 25, 35, 47, 48] Removal of the *n*-type Si surfaces from these electrolyte solutions eliminates the inversion layer, increases the effective surface recombination velocity to values in excess of 1×10^2 cm s^{-1}, and produces values of *S* that are different for all of these chemically different surfaces.[4, 25]

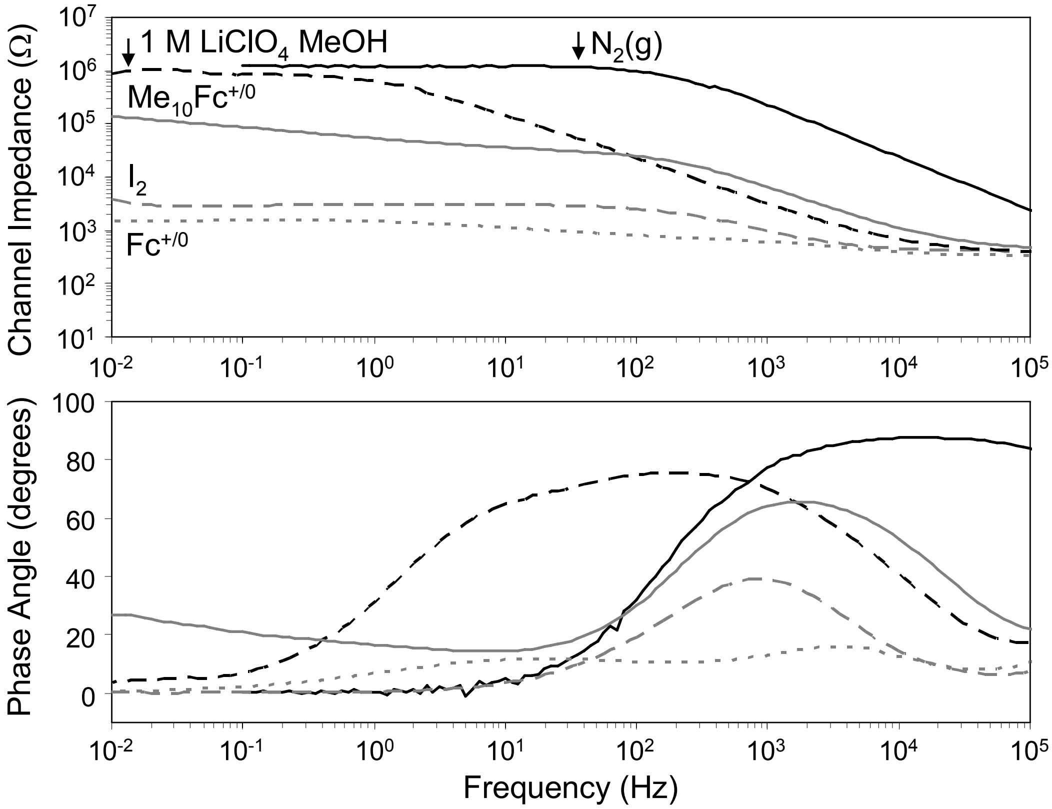

Figure 2: Bode plot for the *p*$^+$-*n*-Si(111)-*p*$^+$ channel impedance device in contact with various redox solutions.

Impedance and phase angle vs. frequency for the *p*$^+$-*n*-Si(100)-*p*$^+$ Si devices in contact with N_2(g) (solid black line), CH_3OH–0.1 M $LiClO_4$ (broken black line), CH_3OH–0.1 M $LiClO_4$–0.5 mM $Me_{10}Fc$−0.5 mM $Me_{10}Fc^+$ (solid gray line), CH_3OH–0.1 M $LiClO_4$–0.5 mM I_2 (broken gray line), and CH_3OH–0.1 M $LiClO_4$–0.5 mM Fc−0.5 mM Fc^+ (dotted gray line).

Table 3: Near-surface channel conductance measurements and surface recombination velocities for silicon in various ambients.

Device Contact	$\lvert Z_0 \rvert^{a}$ (kΩ)	S (cm sec^{-1})
N_2(g)	2,700 ± 900	1160 ± 190
CH_3OH – 0.1 M $LiClO_4$	2,400 ± 200	1110 ± 110
CH_3OH – 0.1 M $LiClO_4$ – 0.5 mM $Me_{10}Fc^{+/0}$	150 ± 10 [b]	1765 ± 95
CH_3OH – 0.1 M $LiClO_4$ – 0.5 mM I_2	2.9 ± 0.1	63 ± 20
CH_3OH – 0.1 M $LiClO_4$ – 0.5 mM $Fc^{+/0}$	1.5 ± 0.1	38 ± 7

[a] Magnitude of the channel impedance as the measurement frequency, *f*, goes to zero. Standard deviations of Z_0 and S represent variations in the mean values for at least three independent trials of each type of Si contact. [b] The channel impedance presented for $Me_{10}Fc^{+/0}$ represents the mean impedance value evaluated at 0.01 Hz and does not represent a true extrapolation to $f = 0$. A major contribution of this impedance is due to Faradaic charge transfer into the solution as indicated by both a non-zero phase angle and a frequency-dependent impedance.

Table 4: Barrier height and surface recombination velocities for various Si/liquid contacts.

Si/Liquid Contact	Barrier Height (V)	S (cm sec^{-1})[a]
CH_3OH – 0.1 M $LiClO_4$ – 0.05 M $Fc^{+/0}$	0.95 ± 0.03	16 ± 1
CH_3OH – 0.1 M $LiClO_4$ – 0.05 M I_2/I^-	0.83 ± 0.05	14 ± 4
THF – 0.1 M $LiClO_4$ – 0.05 M Fc^0 – 0.005 M Fc^+	1.04 ± 0.03	50 ± 30
THF – 0.1 M $LiClO_4$ – 0.05 M I_2/I^-	0.93 ± 0.09	30 ± 10

[a] Data are from Gstrein *et al*.[4]

2.3 Measurement of the Barrier Heights for Contacts that Form High Surface Electron Concentrations

ABSTRACT

The surface properties of silicon in contact with various redox couples have been measured to demonstrate the absence of Fermi-level pinning. Specifically, the barrier heights of both *n*-Si(111) and *p*-Si(111) have been measured in solutions of MeCN-$Me_{10}Fc^{+/0}$ and MeCN-$CoCp_2^{+/0}$ as 0.66 ± 0.1 and 0.09 ± 0.01 for *n*-Si(111), and 0.69 ± 0.1 and 1.1 ± 0.1 for *p*-Si(111), respectively. These measurements indicate that silicon in contact with solutions of well-defined redox potentials can display barrier heights that track the cell potential by a slope of close to 1, instead of the experimentally observed value of 0.27 for silicon-metal contacts.

I. INTRODUCTION

Semiconductor/liquid junctions offer a promising approach to the direct photoelectrolysis of water, providing an alternative to supplying photovoltaic-based electricity to an electrolysis unit. Amongst the potential advantages of direct photoelectrolysis are system integration of the energy production and storage functions, elimination of fixed costs associated with an invertor, grid, bus wiring, unfavorable scaling of the efficiency of electrolysis units at high input currents, and the ability to make massively parallel connections to a series of microscale absorber devices.

However, to compete favorably on an efficiency basis with diffused homojunctions, Fermi level pinning must be avoided at semiconductor/liquid interfaces. For example, Si/metal contacts generally have resulted in the equilibrium Fermi level, $\boldsymbol{E_{F}}$,, located at 0.4−0.9 eV from the Si conduction band edge energy ($\boldsymbol{E_{CB}}$), which, along with majority-carrier based thermionic emission currents, leads to only moderate (0.3−0.4 V) open-circuit voltages (V_{oc}) on *n*-Si and typically produces near-Ohmic contacts on *p*-Si. In contrast, *p*-type Si/CH_3CN-cobaltocene ($CoCp_2^{+/0}$) contacts yield V_{oc} values of 0.52−0.6 V,[50] which is comparable to the V_{oc} values obtained under such conditions from diffused Si homojunctions. We have previously suggested that the extremely low surface recombination velocity, *S*, values (<10 cm s^{-1}) of *p*-Si/CH_3CN-$CoCp_2^{+/0}$ contacts is consistent with screening of surface trap recombination resulting from a very small difference between $\mathbf{E}_{f}$ and $\mathbf{E}_{cb}$ that is produced by equilibration with the $CoCp_2^{+/0}$ redox couple.[4] The resulting large surface electron concentration (n_s) will thereby produce a low effective *S* through an increase in the denominator of the Shockley-Read-Hall expression for surface recombination.[4] In this work, we provide direct evidence, obtained from near-surface channel conductance measurements, open-circuit frequency spectra, and differential capacitance vs. voltage measurements supporting the hypothesis that *p*-Si/CH_3CN-$CoCp_2^{+/0}$ contacts are under strong inversion, possessing very high equilibrium barrier height ($\phi_b = 1/q(\mathbf{E}_{cb}-\mathbf{E}_f)$) values. We additionally report open-circuit frequency spectra and current density vs. potential (*J*-*E*) data indicating that *n*-Si/CH_3CN-$CoCp_2^{+/0}$ contacts are under accumulation conditions, in contrast to the Fermi level pinning behavior exhibited by Si/metal contacts.

II. EXPERIMENTAL

A. Materials

For differential capacitance vs. potential measurements, wafers of 1.38 Ω-cm ($N_A = 1.0\times10^{16}$ cm^{-3}) *p*-Si(111) ± 4° were obtained from Silicon Quest International and were cut into pieces approximately 1.4 cm × 1.0 cm. Aluminum was sputtered on the unpolished back sides of these wafers, which were subsequently annealed at 450°C in 95:5 N_2(g):H_2(g) for 20-30 min. Wafers of 4.18 Ω-cm ($N_D = 1.03\times10^{15}$ cm^{-3}) *n*-Si(111) ± 0.5° were obtained from Crysteco and were cut into similarly sized pieces. In order to make Ohmic contacts that were free of stray capacitances, it was necessary to first pre-etch the *n*-Si(111) wafer pieces for 30 seconds in buffer HF (BHF) to remove the native oxide and immediately contact the unpolished back side with Ga-In eutectic. The back contact and the edges of the Si samples were covered with insulating white epoxy (Loctite 1C Hysol Epoxi-Patch Adhesive).

A platinum working electrode was obtained from BAS. Prior to use, the electrode was polished with 1 micron diamond polish (South Bay Technology, Inc, P/N: DS010-16, Lot#:6991), rinsed with water and acetone, sonicated in water for 5 min, polished with 0.05 micron alumina polish (South Bay Technology, Inc, P/N: AS0005-16, Lot#:7023), rinsed with water and acetone, sonicated for 5 min in water, rinsed again with water, then blown dry with nitrogen. Subsequent polishing was performed only with the 0.05 micron polish.

B. Differential Capacitance vs. Potential Measurements

A Schlumberger Model 1260 frequency response analyzer and a Solartron SI 1287 Electrochemical Interface potentiostat were controlled through a GPIB port using CorrWare and ZPlot Software (Scribner Associates Inc.). Impedance spectra of the silicon/liquid contacts were obtained using sinusoidal, 10 mV amplitude, ac signals of various frequencies ranging from $1–10^5$ Hz. The frequency range for Mott-Schottky analysis was always 3 decades wide and centered in the region where the phase angle was dominated by the parallel capacitance.

A glass cell, cleaned with aqua regia prior to each use, was used with a piece of Pt mesh for the counter electrode and a Pt wire as a reference electrode. The cell potential of the metallocene solution was measured with an Ag/Ag^+ electrode both before, by removing some solution from the cell, and after measurements with silicon electrodes. The Ag/Ag^+ electrode was not used in the cell to minimize any contamination by Ag^+ that could be electrode deposited on the silicon surface.

In preparation for all electrochemical impedance measurements, each silicon electrode was rinsed twice in succession with water, methanol, acetone, methanol, and water, blown dry with nitrogen, and then etched for 20 min in $N_2(g)$-bubbled 40% NH_4F, which had been degassed with N_2 for at least 1 hour prior to electrode etching, to obtain atomically flat surfaces. After rinsing with water and drying under a stream of nitrogen, these electrodes were quickly brought into a nitrogen flush box for analysis. An initial open-circuit measurement was made in the dark for 5 min to ensure a stable cell had been formed. Then an open-circuit frequency sweep was measured using a 10 mV ac amplitude excitation with 0 V applied bias relative to open circuit with a frequency range of 10^5 to 10 Hz taking 10 data points per frequency decade. Afterwards, an IV curve was taken in the dark followed by another 5 min open-circuit frequency sweep before the Mott-Schottky analysis began. In all cases, the Mott-Schottky sweep would begin at the most negative potential, step in 0.05 V increments toward the most positive potential, and step back to the most negative potential in 0.05 V increments, to assess the reproducibility of the measurement and to make sure the reverse bias potentials were not deleteriously affecting the surface either through oxidation for *n*-type or metallic electroplating for *p*-type. Directly after the Mott-Schottky sweeps, a 5 min open-circuit potential was measured, followed by another open-circuit frequency sweep and one more 5 min open-circuit potential measurement. The presented Mott-Schottky data were always performed on brand new freshly etched electrodes that had not undergone any previous electrochemistry.

The surface area of each electrode was determined photographically by using the ImageSXM program. The dopant densities of each wafer was calculated by running four-point-probe measurements in the dark near the center of a each uncut wafer that had first been pre-etched in BHF for 30 sec to remove any native oxide. After the 4-point probe measurement, the wafer was then cut into the electrode sized pieces and the region where the 4 probes touched the wafer was discarded.

C. Near-Surface Channel Conductance Measurements

The fabrication and data analysis of the near-surface channel device used in this study are described in the Appendix and in Chapter 3 of this thesis.

III. RESULTS AND DISCUSSION

Figure 3 and Figure 4 display differential capacitance vs. potential data for the *p*-Si(111)/CH_3CN-$CoCp_2^{+/0}$, *p*-Si(111)/CH_3CN-$Me_{10}Fc^{+/0}$, and *n*-Si(111)/CH_3CN-$Me_{10}Fc^{+/0}$ contacts. Each solution liquid contact was measured over the potential range four times, which is presented, to show the stability and reproducibility of the contact during measurement. The data show that robust semiconductor liquid contacts were formed. The high frequency capacitive region of the impedance data showed very negligible frequency dispersion with CPE_P values greater than 0.98. The differential capacitance vs. potential data were well-fitted by a straight line with slopes that were within a factor of 1.6 of the dopant density of the sample. The resulting barrier heights were ϕ_b=1.13 ± 0.050 V, 0.69 ± 0.10 V, and 0.66 ± 0.10 V for the *p*-Si(111)/CH_3CN-$CoCp_2^{+/0}$, *p*-Si(111)/CH_3CN-$Me_{10}Fc^{+/0}$, and *n*-Si(111)/CH_3CN-$Me_{10}Fc^{+/0}$ contacts, respectively. The barrier height value for *p*-Si(111) in contact with $CoCp_2^{+/0}$ contrasts with the value of ϕ_b =0.2−0.4 that is observed for Au, Ni, Pt, and other metal contacts to *p*-type Si.[1] Barrier height values for *n*-Si(111) and *p*-Si(111) in $Me_{10}Fc^{+/0}$ demonstrate that the Fermi level is near midgap for these contacts as expected given the recombination rates previously measured.[4, 25] The rectifying current-voltage profiles for these silicon liquid contacts in the dark are presented in Figure 5. As expected from the barrier height data, the *p*-Si(111)/MeCN-$Me_{10}Fc^{+/0}$ contact displays a larger reverse bias dark current than the *p*-Si(111)/MeCN-$CoCp_2^{+/0}$ contact.

Contact of *n*-Si(111) to a MeCN-$CoCp_2^{+/0}$ solution resulted in an Ohmic contact as shown in Figure 6. The data show that the *n*-Si(111) electrode is able to pass milliamps of non-rectifying current up until a current limited by diffusion of redox species to the electrode. This response is only expected for accumulated contacts and demonstrates that *n*-Si(111) contacts possess a high surface electron concentration as postulated based on the charge carrier lifetimes measured in this solution.[4] Due to the Ohmic contact formed in these solutions, differential capacitance vs. voltage data cannot be collected. Frequency spectra were obtained, however, at open circuit. The high frequency, 100 kHz–1 kHz, response of the cell displayed a response expected for a standard three-element circuit containing a resistor in series with a parallel combination of a resistor and capacitor. This data range was fit to the three-element circuit to obtain a capacitance value of 2,000 ± 600 nF cm^{-2}, which is too small for a Helmholtz capacitance, but in the right range for an accumulation layer (see Chapter 3.1). This capacitance value, if it corresponds to the accumulation layer at the silicon surface, leads to a barrier height of 0.091 ± 0.016 V, which is reasonable for an accumulation layer. The low frequency region of the open-circuit frequency spectrum is dominated by a Warburg, diffusion limited, profile. It is possible that the high frequency region of the spectra can adequately probe the differential capacitance of the accumulation layer only if the excitation frequency is faster than the rate constant for electron transfer.

To facilitate the analysis of the C^{-2}-E data using a simple equivalent circuit, the C^{-2}-E data must be collected at reverse bias, *i.e.*, significantly away from equilibrium conditions. To confirm that the *p*-Si/CH_3CN-$CoCp_2^{+/0}$ contact is under inversion at equilibrium, both open-circuit frequency spectra and near-surface channel impedance measurements were performed on such contacts. Open-circuit frequency spectra were also fit to a simple three element circuit, since the silicon in presumed to be under inversion at open circuit, and the resulting capacitance yields barrier heights of 0.87 ± 0.06 V. If, however, the average deviation of the Mott-Schottky slope, 1.6, is presumed to be due to an error in the calculation of the dopant density, then the barrier heights calculated with open-circuit frequency analysis yield barrier heights of 1.15 ± 0.08 V, which is within error to the value obtained using the Mott-Schottky technique. The direct correlation of these two techniques in this manner provide strong evidence that the systematic deviation observed in the Mott-Schottky slope is in fact due to an error in the calculation of the dopant density. Open-circuit frequency analysis was also performed on the *n*-Si(111) and *p*-Si(111) contacts to MeCN-$Me_{10}Fc^{+/0}$ solutions; multiple relaxation processes, however, were observed that obscured analysis.

Channel impedance data for n^+-*p*-Si(111)-n^+ devices exposed to various conditions are shown in Figure 7. Measurement in a clean nitrogen environment displayed a large low frequency resistance, characterized by a phase angle close to zero. This demonstrates that the *p*-Si(111) channel is not under inversion and current is forced through the rectifying n^+-p contacts separating the source and drain. When in contact with pure or 1.0 M $LiClO_4$-containing MeCN, the low frequency channel impedance displays a relatively low resistance. The cause for this is unknown but possible reasons are discussed below. Contact of the devices to 1 mM $CoCp_2^{+/0}$ in 1.0 M $LiClO_4$ MeCN drives the low frequency impedance to an even lower resistance indicating that the surface has been driven further into inversion. Barrier height values can be numerically calculated from the low frequency resistance using an approach demonstrated later in Chapter 3. This method leads to a barrier height of 1.071 ± 0.014 V, which is in very good agreement with the other methods used to calculate the barrier height.

Contact of the n^+-p-Si(111)-n^+ device to a 1 mM $Me_{10}Fc^{+/0}$ solution of 1.0 M $LiClO_4$–MeCN yields a much larger low frequency impedance, which is characterized by a non-zero phase angle, and is expected for Faradaic charge transfer into solution through the exposed source and drain contacts. This result demonstrates that a well-defined stable cell potential is able to reverse the inversion effect observed in pure or 1.0 M LiClO4 MeCN solutions. The current voltage properties of the $Me_{10}Fc^{+/0}$ contact demonstrates that the current is not flowing through the central channel region and that a barrier height can not be extracted from this measurement. Instead only an upper bound on the barrier height can be obtained; an upper bound of 0.91 V is obtained that is consistent with the 0.69 ± 0.10 V value obtained with Mott-Schottky analysis.

The low channel impedance obtained in MeCN solutions will now be discussed. Figure 8 displays the response of the n^+-p-Si(111)-n^+ device to various amounts of liquid or MeCN vapor. The largest channel impedance is observed immediately after bringing the device into the box. Upon exposure of the device to MeCN vapor, by placement near liquid MeCN, the low frequency channel resistance gradually decreases with exposure time. The lowest values are obtained upon exposure of the device to neat MeCN values. This trend can be reversed by pumping the device under vacuum for several tens of minutes and performing a measurement immediately after bringing it into a nitrogen atmosphere. This reversibility indicates that the response is due to physisorbed vapors and explains why it is easily over in the presence of a stable well-defined cell potential such as $Me_{10}Fc^{+/0}$. The nature of the MeCN vapor detection is unknown but could either be due to an inherent response to a quasi-liquid layer of neat MeCN, or to some combined MeCN-H_2O layer.

IV. CONCLUSIONS

The data herein confirm the hypothesis that *p*-Si/$CoCp_2$ contacts are in inversion and that *n*-Si/$CoCp_2$ contacts are in accumulation. These observations provide direct evidence in support of the hypothesis that low SRV values observed for Si/$CoCp_2$ contacts is not a direct result of an inherently low surface trap density but rather is a manifestation of the high surface electron concentration and consequently low surface hole concentration, producing a low steady-state rate of electron-hole surface recombination at such contacts. The data also demonstrate that it is possible to manipulate the Fermi-level at semiconductor/liquid contacts in a way that is not possible at semiconductor/metal contacts. In this fashion, high photovoltages can be produced at suitable Si/liquid contacts without having to form an implanted p-n junction, but only from the inherent energetic equilibration of the semiconductor/liquid interface. As long as catalysts don't disrupt this equilibration, it should be possible to maintain high barrier heights and therefore high photovoltages from such systems.

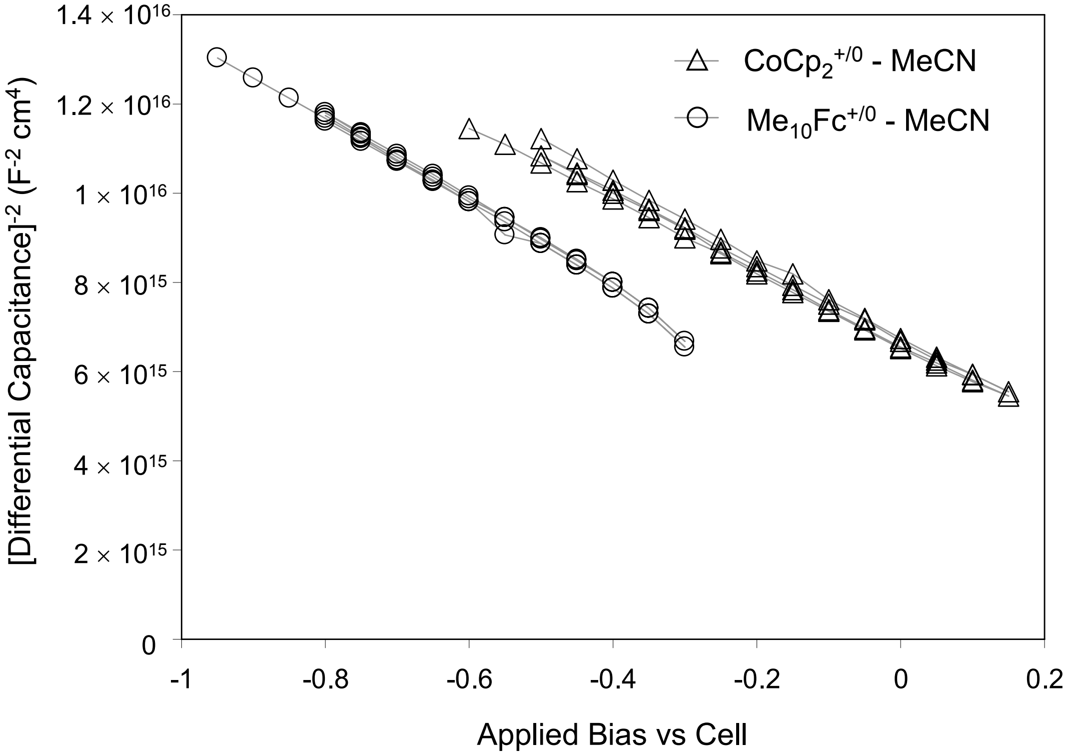

Figure 3: Differential capacitance vs. potential plots for *p*-Si(111) electrodes in contact with metallocene solutions.

Differential capacitance vs. potential plots are displayed for *p*-Si(111) electrodes in contact with solutions of either MeCN-$CoCp_2^{+/0}$ (triangles) or MeCN-$Me_{10}Fc^{+/0}$ (circles). The potential is in volts and is reported with respect to the cell potential.

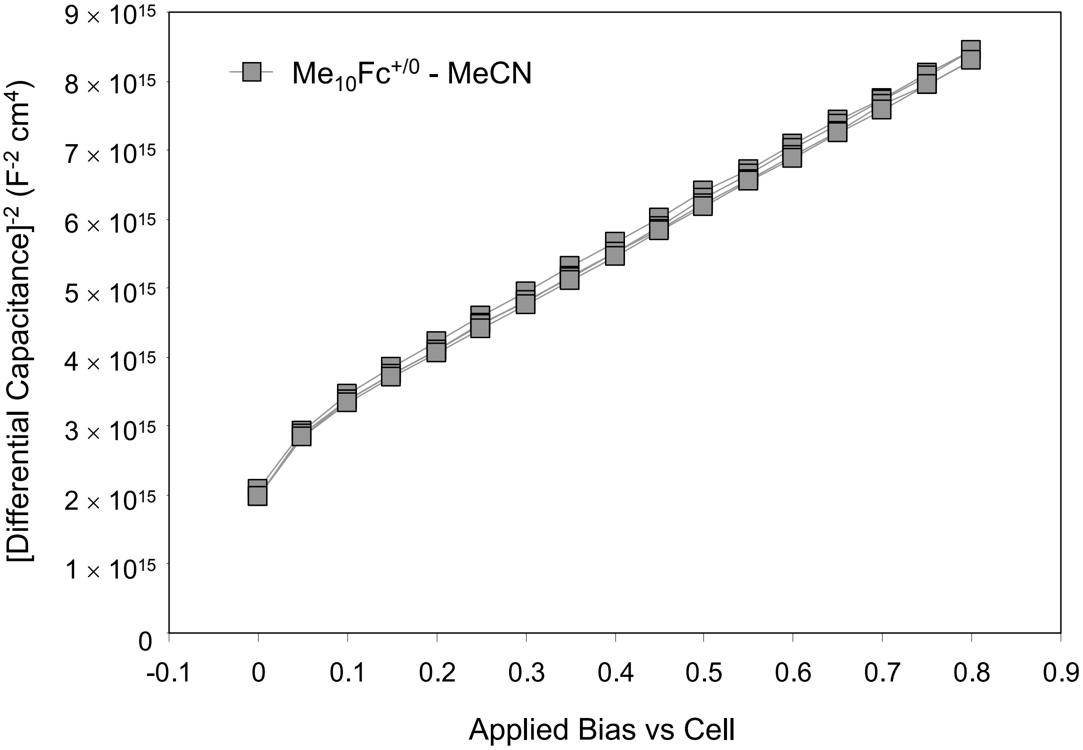

Figure 4: Differential capacitance vs. potential plot for an *n*-Si(111) electrode in contact with an MeCN-Me$_{10}$Fc$^{+/0}$ solution.

The potential is in volts and is reported with respect to the cell potential.

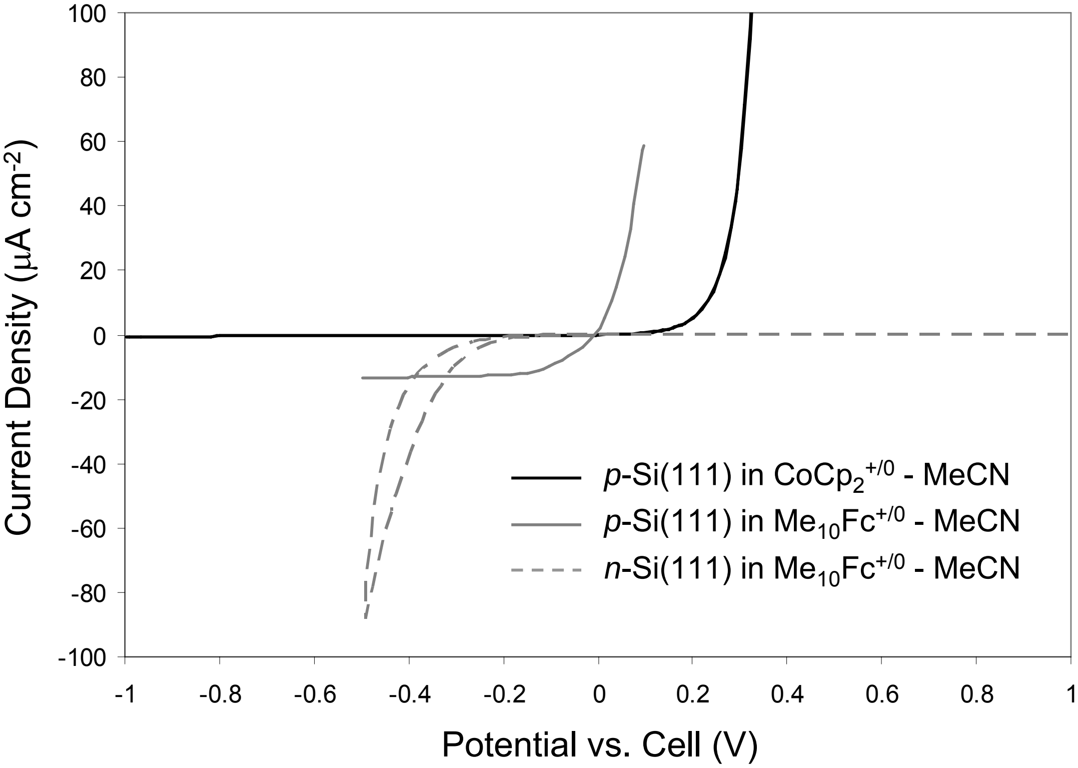

Figure 5: Current vs. potential responses for *n*-Si(111) and *p*-Si(111) electrodes in contact with either MeCN-$CoCp_2^{+/0}$ or MeCN-$Me_{10}Fc^{+/0}$ solutions in the dark.

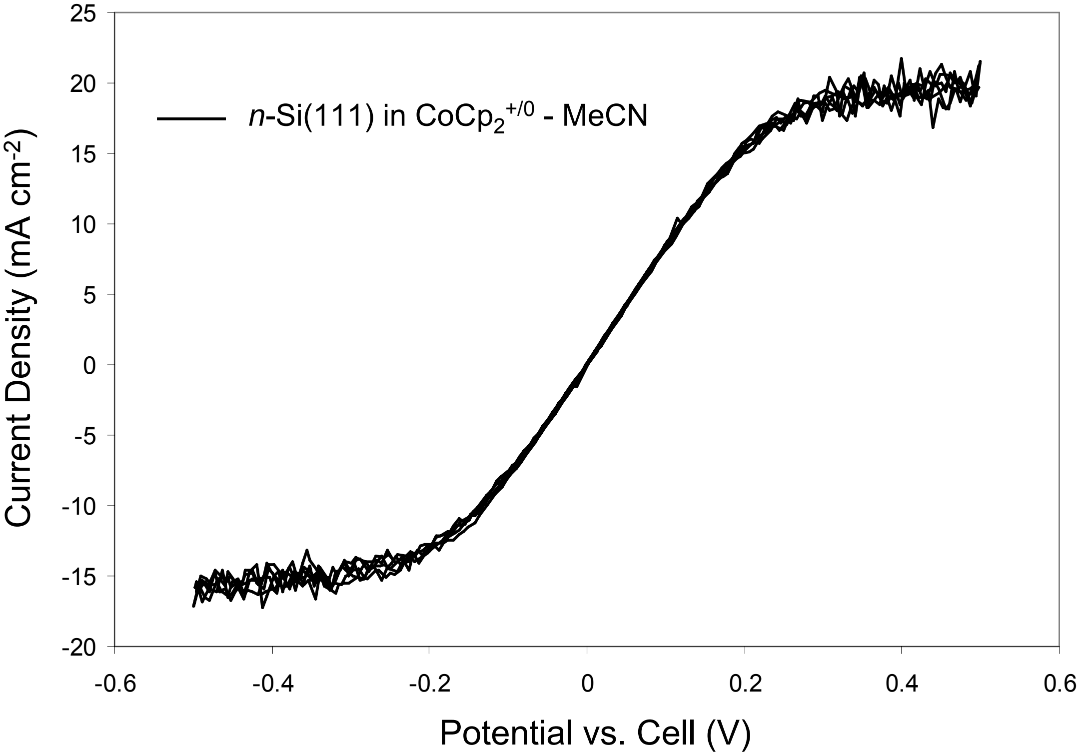

Figure 6: Current-voltage response for an *n*-Si(111) electrode in a MeCN-$CoCp_2^{+/0}$ solution.

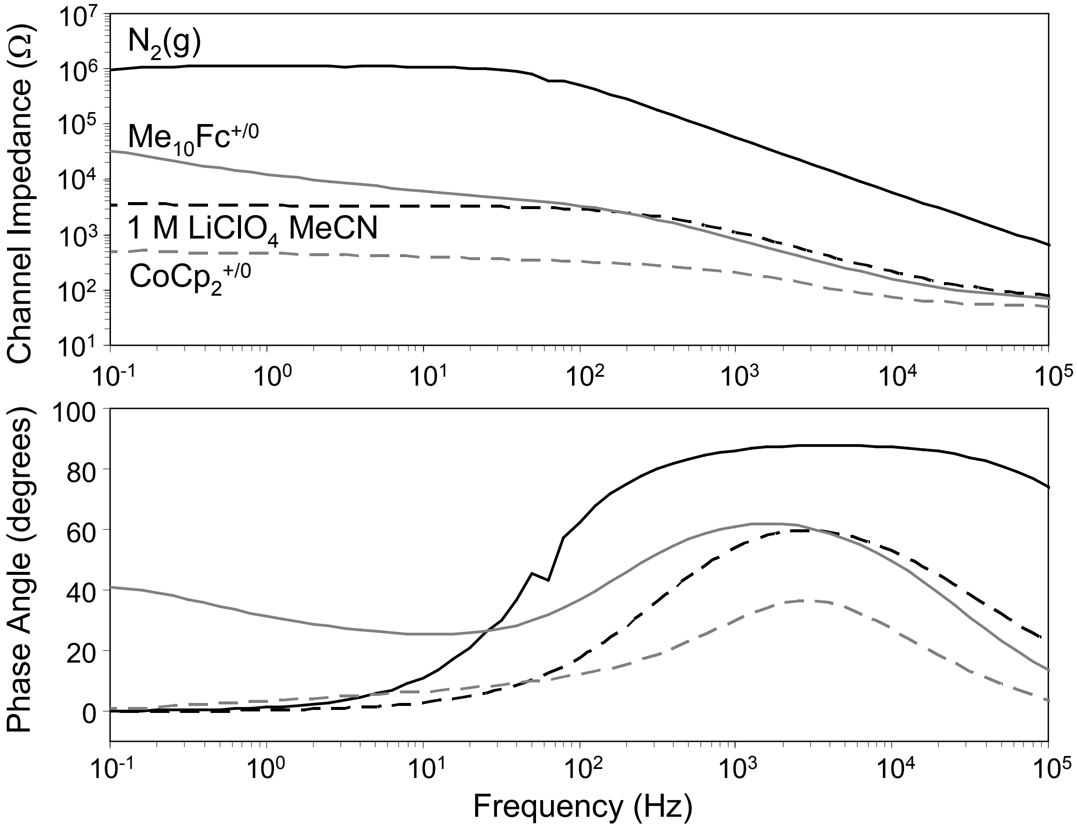

Figure 7: Bode plot for the *n*$^+$-*p*-Si(111)-*n*$^+$ device in a MeCN-$CoCp_2^{+/0}$ solution.

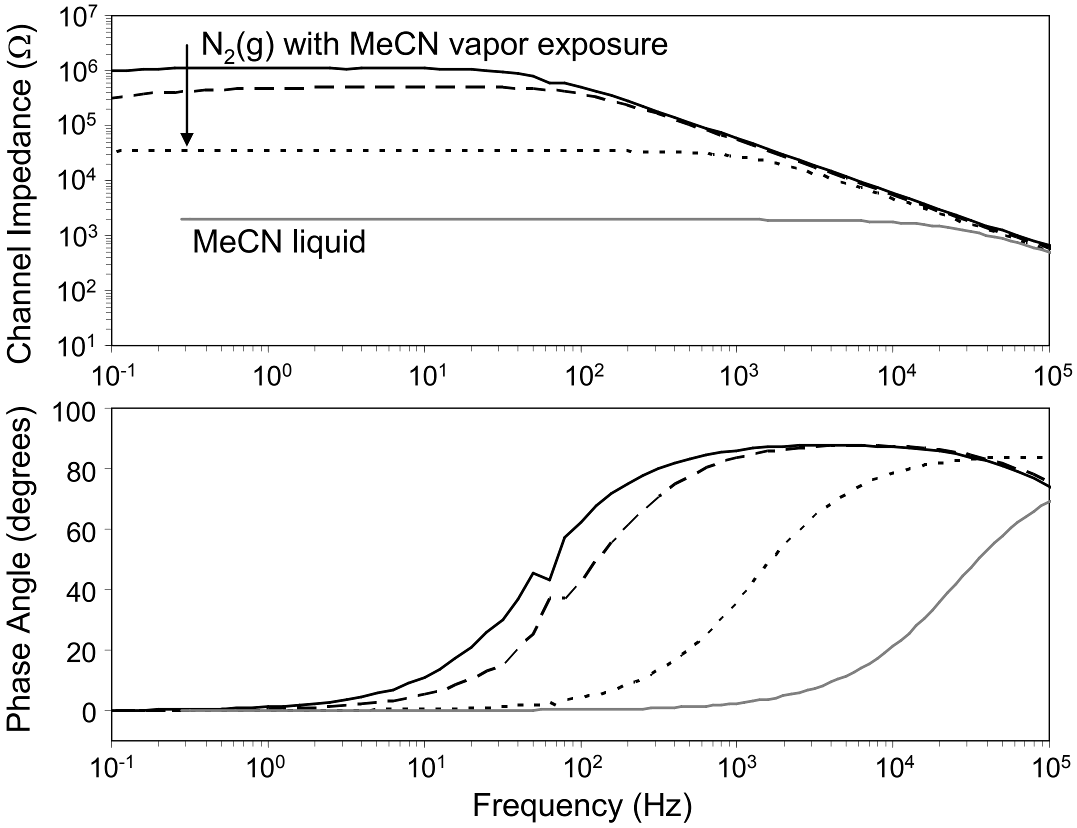

Figure 8: Bode plot for a n^+-p-Si(111)-n^+ device in contact with either liquid MeCN or MeCN vapor for various lengths of time.

The n^+-p-Si(111)-n^+ device was exposed to various amounts of MeCN vapor and liquid. The device was measured initially after bringing it into the nitrogen box (black solid line) and after longer exposures (broken and dotted black line) to MeCN vapor above solution. A measurement was performed in neat anhydrous MeCN (solid gray line).

Table 5: Channel impedance data obtained with an n^+-p-Si(111)-n^+ device in various ambients.

Contact	Z	Qn (C/cm2)	Vbi (1)	Vbi (2)	Bar Hei
Air/N2	3.2 ± 2.1 MΩ	5.7 ± 3.6 ´ 10^{-11}	-	-	-
MeCN Only	2.6 ± 1.3 kΩ	5.8 ± 2.9 ´ 10^{-8}	0.758 ± 0.021	0.763 ± 0.017	1.015 ± 0.026
MeCN LiClO4	2.7 ± 1.4 kΩ	6.5 ± 3.4 ´ 10^{-8}	0.749 ± 0.018	0.751 ± 0.017	1.004 ± 0.025
Me10Fc+/0*	54 ± 9 kΩ	2.3 ± 0.4 ´ 10^{-9}	0.654 ± 0.004	0.658 ± 0.004	0.910 ± 0.006
CoCp2+/0	640 ± 140 Ω	2.0 ± 0.4 ´ 10^{-9}	0.816 ± 0.010	0.817 ± 0.010	1.071 ± 0.014
inversion	*294.1 kΩ*	*4.25 ´ 10^{-10}*	*0.612*	*0.612*	*0.866*

* Data reported for Me10Fc+/0 are observed at a frequency of 0.03 Hz with an average phase angle of 30 deg.

The data observed for the device in $Me_{10}Fc^{+/0}$ displays a significant Warburg impedance at low frequency, and so the reported barrier height and built-in voltages only represent upper bounds.

Table 6: Barrier heights for *n*-Si(111) and *p*-Si(111) in MeCN solutions of $CoCp_2^{+/0}$ or $Me_{10}Fc^{+/0}$.

Liquid Contact	Mott-Schottky	OC Freq. Spectra	Channel Impedance
n-Si(111)			
MeCN-$Me_{10}Fc^{+/0}$	0.66 ± 0.10	N/A	-
MeCN-$CoCp_2^{+/0}$	N/A	0.091 ± 0.016	-
p-Si(111)			
MeCN-$Me_{10}Fc^{+/0}$	0.69 ± 0.10	N/A	*not inverted*
MeCN-$CoCp_2^{+/0}$	1.13 ± 0.050	0.87 ± 0.06 (1.15 ± 0.08)	1.071 ± 0.014

Mott-Schottky experiments could not be performed for the MeCN-$CoCp_2^{+/0}$ contact because an Ohmic response was observed (Figure 6). Open-circuit frequency sweeps in MeCN-$Me_{10}Fc^{+/0}$ solution were complicated by many relaxation processes, possibly including charge transfer into solution, and a straight forward analysis of the barrier height was not possible. The high frequency region of the open-circuit frequency sweep of *n*-Si/MeCN-$CoCp_2^{+/0}$ contacts displayed a semicircle process that could be fit to extract a barrier height. A Warburg diffusion profile was obtained at lower frequencies where the charge transfer into solution could take place at a sufficient rate to dominate the current voltage response.

3 Investigation of the Passivation Mechanism for Aqueous Fluoride Solutions

3.1 Barrier Height Measurements

ABSTRACT

Two measurement techniques at open circuit were employed for the first time along with conventional differential-capacitance vs. potential measurements (Mott-Schottky analysis) to determine the open-circuit band structure of *n*-Si(111), *n*-Si(100), and *p*-Si(111) in contact with 40% NH_4F, buffer HF (BHF), 48% HF, or concentrated H_2SO_4. Since Mott-Schottky analysis requires measuring the differential capacitance under reverse bias, where oxidation or etching can occur for *n*-Si and where electroplating of metal contaminants can occur for *p*-type, the possible reactive nature of the surface under these conditions demands the use of open-circuit methods to verify the band structure. Near-surface channel conductance measurements have been performed at open circuit using solution-gated n^+-*p*-Si(111)-n^+ and p^+-*n*-Si(100)-p^+ devices. Additionally, open-circuit frequency spectra were obtained for silicon in contact with these solutions. Mott-Schottky analysis was not reliable for the systems of *n*-Si(111) or *n*-Si(100) in NH_4F and *n*-Si(100) or *p*-Si(111) in H_2SO_4. However the combination of the three techniques demonstrated that the surfaces of *n*-Si(111) and *n*-Si(100) are under accumulation when in contact with either NH_4F or BHF, while *p*-Si(111) are under inversion. Normal depletion was observed for *n*-Si(111) and *n*-Si(100) in contact with

HF, but *p*-Si(111) was under inversion. The difficulty in obtaining reliable barrier heights for silicon in contact with H_2SO_4 is likely due to the fluctuation in the open-circuit potentials observed for these contacts.

INTRODUCTION

The properties of silicon in hydrofluoric acid and ammonium fluoride solutions are of immense technological importance for the semiconductor industry.[51-53] Many etching mechanisms have been proposed for silicon[46, 54-65] that critically depend on the surface concentrations of electrons or holes. The rates for these mechanisms are thus dependent on the surface electron and hole concentrations that are determined by the band structure. For this reason, the open-circuit band structure for silicon in contact with etching solutions is critical towards understanding the rates at which etching mechanism could occur.

Measurements of the surface recombination velocity (SRV) have been attributed to a low surface trap state density of silicon in contact with HF, NH_4F, and concentrated H_2SO_4.[9, 33, 34] The band structure of silicon, however, is critical in determining the SRVs of these interfaces, and it determines whether the SRV can be correlated with a surface trap state density at all.[4, 25] It has already been shown that a large imbalance in the surface electron and hole concentrations, either due to inversion or accumulation, shuts off surface recombination due to the lack of one charge carrier type or the other at the surface.[4, 25] In these cases, recombination occurs predominately in the bulk and hence the effective lifetime does not indicate the quality of the surface. This chapter addresses the band structure of silicon in contact with various etching solutions. The effective lifetimes of silicon in these solutions are the focus of subsequent work in this chapter.

Despite numerous reports describing the anodic oxidation of Si(111),[46, 56-58, 66-69] the pH-dependence of the open-circuit potential of Si in aqueous fluoride solutions,[46, 58, 69] and the kinetics of etching of Si in fluoride solutions,[46, 70, 71] the nature of the band bending of Si in contact with aqueous fluoride solutions is still not well agreed upon.[72] Differential capacitance vs. potential data must be collected under reverse bias, which for *n*-type silicon often involves anodic current flow with a concomitant change in the surface condition due to anodic etching or the formation, and in some cases the subsequent dissolution, of Si oxides.[73] The changing surface condition that accompanies these measurements requires skepticism about the extrapolation of the band structure from reverse bias to obtain values of the built-in voltage.

To circumvent the surface reactivity associated with Mott-Schottky analysis, measurements in this work were also made under open-circuit conditions for the first time using both open-circuit frequency analysis and near-surface channel conductance measurements on solution-gated n^+-p-Si(111)-n^+ and p^+-n-Si(100)-p^+ devices[23, 74] to assess the degree of band bending for Si in aqueous fluoride solutions and concentrated H_2SO_4. The use of the near-surface channel conductance measurements has several advantages. First, these devices only require the application of a small 10 mV alternating voltage across the source and drain contacts at open circuit; no biasing of the substrate relative to the solution is required. Second, the channel impedance data are not nearly as sensitive to trapped surface charges that often confound the interpretation of differential capacitance vs. potential measurements because only mobile charge carriers can contribute to the channel impedance measurements. While trapped surface charge can increase carrier scattering, which lowers the effective mobility[75-77] and, hence, the near-surface channel conductance, this is expected to have only a slight effect. Additionally, given that the source-channel and drain-channel interfaces are high impedance *n*$^+$-*p* or *p*$^+$-*n* junctions at equilibrium, a low observed impedance clearly indicates the presence of a high surface electron concentration in the *p*-Si(111) channel or a high surface hole concentration in the *n*-Si(100) channel. Finally, experiments performed with these devices in contact redox solutions that form robust semiconductor liquid junctions have produced barrier heights in agreement with Mott-Schottky analysis.[23, 74]

EXPERIMENTAL

1. *Materials*

For differential capacitance vs. potential measurements, wafers of *n*-Si(111) were obtained from Crysteco with a measured resistivity of 4.18 Ω-cm ($N_D = 1.03\times10^{15}$ cm^{-3}) and a miscut angel of less than 0.5°, and were cut into pieces approximately 1.4 cm × 1.0 cm. Prime grade wafers of phosphorus-doped, *n*-Si(100) were obtained from Wacker that were 500 microns thick with a measured resistivity of 5.9 Ω-cm ($N_D = 8.30\times10^{14}$ cm^{-3}), and were cut into similarly sized pieces. In order to make Ohmic contacts that were free of stray capacitances, it was necessary to first pre-etch the *n*-Si(111) and *n*-Si(100) wafer pieces for 30 seconds in buffer HF (BHF) to remove the native oxide and immediately contact the unpolished back side with Ga-In eutectic. Wafers of *p*-Si(111) were obtained from Silicon Quest International with a measured resistivity of 1.39 Ω-cm ($N_A = 1.0\times10^{16}$ cm^{-3}) and a miscut angel of less than 4°, and were cut into similarly sized pieces. These wafers were contacted on the unpolished back side with Al from a sputtering source and were annealed at 450°C in 95:5 $N_2(g):H_2(g)$ for 20-30 min. The back sides, edges, and a 3 mm rim around the face of all electrodes were covered with either insulating epoxy or paraffin wax. The surface area of each electrode was determined photographically by using the ImageSXM program. The dopant density of each wafer was calculated through a four-point-probe method.

Glassy Carbon (GCE) and platinum working electrodes were obtained from BAS. Prior to each use in a given solution, the electrodes were polished with 0.05 micron alumina polish (South Bay Technology, Inc, P/N: AS0005-16, Lot#:7023), sonicated in water for 5 min, rinsed, and dried before use.

Concentrated (18 M) H_2SO_4 and 48% HF were obtained from EM Science. Buffer HF and 40% NH_4F were obtained from Transene Co. CAUTION: concentrated sulfuric acid is highly toxic and corrosive and can cause serious burns. CAUTION: fluoride-containing solutions such as 40% NH_4F, buffered HF, and 48% HF pose as a serious contact hazard. Hydrofluoric acid is highly toxic and corrosive and may cause serious burns that may not be immediately painful or visible. Fluoride ions readily penetrate the skin and can cause destruction of deep tissue and bone. In this work, the term “water” always refers to 18 MΩ-cm water that has been freshly obtained from a Millipore purifier system.

2. Differential Capacitance Measurements

The electrochemical cell consisted of a plastic cup inserted into an enclosed glass cell that could be purged to minimize air contamination. The counter electrode was a piece of Pt mesh at least four times the area of the working electrode. A saturated calomel electrode (SCE), connected through a salt bridge, was used as a reference electrode for concentrated H_2SO_4. Glass frits of the bridge tube needed to be changed frequency as the acid would slowly dissolve them. For the 40% NH_4F, BHF, and 48% HF solutions, a commercially available (Innovative Instruments, Inc - Tampa, FL), all plastic, leak-free, Ag/AgCl reference electrode was used. This reference electrode was typically stable over the course of an entire day to within 5 mV, but never more than 20 mV.

After solvent rinses, the *n*-Si(111) and *p*-Si(111) electrodes were etched for 20 minutes in N_2(g)-bubbled 40% NH_4F to obtain atomically-smooth surfaces; the *n*-Si(100) electrodes were etched for 2 min in N_2(g)-bubbled BHF. Electrodes were then stowed into a cell above the solution for a 20 min or longer argon purge in the dark to remove any air introduced during cell assembly. Prior to use, each solution was always bubbled with argon for at least 30 min to 1 hour or until no oxygen was detected by cyclic voltammetric analysis.

Impedance spectra were recorded with Zplot impedance software (Scribner Associates Inc.) using a Schlumberger Model 1260 frequency response analyzer and a Solartron SI 1287 potentiostat. A 10 mV ac signal of frequencies ranging from $0.1–10^5$ Hz was applied on top of the desired dc bias. The frequency range for a given silicon/solution contact was chosen so that measurement time was kept to a minimum. The frequency range was always at least 2 decades wide and centered in the region where the phase angle was dominated by the parallel capacitance.

3. *Fabrication of the Channel Impedance Devices*

Figure 9 depicts schematically the process used to fabricate the n^+-p-Si(111)-n^+ and p^+-n-Si(100)-p^+ devices, and Figure 10 presents the equivalent circuit during operation. A more specific description of the fabrication process is described elsewhere. Test grade boron-doped p-Si(111) ± 4° wafers (University Wafer, Inc.) with a dopant density of 2×10^{15} cm^{-3} and phosphorus doped n-Si(100) ± 0.5° wafers of dopant density of 1×10^{14} cm^{-3} were cut into 2 cm × 2 cm pieces and cleaned by an SC1 and SC2 technique. A thick oxide layer (10 kÅ) was grown on each wafer by a commercial foundry (Silicon Quest International, Inc.) to provide an effective mask for phosphorous or boron doping.

Standard lithographic techniques, employing an AZ 5214 E photoresist, an AZ 327 MIF developer (Clariant), and a Karl Suess KSM mask aligner were used to define regions for the source and drain doping. The source and drain regions were then doped either p^+-type with a boron planar diffusion source BN-HT (lot # X59005 - Carborundum) on the n-Si(100) wafers, or n^+-type using a phosphorus planar diffusion source PH-1000N (lot#3082 - Saint Gobain) on the p-Si(111) samples as outlined by Saint Gobain. Metal Ohmic contact regions were produced by sputtering 200 nm of Al alloyed with 1 wt% Si onto photolithographically defined regions (Figure 9).

The wafers were glued to polycarbonate plates, and contacts to the Al contacts were made on a grounded metal surface to avoid electrostatic discharge. The wafers were subsequently encapsulated in white insulating epoxy so that only the center channel and very small regions of the source and drain were left exposed; this was done to ensure complete liquid contact over the entire channel region. Measurements in contact with concentrated H_2SO_4 required insulation with paraffin wax (Paxter Household wax) instead of epoxy. Devices were etched for 10 min in buffered HF to remove the initial 1000 Å oxide layer that protected the central channel; the *p*-Si(111) channel was occasionally etched in NH_4F for 20 min to obtain a flat surface.

Working devices had a less than 4 Ω resistance across a common source or drain contact (A to C or B to D in Figure 9) and showed a symmetrical double-diode behavior, with large (greater than 1 MΩ) low bias resistance across the central channel (A+C to B+D in Figure 9). Impedance spectra across the source and drain were collected as described above. Measurements in all solutions were carried out both in an N_2-purged environment as well as in laboratory air conditions, and the data are within error the same. All experiments reported in this work were carried out inside a metal-mesh Faraday cage, in the dark, and in unstirred solutions.

RESULTS

1. *Differential Capacitance vs. Voltage Measurements*

Open-circuit voltage measurements and open-circuit frequency spectra were obtained both before and after Mott-Schottky analysis to observe any changes in the open-circuit condition. The Mott-Schottky sweep involved potential steps of 0.05 V beginning at the most negative potential for cathodic protection, stepping toward the most positive potential, stepping back to the most negative potential, and this entire procedure was repeated once more in exactly the same manner. This four-fold repetition of the potential range was necessary to assess the stability and reproducibility of the Mott-Schottky experiments. The voltage range of the Mott-Schottky was chosen to yield the best reproducibility among subsequent Mott-Schottky scans and to minimize changes in the open-circuit frequency spectra.

Figure 11, Figure 12, and Figure 13 display representative Mott-Schottky plots for *n*-Si(111), *n*-Si(100), and *p*-Si(111) electrodes respectively in 40% NH_4F, buffered HF, 48% HF, or concentrated H_2SO_4 solutions. Table 7 summarizes the average values and standard deviations of all the electrodes used in the Mott-Schottky analysis. For data displayed in Table 7, the average and standard deviation for all electrodes over all four scanned directions is reported. The potential range, frequency range, and the R^2 line fits are displayed. All potentials have been referenced with respect to SCE.

The flatband potential, E_{fb}, was calculated using the Mott-Schottky equation, shown in equation 8 for an *n*-type semiconductor and in equation 9 for a *p*-type semiconductor,[1] where q is the charge of an electron, κ is the relative permittivity of silicon, ε_0 is the permittivity of vacuum, N_D^+ and N_A^- represent the ionized dopant densities for *n*-type and *p*-type respectively, A is the interfacial area, E_{app} is the applied bias, and kT/q represents the thermal energy.

n-type:
$$C_{SC}^{-2} = \frac{2}{q\kappa\varepsilon_o A^2 N_D^+}\left(E_{app} - E_{fb} - \frac{kT}{q}\right) \tag{8}$$

p-type:
$$C_{SC}^{-2} = \frac{2}{q\kappa\varepsilon_o A^2 N_A^-}\left(-E_{app} + E_{fb} - \frac{kT}{q}\right) \tag{9}$$

Since q, κ, and ε_0 in the equations 8 and 9 are known constants and the area and dopant density can be independently measured, a theoretical slope of the Mott-Schottky plot can be calculated and compared to the experimentally observed slope. The ratio of the theoretical slope to the observed slope is reported in Table 7; values close to unity indicate the absence of charged trap states.[78]

In equations 8 and 9, C_{SC} is the capacitance of the space charge region that was obtained by fitting the impedance spectrum at each E_{app} to a 3-element model circuit consisting of a resistor in series with a parallel combination of a resistor and a capacitor. In the presence of trap states, the space charge capacitance will display a frequency dependence that is better fit by a constant phase element (CPE). The expressions for the impedance of a pure capacitor, Z_C, and CPE, Z_{CPE}, are given in equation 10.

$$Z_{CPE} = \frac{1}{C_{SC}\,j\omega}, \qquad Z_{CPE} = \frac{1}{CPE_T\left(j\omega\right)^{CPE_P}} \tag{10}$$

CPE_P values close to unity indicate the absence of frequency dispersion and that charged trap states are not present at that bias. CPE_P values at each potential in the Mott-Schottky range were averaged together and reported in Table 7. C_{SC} was always obtained from the capacitor-containing 3-element circuit while the CPE-containing circuit was used only to assess the ideality of the previous fit.[79, 80]

The open-circuit potentials reported in Table 7 are the average of all open-circuit potentials measured both before and after Mott-Schottky analysis. For a given electrode, the built-in voltage value, V_{bi}, was calculated as $V_{oc} - E_{fb}$ for *n*-type and as $E_{fb} - V_{oc}$ for *p*-type electrodes. The barrier height, ϕ_b, was calculated using equation 11; the second term in equation 11 is equal to V_n or V_p (Figure 14), where $\mathbf{E_g}$ represents the band gap energy and V_i is the voltage necessary to reach inversion. V_i can be calculated using equation 12 where n_i is the intrinsic free carrier concentration and N_B represents a generalized dopant density that could either be N_D^+ or N_A^-.

$$\varphi_b = V_{bi} + \frac{\mathbf{E_g} - V_i}{2} \tag{11}$$

$$V_i = \frac{2}{\beta} \cdot \ln\left(\frac{N_B}{n_i}\right) \tag{12}$$

The Mott-Schottky (M-S) plots in Figure 11, Figure 12, and Figure 13 and the data in Table 7 show that most M-S experiments displayed good reproducibility, high linearity, ideal slopes, and very little frequency dispersion. Notable exceptions are *n*-Si(111) and *n*-Si(100) in 40% NH_4F, and *n*-Si(100) and *p*-Si(111) in concentrated H_2SO_4. For *n*-type electrodes in NH_4F, M-S plots were not very linear or reproducible, and the slopes were about a factor of 2 greater than expected; all of these trends were magnified when the potential was scanned to more positive biases. The reason for this is likely due to the generation of small gas bubbles observed on the surface after the application of reverse biases. These bubbles would decrease the area of the electrode and lead to a larger and noisier M-S slope. Figure 15, Figure 16, and Figure 17 display the cyclic voltammograms obtained for *n*-Si(111), *n*-Si(100), and *p*-Si(111) respectively in these solutions. Figure 15 and Figure 16 show that *n*-type silicon has large reverse bias current densities in both NH_4F and BHF. Since M-S plots of *n*-type silicon in BHF display ideal behavior, the issues with NH_4F cannot be ascribed strictly to the passage of large reverse bias current alone; instead, small bubbles were never observed on electrodes in BHF upon completion of the M-S analysis. These observations indicate that the reverse bias etching mechanisms for NH_4F and BHF may be different. For *n*-Si(100) and *p*-Si(111) in concentrated sulfuric acid, M-S plots displayed significant frequency dispersion and very small slopes for *n*-Si(100) or regions of multiple slopes for *p*-Si(111). The failure of these silicon-liquid contacts to produce ideal M-S plots prevents the determination of reliable barrier heights and necessitates the use of open-circuit methods.

2. Open-circuit Frequency Spectra

Since the open-circuit frequency response did not vary by more than a factor of 2 before and after Mott-Schottky analysis, all data were averaged together and displayed in Table 8. The error in these measurements is more representative of variations from electrode to electrode than from changes due to the Mott-Schottky analysis. Each open-circuit frequency spectrum was fit to the same three-element equivalent circuits mentioned above in order to obtain the differential capacitance, C_D, and CPE_P values. At open circuit, the surface may not be in depletion so C_D could represent the solution capacitance, C_H, the differential capacitance of the semiconductor, $C_{D,s}$, or the capacitance of any grown oxide layer present. The measured capacitance might also be convoluted with a trap state capacitance; the $\mathrm{CPE_P}$ value will identify the extent of frequency dispersion that might be the result of trap states or other surface inhomogeneities.

In order to compare the C_D values to C_H, frequency spectra in each solution were collected on both polished GCE and Pt electrodes and are reported in Table 9. Measured C_H values were generally in the range of 10-60 μF cm^{-2}, which are in agreement with other sources.[81] The lower CPE_P values are also in agreement with other sources and could be due to a distribution of surface adsorbed charge,[1] a distribution of surface adsorbed function groups,[82] the conductivity of the solution,[83, 84] or a surface roughness.[83] Low CPE_P values, ranging from 0.95 to 0.90, for GCE electrodes in 0.5 M H_2SO_4 have been correlated with surface adsorbed functional groups,[82] and the CPE_P value of 0.87 observed for concentrated sulfuric acid in this study is not unreasonable. The relatively low CPE_P values for these interfaces limit the precision by which the C_H can be estimated.[79] Observed C_D values were always at least one order of magnitude lower than the measured C_H values and, hence, do not represent diffuse layer capacitances.

The differential capacitance at the surface of the semiconductor, $C_{D,s}$, is defined as the differential change in surface charge, Q_s, with surface voltage, V_s, and is described in equation 13, which holds for cases of accumulation, depletion, and inversion.[1]

$$C_D \equiv \frac{dQ_s}{dV_s} = \pm\sqrt{\frac{q\beta\kappa\varepsilon_0}{2}} \cdot \frac{\left[p_{b,0}\left(1-e^{-\beta V_s}\right)+n_{b,0}\left(e^{\beta V_s}-1\right)\right]}{F(V=V_s)} \tag{13}$$

$$\beta = \frac{q}{kT} \tag{14}$$

$$F(V) = \sqrt{p_{b,0}\left(e^{-\beta V(x)}+\beta V(x)-1\right)+n_{b,0}\left(e^{\beta V(x)}-\beta V(x)-1\right)} \tag{15}$$

The positive sign in equation 13 is used for $V_s > 0$ and the negative sign is used for $V_s < 0$ so that the capacitance always has a positive value. V_s is defined as the voltage difference between the surface and the bulk, and, at open circuit, it is related to V_{bi} but may be of a different sign. (For example, for *n*-type electrodes, $V_s = -V_{bi}$, while for *p*-type electrodes

$V_s = V_{bi}$.) The $e^{+\beta V}$ terms should not be included for high frequency measurements where the rates of recombination-generation or diffusion of minority carriers to the surface cannot follow the excitation signal.[1] For cases of depletion or inversion at high frequencies all exponential terms are negligible and the Mott-Schottky equation is obtained.

Each observed C_D value was used with equations 13 through 15 to numerically calculate V_s values that were averaged and reported as V_{bi} values in Table 8. The barrier heights were calculated using equation 11. The low frequency region of the spectra always tended towards a parallel resistance, R_p, which is reported in Table 8, normalized by the electrode area, to estimate the low frequency charge transfer resistance of the channel impedance devices, *vide infra*.

For cases of *n*-Si(111) and *n*-Si(100) in either NH_4F or buffer HF, the relatively large C_D values of 1-3 μF/cm^2 are most likely due to the presence of an accumulation layer. If this capacitance were due to trap states that pin the Fermi level, a resonance within the measured frequency range, due to the time constant for electrical trap, would be expected. Open-circuit frequency spectra were, however, dominated by a capacitance down to about 10 Hz indicating that the presence of trap states near the Fermi level is not likely. An oxide layer 1-3 nm in thickness would yield a similar capacitance value but both NH_4F and BHF are known to etch oxide layers at open circuit. An inversion layer, with barrier height 0.72-0.78 V, would yield similar capacitances but only at low frequencies where minority carriers can respond to the excitation frequency through a recombination-generation mechanism. Furthermore, an inversion layer of this magnitude would have produced a low frequency channel impedance value of 2-8 kΩ on the p^+-*n*-

Si(100)-p^+ devices but values a thousand times greater were observed instead, *vide infra*. For these reasons, the C_D values for *n*-Si(100) and *n*-Si(111) in NH_4F and buffer HF were set equal to an accumulation capacitance. Since these values were typically within a factor of 10 of C_H, a second order correction was used such that C_D was set equal to a series combination of the accumulation capacitance, C_A, and total solution capacitance, C_H, as shown in equation 16.

$$C_D = \frac{C_A C_H}{C_A + C_H} \tag{16}$$

C_A values were evaluated, using the C_H values measured with the GCE electrode since it would have the greatest influence, and V_{bi} values were numerically calculated as before and displayed in the last column of Table 8. This correction corresponded to only a 5-20 mV change in V_{bi} so it was ignored for the calculation of the barrier height.

Most open-circuit frequency spectra displayed negligible frequency dispersion and yielded barrier heights within error of those measured reliably with Mott-Schottky analysis. For all silicon, the CPE_P values of BHF contacts were consistently lower than most other contacts and this is discussed below. For the cases where Mott-Schottky analysis was not reliable, barrier heights calculated for *n*-Si(111) and *n*-Si(100) in 40% NH_4F were 0.084 ± 0.014 V and 0.074 ± 0.003 V respectively, which is indicative of accumulation. The barrier height of *n*-Si(100) in contact with concentrated sulfuric acid was measured to be 0.611 ± 0.038 V. Open-circuit frequency spectra for *p*-Si(111) in concentrated sulfuric acid were not reliable due to extreme frequency dispersion, which may indicate that the Fermi level is pinned at trap states.

3. *Near-Surface Channel Conductance Measurements*

Table 10 and Table 11 display the data obtained from the n^+-p-Si(111)-n^+ and p^+-n-Si(100)-p^+ devices respectively, and the Bode plots are represented in Figure 18 and Figure 19. The low frequency source to drain impedance values, Z_{LF}, approach resistance values, which are characterized by a phase angle less than 4 degrees, and are reported in the first column; the error is more representative of the range of values measured with one device at different times than of differences between devices.

The equivalent circuit for the near-surface channel impedance device is shown in Figure 10. The desired observable is R_{ch}, the resistance of the channel near the surface, since it can be related to the built-in voltage *vide infra*. The pathway through the bulk of the device is dominated by a large resistance at low frequencies because either $R_{SC,b}$ or $R_{CD,b}$ is a high impedance n-p^+ or n^+-p junction. When the surface of the channel region is under inversion, both $R_{SC,s}$ and $R_{CD,s}$ are negligible because the barrier to an inversion layer from an oppositely doped source or drain contact is low, and the measured low frequency impedance, Z_{LF}, will asymptote to R_{ch}.

When the channel is under inversion, only the mobile charge carriers in the channel will contribute to Z_{LF}; fixed charges, such as ionized dopants or even charged trap states, will not contribute to the channel conductance. Furthermore, only those minority carriers in an inversion layer, Q_n, are of the correct energy to contribute to the channel conductance, and Q_n can be approximated as a sheet charge as defined by equation 17 where L denotes the separation between the source and drain contacts, W is the width of the channel, $\mu_{\min}$ is the mobility of minority carriers in the inversion layer

(1000 cm^2 V^{-1} s^{-1} for electrons and 100 cm^2 V^{-1} s^{-1} for holes),[75, 76] and R_{ch} is the low frequency resistance of the channel.

$$Q_n = \frac{L}{\mu_{\min} \cdot W \cdot R_{ch}} \tag{17}$$

The observed Z_{LF} values of Table 10 and Table 11 are set equal to R_{ch} and the corresponding Q_n values are calculated according to equation 17.

Estimation of the V_{bi} for the channel was performed using two different methods.[23, 85] The first[23] adds Q_n to the charge needed to reach inversion, Q_b, to obtain the total charge in the space charge region, Q_s, which can be used to calculate the built-in voltage.

$$Q_s = Q_n + Q_b \tag{18}$$

An expression for Q_b can be obtained by integration of Poisson's equation and using Gauss' Law to equate the field to a total charge at the surface.[1]

$$Q_b = \frac{\sqrt{2} \cdot \kappa \varepsilon_0 kT}{qL_B} \cdot F(V = V_i) \tag{19}$$

Q_b can be readily calculated since V_i, the voltage necessary to reach inversion, is only dependent on the dopant density that has been measured. The total charge in the space charge region, Q_s, can be expressed in an analogous manner using V_{bi} instead of V_i.

$$Q_s = \frac{\sqrt{2} \cdot \kappa \varepsilon_0 kT}{qL_B} \cdot F(V = V_{bi}) \tag{20}$$

Once Q_s has been calculated Q_b and Q_n, V_{bi} can be solved by numerical methods. The V_{bi} values observed by this method are reported in Table 10 under the $V_{bi}(1)$ column.

The second method[85] provides an immediate calculation of V_{bi} from Q_n as shown in equation 21. Numerically-evaluated vales of V_{bi} are reported in Table 10 under the $V_{bi}(2)$ column.

$$Q_n = \sqrt{2} \cdot qN_B L_B \left(\sqrt{\beta V_{bi} - 1 + \left(\frac{n_i^2}{N_B^2} \right) e^{\beta V_{bi}}} - \sqrt{\beta V_{bi}} \right) \tag{21}$$

Equation 21 provides intuition on the range over which the assumption that $Z_{LF} = R_{ch}$ is valid. By substituting V_i for V_{bi} in equation 21, a minimum minority carrier charge necessary for strong inversion, Q_i, can be calculated that can then be used to calculate R_i, the maximum channel resistance observed at the onset of inversion, by using equation 17. Values of V_i, Q_i, and R_i are displayed in Table 10 and Table 11 in the last row. For measurements in solution, all Z_{LF} values are lower than R_i meaning that the surfaces are either under inversion or Faradaic charge transfer through solution is occurring.

A small portion of each of the highly doped source and drain regions was exposed to the solution of interest in order to insure the uninterrupted formation of any inversion layer across the entire channel. This presents a second parallel pathway that consists of a series combination of a generalized source/solution impedance, Z_{ct}, the solution resistance, R_{soln}, and another Z_{ct} associated with the solution/drain interface (Figure 11). This undesirable but unavoidable component of the current has previously been resolved for the case of dilute redox couples in solution because the low frequency behavior is dominated by a diffusion-controlled Warburg-style 45° phase angle.[23] However, there is no well-defined redox couple in the solutions of this work, so it is unclear whether a Warburg-style diffusion should be observed. In this case, Z_{ct} depends on the resistance associated with any open-circuit surface reactions, such as etching or oxidation. Since the open-circuit frequency spectra are performed under conditions similar to this Faradaic pathway, a reasonable estimate of Z_{ct} can be made by dividing the Rp×A values by the areas of the exposed source or drain contacts, which are approximately 0.04 cm^2 (0.5 mm x 8 mm); these estimated Z_{ct} values are reported in Table 10 and Table 11. Due to the error in the Rp×A values and estimate of the exposed area, R_{ch} values must be at least two orders of magnitude less than the estimated Z_{ct} values in order for a reliable barrier height to be inferred from these measurements. The n^+-p-Si(111)-n^+ devices clearly satisfy this requirement while the p^+-n-Si(100)-p^+ devices do not. (Only the measurement of 1 mM Fc^+ in MeOH with the p^+-n-Si(100)-p^+ devices provides an R_{ch} value low enough, 1.4 kΩ, to yield a reliable barrier height of 1.1 V, which is in accord with previous measurements.[23, 74]) The low frequency impedance values measured with the p^+-n-Si(100)-p^+ devices most likely involve Faradaic charge transfer into solution, and Z_{LF} values can only provide an upper bound on the V_{bi} and ϕ_b values. These upper bounds are averaged from values using the two models and presented in Table 11.

Near-surface channel conductance measurements on the n^+-p-Si(111)-n^+ devices yield barrier heights that are between the values obtained through M-S and open-circuit frequency spectra. M-S and open-circuit frequency measurements for *p*-Si(100) in concentrated sulfuric acid were confounded by a large frequency-dependent interfacial impedance. Since the near-surface channel conductance measurements do not involve charge transfer into solution, they are free from these complications and indicate a barrier height of 0.909 ± 0.020 V for *p*-Si(111).

Table 12 summarizes the barrier heights calculated for the silicon liquid contacts from each method and displays a final value, averaged over trusted methods, to describe the open-circuit band structure in that solution.

DISCUSSION

Each of the three techniques used in this work has its own benefits and drawbacks. The benefit of Mott-Schottky analysis is that the space charge capacitance can be shown to have the right dependence on the applied bias; however the reverse bias conditions necessary to demonstrate this can lead to a changing surface condition. Open-circuit frequency spectra have the benefit of probing the surface condition at open circuit, but the differential capacitance cannot be shown to have the expected potential dependence. Channel impedance data also have the benefit of being performed at open circuit, but barrier height values can only be obtained for cases of inversion. Thus, the combination of all these techniques helps to provide a clearer picture of the band structure for silicon in contact with these solutions.

The frequency dispersion observed at open circuit for all electrodes exposed to BHF was potential dependent. The CPE_P values of 0.945 ± 0.014 and 0.952 ± 0.011 for *n*-Si(111) and *n*-Si(100) at open circuit reversibly increase to 0.990 ± 0.005 and 0.995 ± 0.002 respectively when the Fermi level is moved to more positive voltages during the Mott-Schottky analysis. For *p*-Si(111), however, CPE_P values around 0.96 are observed for both Mott-Schottky analysis and open-circuit frequency spectra, which suggests that a relatively negative Fermi level is required to observe this frequency dispersion. The presence of a small density of surface electrical states near the conduction band or the lossy adsorption of species in solution could be responsible from this observation.

Since the open-circuit potentials are roughly equal and the barrier heights of *n*-Si(111) and *p*-Si(111) add up to the bandgap for each of the fluoride-containing solutions, the band edges and the Fermi-level are fixed regardless of doping type. Because of this, the surface electron and hole concentrations are independent of dopant type, and surface reactions involving either electrons or holes would proceed at roughly the same rate for *n*-type and *p*-type at open circuit. For buffered HF and 40% NH_4F solutions, *n*-Si is in accumulation and *p*-Si is under inversion, which means an excess of electrons is present at the surface with a small number of holes in both cases. Thus, in these solutions it is *not* a good assumption that the rate of any surface reactions involving holes will proceed significantly faster with *p*-type compared to *n*-type since they have the same surface electron and hole concentrations. The hole-mediated etching of silicon in these solutions probably requires light for both dopant types. Secondly, the magnitude of accumulation on *n*-type and inversion on *p*-type indicates a truly large surface electron concentration, and a very negative Fermi level could indicate that the formation of hydrogen gas bubbles often observed at the surface is through some form of some conduction band assisted reduction.[86] Chidsey *et al.* report that the open-circuit step-flow etching rate of step edges is 4.2 ± 1.3 nm sec^{-1},[87] which is about 10 rows of surface silicon atoms per second.[88] Assuming that each etched silicon atom promotes at least one electron to the conduction band, and that step edges are separated by about 100 nm,[87] it only takes one second to generate an injected charge of 10^{-7} C cm^{-2}, which is equal to the observed Q_n on the n^+-p-Si(111)-n^+ devices in NH_4F.

For 48% HF, *n*-type surfaces appear to be in normal depletion so that the surface electron and hole concentrations are approximately equal with a surface charge carrier concentration on the order of about 10^{10} cm^{-3} carriers; no one carrier is in great excess and, thus, surface reactions that involve either or both carriers could occur, albeit relatively slowly. The band structure also indicates that surface recombination rates will occur in proportion to their trap state density. Inversion conditions were reliably measured for *p*-type, which indicates a significant excess of surface electrons over holes.

Measurements in concentrated H_2SO_4 indicate that both *n*-Si(111) and *p*-Si(111) are in strong inversion while *n*-Si(100) is in weak inversion with a barrier height 0.7 V less than *n*-Si(111). These observations require that the band edges are not fixed for different crystallographic faces or for different dopant types of the same crystallographic face. The reason for this observation is unknown, but the absence of any formal redox couple is likely the cause for the wide range in open-circuit voltages. While the fluoride solutions also do not contain any formal redox couple, the occurrence of an open-circuit etching mechanism that injects electrons into the surface may define a constant open-circuit voltage by virtue of defining a surface carrier concentration.

The presence of a thin surficial oxide layer on silicon in contact with concentrated H_2SO_4 cannot be ruled out because the capacitance of a thin oxide layer would be larger than the space charge capacitance and may not dominate the circuit properties. Pinning of the Fermi level to trap states formed during the growth of an oxide may be responsible for the low CPE_P values observed for *p*-Si(111) in H_2SO_4. The growth of a large oxide is observed after the cyclic voltammetric analysis of *n*-Si(100) displayed in Figure 16; the open-circuit capacitance changes dramatically to values in the 100 nF cm^{-2} range, which is consistent with a 5-10 nm thick oxide layer, and the fast photoresponse, previously observed before cyclic voltammetry, changed to display an RC charging time constant that is expected for an oxide layer of similar thickness.

CONCLUSIONS

The use of two different techniques has allowed the measurement of the band structure of silicon to be performed at open circuit for the first time in solutions where standard differential capacitance versus voltage (Mott-Schottky) experiments are not valid. The systems of *n*-Si(111) or *n*-Si(100) in 40% NH_4F, and *n*-Si(100) or *p*-Si(111) in concentrated H_2SO_4 demonstrated Mott-Schottky plots that deviated from ideality either in terms of their irreproducibility with time, their nontheoretical slopes, or the observation of significant frequency dispersion. The use of open-circuit frequency spectra and near-surface channel conductance measurements were used to evaluate the open-circuit barrier heights in these cases. The combined data indicate that silicon in contact with 40% NH_4F and buffered HF display a high surface electron concentration; *n*-type silicon is under accumulation while *p*-type silicon is in inversion. Silicon contacts to

48% HF indicate depletion for n-type silicon and inversion conditions for *p*-Si(111). Measurements performed in 18 M H_2SO_4 indicate that both *p*-type and *n*-type silicon (111) surfaces are strongly inverted, while *n*-Si(100) exhibits very weak inversion. Finally, the use of open-circuit frequency spectra and channel impedance devices has been shown to provide a better understanding of systems that are sensitive to reverse bias conditions.

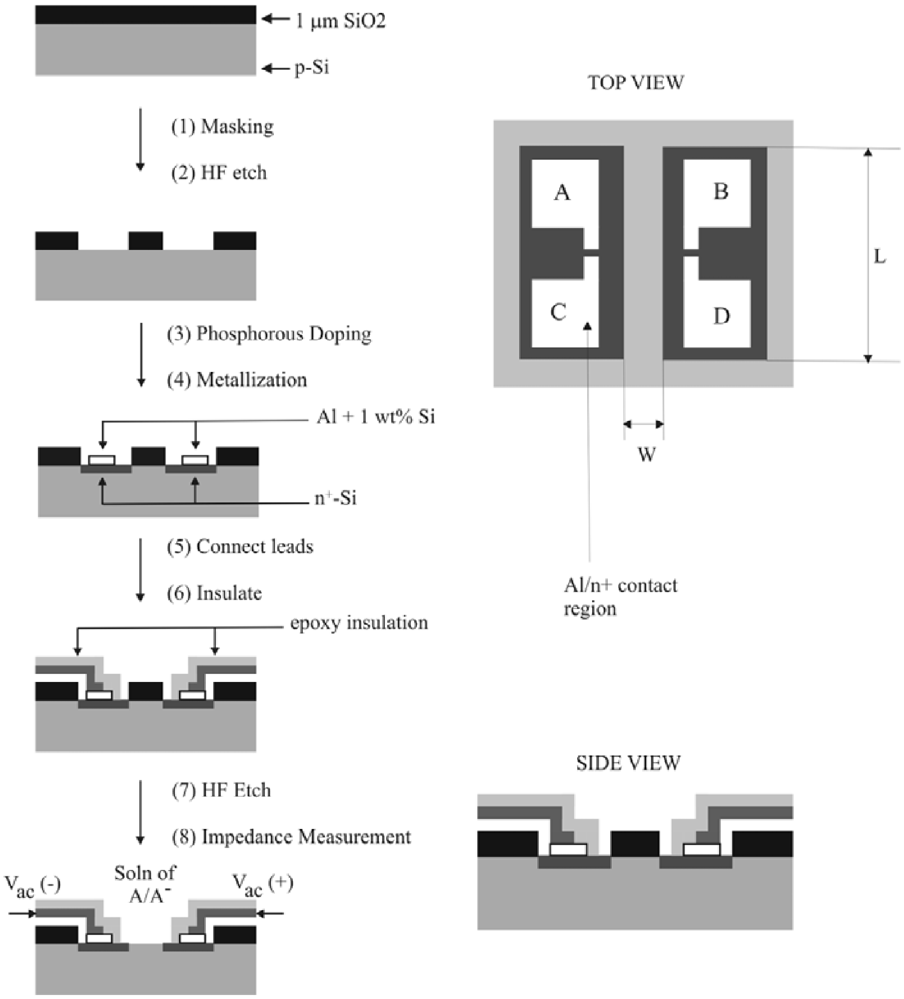

Figure 9: A schematic drawing of the fabrication of the n^+-p-Si(111)-n^+ devices.

An analogous approach was used to generate the p^+-n-Si(100)-p^+ devices.

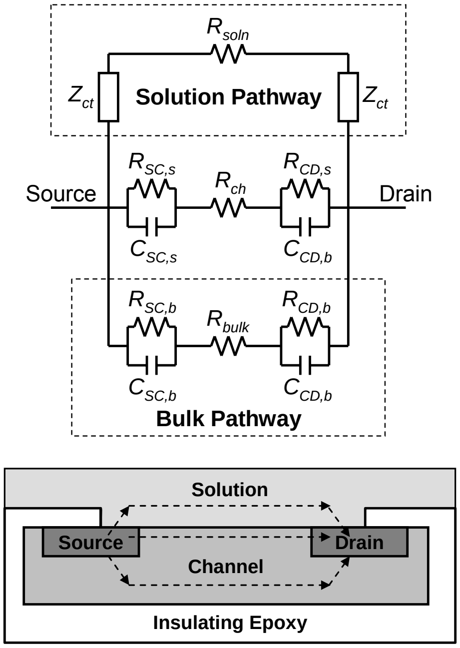

Figure 10: A schematic of the equivalent circuit for the channel impedance devices. There are 3 parallel impedance pathways. The lower pathway indicates the impedance through the bulk of the semiconductor, which is represented as a source to channel impedance, $R_{SC,b}$ and $C_{SC,b,}$ in series with a resistance of the bulk, R_{bulk}, and the channel to drain impedance, $R_{CD,b}$ and $C_{CD,b}$. Impedance through the near-surface region of the channel is similarly represented as a source to channel impedance, $R_{SC,s}$ and $C_{SC,s,}$ in series with a near-surface channel resistance, R_{ch}, and the channel to drain impedance, $R_{CD,s}$ and $C_{CD,s}$. When the surface is under strong inversion, $R_{SC,s}$ and $R_{CD,s}$ are small and the dominant circuit element is just R_{ch}. Since some areas of the source and drain are exposed to the solution, a current pathway involving a generalized impedance into the solution from the source and drain contacts, Z_{ct}, is included in series with a solution resistance. The impedance across the source- and drain-solution contacts is kept general

because the absence of a well-defined redox couple and the possibility for an etching or oxidation mechanism leads to an unknown impedance.

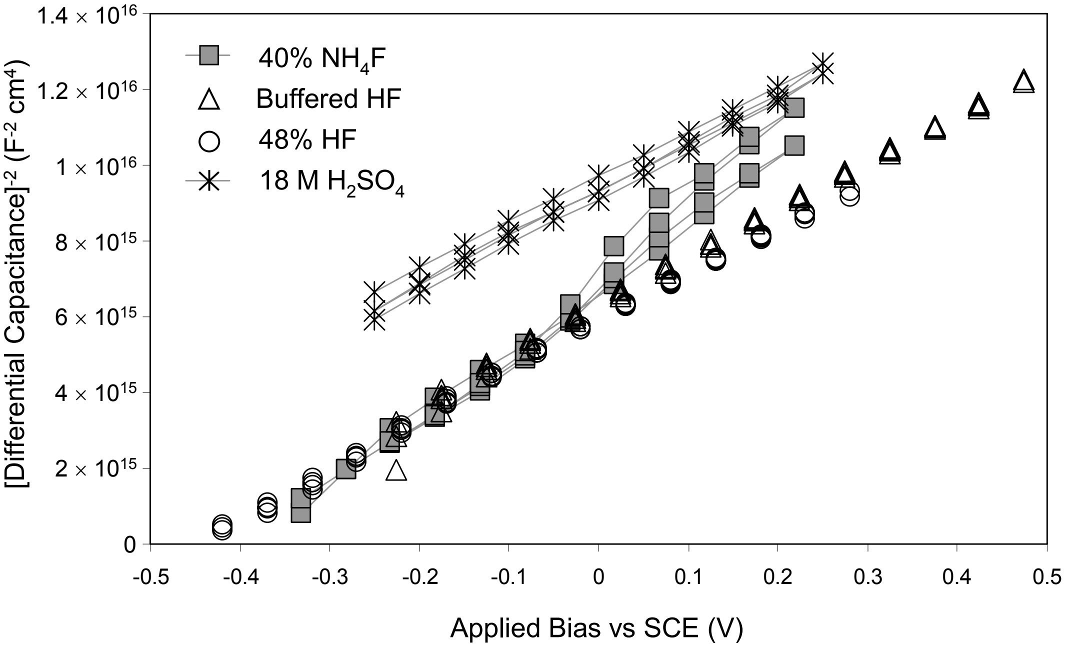

Figure 11: Representative Mott-Schottky plots for *n*-Si(111) in 40% NH$_4$F, buffered HF, 48% HF, and concentrated H$_2$SO$_4$.

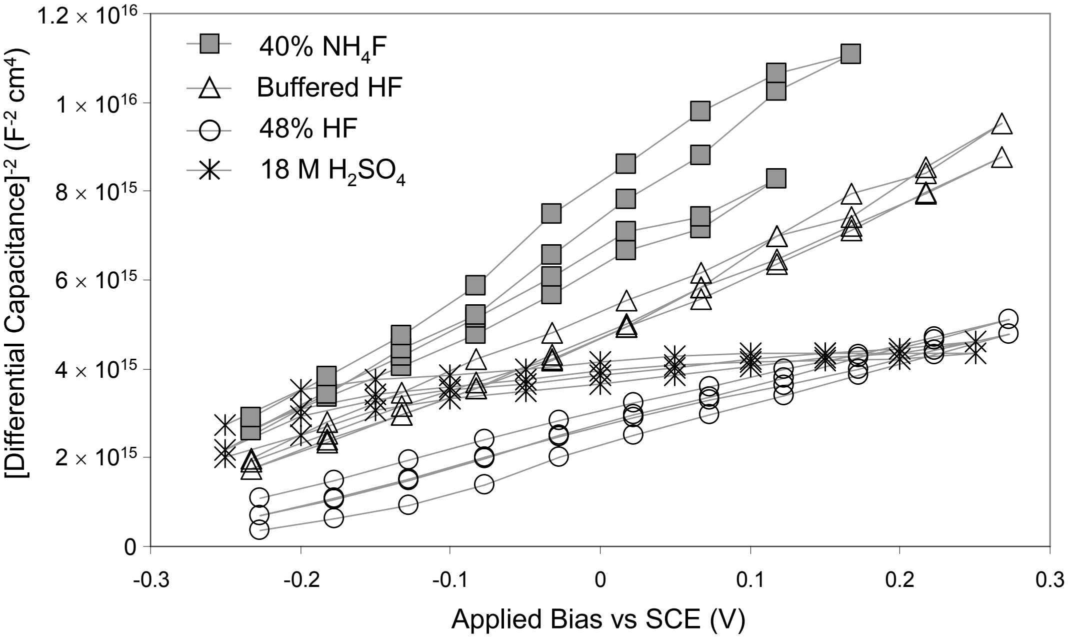

Figure 12: Representative Mott-Schottky plots for *n*-Si(100) in 40% NH_4F, buffered HF, 48% HF, and concentrated H_2SO_4.

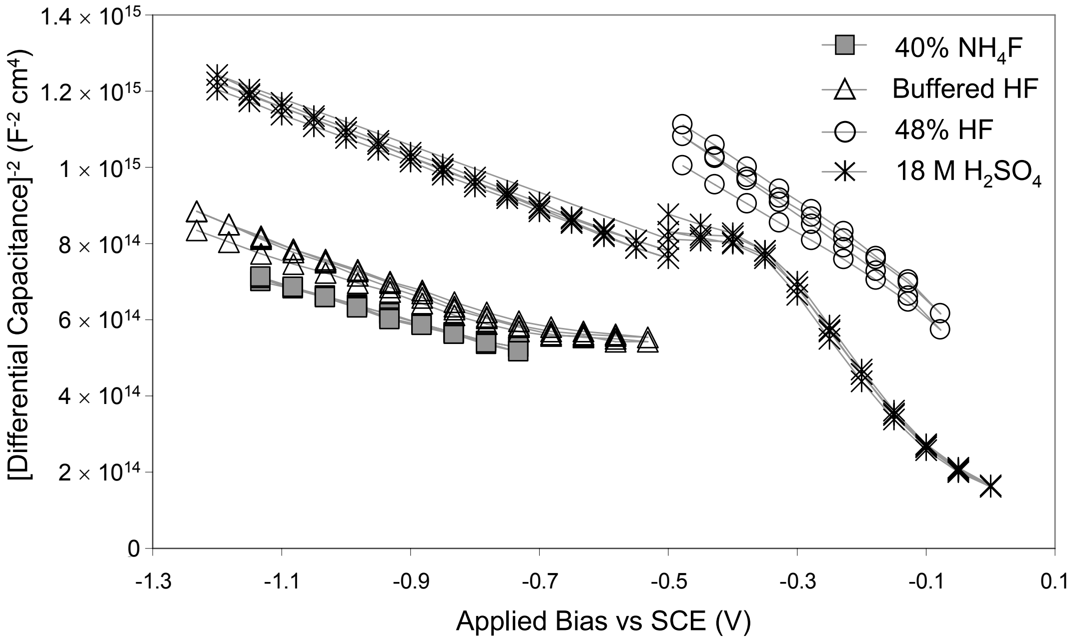

Figure 13: Representative Mott-Schottky plots for *p*-Si(111) in 40% NH_4F, buffered HF, 48% HF, and concentrated H_2SO_4.

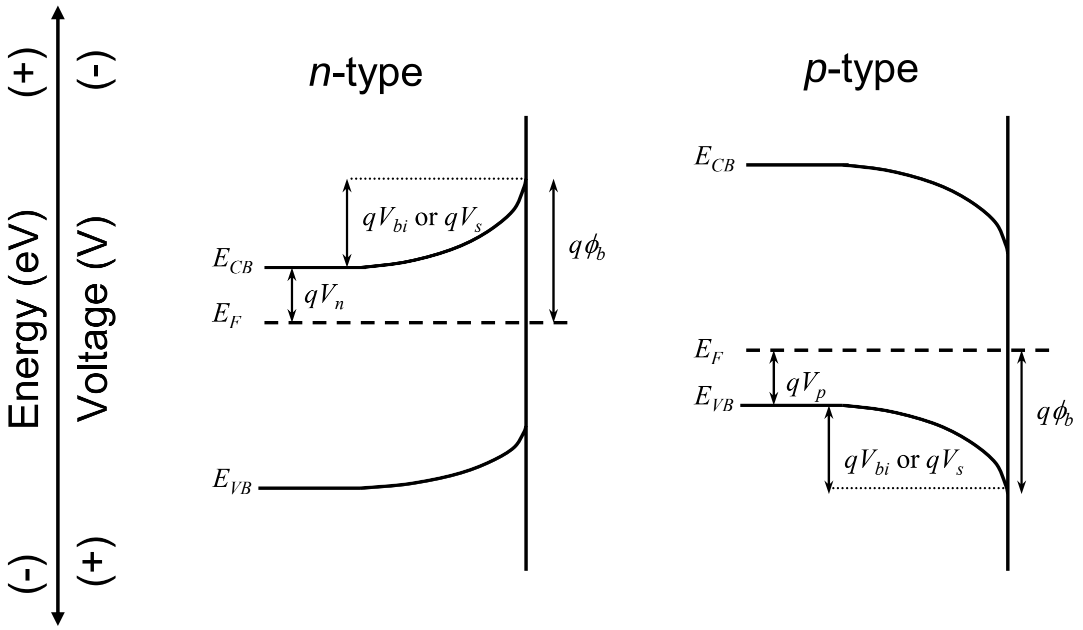

Figure 14: A schematic representation of the band structure for *n*-type and *p*-type semiconductors in depletion.

Terms such as built-in voltage, V_s or V_{bi}, the barrier height, ϕ_b, and others, V_n, V_p, E_{CB}, E_F, E_{VB}, are shown. As depicted, both *n*-type and *p*-type are in depletion and the built-in voltage, V_s, is positive in both cases.

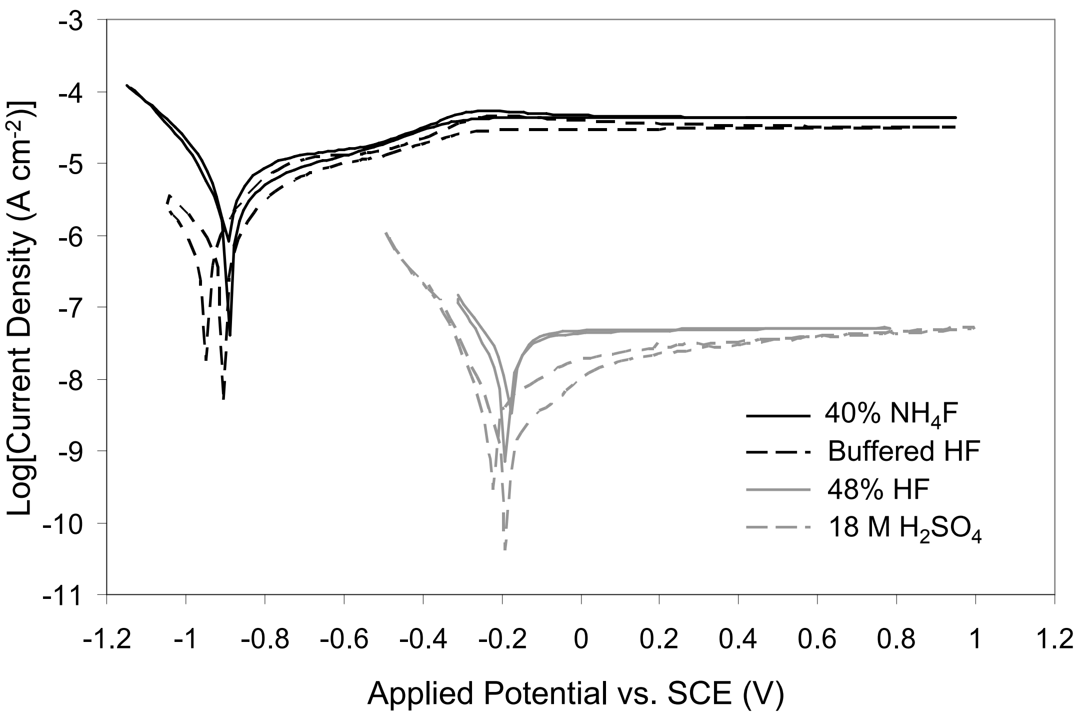

Figure 15: Representative Log(I) vs. E plots for *n*-Si(111) in 40% NH_4F, buffered HF, 48% HF, and 18 M H_2SO_4.

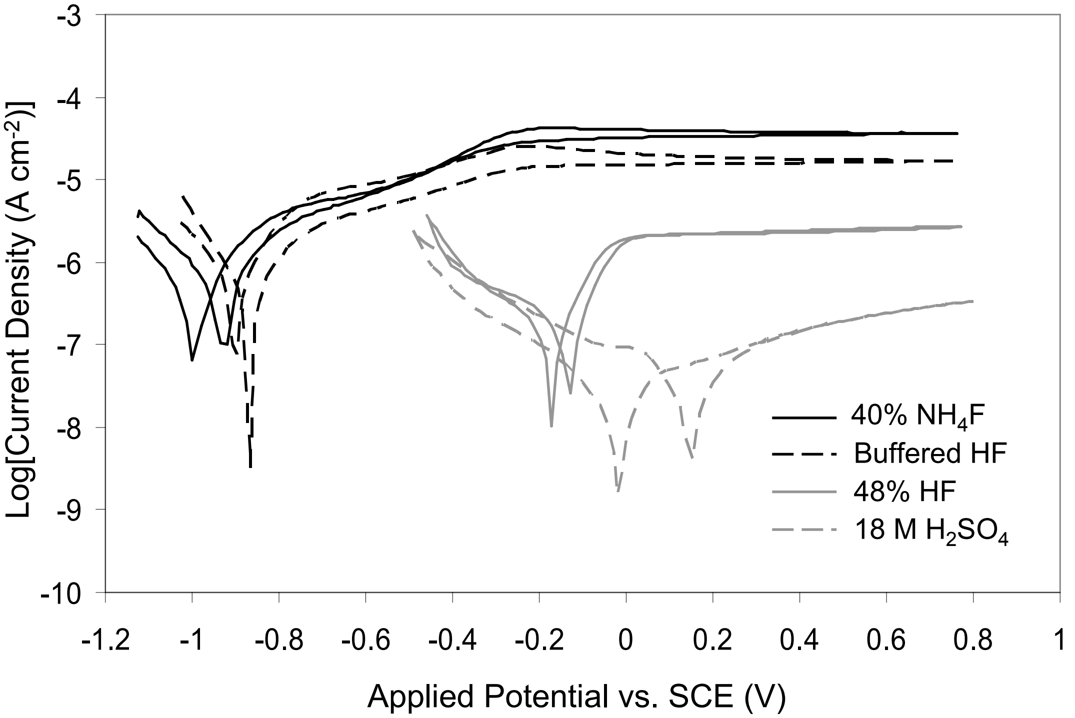

Figure 16: Representative Log(I) vs. E plots for n-Si(100) in 40% NH_4F, buffered HF, 48% HF, and 18 M H_2SO_4.

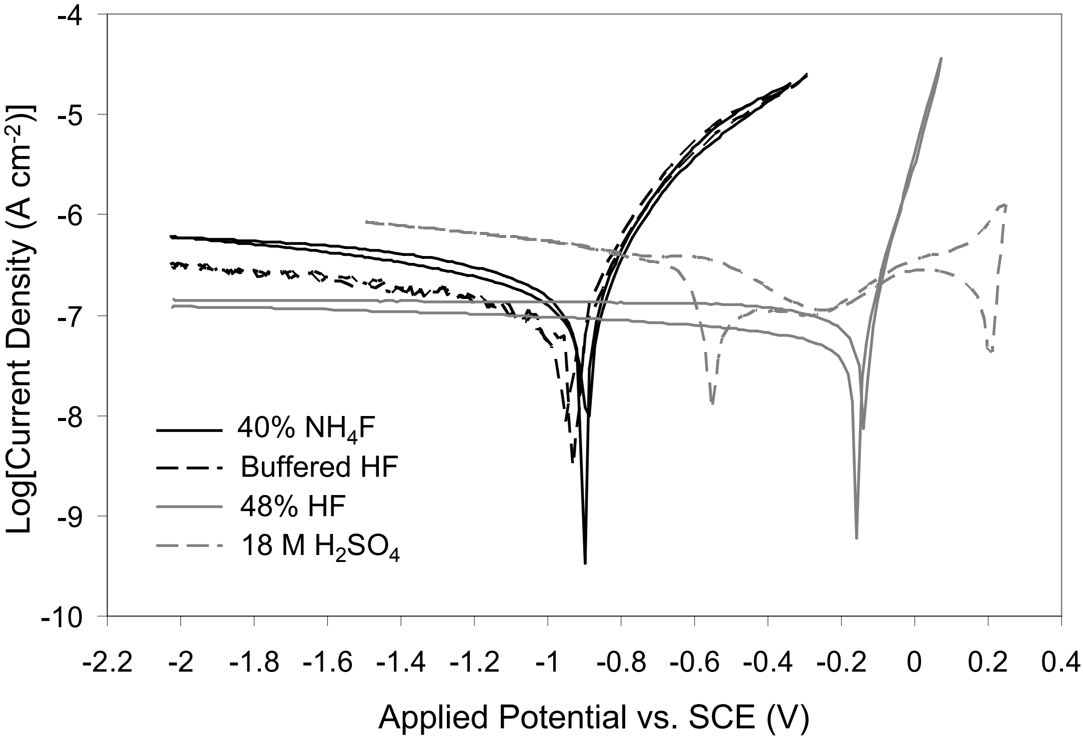

Figure 17: Representative Log(I) vs. E plots of *p*-Si(111) in 40% NH_4F, buffered HF, 48% HF, and concentrated H_2SO_4.

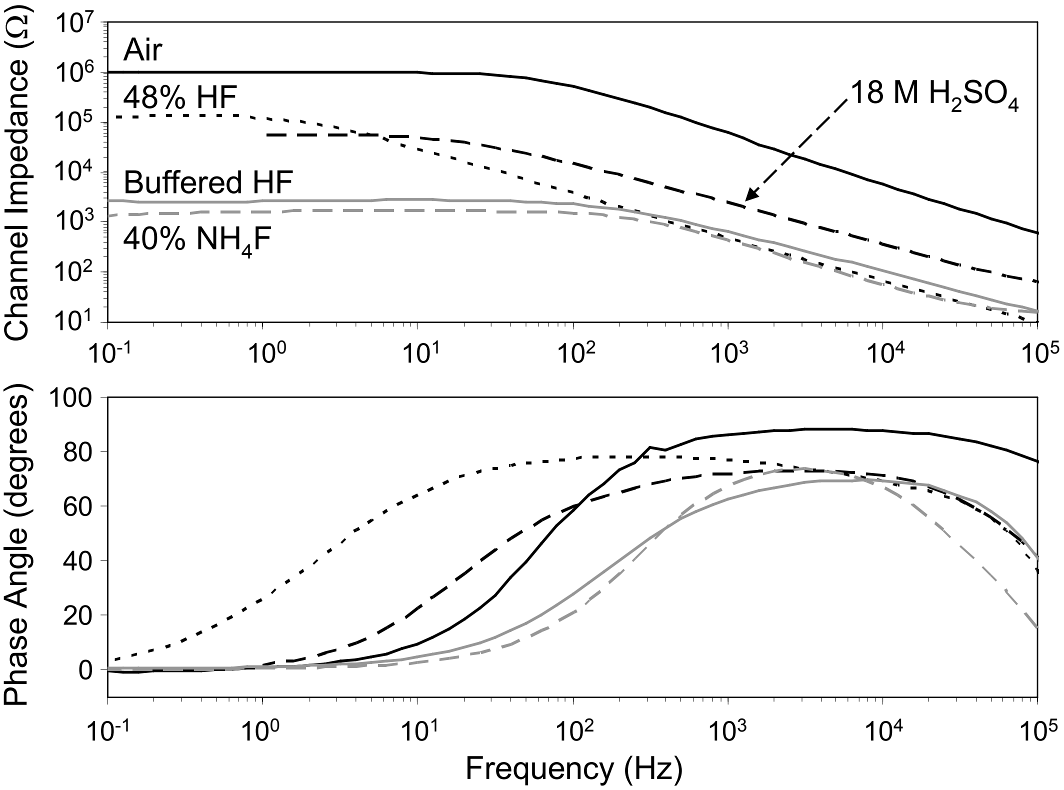

Figure 18: Representative Bode plots for the *n*$^+$-*p*-Si(111)-*n*$^+$ devices in contact with 40% NH_4F, buffered HF, 48% HF, and concentrated H_2SO_4.

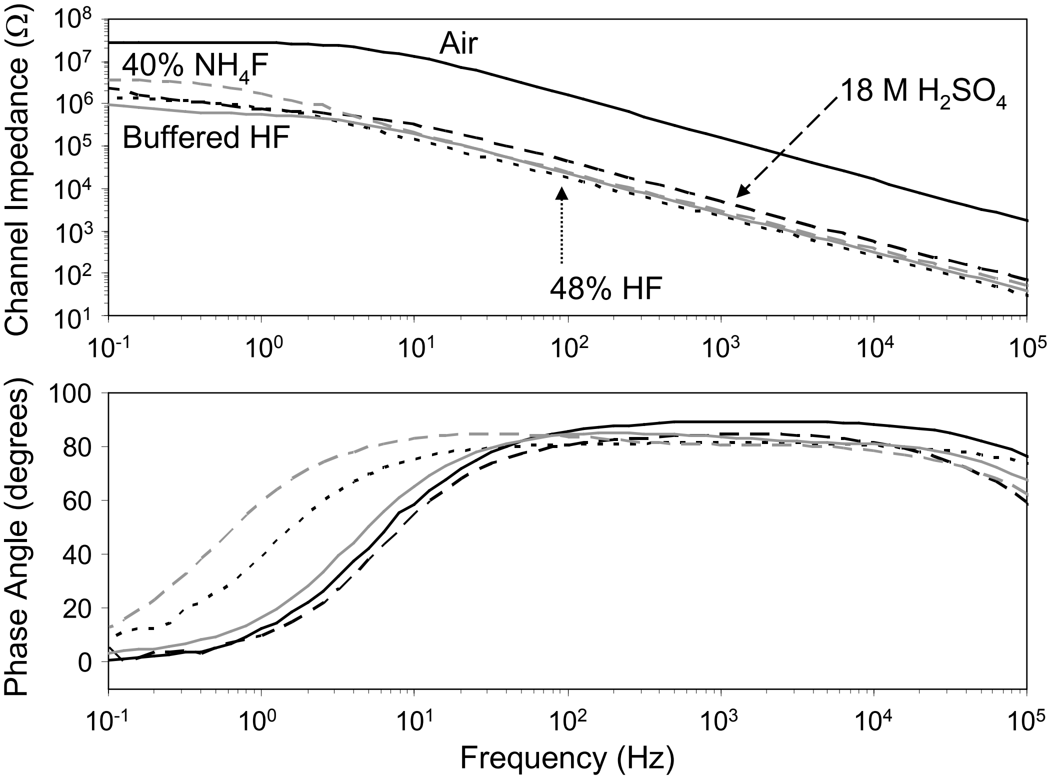

Figure 19: Representative Bode plots for the p^+-n-Si(100)-p^+ devices in contact with 40% NH_4F, buffered HF, 48% HF, and H_2SO_4.

Table 7: Mott-Schottky data for silicon in 40% NH_4F, buffered HF, 48% HF, and conc. H_2SO_4.

Liquid Contact	V Range *vs.* SCE	Freq Range	MS slope T/O	R^2 Line Fit	CPE_P	E_{fb} (V *vs.* SCE)	V_{oc} (V *vs.* SCE)	V_{bi} (V)	ϕ_b (V)
n-Si(111)									
40% NH4F	-0.333 to -0.167	100 kHz - 100 Hz	0.41 ± 0.13	0.9966 ± 0.0018	0.982 ± 0.009	-0.432 ± 0.037	-0.962 ± 0.029	-0.535 ± 0.019	-0.263 ± 0.019
BHF	-0.251 to 0.475	100 kHz - 100 Hz	0.86 ± 0.07	0.9993 ± 0.0003	0.990 ± 0.005	-0.562 ± 0.031	-0.846 ± 0.169	-0.285 ± 0.139	-0.013 ± 0.139
48% HF	-0.219 to 0.382	10 kHz - 10 Hz	0.94 ± 0.48	0.9987 ± 0.0007	0.980 ± 0.021	-0.453 ± 0.087	-0.290 ± 0.055	0.159 ± 0.128	0.430 ± 0.128
18 M H2SO4	-0.25 to 0.25	10 kHz - 100 Hz	1.21 ± 0.35	0.984 ± 0.011	0.979 ± 0.017	-1.027 ± 0.204	-0.088 ± 0.200	0.938 ± 0.403	1.239 ± 0.436
n-Si(100)									
40% NH4F*	-0.333 to -0.167	100 kHz - 100 Hz	0.53 ± 0.33	0.9967 ± 0.0023	0.976 ± 0.005	-0.407 ± 0.010	-1.032 ± 0.015	-0.624 ± 0.006	-0.348 ± 0.005
BHF	-0.225 to 0.475	100 kHz - 100 Hz	0.79 ± 0.19	0.9968 ± 0.0023	0.995 ± 0.002	-0.459 ± 0.075	-0.838 ± 0.144	-0.379 ± 0.194	-0.102 ± 0.193
48% HF	-0.227 to 0.281	100 kHz - 10 Hz	1.40 ± 0.28	0.9982 ± 0.0017	0.971 ± 0.020	-0.349 ± 0.062	-0.235 ± 0.038	0.115 ± 0.032	0.391 ± 0.031
18 M H2SO4	-0.150 to 0.05	31.6 kHz - 316 Hz	4.32	0.9959	0.949	-1.21	-0.055	1.16	1.43
*p-Si(111)***									
40% NH4F*	-1.133 to -0.726	100 kHz - 100 Hz	1.72 ± 0.97	0.9986 ± 0.0011	0.988 ± 0.008	0.140 ± 0.353	-0.963 ± 0.067	1.103 ± 0.420	1.314 ± 0.419
BHF*	-1.234 to -0.732	100 kHz - 100 Hz	1.76 ± 0.25	0.9961 ± 0.003	0.960 ± 0.019	0.188 ± 0.109	-0.866 ± 0.013	1.054 ± 0.095	1.266 ± 0.093
48% HF*	-0.477 to -0.127	100 kHz - 100 Hz	1.25 ± 0.32	0.9960 ± 0.0011	0.983 ± 0.018	0.479 ± 0.075	-0.237 ± 0.091	0.716 ± 0.041	0.927 ± 0.041
18 M H2SO4	-1.20 to -0.50	100 kHz - 1 kHz	1.742	0.9997	0.922	0.651	0.015	0.636	0.847

Data without error bars mean that only one electrode had a CPE_P value greater than 0.90. All other electrodes were not used since the frequency dispersion was too great.

* Only two electrodes satisfied the CPE_P > 0.94 requirements. More data will be taken before publishment.

** The systematicly large slope ratios are likely due to an error in calculating the dopant density

Table 8: Open-circuit frequency spectra for silicon in contact with 40% NH_4F, buffered HF, 48% HF, and conc. H_2SO_4.

Liquid Contact	C_D (nF/cm^2)	CPE_P	V_{bi}	ϕ_b	$R_p{'}A$ (MΩ cm^2)	V_{bi} using C_H
n-Si(111)						
40% NH4F	2300 ± 681	0.971 ± 0.007	-0.187 ± 0.014	0.084 ± 0.014	0.025 ± 0.015	-0.198 ± 0.018
BHF	2450 ± 1100	0.945 ± 0.014	-0.188 ± 0.025	0.083 ± 0.025	0.024 ± 0.009	-0.199 ± 0.031
48% HF	20.9 ± 3.9	0.978 ± 0.014	0.254 ± 0.077	0.525 ± 0.078	2.8 ± 2.2	
18 M H2SO4	8.84 ± 0.42	0.994 ± 0.007	1.140 ± 0.107	1.411 ± 0.107	17 ± 13	
n-Si(100)						
40% NH4F*	2673 ± 152	0.976 ± 0.011	-0.203 ± 0.003	0.074 ± 0.003	0.035 ± 0.001	-0.216 ± 0.004
BHF	2245 ± 1182	0.952 ± 0.011	-0.188 ± 0.035	0.089 ± 0.035	0.020 ± 0.012	-0.198 ± 0.041
48% HF*	31.5 ± 4.3	0.963 ± 0.033	0.0975 ± 0.022	0.374 ± 0.023	0.66 ± 0.02	
18 M H2SO4*	15.4 ± 0.8	0.968 ± 0.006	0.335 ± 0.039	0.611 ± 0.038	0.88 ± 0.59	
*p-Si(111)***						
40% NH4F*	37 ± 3	0.989 ± 0.011	0.672 ± 0.107	0.883 ± 0.107	1.1 ± 1.3	
BHF*	41.4 ± 1.7	0.966 ± 0.025	0.542 ± 0.043	0.753 ± 0.042	0.42 ± 0.06	
48% HF*	50 ± 18	0.977 ± 0.023	0.443 ± 0.272	0.655 ± 0.272	0.43 ± 0.12	
18 M H2SO4	46.3	0.901	0.456	0.667	0.083	

Data without error bars mean that only one electrode had a $CPE_P > 0.90$. All other electrodes were not used due to excessive frequency dispersion.

* Only two electrodes satisfied the CPE-P > 0.94 requirements. More data will be taken before publishment.

** If the error in the slope of MS plots is due to an error in the measurement of N_A, then the ϕ_b values presented here agree much better with other methods.

Table 9: Open-circuit frequency spectra with metallic electrodes.

	GCE		Pt	
Liquid Contact	nF/cm2	CPE-P	nF/cm2	CPE-P
40% NH4F	12,600 ± 4,900	0.939 ± 0.004	34,900 ± 13,200	0.920 ± 0.014
Buffer HF	12,500 ± 5,700	0.943 ± 0.007	25,600 ± 10,400	0.935 ± 0.023
48% HF	48,600 ± 11,700	0.833 ± 0.031	27,100 ± 3,000	0.912 ± 0.007
conc. H2SO4	111,000 ± 36,000	0.869 ± 0.018	52,700 ± 19,500	0.749 ± 0.028

Table 10: Channel impedance data for n^+-p-Si(111)-n^+ devices.

Contact	Z_{LF}	Q_n (C cm^{-2})	V_{bi} (1)	V_{bi} (2)	ϕ_b*	Estimated Z_{CT}
air/N2	6.3 ± 4.4 MΩ	$4.6 \pm 4.8 \times 10^{-11}$	-	-	-	-
40% NH4F	1.7 ± 1.0 kΩ	$1.1 \pm 0.7 \times 10^{-7}$	0.781 ± 0.029	0.782 ± 0.028	1.036 ± 0.028	310 kΩ
BHF	2.4 ± 1.2 kΩ	$6.7 \pm 3.4 \times 10^{-8}$	0.762 ± 0.022	0.764 ± 0.022	1.017 ± 0.022	300 kΩ
48% HF	79 ± 73 kΩ	$3.7 \pm 3.4 \times 10^{-9}$	0.657 ± 0.025	0.660 ± 0.028	0.912 ± 0.026	35 MΩ
c. H2SO4	73 ± 60 kΩ	$2.7 \pm 2.2 \times 10^{-9}$	0.654 ± 0.019	0.656 ± 0.022	0.909 ± 0.020	200 MΩ
inversion	*294.1 kΩ*	*4.25×10^{-10}*	-	*0.612*	*0.866*	

* The two models led to V_{bi} values that differed by only millivolts, so only one barrier height was calculated by using equation 10.

Table 11: Channel impedance data for *p^+-n*-Si(100)-*p^+* devices.

Contact	Z_{LF}	Q_n (C cm^{-2})	V_{bi} (max)	ϕ_b (max)	Estimated Z_{CT}
air/N2	26.4 ± 1.6 MΩ	-	-	-	-
40% NH4F	2.5 ± 1.2 MΩ	N/A	0.500	0.832	12 MΩ
BHF	2.4 ± 1.1 MΩ	N/A	0.499	0.831	5 MΩ
48% HF	2.0 ± 0.6 MΩ	N/A	0.503	0.834	5 MΩ
c. H2SO4	1.5 ± 1.1 MΩ	N/A	0.516	0.847	1 MΩ
inversion	*11.4 MΩ*	*1.10×10^{-10}*	*0.457*	*0.789*	

Table 12: Barrier height summary table.

Liquid Contact	Mott-Schottky	OC Freq. Spectra	Channel Impedance	Grand Total
n-Si(111)				
40% NH4F	*-0.263 ± 0.019*	0.084 ± 0.014		0.08 ± 0.01
BHF	-0.013 ± 0.139	0.083 ± 0.025		0.04 ± 0.15
48% HF	0.430 ± 0.128	0.525 ± 0.078		0.48 ± 0.10
18 M H2SO4	1.239 ± 0.436	1.411 ± 0.107		1.33 ± 0.27
n-Si(100)				
40% NH4F	*-0.348 ± 0.005*	0.074 ± 0.003	*not inverted*	0.07 ± 0.01
BHF	-0.102 ± 0.193	0.089 ± 0.035	*not inverted*	-0.01 ± 0.14
48% HF	0.391 ± 0.031	0.374 ± 0.023	*not inverted*	0.38 ± 0.03
18 M H2SO4	*1.43*	0.611 ± 0.038	*not inverted*	0.61 ± 0.04
p-Si(111)				
40% NH4F	1.314 ± 0.419	0.883 ± 0.107	1.036 ± 0.028	1.08 ± 0.22
BHF	1.266 ± 0.093	0.753 ± 0.042	1.017 ± 0.022	1.01 ± 0.26
48% HF	0.927 ± 0.041	0.655 ± 0.272	0.912 ± 0.026	0.83 ± 0.15
18 M H2SO4	*0.847*	*0.667*	0.909 ± 0.020	0.91 ± 0.02

Unreliable data are italicized and are not included in the grand total

3.2 Effective Lifetimes

I. INTRODUCTION

The barrier heights for various silicon-liquid contacts have recently been measured using a conventional differential-capacitance vs. potential (Mott-Schottky) technique that has been compared to frequency spectra and channel impedance data of n^+-p-Si(111)-n^+ and p^+-n-Si(100)-p^+ devices measured at open circuit. (See previous section.) The data demonstrate that n-type silicon surfaces are under accumulation when in contact with 40% NH_4F and buffered HF solutions, while they are under normal depletion conditions when in contact with 48% HF, and either depletion or inversion conditions when contacted with 18 M H_2SO_4 depending on the crystallographic face. These results hold interesting implications on the effective charge carrier lifetimes for silicon measured while immersed in these solutions. We have previously shown that a large imbalance in the surface carrier concentrations of electron and holes, which result from either very large (inversion) or very small (accumulation) barrier heights, can result in long charge carrier lifetimes even in the presence of a large number of surface electrical trap states.[4, 25] This implies that only the electronic lifetimes measured for silicon in contact with 48% HF can be used to infer a surface trap state density because only this contact results in roughly equal surface concentrations of electrons and holes. In order to demonstrate the validity of this model, measurement of the charge carrier lifetimes of silicon in contact with these solutions is the focus of this work.

II. EXPERIMENTAL

Double side polished, float-zone, 3 ms lifetime, 4-6 kOhm, *n*-type silicon (111) ± 0.5º wafers with a thickness of 475-525 microns were cut into approximately 1.5 cm × 1.5 cm pieces. Buffered HF (BHF) and 40% ammonium fluoride (NH_4F) solutions were used as received from Transene. Concentrated sulfuric acid (H_2SO_4) and 48% hydrofluoric acid (HF) were used as receive from EM Science. In this work, water will always refer to freshly-obtained 18 MΩ cm water from a Millipore system.

To measure the SRVs of silicon samples in the various etching solutions, sandwich cells were made using 35 x 10 mm Falcon polystyrene petridishes. The lid was turned upside down and used as the base of the cell. Silicon samples were sandwiched between two drops of solution and the polystyrene plates, the lid and bottom, of the petridishes. Since the conductivity of these solutions limits the total dark conductivity of the cell and hence the signal to noise, it is important to minimize the volume of liquid in this way. Hydrogen-terminated silicon, formed through contact with these etching solutions, is hydrophobic and had a tendency to come out of solution, which often changed the observed lifetime. To circumvent this issue it was necessary to completely engulf the sample by adding more liquid to the cell. A small hole was added to the upper portion of the cell by pushing a very hot, flame-heated, glass tube through the polystyrene plate. To assemble the final cell, the silicon sample was sandwiched between two very small drops of liquid and excess solution was added to fully surround the sample.

The etching solutions are conductive and hence also inductively couple with the coil of the SRV system (see Appendix). Since the volume of liquid varied from cell to cell it was necessary to separately tune the matching capacitor and frequency for each sandwich cell; this was necessary to increase the reproducibility between identically prepared samples.

III. RESULTS

Figure 20 shows the lifetimes for silicon samples after repeated exposures of HF, BHF, or NH_4F separated by water rinsing steps, which involved dunking the sample in a bath of water, rinsing under a flowing stream of water, and blowing dry with $N_2(g)$. Exposure number 1 corresponds to solvent-rinsed native oxide terminated samples, which have lifetime values so short that they are indicative of carrier diffusion times to the surface. (See the Appendix) For these measurements, the surface is so electrically defective that the observed photoconductivity decay corresponds only to the time it takes for the carrier to diffuse to the surface. Exposure number 2 corresponds to oxide terminated samples that were placed directly into the etching solution of interest and measured in solution; no pre-etching of the samples was performed. Exposure numbers 3 through 10 were obtained sequentially by removing the sample from the cell, rinsing with water, drying with nitrogen, and measuring the lifetime once immersed in the etching solution again. Exposure number 11 was obtained by measurement in air after a final water rinsing and nitrogen drying step.

IV. DISCUSSION

The data show that the electronic lifetimes for silicon samples immersed in 48% HF decrease with water rinsing steps, while the lifetimes of NH_4F and BHF remain relatively unaffected. M'saad and co-workers have observed a similar trend for the lifetime of *n*-Si(100) samples immersed in 48% HF after successive water rinsing steps.[48] Since the electronic lifetimes for silicon in HF vary over a wide range it is clear that the passivation observed in HF is a chemical one. As shown in the previous section, the barrier height for *n*-Si(111) in contact with HF generates about equal surface electrons and surface holes, which requires the charge carrier lifetime to be dependent on the surface trap state density. These observations demonstrate that the very low surface recombination velocity of 0.25 cm sec^{-1} measured by Yablonovitch *et al.* does in fact correlate to surface electrical trap state densities as low at 10^7 cm^{-2}.[33]

The passivation of HF by the reduction of trap states is demonstrated in exposure number 11 where the lifetime for *n*-Si(111) exposed to air (200 ± 60) is only slightly shorter than the previous measurement in HF (350 ± 150). The measurements under air must depend on the electrical trap state density since gaseous contacts cannot significantly alter the band structure to induce electrochemical passivation.

Lifetime measurements in NH_4F and BHF remain long independent of the interspersed water rinsing steps. These measurements are consistent with the observation of an accumulation layer at the surface of these interfaces. A large excess of surface electrons can minimize the surface recombination rate even in the presence of a large number of surface electrical traps. It is also possible, however, that the NH_4F and BHF solutions have the ability to repair any surface defects introduced by the water rinse steps that the 48% HF solution cannot. In order to verify that the long lifetimes observed in NH_4F and BHF solutions are indeed due to the electrochemical passivation of an accumulation layer, an electrically defective surface must exhibit long lifetimes when in contact with these solutions. This is the focus of the next section of this thesis.

Since the accumulation layer screens out the influence of any surface trap states, the electrical perfection of the silicon surface in NH_4F or BHF cannot be inferred from these measurements. One clue, however, is given by the results of exposure number 11, which could suggest that surfaces in contact with buffered HF have reasonably low electrical defect densities while those in NH_4F may have higher electrical defect densities; the BHF-contacted samples display reasonably long lifetimes in air (173 ± 50), which are consistent with those measured in air after previous contact with HF (200 ± 60). The air-exposed lifetimes measured for samples immediately after contact with NH_4F are, however, very short (50 ± 11 μs) and are only a factor of 2 greater than the diffusion-limited lifetimes. These results are consistent with more detailed study of the surface trap state density for silicon in buffered NH_4F solutions.[89, 90] These researchers have observed a transition from a trap state density of 10^{12} cm^{-2} for pH values greater than 8 to a trap state density of 10^{10} cm^{-2} for pH values lower than 6. However we refrain from drawing a firm conclusion based on our findings because it is also possible that the water rinsing steps, performed with traces of NH_4F, lead more surface electrical traps than water rinsing steps with traces of BHF.

V. CONCLUSIONS

Consistent with the band structure for *n*-Si(111) measured previously, a range of charge carrier lifetime values was obtained for silicon in contact with 48% HF. This range can only be explained by the presence of a moderate barrier height, previously measured to be 0.48 ± 0.10 V, that determines a roughly equal surface electron and hole concentration so that the charge carrier lifetimes can occur with a rate determined by the surface trap state density. The decrease in charge carrier lifetime with water rinsing steps is most likely due to an increase in the level of surface contamination. The charge carrier lifetimes for silicon in contact with NH_4F and BHF are always long, which is expected given the observation of a surface accumulation layer.

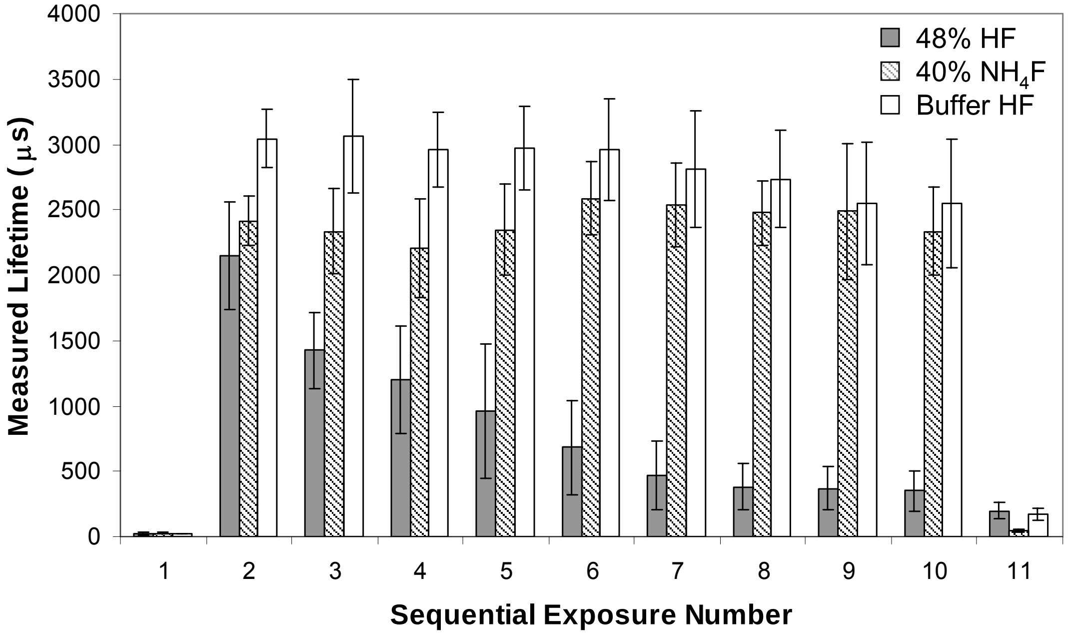

Figure 20: Electronic lifetimes for silicon immersed in etching solutions after sequential rinsing steps.

Exposure number 1 corresponds to solvent-rinsed surfaces covered with a native oxide. Exposure number 2 is obtained immediately after placing the native oxide surface directly into the etchant solution with no pre-etch. Exposure numbers 3 through 10 correspond to sequential water rinsing steps followed by measurement while immersed in the etchant solution. Exposure number 11 represents water-rinsed and N_2(g)-dried samples measured under air.

3.3 Addition of Copper Ions

I. INTRODUCTION

In the previous section the charge carrier lifetimes for silicon were measured in succession while in contact with either 40% NH_4F, buffered HF, or 48% HF after water rinsing steps. The results were expected given the barrier heights previously measured for silicon in these solutions; however, the true test of chemical or electrochemical passivation is performed by using a surface with a high density of electrical defects. The presence of a large imbalance in the surface concentration of electrons and holes, due to the formation of either an accumulation or inversion layer, will display a long charge carrier lifetime even in the presence of a high surface state density as expected by the Shockley-Read-Hall expression.[2-4, 25] Silicon liquid contacts that have a relatively equal surface concentration of electrons and holes, which are characterized by barrier heights around 0.55 V, should display recombination rates proportional to the trap state density. This concept was demonstrated previously (See Chapter 2) by using electrically defective native oxide terminated samples, and long charge carrier lifetimes were observed for those surfaces only when in redox solutions that created an inversion layer, $Fc^{+/0}$-MeOH and I_2-MeOH. [4, 25]

Long charge carrier lifetimes measured for electrically defective silicon samples in NH_4F and buffered HF would further demonstrate that the passivation is due to the formation of accumulation layers as previously measured. Native oxide terminated surfaces, however, cannot be used as controls for this study since oxide layers are actively removed and possibly passivated chemically by the resulting hydrogen-termination. Electrically defective surfaces for this study must be prepared through another method.

Transition metal elements, such as copper, iron, and gold, are known to significantly increase recombination rates.[91-94] The presence of these ions at the Si-SiO_2 interface has been shown to deleteriously effect the performance of MOS devices.[91] *in situ* effective lifetime measurements of silicon samples in 48% HF have been performed by Norga *et al.* upon the addition of trace amounts of copper, and they have observed a significant decrease in the effective lifetime of silicon samples in the presence of copper.[95] However, to our knowledge the electronic lifetimes of copper in NH_4F and BHF have not yet been reported.

The spontaneous electroless deposition of trace copper(II) species onto silicon surfaces has also been well documented.[96-103] Since the Fermi levels for silicon in these solutions are more negative than the formal reduction potential of Cu^{2+}, at least as measured in water, it is suggested that electrons in the conduction band are capable of spontaneously reducing Cu^{2+} to Cu^0.[100, 101] Thus, the spontaneous deposition of copper can be used for the *in situ* generation of a highly defective surface in order to study the charge carrier lifetimes for silicon immersed in solutions of 40% NH_4F, buffered HF, and 48% HF.

II. EXPERIMENTAL

Double side polished, float-zone, 3 ms lifetime, 4-6 kOhm, n-type silicon (111) ± 0.5° wafers with a thickness of 475-525 microns were used for the SRV study in similar polystyrene sandwich cells mentioned in Section 3.2.

Buffer HF (BHF) and 40% ammonium fluoride (NH_4F) were used as received from Transene. Concentrated sulfuric acid (H_2SO_4) and 48% hydrofluoric acid (HF) were used as receive from EM Science. Copper(II) chloride (Aldrich 99.999%) was used as received. The 10 ppm Cu^{2+} solutions were made by dissolving 21 mg of $CuCl_2$ (FW = 134.45) into 100 mL of solution to generate a 100 ppm stock solution that was subsequently diluted to form the 10 ppm solution. Water-rinsed Nalgene bottles were used to store the solutions.

Due to the sensitivity of silicon to trace quantities of copper, extreme care was necessary in order to prevent the cross contamination of copper ions. Separate wafer handling tweezers, pipets, and beakers for water rinses were used. Sandwich cells exposed to a copper-containing solution were only used once then discarded.

Cyclic voltammetric analysis of the copper solutions was performed with a glassy carbon electrode (GCE) to identify the potentials at which copper ions are reduced to metallic copper. The electrochemical cell was similar to that used to study the clean solutions in section 3.1. A plastic cup insert, solely dedicated to copper contaminated solutions, was used. Solutions were purged with ultra high purity argon gas for at least 30 minutes prior to analysis. During measurement, the head space above the cell was purged. Purging of the solution during cyclic voltammetry was not performed since bubbles of argon gas can deposit on the working electrode. The working electrode was a glassy carbon electrode obtained from BAS with an area of 0.068 cm^{-2}. The counter electrode was a piece of Pt gauze, and the reference electrode was another leak-free Ag/AgCl reference electrode (Innovative Instruments, Inc. - Tampa, FL) solely dedicated to the study of copper-containing solutions. All potentials are reported relative to an SCE electrode.

III. RESULTS AND DISCUSSION

A. Surface Recombination Velocities

Table 13 displays the effective lifetimes for samples exposed to clean and copper-containing solutions of HF, BHF, and NH_4F in various orders. The upper left and lower left quadrants of the table display the results for copper-containing solutions while the upper right and lower right quadrants display lifetimes for samples exposed to the same sequence of solutions that were, however, free from copper contamination. The upper half of the table observes the lifetimes when exposed to NH_4F, and the lower half of the table investigates change in lifetime upon exposure to BHF.

Initial lifetime measurements of the native-oxide terminated surfaces were obtained in order to determine the diffusion-limited lifetime. Samples were then put directly into sandwich cells of clean 48% HF for measurement of the surface quality. The oxide and HF-contacted measurements reproduce the data observed in Figure 20.

Upon exposure of the silicon samples to 48% HF containing 10 ppm Cu^{2+}, the electronic lifetimes were drastically lower than those exposed to only to clean HF instead; lifetimes in Cu^{2+}-containing HF approached the diffusion limit, which is indicative of a near infinite surface recombination velocity. Subsequent contact of these samples to clean HF was not able to significantly increase the electronic lifetime. This shows that the electrolessly deposited copper remains on the surface as an active trap state throughout the water-rinsing and re-immersion steps. It also demonstrates that the electrolessly deposited copper acts as the dominate recombination center on these surfaces and not free Cu^{2+} in solution.

Subsequent contact of these copper-containing samples to either NH_4F or BHF solutions containing 10 ppm Cu^{2+} yields significantly longer lifetimes despite the presence of both the deposited Cu^0 on the surface and the free Cu^{2+} in solution. It is interesting that the lifetimes observed in these solutions are considerably longer than those observed immediately before in clean HF, but nevertheless quite a bit shorter than those observed for uncontaminated silicon samples in clean solutions. This will be discussed later. Subsequent contact of these samples to clean HF again displays short, diffusion-limited lifetimes.

Two possible mechanisms could result in the longer lifetimes observed for the copper-deposited surfaces in either NH_4F or BHF relative to HF. First, since NH_4F and, to a lesser extent, BHF are known to etch the silicon surface, it is possible that these solutions are removing the copper contaminants and hence lowering the surface trap state density. Alternatively, the presence of an accumulation layer, which has been demonstrated previously in Section 3.1 for clean NH_4F and BHF solutions, could be responsible for the longer lifetimes, despite the same surface copper concentration and hence the same electrical trap state density. The presence of electrodeposited copper, far in excess of that necessary for the observation of a low lifetime, has been verified for silicon in contact with copper-containing solutions of either NH_4F[101] or BHF.[104] This strongly suggests that the presence of an accumulation layer is responsible for the passivation.

The last measurement in clean HF always displays diffusion-limited lifetimes. If the NH_4F and BHF solutions were removing the copper contamination, then similar lifetimes would be expected when subsequently contacted with *clean* HF. Instead, very short diffusion-limited lifetimes were observed that were similar to the measurements in clean HF directly prior to the Cu-containing NH_4F or BHF solutions. This strongly suggests that the same copper contamination is present throughout the entire process and that the presence of a weak accumulation layer was responsible for the longer lifetimes for silicon in the Cu-containing NH_4F and BHF solutions.

It has, however, also been demonstrated that silicon oxides are formed during the water-rinsing steps immediately after exposure to Cu(II)-containing NH_4F solutions.[102] The growth of these oxides could result in a high density of surface trap states; however subsequent contact to clean HF solutions should remove this oxide and any trap states associated with it. Furthermore, identical lifetimes were measured in the final clean HF step whether the water-rinsing step was performed or excluded.

While the 40% NH_4F and buffered HF solutions passivate the surface to a certain extent while in the presence of surface copper contamination, the lifetimes are still much shorter than those observed in clean, copper-free, solutions. This is surprising if the mechanism for passivation is indeed electrochemical; long lifetimes due to the accumulation layer of electrons should be observed independent of the surface trap state density. The presence of surface copper contamination may, however, change the band structure. The Fermi-level may be pinned at lower energies, which will affect the surface electron and hole concentrations and, hence, the passivation. While significant frequency dispersion prevented the use of Mott-Schottky analysis to determine the barrier heights of silicon in these solutions, open-circuit voltages can be compared for clean and copper-containing solutions under the assumption that the band edges do not move. Figure 21 presents the open-circuit potentials of *n*-Si(111) electrodes immersed in clean and copper-containing solutions as a function of time immediately upon exposure.

Open-circuit voltages for silicon in contact with copper-containing solutions of NH_4F and BHF were consistently 200 mV less than those in the clean, copper-free, solutions. If the band edges remain the same in the presence and absence of copper, then the change in open-circuit voltage corresponds to approximately a three order of magnitude lower surface electron concentration in the copper-containing solutions. The accumulation layer is hence much smaller in the copper-containing solution, and the passivation is expected to be less, as observed. Similarly, the open-circuit voltage observed for silicon in contact with copper-containing BHF is about 150 mV less than the copper-containing NH_4F, which explains the lower lifetimes observed for silicon in the copper-containing BHF (112 ± 9 μs) relative to copper-containing NH_4F (360 ± 190 μs).

The lower open-circuit potentials observed for silicon in copper-containing NH_4F and BHF solutions can be explained in two ways. In the previous section, it was suggested that the step-flow etching mechanism could be responsible to the injection of charge into the conduction band that led to the accumulation layer. Copper has been shown to reduce the extent of the step-flow etching mechanism and so the open-circuit potential could be more positive due to the decrease in this charge-injecting mechanism. Alternatively, the loss of surface electrons during the spontaneous reduction of cupric ions to metallic copper could be the result of the lower Fermi level. Both processes could occur at the same time to establish a steady state current flux that positions the open-circuit voltage where it is. As opposed to suggestions from other reports,[99] the spontaneous electrodeposition of copper may not require charge neutrality if the Fermi level changes and, hence, the anodic dissolution of silicon is not necessarily required to balance the charge used during the reduction of copper onto the surface for these cases of NH_4F and BHF. We are unaware of any reports regarding the concomitant anodic etching of silicon with deposition of copper in either buffered HF or NH_4F.

The open-circuit voltage for silicon in contact with copper-containing 48% HF is roughly the same as that for silicon in contact with clean 48% HF solution, and both are quite a bit more positive than those in either BHF or NH_4F. The difference in acidity and ammonia ligand concentration between the HF, BHF, and NH_4F solutions may change the redox potentials of the Cu^{2+} ions in solution. For this reason, each solution was studied by cyclic voltammetric analysis.

This result is also very interesting with regard to the formation of copper on the surface. As observed by STM, copper deposits form as small clusters,[98, 101] predominantly near the step edges.[101] However, the results presented in this work indicate that they are not able to pin the Fermi level at least globally. Small regions of pinch-off, which have been demonstrated for well-defined Ni metal clusters on silicon,[105, 106] may occur in the vicinity around the particle. The particles, however, must be small enough so that the pinch-off effect still dominates the band structure. The application of sufficient deposition charge, on the other hand, can lead to electrodeposited films of copper that have well-behaved diode qualities with a barrier height of 0.68 V.[98]

B. Cyclic Voltammetry Using a GCE Electrode

Cyclic voltammograms of 10 ppm Cu^{2+} in 48% HF, buffered HF, and 40% NH_4F are overlaid in Figure 22. It is readily observed that the redox activity of copper is quite different in these solutions, which is due to the difference in acidity and ammonia ligand concentration. Similar results have been demonstrated by Grujicic *et al.* for $(NH_4)_2SO_4$ solutions of copper at pH 4, pH 6, and pH 8.[107] The CVs of $(NH_4)_2SO_4$ at pH 4 and pH 8 serve as guides for the CVs in the buffered HF (BHF) and 40% NH_4F solution of this work since they have similar pH values.

Cyclic Voltammetry in 40% NH_4F

The cyclic voltammograms for 10 ppm Cu^{2+} in 40% NH_4F are shown in Figure 23, Figure 24, and Figure 25 and are similar to the cyclic voltammograms of copper species in ammonium sulfate solutions at pH 8. [107] Table 14 compares the redox potentials in this study with potentials and assignments presented in the work of Grujicic *et al.*[107] Three reductive peaks and two anodic peaks are observed for the GCE electrode in the Cu^{2+}-containing NH_4F solution studied in this work. The first reduction peak occurs at −0.13 V vs. SCE and represents the reduction of cupric ammine to cuprous ammine. The second reduction peak is very small and independent of scan rate and occurs at −0.54 V vs. SCE; the nature of this peak is unknown, as it was not observed in the work by Grujicic *et al.*, but it might represent the reduction of cupric fluoride species to cuprous fluoride species. The third cathodic peak is less evident from the results shown here as it is right near the turn-around potential. This peak is however scan-rate dependent and occurs around −0.78 V vs. SCE and is consistent with the reports of Grujicic *et al.* for the reduction of cuprous ammine to metallic copper. The oxidation of metallic copper to cupric ammine in 40% NH_4F occurs at −0.178 V vs. SCE. This is verified by its thin sharp shape that is typically observed for species adsorbed on an electrode surface. The resulting cupric ammine can react with nearby metallic copper in a conproportionation reaction to generate cuprous ammine as shown below.

$$Cu^0 + Cu(NH_3)_4^{2+} = 2Cu(NH_3)_2^{+} \qquad (22)$$

The cuprous ammine, generated in this manner, can then be reduced to cupric ammine at −0.065 V vs. SCE. This assignment is well supported by the near 60 mV difference between the cathodic and anodic peaks as shown in Figure 25 (62 mV peak separation at 10 mV/sec scan rate). The broad anodic peak at −0.226 V was not observed in the $(NH_4)_2SO_4$ study and most likely represents the oxidation of the cathodic peak at −0.54 V vs. SCE.

Cyclic Voltammetry in Buffered HF

Cyclic voltammetric analysis of 10 ppm Cu^{2+} in buffered HF (BHF) yielded results similar to the studies of copper in ammonium sulfate solutions of pH 4, which are displayed in Table 14. A scan-rate-dependent reduction peak at -0.21 V (25 mV/s) vs. SCE represents the reduction of cupric species to metallic copper. Due to the acidity of the solution, most of the ammonia molecules are presumed to be protonated and hence are not suitable as ligands. Copper species with aquo ligands are easier to reduce than the ammine stabilized species. This presence of aquo ligands in BHF is demonstrated further by the occurrence of the sharp anodic wave due to the oxidation of metallic copper even when the potential is only scanned as negative as −0.4 V vs. SCE (Figure 27), while the −0.4 V vertex potential is not negative enough to reduce the ammine complex (Figure 24). The shoulder preceding the peak at -0.21 V is attributed to the reduction of cupric species to cuprous species, which disproportionates as described below.

$$2Cu(H_2O)_4^{+} = Cu^0 + Cu(H_2O)_6^{2+} + 2H_2O \qquad (23)$$

The anodic region shows only one sharp peak at −0.02 V vs. SCE with no diffusion component and represents the oxidation of metallic copper to cupric species. No other peaks are observed except the reduction of hydrogen, catalyzed on the metallic copper, at potentials less that -0.9 V vs. SCE.

Cyclic Voltammetry in 48% HF

Analysis of copper species in ammonium sulfate solutions was not performed at pH values less than 4 in the study by Grujicic *et al*. and therefore the cyclic voltammetric analysis of Cu^{2+} in 48% HF cannot be directly compared as could be the other solutions. The sharp shape of the anodic peak at 0.07 V vs. SCE is most likely due to the oxidation of metallic copper. The cathodic peak at -0.2 V likely represents the reduction of cupric species to metallic copper. The shifting of both of these peaks to more positive potentials, by about 100 mV relative to BHF, makes sense because the more acidic nature of the 48% HF solution is even less able to adequately ligate the copper ion; this destabilizes the ions and forces the oxidation and reduction to occur at more positive potentials. Furthermore, while the peaks are shifted, the peak separation between the oxidation and reduction peaks (at 100 mV/s) is 0.27 V in 48% HF, which is within error the same peak separation of 0.27 V observed for these species in buffered HF at the same scan rate. The cathodic peak at −0.5 V vs. SCE corresponds to the catalytic reduction of hydrogen on copper in the highly acidic 48% HF solution. The other peaks at more positive potentials are unknown but not as important towards the understanding of deposition potentials for metallic copper.

Summary of Cyclic Voltammetry on a GCE electrode

Of most importance is the potential at which copper species in solution are reduced to metallic copper. These potentials are −0.78 V, −0.21 V, and ≈−0.15 V for 40% NH_4F, buffered HF, and 48% HF respectively. The shift in potential is due to the differing ability of the ligands in solution to stabilize the copper ions in solution. The ammonia ligands present in 40% NH_4F solutions cause a strong stability of the copper species. At lower pHs, the ammonia molecules are protonated and predominantly only water ligands are available for bonding with the copper ions. The water ligands are not nearly as electron-donating, and these copper species are corresponding reduced at more positive potentials. In 48% HF, the copper species are even more destabilized, and deposition of metallic copper occurs at more positive potentials.

The cyclic voltammograms for Cu(II) ions in NH_4F and BHF corroborate other studies performed in ammonium hydroxide solutions of various pH. The shapes of the cyclic voltammetric responses and scan rate dependencies were nearly identical to results of this study, which indicates that the fluoride ion does not significantly alter the electrochemistry in these solutions, however, it may be responsible for an anodic and cathode peak observed in NH_4F. In all cases the reduction potential of Cu^+ or Cu^{2+} to

Cu^0 is more positive than the open-circuit potentials of silicon in clean etching solutions. This means the spontaneous reduction of copper is thermodynamically downhill.

C. Cyclic Voltammetry with Silicon Electrodes

The reduction of cupric or cuprous species to metallic copper may be different on glassy carbon than it is on silicon due to the difference in stability of copper on these surfaces. To test this, cyclic voltammograms of freshly etched *n*-Si(111) electrodes were performed in the copper-containing etching solutions and compared with those of clean solutions. The results are shown in Figure 30, Figure 31, and Figure 32. Similar studies have been performed for silicon in solution NaOH solutions of CuCN and NaCN.[98]

Large anodic peaks are observed on the *n*-Si(111) electrodes at −0.56 V vs. SCE in NH_4F and at -0.41 V vs. SCE in BHF in the Cu^{2+}-containing solutions that are not present in the clean solutions. These peaks are very likely due to the oxidation of metallic copper to the analogous solvated cupric species as described for the GCE electrode above. This is supported by the fact that the difference in oxidation potential (≈ 0.15 V) of metallic copper on silicon electrodes in NH_4F and BHF is reflected by the same change in oxidation potential (≈ 0.15 V) between the NH_4F and BHF solutions using the GCE electrode. Since the aqueous cupric species constitute the same oxidation product when using a GCE or silicon electrode, the difference in oxidation potential must indicate the stability of the adsorbed metallic copper. Since the oxidation of copper occurs at a much more negative potential on silicon, the stability of copper on silicon is lower than on a GCE electrode.

The CV of *n*-Si(111) in 10 ppm Cu^{2+}-containing HF does not show any resolvable peaks, although there is in general more anodic and cathodic current. Using the same analysis above, the oxidation of metallic copper on a GCE electrode in HF occurs at a potential 100 mV more positive than in BHF. This would suggest that metallic copper on silicon should oxidize at -0.3 V vs. SCE, however no oxidative peak appears here. This hypothesis also fails because the open-circuit potential of silicon is more positive of −0.3 V (typically it is around −0.2 V), and the electroless deposition of copper is known to occur spontaneously at this potential.

The open-circuit deposition of copper on silicon surfaces in HF solutions has been demonstrated to occur with concomitant oxidative dissolution of silicon. This has been shown by AFM measurements where etch pits have been observed surrounding copper deposits.[99] This anodic etching of silicon has been rationalized as necessary to maintain charge neutrality during the reduction of copper onto the surface. As presented above, the arguments in favor of charge neutrality are only necessary if the Fermi level remains the same in both clean and copper-containing solutions. For HF solutions, the open-circuit voltage, and hence the Fermi level, is roughly the same for clean and copper-containing HF solutions, so a mechanism for charge neutrality is necessary in this case. If the spontaneous deposition of copper and the concomitant anodic dissolution of silicon occur at open circuit as observed,[99] it seems logical that cyclic voltammetric analysis would not display a well-defined peak for the oxidation of metallic copper; the anodic dissolution of silicon is preferred over the oxidation of metallic copper at positive potentials since this is preferred even at open circuit. This hypothesis explains not only the absence of a well-defined oxidation peak for metallic copper but it also accounts for the general increase in anodic current, which has the same profile as anodic oxidation of silicon; the presence of copper enhances the anodic dissolution of silicon at positive potentials rather than the oxidation of metallic copper deposits. Furthermore, the presence of copper facilitates the reduction of hydrogen relative to silicon so an increase in the hydrogen reduction current is also observed in the cyclic voltammogram.

The presence of copper on the surface of silicon in each of these solutions is verified by the reduction of hydrogen on the copper regions that occurs at a similar potential on silicon and GCE. The reduction of hydrogen occurs around −0.45 V in Cu^{2+}-containing HF solution on both silicon and GCE, while the reduction of hydrogen occurs at −0.8 V in Cu^{2+}-containing buffered HF on both electrodes. The reduction of hydrogen is shifted to even more negative potentials in NH_4F because the pH continues to increase.

Finally, the open-circuit potential of silicon in Cu^{2+}-containing buffered HF is poised between the oxidation and reduction potentials of copper on these surfaces as expected for Fermi-level equilibration with the copper species. The open-circuit potential for silicon in clean buffered HF is more negative that the cathodic reduction potential of copper on silicon, which indicates that the electroless deposition occurs spontaneously.

IV. CONCLUSIONS:

Electronic passivation of *n*-Si(111) surfaces has been observed even in the presence of copper-contaminated for 10 ppm Cu^{2+}-containing solutions of 40% NH_4F and buffered HF, which is ascribed to the formation of a weak accumulation layer. Electronic passivation is not observed in 48% HF solutions since the band structure dictates equal electron and hole concentrations at the surface. The thermodynamics of copper deposition onto *n*-Si(111) in solutions has been studied in solutions of 40% NH_4F and buffered HF. In clean solutions the open-circuit potentials of *n*-Si(111) are more negative than the observed reduction potentials of copper on silicon surfaces, which is responsible for the spontaneous electroless deposition. At equilibrium the open-circuit potential is poised between the reduction and oxidation potentials of metallic copper, which is expected for Fermi-level equilibration. The copper particles that form on the surface are either not large enough to overcome the pinch-off region, or do not have sufficient metallic band structure to pin the Fermi as expected for significant metallic copper coverage.

Table 13: Charge carrier lifetimes for *n*-Si(111) exposed to Cu^{2+}-containing etching solutions.

Sequential Exposure	Lifetime (μs)	Sequential Exposure	Lifetime (μs)
In Air	22 ± 1	In Air	20 ± 2
Clean HF	1850 ± 200	Clean HF	2100 ± 200
HF 10 ppm Cu^{2+}	37 ± 9	Clean HF	1840 ± 350
Clean HF	50 ± 20	Clean HF	1310 ± 740
NH_4F 10 ppm Cu^{2+}	360 ± 190	Clean NH_4F	2900 ± 930
Clean HF	22 ± 1	Clean HF	990 ± 530
In Air	17.7 ± 0.5	In Air	270 ± 20

Sequential Exposure	Lifetime (μs)	Sequential Exposure	Lifetime (μs)
In Air	21 ± 1	In Air	22 ± 2
Clean HF	2070 ± 910	Clean HF	1940 ± 240
HF 10 ppm Cu^{2+}	26 ± 5	Clean HF	1790 ± 180
Clean HF	28 ± 7	Clean HF	1790 ± 240
BHF 10 ppm Cu^{2+}	112 ± 9	Clean BHF	2420 ± 120
Clean HF	22 ± 2	Clean HF	1600 ± 500
In Air	21 ± 1	In Air	230 ± 90

Table 14: Cyclic voltammetric data for Cu-containing 40% NH_4F, buffered HF, and 48% HF solutions.

	Potential (V vs SCE)		
Reaction[1]	40% NH_4F	$(NH_4)_2SO_4$ (pH 8)[1]	*n*-Si(111)
$Cu(NH_3)_4^{2+} + e^- = Cu(NH_3)_2^+ + 2NH_3$	−0.13	−0.122	-
$Cu(NH_3)_2^+ + e^- = Cu^0 + 2NH_3$	−0.78*	−0.84*	-
$Cu^0 + 4NH_3 = Cu(NH_3)_4^{2+} + 2e^-$	−0.178	−0.222	−0.56
$Cu(NH_3)_2^+ + 2NH_3 = Cu(NH_3)_4^{2+} + e^-$	−0.065	−0.022	-

Reaction[1]	Buffered HF	$(NH_4)_2SO_4$ (pH 8)[1]	*n*-Si(111)
$Cu(H_2O)_6^{2+} + e^- = Cu(H_2O)_4^+$	≈ −0.18	≈ −0.12	-
$Cu(H_2O)_6^{2+} + 2e^- = Cu^0 + 6H_2O$	≈ -0.21*	≈ −0.24*	-0.73
$Cu^0 + 6H_2O = Cu(H_2O)_6^{2+} + 2e^-$	−0.02	−0.04	−0.41

Reaction	48% HF	$(NH_4)_2SO_4$	*n*-Si(111)
$Cu^{2+}(L)_x + 2e^- = Cu^0 + xL$	≈ -0.15*	-	N/A
$Cu^0 + xL = Cu^{2+}(L)_x + 2e^-$	0.07	-	N/A

[1] Information provided by Grujicic *et. al*.

* The reaction is scan rate dependent.

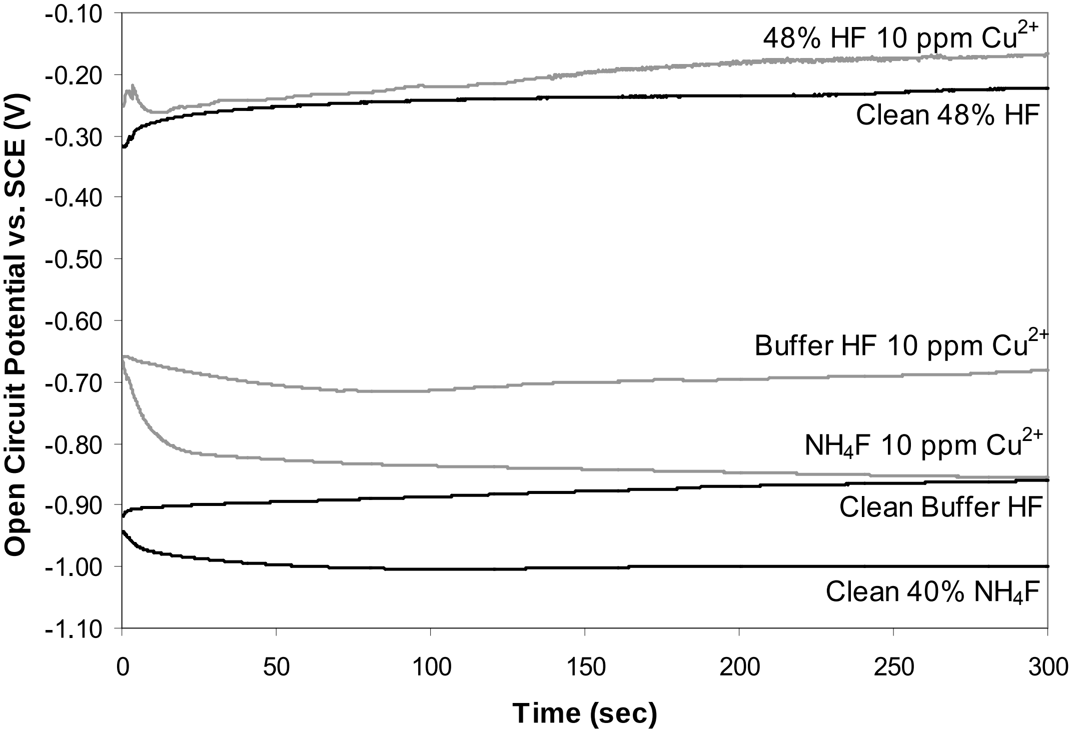

Figure 21: Open-circuit voltages for silicon in contact with clean and Cu^{2+}-containing etching solutions.

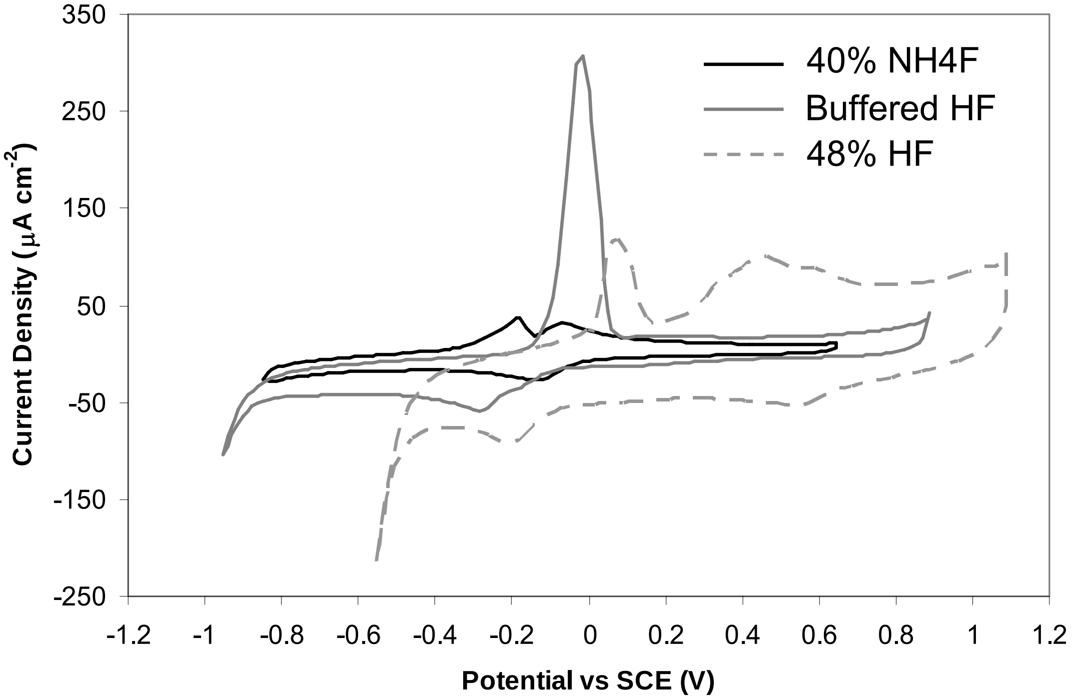

Figure 22: Cyclic voltammogram of a GCE electrode in etching solutions containing 10 ppm Cu^{2+}.

The cell consisted of a glassy carbon working electrode, a Pt gauze counter electrode, and a leak-free Ag/AgCl reference electrode. Potentials are reported vs. SCE. All solutions were purged with argon for 30 min. The CVs are: black solid line, 10 ppm Cu^{2+} in 40% NH_4F; gray solid line, 10 ppm Cu^{2+} in buffered HF; and gray broken line, 10 ppm Cu^{2+} in 48% HF.

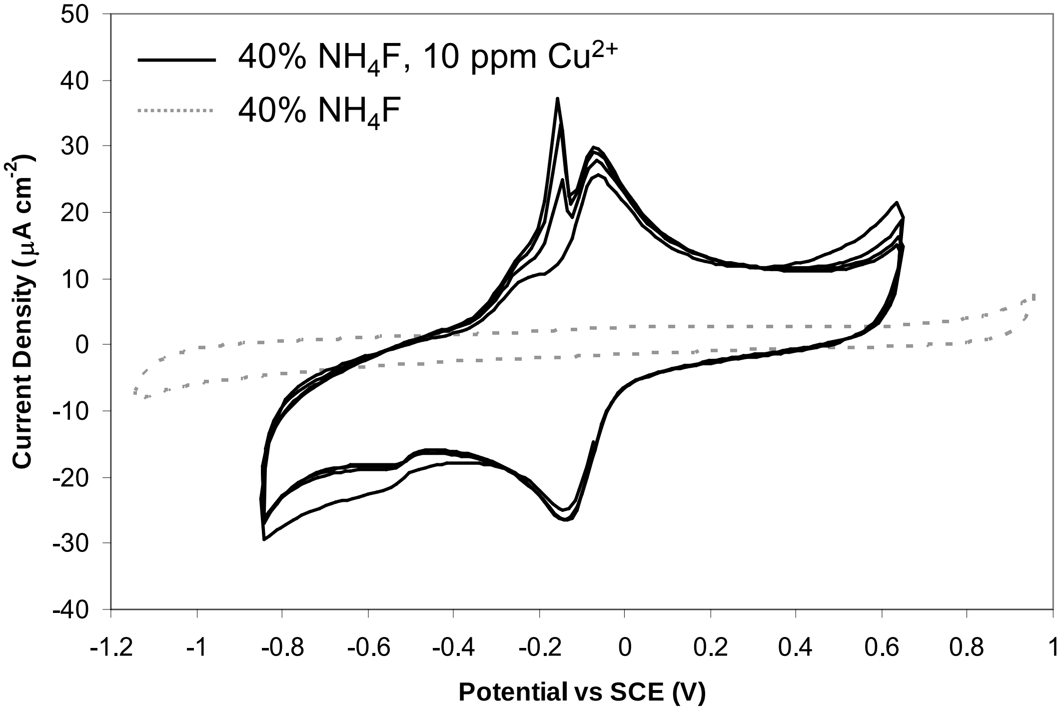

Figure 23: Cyclic voltammogram of clean and 10 ppm Cu^{2+}-containing 40% NH_4F. The cell consisted of a glassy carbon working electrode, a Pt gauze counter electrode, and a leak-free Ag/AgCl reference electrode. Potentials are reported vs. SCE. Both solutions were purged with argon for 30 min. The CVs are: black solid line, the first several cyclic voltammograms of 10 ppm Cu^{2+} in 40% NH_4F; and gray dotted line, clean 40% NH_4F.

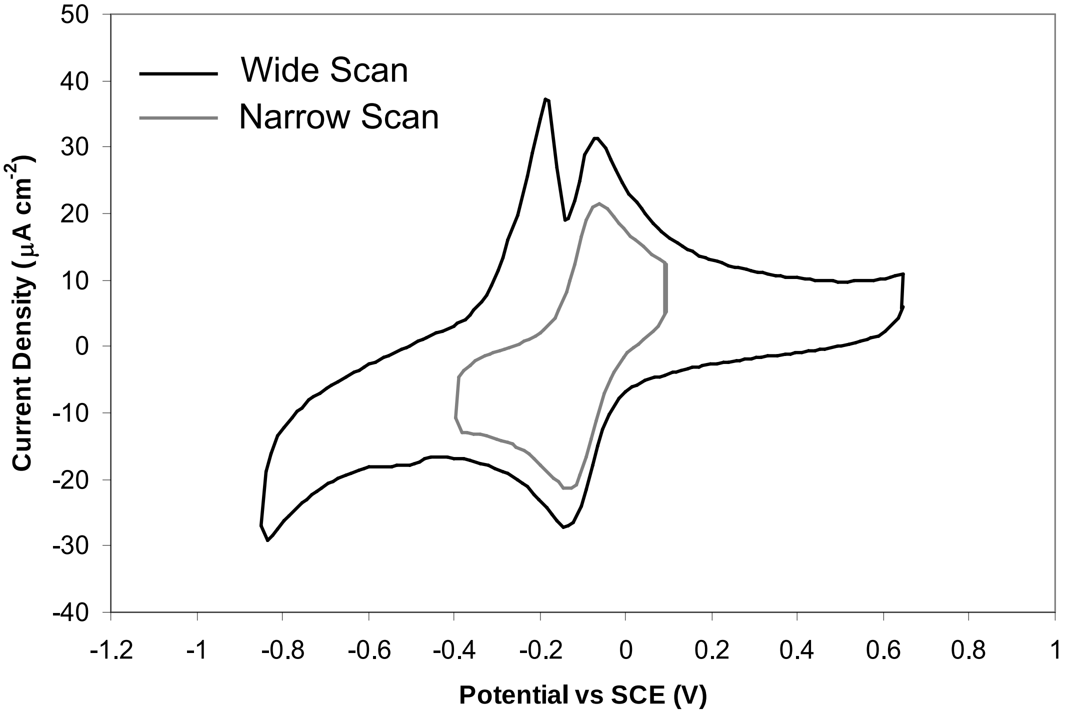

Figure 24: Wide and narrow cyclic voltammograms of 10 ppm Cu^{2+} in 40% NH_4F. The cell consisted of a glassy carbon working electrode, a Pt gauze counter electrode, and a leak-free Ag/AgCl reference electrode. Potentials are reported vs. SCE. The solution was purged with argon for 30 min. The CVs are: black solid line, wide scan of 10 ppm Cu^{2+} in 40% NH_4F; and gray solid line, narrow scan of 10 ppm Cu^{2+} in 40% NH_4F.

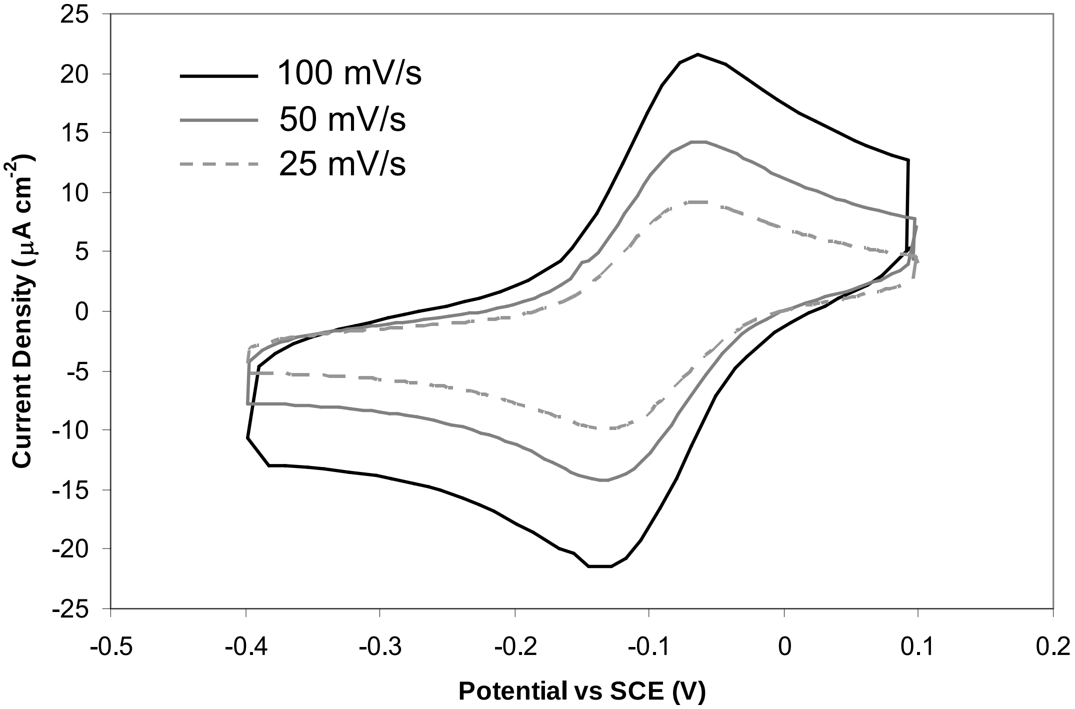

Figure 25: Scan rate dependence of the 10 ppm Cu^{2+}-containing 40% NH_4F solution.

The cell consisted of a glassy carbon working electrode, a Pt gauze counter electrode, and a leak-free Ag/AgCl reference electrode. Potentials are reported vs. SCE. The solution was purged with argon for 30 min. The CVs are: black solid line, 100 mV/s scan rate; gray solid line, 50 mV/s scan rate; and gray broken line, 25 mV/s scan rate.

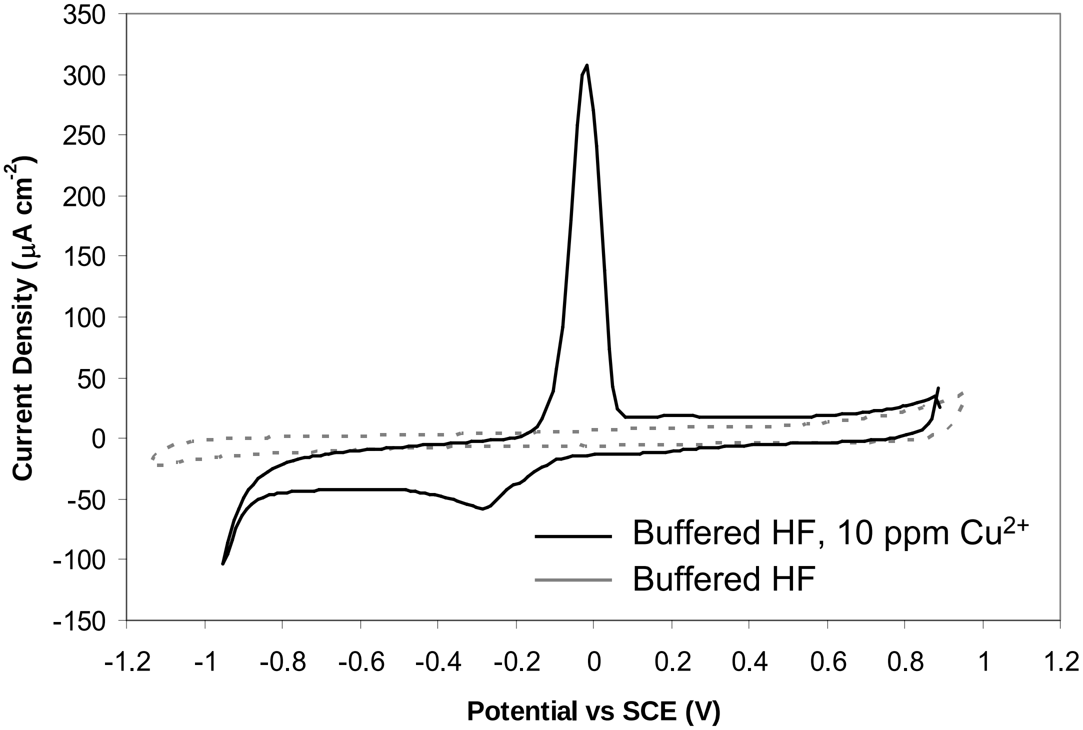

Figure 26: Cyclic voltammogram of clean and 10 ppm Cu^{2+}-containing buffered HF.

The cell consisted of a glassy carbon working electrode, a Pt gauze counter electrode, and a leak-free Ag/AgCl reference electrode. Potentials are reported vs. SCE. Both solutions were purged with argon for 30 min. The CVs are: black solid line, 10 ppm Cu^{2+} in buffered HF; and gray dotted line, clean buffered HF.

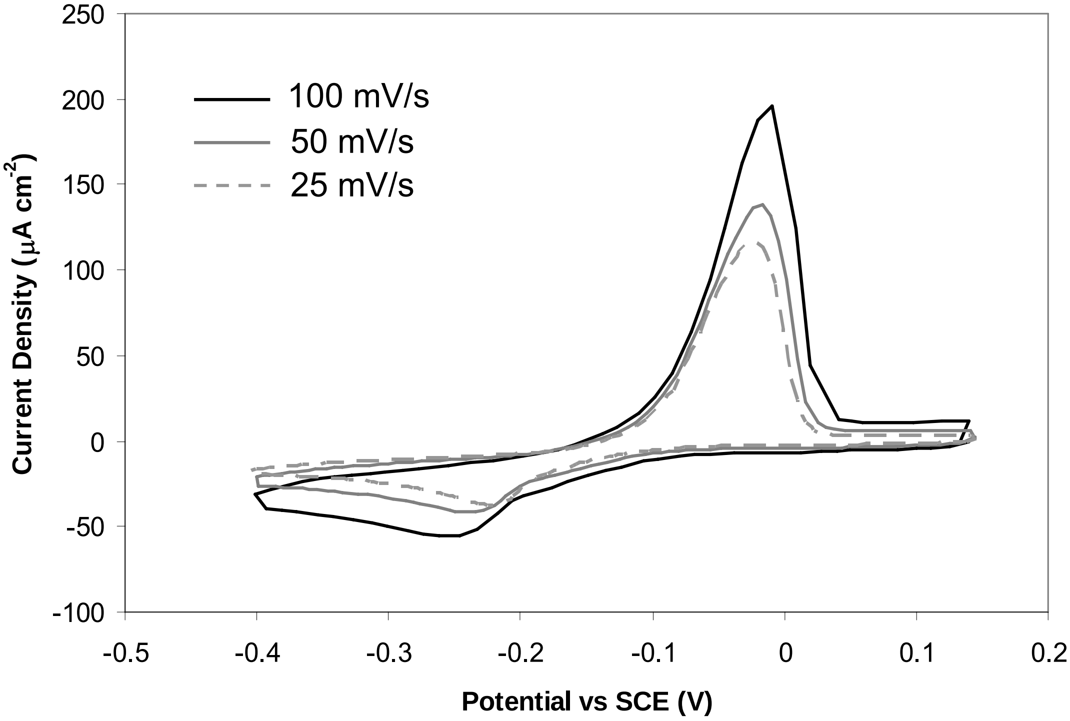

Figure 27: Scan rate dependence of the 10 ppm Cu^{2+}-containing buffered HF solution.

The cell consisted of a glassy carbon working electrode, a Pt gauze counter electrode, and a leak-free Ag/AgCl reference electrode. Potentials are reported vs. SCE. The solution was purged with argon for 30 min. The CVs are: black solid line, 100 mV/s scan rate; gray solid line, 50 mV/s scan rate; and gray broken line, 25 mV/s scan rate.

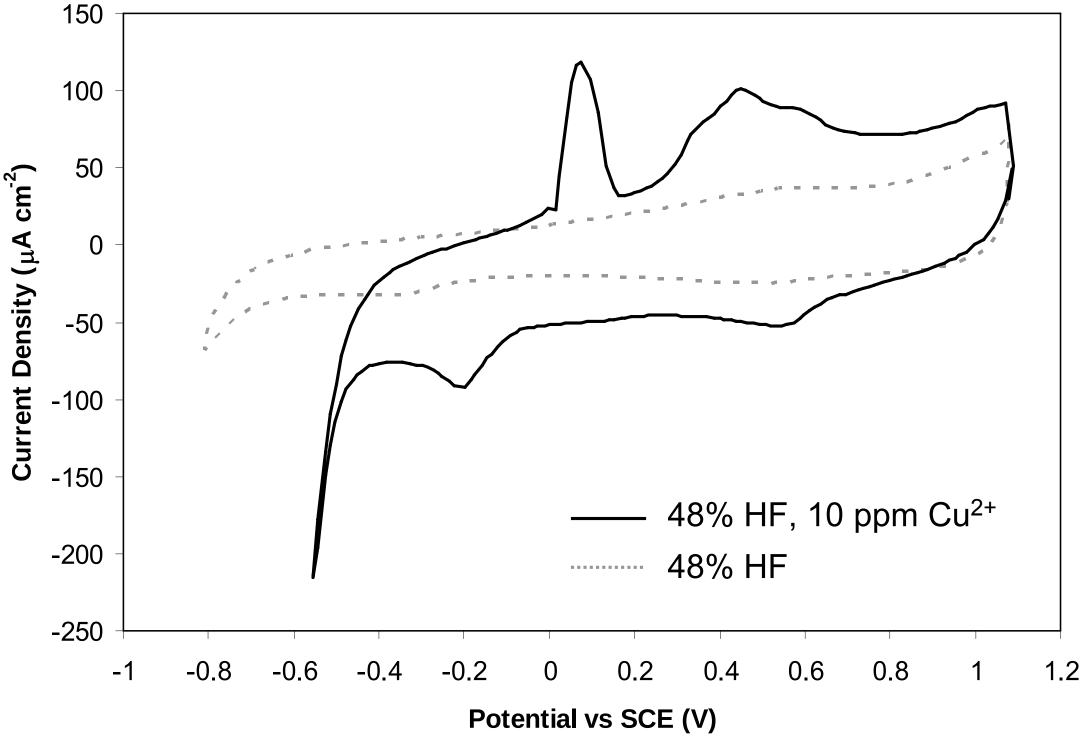

Figure 28: Cyclic voltammogram of clean and 10 ppm Cu^{2+}-containing 48% HF. The cell consisted of a glassy carbon working electrode, a Pt gauze counter electrode, and a leak-free Ag/AgCl reference electrode. Potentials are reported vs. SCE. Both solutions were purged with argon for 30 min. The CVs are: black solid line, 10 ppm Cu^{2+} in 48% HF; and gray dotted line, clean 48% HF.

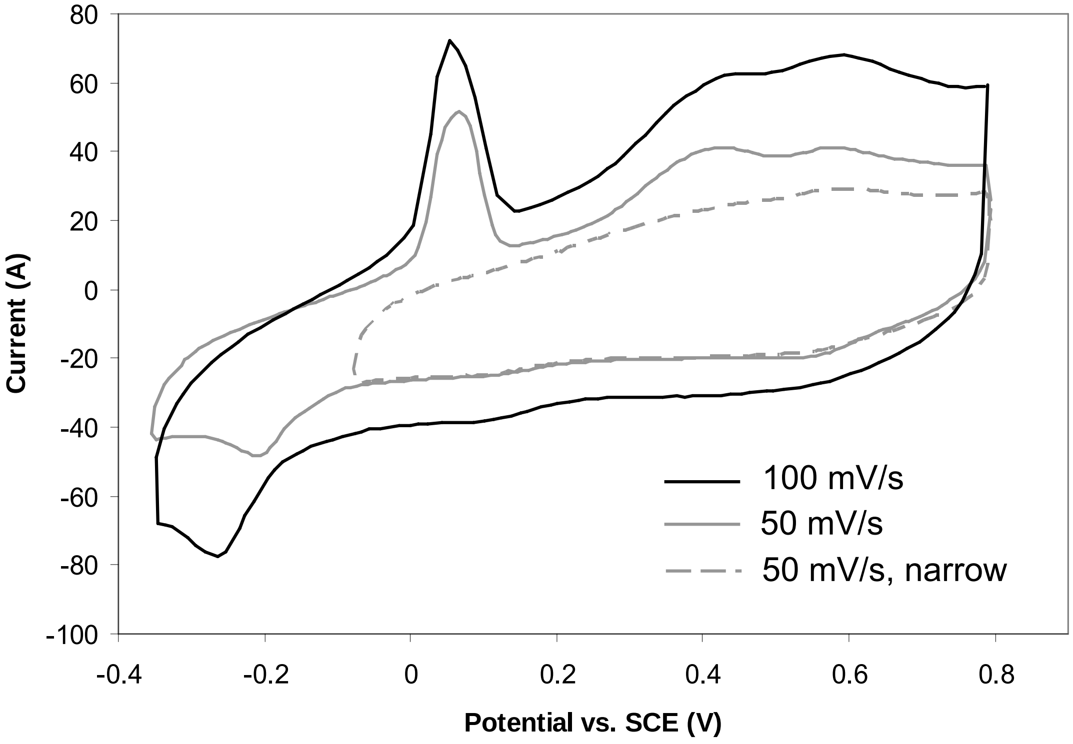

Figure 29: Wide and narrow cyclic voltammograms of 10 ppm Cu^{2+} in 48% HF. The cell consisted of a glassy carbon working electrode, a Pt gauze counter electrode, and a leak-free Ag/AgCl reference electrode. Potentials are reported vs. SCE. The solution was purged with argon for 30 min. The CVs are: black solid line, 100 mV sec^{-1} wide scan of 10 ppm Cu^{2+} in 48% HF; gray solid line, 50 mV sec^{-1} wide scan of 10 ppm Cu^{2+} in 48% HF; and gray broken line, 50 mV sec^{-1} narrow scan of 10 ppm Cu^{2+} in 48% HF.

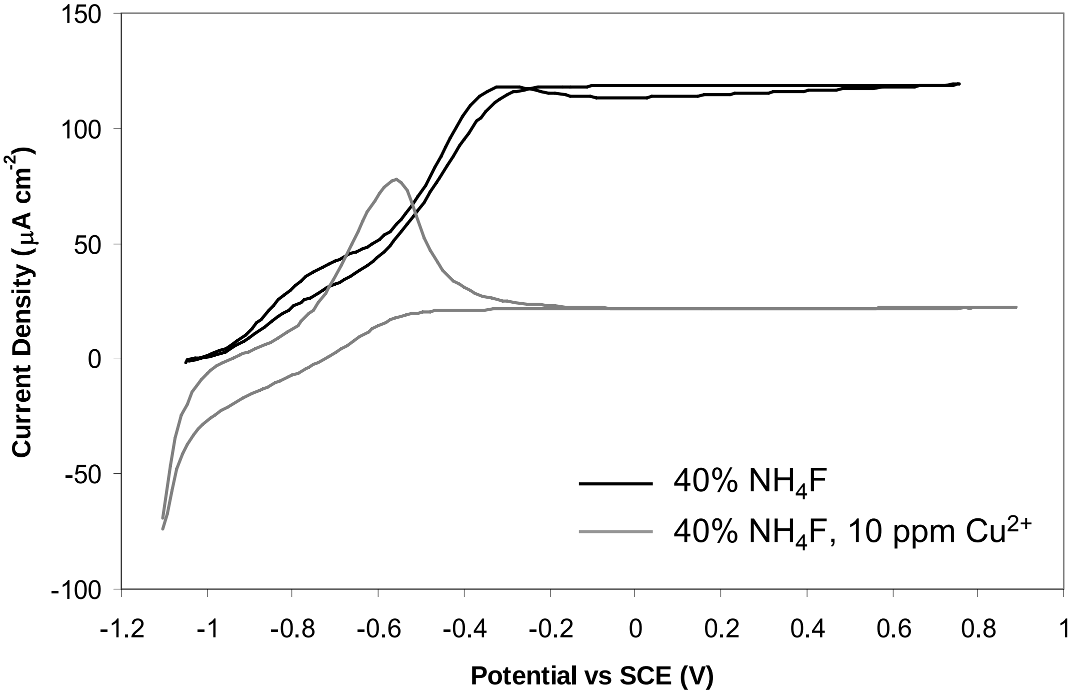

Figure 30: Cyclic voltammograms for *n*-Si(111) in clean and Cu^{2+}-containing 40% NH_4F.

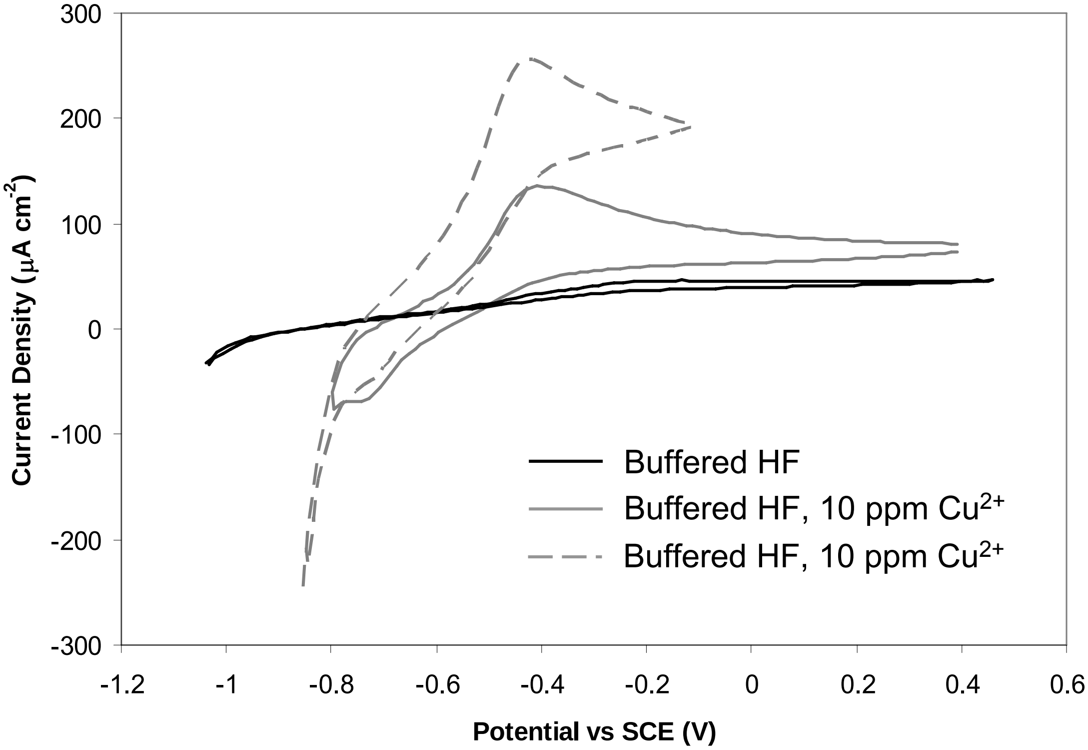

Figure 31: Cyclic voltammograms for *n*-Si(111) in clean and Cu^{2+}-containing buffered HF.

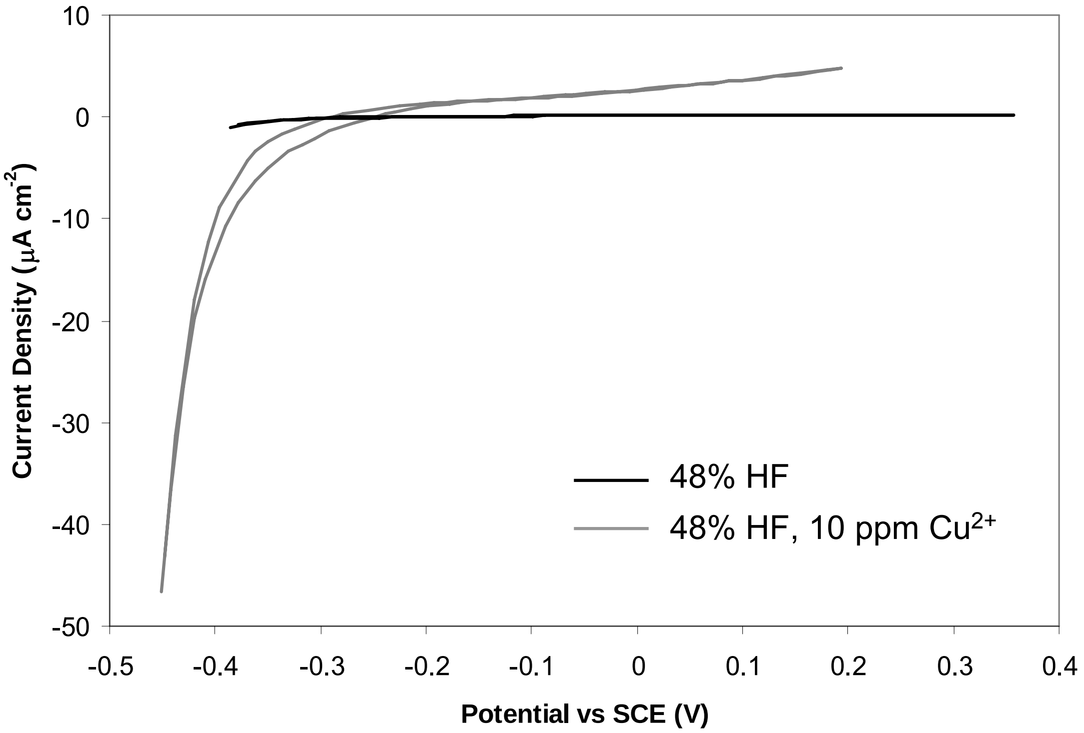

Figure 32: Cyclic voltammogram of *n*-Si(111) in clean and Cu^{2+}-containing 48% HF.

3.4 Time-Dependent Effects

The band structure and surface recombination properties of some silicon liquid contacts have been observed to display effects on immersion time and previous history. These effects have been observed both during channel impedance and lifetime measurement studies. Specifically, contact of silicon with a given etching solution after exposure to a variety of other ambients lead to irreproducibility. This is not unexpected since samples have been treated to a variety of harsh conditions; however they are studied in more detail in this section.

Most notable is the decrease in electronic lifetime for samples measured in 48% HF after contact with other solutions or ambients. This trend is observed even in Figure 20 where the rinsing of the sample with 18 MΩ cm water causes sequentially lower lifetimes measured in 48% HF. This was attributed to the gradual increase in surface contamination during the water-rinsing steps. This trend has been observed in other cases as well.

Figure 33 shows the lifetimes measured with one sample exposed to sequential solutions. While this figure describes the performance of only one sample, and hence does not have error bars, the performance of this sample is representative of the trends observed with other samples. Diffusion limited lifetimes are observed for the sample when measured in air as received with its native oxide covering, after subsequent solvent rinses, and after exposure to a 3:1 mixture of concentrated sulfuric acid and 30% H_2O_2 (piranha solution). When placed directly into 48% HF, the sample displays long lifetimes indicative of a low defect density. After a water-rinsing step, the lifetime measured under air is quite short. (It should be noted that the lifetimes measured in air in section 3.2 were performed under the cleanest situations and tend to have longer lifetimes than those measured in other studies.) Subsequent exposure of that sample to 40% NH_4F restores the long lifetime. Subsequent lifetimes measured in air and 48% HF are very short owing to the increase in surface contamination during the rinsing and handling steps. Subsequent measurement in NH_4F displays lifetimes that are quite a bit shorter than previously observed in NH_4F. The sample was then oxidized for 10 minutes in piranha solution to remove any surface contamination. Subsequent measurements in 48% HF and 40% NH_4F restore the initially observed long lifetimes. With more rinsing and handling steps, the lifetime decreases again in a similar manner. This experiment illustrates a couple important points. First, the lifetimes in HF, and to a lesser extent in NH_4F, are a function of the previous history of the sample. Second, impurities can be successfully removed through a 10 minute exposure to piranha solution. The lifetimes for silicon samples in HF are much more sensitive to the level of contamination than for silicon samples in NH_4F, as has been observed and explained above.

The equilibration effect, observed for samples immersed for long times in 40% NH_4F, is demonstrated in Figure 34. In this figure, the lifetimes obtained from the sequential exposure of a single *n*-Si(111) wafer piece to various etching solutions are displayed. While only the results from one sample are presented they adequately represent the trends observed in other samples in similar sequential exposure studies. The first several exposures of the sample to various etching solutions show trends in corroboration with the history effect. In this study, however, the longer lifetimes observed in 48% HF indicate that the rinsing and handling steps introduced less contamination than during the study presented in Figure 33. Of particular interest are the lifetimes observed in the last two exposures of the sample to 40% NH_4F. While the first several measurements in all solutions have been relatively independent of immersion time in solution, the initially low lifetimes observed during the last two exposures to NH_4F increase with time. After about 10 minutes, the lifetime approaches values initially observed in NH_4F. Longer exposure times to NH_4F have been measured but are unfortunately complicated by the bubbles that form at the interface and prevent intimate contact of the liquid to the surface of the sample. At times much longer than those presented here, the samples tend to slip out of solution due to the hydrophobic nature of the surface and the formation of bubbles at the interface.

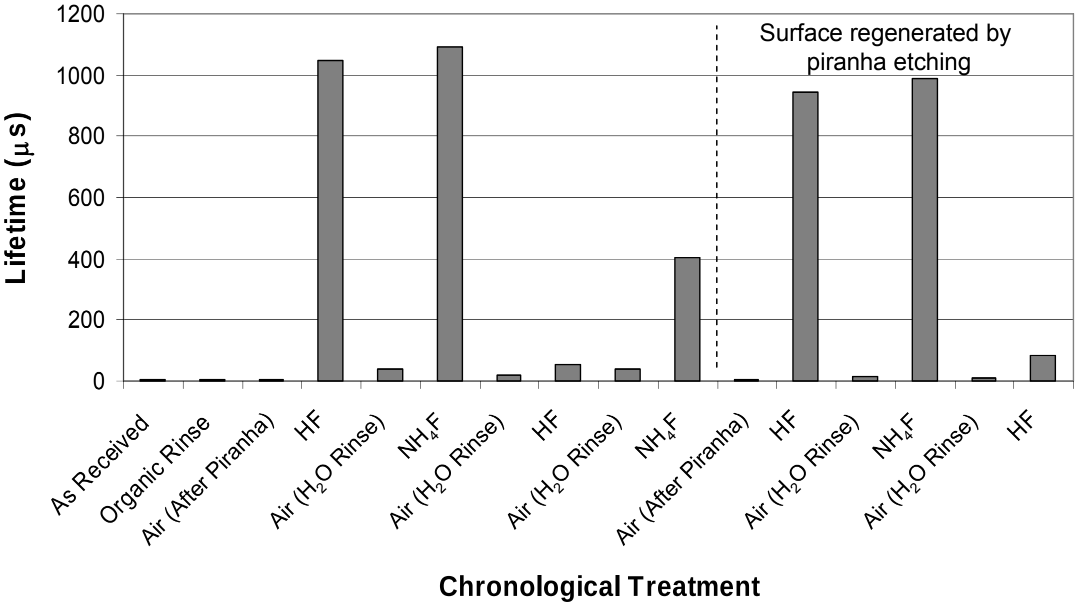

Figure 33: Electronic lifetimes for a silicon wafer demonstrating the history effect. The electronic lifetime an *n*-Si(111) wafer was measured as received with a native oxide, after solvent rinsing, after a 30 sec buffered HF pre etch and subsequent 10 min exposure to a 3:1 mixture of concentrated H_2SO_4 and H_2O_2 (Piranha) solution. The wafer was then measured while immersed in a 48% HF solution, under air following a water rinse, in 40% NH_4F, in air following a water rinse, in 48% HF solution again, in air after a water rinse, and finally in 40% NH_4F again. The sample was then exposed to the piranha solution again for 10 min as indicated by the vertical broken line. The sample was subsequently measured in air, in 48% HF solution, in air after a water rinse, in 40% NH_4F, in air after a water rinse, and finally in 48% HF again.

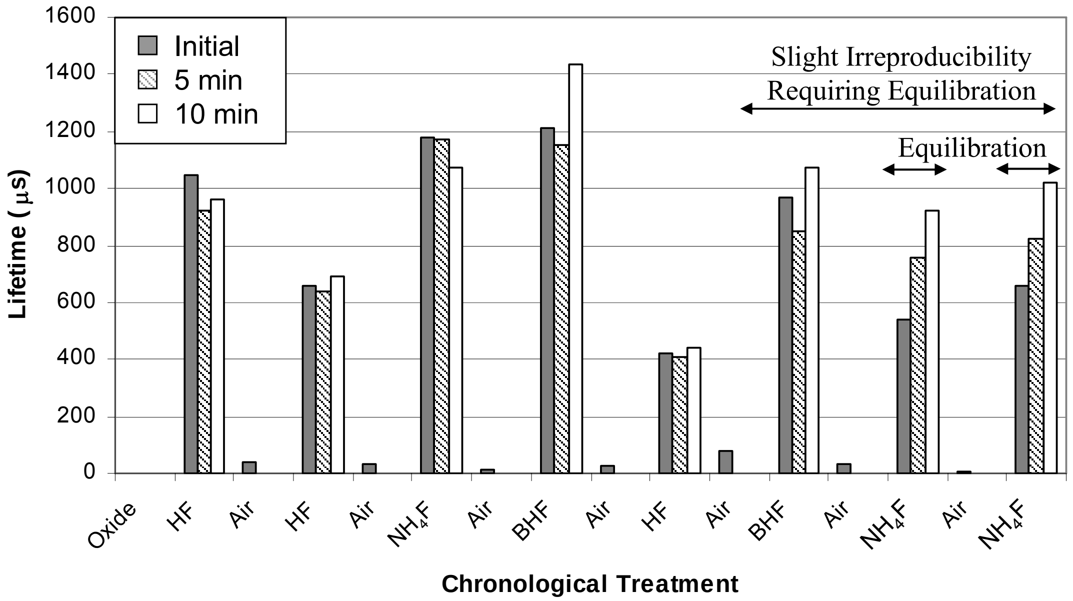

Figure 34: Electronic lifetimes for a silicon wafer demonstrating the equilibration effect.

The electronic lifetime of an *n*-Si(111) wafer was measured in each solution immediately upon immersion and after 5 and 10 min of equilibration in that solution for the chronological treatment displayed. During the first several measurements the sample shows no dependence on immersion time; however the last measurements in NH_4F display initially low lifetimes, consistent with the history effect, that rise with immersion time.

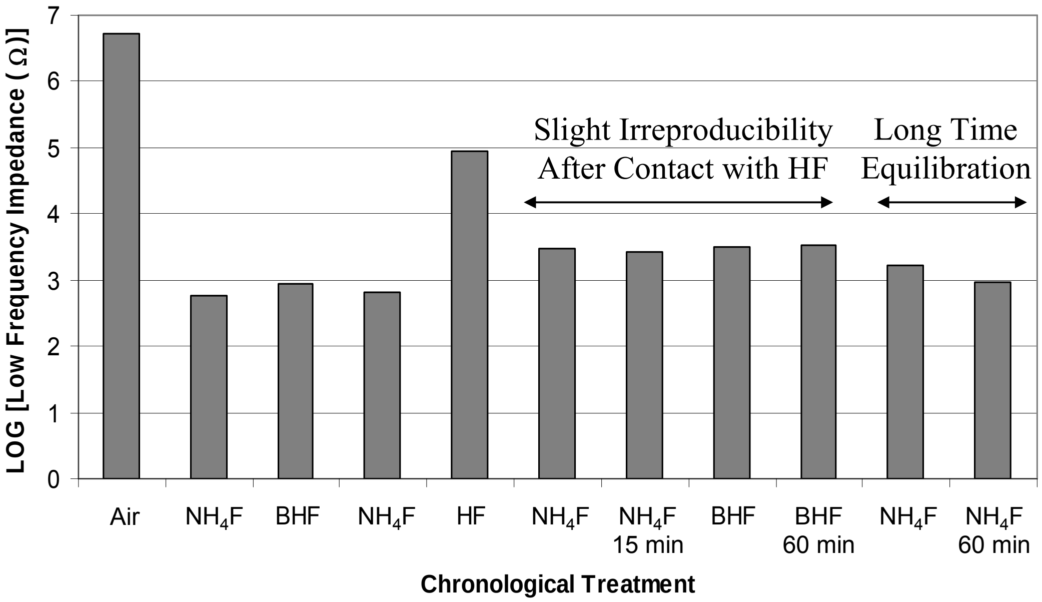

Figure 35: Low frequency channel impedances demonstrating the history and equilibration effects.

Low frequency channel impedance values for an n^+-p-Si(111)-n^+ device immersed successively in different etching solutions.

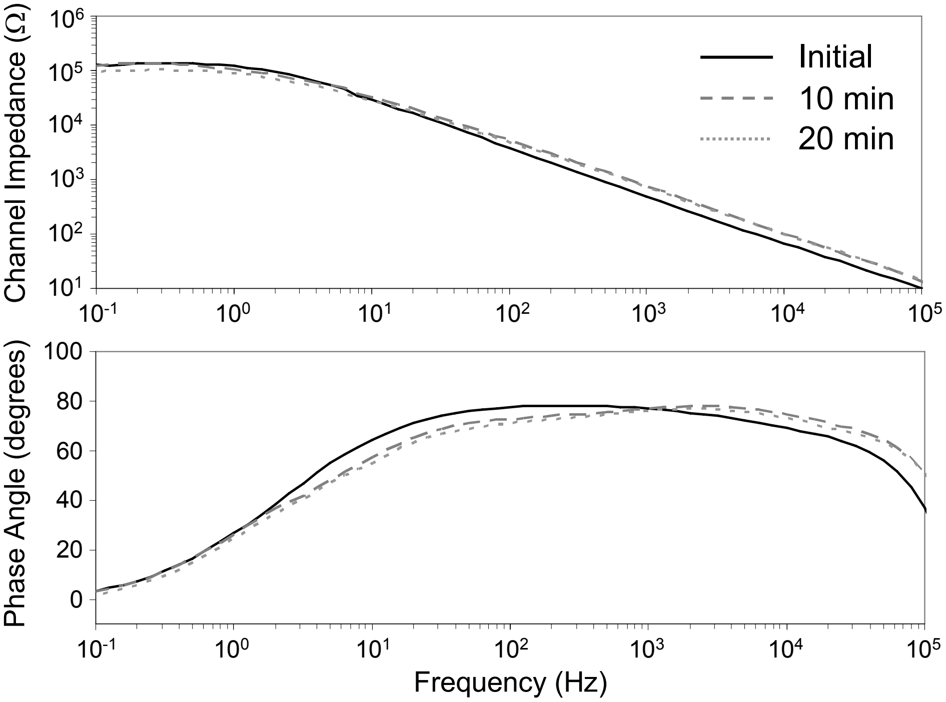

Figure 36: Channel impedance data in 48% HF with equilibration time.

Channel impedance and phase angle vs. frequency for the n^+-p-Si(111)-n^+ devices immersed in 48% HF as a function of time exposed to room light between measurements. All measurements were performed in the dark.

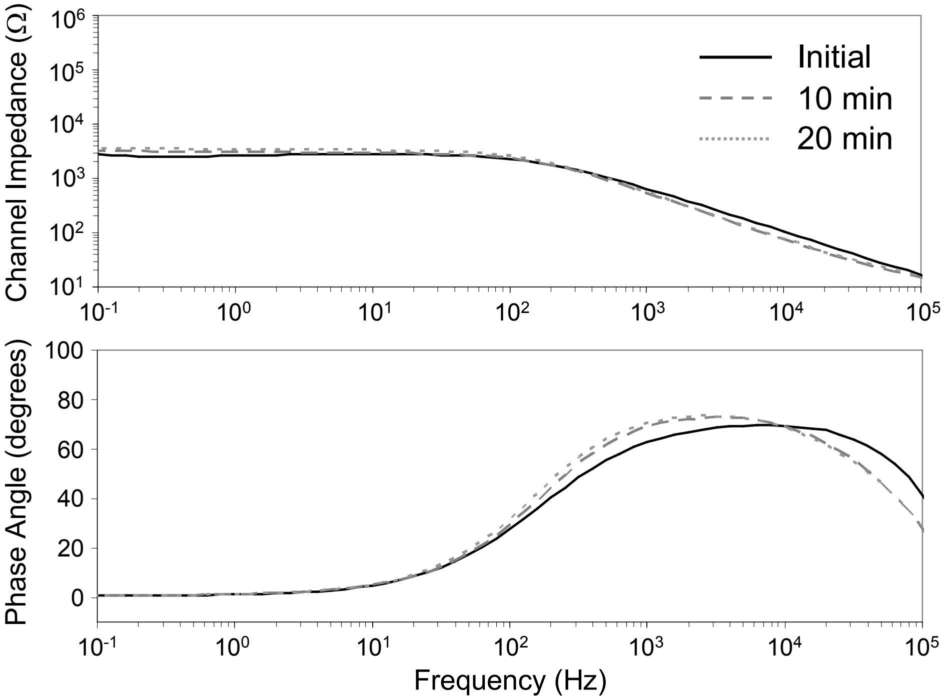

Figure 37: Channel impedance data in buffered HF with equilibration time. Channel impedance and phase angle vs. frequency for the n^+-p-Si(111)-n^+ devices immersed in 48% HF as a function of time exposed to room light between measurements. All measurements were performed in the dark.

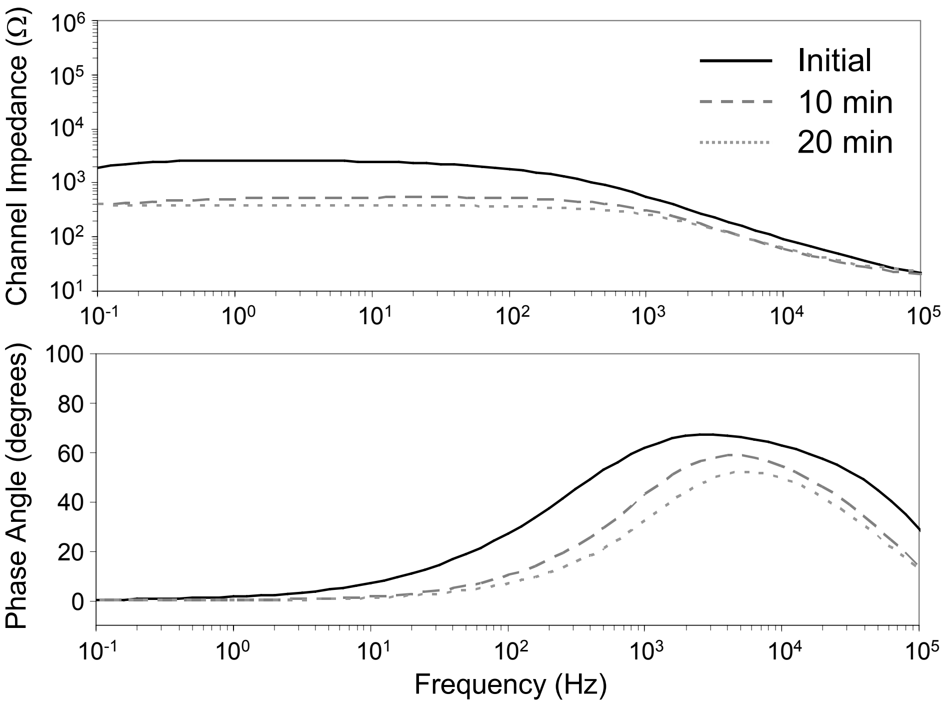

Figure 38: Channel impedance data in 40% NH_4F with equilibration time. Channel impedance and phase angle vs. frequency for the n^+-*p*-Si(111)-n^+ devices immersed in 40% NH_4F as a function of time exposed to room light between measurements. All measurements were performed in the dark.

3.5 Implications of the Etching Mechanism on Band Structure

While *n*-type silicon samples are in accumulation when in contact with either $CoCp_2^{+/0}$, NH_4F, or buffered HF, there are distinct differences. The formation of an accumulation layer is easy to understand in the case of $CoCp_2^{+/0}$ contacts. The Fermi level of silicon is raised by electron injection from $CoCp_2^0$ molecules into the conduction band. The concentration of $CoCp_2^0$ and $CoCp^{2+}$ species is so great that the oxidation of $CoCp_2^0$ species, necessary to raise the silicon Fermi level, does not significantly affect the ratio of oxidized and reduced species so the cell potential does not change. The end result is that for reasonable concentrations of redox species, the Fermi level of the silicon always raises or lowers to the cell potential of the solution.

This is not the case for silicon in contact with NH_4F and BHF solution. These solutions do not have a well-defined redox couple that can adequately supply enough charge necessary for the formation of an accumulation layer. How can these solutions regulate such a high surface electron concentration in the silicon sample without a significant concentration of easily oxidizable species in solution? The high surface electron concentration could be explained by an etching mechanism of silicon that injects electrons into the conduction band; both NH_4F and BHF solutions are known to etch silicon slowly primarily at the step edge defects.

The difference between these two types of solutions is clearly observed by the open-circuit frequency spectra of silicon in them. The open-circuit frequency spectra of silicon in a 20 mM $CoCp_2^{+/0}$ - 0.5 M LiClO4 - MeCN solution shows a diffusion-limited

(Warburg) profile of redox species to the surface. In this case, the current is dominated by the diffusion of redox species to the surface, where reduction of $CoCp^{2+}$ occurs during the cathodic half cycle and oxidation of $CoCp_2^0$ occurs during the anodic half cycle, depending on the polarity of half cycle.

Open-circuit frequency spectra of silicon in NH_4F and BHF do not display a Warburg diffusion profile, only a capacitive element appears down to 10 Hz. This provides further evidence of the lack of a chemical species that can be oxidized or reduced near the open-circuit potential of the silicon. This suggests that the formation of the accumulation layer is not due to Fermi level equilibration with a stable cell potential, but by some other mechanism.

Since both *n*-type and *p*-type silicon show very large surface electron concentrations as evidenced by the low channel impedance on the n^+-*p*-Si(111)-n^+ devices and other barrier height techniques, a significant source of electrons must be supplied. It has previously been shown (Blackwood *et al.*) that the etching mechanism of silicon in the light injects electrons into the conduction band. Quantum yield doubling has been observed to transition to quadrupling at low light intensities. This initial quantum yield doubling has been described through an electron injection mechanism during the anodic oxidation of silicon. The quadrupling observed at low light intensities may suggest that electrons could be injected into the silicon during the open-circuit etching process, which would account for the electrons necessary to produce the accumulation layers on *n*-type and inversion layers on *p*-type. Chidsey *et al.* report that the etching mechanism removes approximately 10 layers of silicon per second.[86] Using this model, and assuming only one electron is injected per silicon atom removed, enough electrons can be supplied to form the surface charge measured with the channel impedance devices within the first couple seconds of light exposure.

Further evidence is suggested by the open-circuit potentials observed in the presence of copper in this work. Chidsey *et al.* have shown that copper electrolessly deposits on the step edges of silicon and prevents the silicon dissolution reaction from taking place. Since the step edge etching is minimized in these solutions, the electron injection is expected to be less, and consequently lower open-circuit voltages are observed in the presence of copper. It seems likely that the lower open-circuit potential observed in these solutions in the presence of copper is due to the inhibition of an electron-injecting open-circuit etching mechanism of silicon.

The pH of the fluoride solution is known to affect the rate of open-circuit etching. Since solutions such as HF and H_2SO_4 are so acidic, the open-circuit etching of silicon is essentially ceased. Since the etching of silicon does not occur in these solutions when oxygen-free, no electrons are injected into the conduction band, and hence accumulation conditions are not observed.

Fluoride ions are not necessary for the formation of accumulation layers at open circuit. Lifetimes measurements of silicon in 0.1 N and 1.0 N NaOH (data not shown) are always long, and this can be combined with the observed very negative open-circuit potentials[108] to assume an accumulation layer is present. For these reasons it is possible that the accumulation layer formed at silicon surfaces when in contact with basic etching solutions is due to electron injection during the hydroxide-initiated open-circuit etching of silicon.

4 Chemical Characterization of the Electrically Passive Methoxyl Surface

4.1 Introduction and Review

In Chapter 2, it was demonstrated that silicon surfaces methoxylated in different manners produced different lifetimes under an inert N_2(g) atmosphere. Hydrogen-terminated surfaces exposed to Fc^+-MeOH solutions displayed relatively long lifetimes under a nitrogen ambient (Figure 1), while I_2-MeOH solutions displayed short lifetimes under nitrogen. Since these lifetimes were measured in the absence of a liquid contact, the electrical passivation observed for Fc^+-MeOH-treated surfaces must be the result of chemical passivation through the reduction in the surface trap state density. This chapter studies the chemical differences between surfaces methoxylated under different conditions in hopes of understanding the chemical structure responsible for the passivation.

4.2 Electronic Properties of Methoxyl Surfaces: Mott-Schottky, and IV Curves

Previous work has demonstrated, by infrared and XPS techniques, that freshly etched hydrogen-terminated silicon will quickly become alkoxylated by exposure to an alcohol solution of an oxidant such as Fc^+ or I_2.[35, 47, 109] The surfaces have exhibited electrical passivation even out of solution under an inert atmosphere such as nitrogen,[4, 25] where electrochemical passivation cannot occur; passivation must be due to a reduction in the number of surface electric trap states. These surfaces are, hence, technologically important and warrant more study. This section presents the electrical characterization of methoxylated surfaces formed by exposure to methanol solutions under various oxidative conditions.

The electrochemical behavior of methoxylated surfaces was evaluated in CH_3CN after preparation through various routes. Figure 39 depicts the voltammetric behavior of H-terminated (111)-oriented Si surfaces as well as the behavior of H-terminated surfaces that were exposed to either CH_3OH − 50 mM Fc^+, or CH_3OH − 50 mM I_2, or that were photoanozided in contact with CH_3OH. All of the surfaces except the H-terminated surface exhibited similar behavior in CH_3CN, and all of the current vs. potential curves were shifted along the potential axis by approximately −110 mV relative to that of the H-terminated (111)-oriented Si surface. Mott-Schottky plots indicated that the flat-band potential of these surfaces shifted from a value of –535±20 mV for the H-terminated surface to values of −645±20 mV, −640±20 mV, and –610±20 mV vs. the Nernstian potential of the cell, for the CH_3OH−50 mM I_2 exposed surfaces, CH_3OH−50 mM Fc^+ exposed surfaces, and CH_3OH−1.0 M $LiClO_4$ anodized surfaces, respectively.

These data allow correlation between various observations of the electrical properties and chemical reactivity of Si reported previously.[35, 47] A mechanism that is consistent with the observed reaction chemistry involves activation of the H−Si bonds through outer-sphere oxidation (Scheme I).

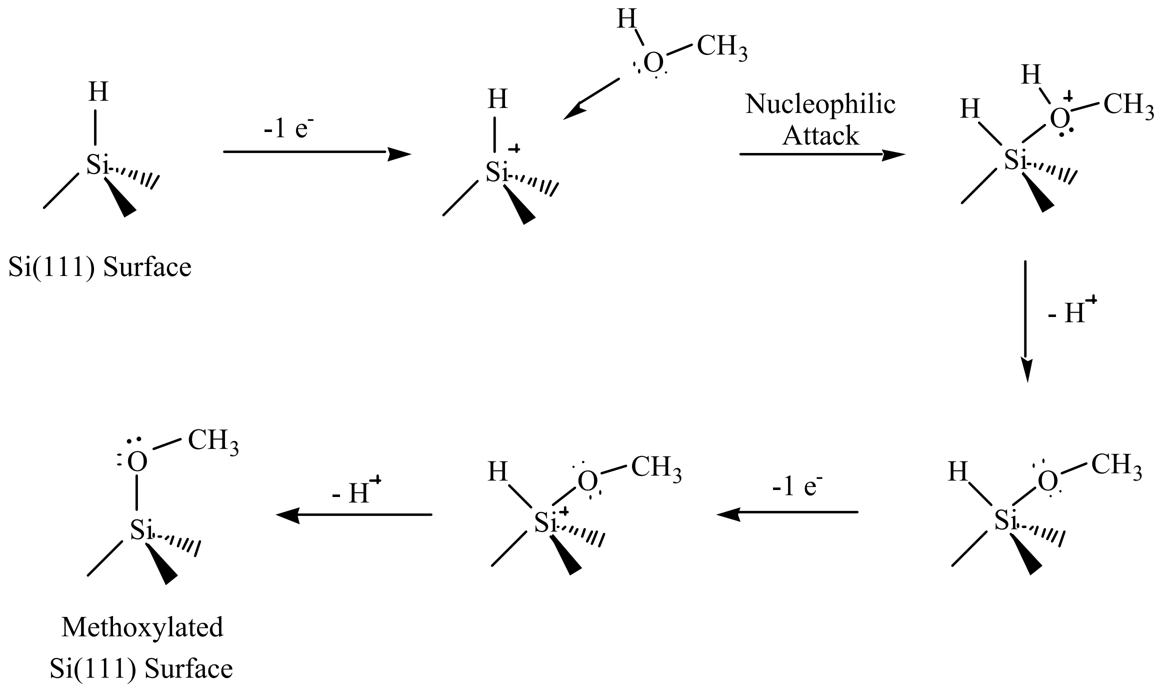

Upon oxidation of the H−Si surface species, the resulting $[H{-}Si]^+$ species is then susceptible to nucleophilic attack by methanol, with subsequent loss of a proton. Another one-electron oxidation step ensues with loss of another proton, producing the final methoxylated Si surface. The five-coordinate Si intermediate has ample precedent in the chemistry of molecular Si species.[110] An alternative pathway, analogous to that proposed for the electrochemical etching of Si in aqueous base[108, 111] or in aqueous fluoride[46, 62] solutions, has been proposed for the anodic methoxylation of porous Si.[112] In this mechanism, following production of the $[H{-}Si]^+$ species, the second electron in the H−Si bond is transferred into the conduction band of Si during the nucleophilic attack rather than being immediately captured by a second equivalent of oxidant. In either pathway, the role of I_2 or Fc^+ to produce the initial activated $[H{-}Si]^+$ species of scheme 1.

The data and scheme described above explain a variety of observations regarding the surface chemistry and electrochemistry of Si. The observation of the anodic "grafting" of methoxyl groups to porous Si surfaces is consistent with the above reaction scheme.[112] The low effective surface recombination velocity of Si surfaces in contact with CH_3OH-$Me_2Fc^{+/0}$ electrolytes,[11, 36] as well as the minority carrier limited photoelectrochemical performance of *n*-Si/CH_3OH-$Me_2Fc^{+/0}$ junctions,[36] can be explained by the formation of a partially-methoxylated Si passivated by the Si−OCH_3 groups. This chemical modification, along with the formation of an inversion layer in contact with the electrolyte solutions, further reduces the recombination rates of these interfaces.[4, 23, 25] The surface recombination velocity values for CH_3OH-$Me_2Fc^{+/0}$ and for CH_3OH-I_2 contacts are similar because of the similar redox potential of the species in both solutions.[11, 15, 16, 18, 36, 109]

The flat-band shifts observed for Si electrodes in CH_3OH after photoelectrochemical stabilization in CH_3OH-$Me_2Fc^{+/0}$,[36] as well as the flat-band shifts observed in this work in CH_3CN solutions for alkoxylated surfaces, can also be understood by the change in surface dipole due to the replacement of H−Si bonding by Si-OCH_3 groups, as proposed by Chazalviel previously.[113] The observation that Si photoanodes in contact with acetone−75 mM $Fc^{+/0}$ solutions are dominated by surface recombination processes,[114] whereas Si/CH_3OH-$Me_2Fc^{+/0}$ or Si/propylene carbonate-methanol-$Me_2Fc^{+/0}$ contacts exhibit bulk recombination-limited junction behavior,[36] is consistent with the formation of electrically passive alkoxylated surfaces in the alcohol-containing electrolytes.

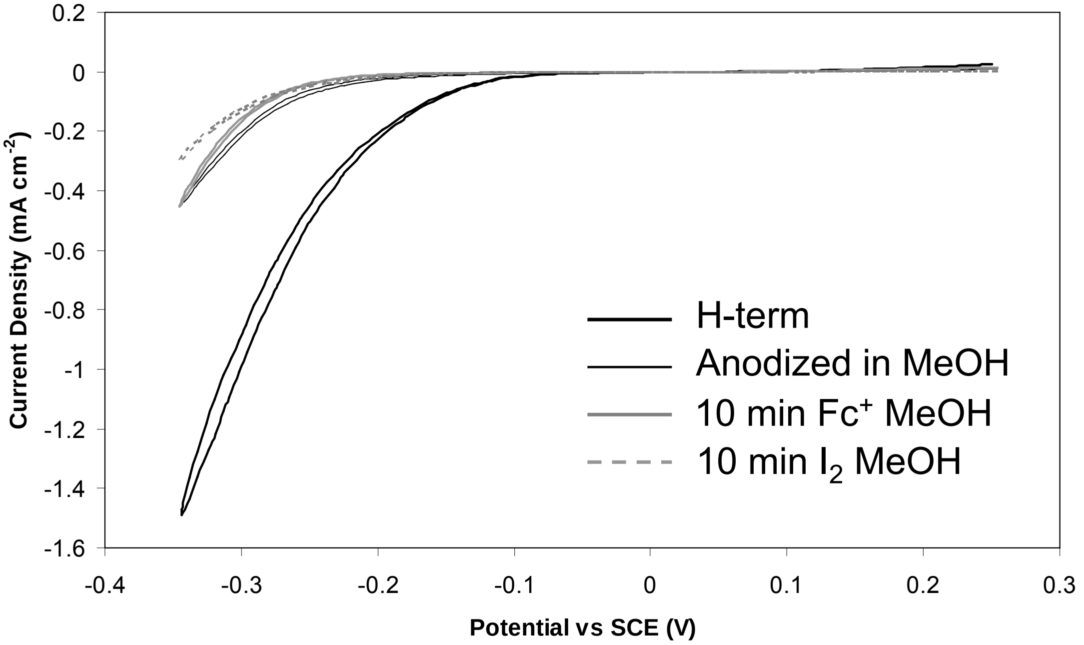

Figure 39: Current density vs. potential plot for methoxylated silicon surfaces in a MeCN solution.

Current-density vs. potential data in CH_3CN−40 mM Fc−20 mM $Fc^+BF_4^-$−1.0 M $LiClO_4$ for 8 ohm-cm resistivity H-terminated *n*-Si(111) (thick black solid line), and for H-terminated *n*-Si(111) that had been exposed to 50 mM I_2/CH_3OH (gray dotted line), or to 50 mM $Fc^+BF_4^-/CH_3OH$ (gray solid line), or that had been photoanodized in CH_3OH-1.0 M $LiClO_4$ (thin black solid line).

4.3 Methoxylation from Neat Methanol

ABSTRACT

The room temperature reaction of atomically smooth hydrogen-terminated Si(111) with methanol was examined in detail. The appearance of a sharp Si−O−C stretch appears within 10 min that could correspond to as much as 8% of the surface. The H−Si stretching intensity decreases, and the Si−O−C stretching, CH_3 stretching, and CH_3 rocking modes all increase with time exposed to methanol. Studies with deuterated methanol suggest the presence of two possible reactions occurring in parallel. The first is a chemical attack of terrace H−Si species to form Si−OCH_3 species oriented normal to the surface. The second reaction involves exchange of normal-oriented H−Si bonds to normal oriented D−Si bonds, which could occur either through a direct H-to-D exchange mechanism or a chemical step-flow etching mechanism of silicon step sites.

I. INTRODUCTION

The reactivity of hydrogen-terminated surfaces is of extreme importance due to its use as a starting surface for further chemical or processing steps.[115-118] It is generally assumed to be unreactive with a number of solvents, although reports of its reactivity with alcohols under certain conditions have been published.[35, 112, 113, 119-122] It is clear that a number of different surface reactions can occur that produce different coverage of surface species depending on the purity of the solvent, amount of dissolved oxygen, and crystallographic face or porosity of silicon.

Infrared spectroscopy is a useful tool for the identification of surface-bound species. One limitation of the spectroscopic analysis of surfaces has been the low number of species available for optical absorption. This has forced researchers to adopt the multiple internal reflection (MIR) geometry[122, 123] that amplifies the surface signal, but at the expense of spectral range because increased multiphonon absorption renders the silicon opaque below 1500 cm^{-1}.[124, 125] To investigate the absorption process at lower frequencies, techniques such as transmission mode or diffuse reflectance must be employed, and typically, in order to regain signal, porous[112, 120, 121, 126] or abraded[120, 121] silicon samples have been used to increase the surface area.

Recent advances in optical detection technologies have now allowed the measurement of low frequency modes to be observed on atomically-smooth silicon surfaces using transmission mode geometries.[127, 128] The reaction of neat anhydrous methyl alcohol with *atomically-smooth* hydrogen-terminated Si(111) surfaces at room temperature and under a nitrogen atmosphere is the focus in this work.

II. EXPERIMENTAL

Wafers of 480 micron thick, float zone, double side polished, phosphorus-doped >30 Ω-cm *n*-Si(111) were purchased from Silicon Valley Microelectronics (Lot #12945) and cut into pieces approximately 2 cm × 5 cm pieces for transmission mode analysis. Anhydrous methanol (99.8%, Lot 00434: 0.0012% H_2O and Lot 00253JC: 0.0009% H_2O), methanol-*d* (Batch 10517PC: 99.62 Atom % D, 0.0005% H_2O and Batch 13213EB: 99.59 Atom % D, 0.0017% H_2O), and anhydrous methyl-d_3 alcohol-*d* (Batch 04526MC: 99.91 Atom % D, 0.0065% H_2O and Batch 18324HA: 99.93 Atom % D, 36.9

ppm H_2O) were purchased from Aldrich. Cobaltocene was purchased from Alfa Aesar and was used as received. All chemicals were used as received inside a nitrogen purged glove box.

After a given preparation, samples were quickly put into a home-built sample holder within the nitrogen purged bench of a Fourier transform infrared (FTIR) spectrometer (Nicolet Nexus 6700, Nexus 670, or Magna 760) using either a liquid nitrogen cooled MCT-B detector or a room temperature pyroelectric detector made of deuterated triglycine selenate compounds (DTGS). Single beam spectra were recorded in transmission mode with samples positioned in the light path at either 74° (Brewster angle for silicon) or 10° relative to the surface normal, which allowed the orientation of any absorbance modes to be determined. The sample bench containing the sample was allowed to purge with nitrogen at 30 scfh for 10 min prior to data acquisition. For each sample, 5 consecutive loops of 1000-scan averaged spectra were obtained. For each silicon sample, single beam spectra are obtained for the solvent-rinsed native oxide surface, the hydrogen-terminated surface, and after each given preparation.

All single beam spectra are reprocessed using either the native oxide or freshly etched single beam spectrum obtained for that sample. The resulting absorbance spectra are difference spectra and are corrected by subtracting water and CO_2 peaks and by flattening the baseline.

Native-oxide terminated silicon samples were initially rinsed in succession with water, methanol, acetone, methanol, and water. These samples were dried under a flowing stream of nitrogen and subsequently measured in the FTIR. Following data acquisition, samples were hydrogen-terminated by immersion in nitrogen-purging 40%

NH_4F solution in a polypropylene tube. In order to minimize carbon and oxygen contamination, it was necessary to outgas the nitrogen line for at least 1 hour through a sacrificial solution of 40% NH_4F, which was subsequently discarded. Another allotment of 40% NH_4F was used for sample etching and was always purged with a stream of nitrogen for at least 45 min before immersion of the sample. Samples were etched for 20 min with nitrogen purging through the solution; they were rinsed with 18 MΩ cm water by immersion and dried under a flowing stream of nitrogen gas, and measured in the FTIR. After FTIR analysis, samples were quickly brought into the nitrogen atmosphere of a glove box through an antechamber. The antechamber was backfilled to -10 psi twice at 10 min intervals and samples were brought into the box 10 min later. In order to minimize silicon surface exposure to contaminants within the antechamber during evacuation, samples were very lightly capped in polypropylene centrifuge tubes. This provides a diffusion barrier against the introduction of reactive contaminant while still allowing the evacuation of the tube. It has been observed that a freshly etched hydrogen-terminated sample exposed to active vacuum within the antechamber for 8 hours lost nearly all its H−Si intensity and displayed significant C−H contamination. The antechamber, although at low pressure, is not a safe place to store wafers.

Samples were exposed to methanol solutions by immersion into large (≈ 1" diameter) glass test tubes that were capped with a rubber stopper and in some cases shielded from light by wrapping in aluminum foil. All glassware was cleaned with aqua regia followed by a 3:1 mixture of concentrated H_2SO_4 and 30% H_2O_2 (piranha etch). These two cleaning techniques should remove traces of metallic and carbon-containing contamination from the surface of the glass. The glassware was then rinsed with copious amounts of 18 MΩ cm water and dried with a heat gun before entrance into the box. Certain reaction tubes were dedicated for specific reactions. A tube, once contacted with cobaltocene was only used for other cobaltocene studies. For reactions with deuterated methanol, dedicated tubes and glass pipets were first pre-rinsed and then filled with CH_3OD for soaking overnight. This would exchange any Si−OH groups on the glass surface with Si−OD groups so that H-to-D exchange on the glass surface would not dilute the CH_3OD concentration during the reaction with silicon samples. When not in use, the deuterated tubes were capped so that no further exchange would occur in the presence of CH_3OH vapor used in other experiments.

Solutions of $CoCp_2^0$ were made by making a concentrated solution of the metallocene in methanol and then filtering off any remaining precipitate. Etched silicon samples were immersed in the dark reddish brown (coca cola) colored solution for 10 min. Samples were then rinsed with at least 6 pipets of methanol on each side of the wafer, and the solvent was allowed to evaporate down to a corner.

III. RESULTS

The left panel of Figure 40 depicts the FTIR spectral of freshly etched H−Si(111) surfaces exposed to neat anhydrous methanol for various lengths of time. The freshly etched H−Si(111) surface displays a sharp H−Si stretching mode at 2083.5 ± 0.1 cm^{-1} with a full-width half maximum of 4.46 ± 0.07 cm^{-1}, which indicates that the surface is comprised of long terraces of atomically smooth silicon atoms.[129] Upon exposure of the H−Si(111) surface to neat anhydrous methanol at room temperature, the H−Si stretching mode changes with time. The decrease in intensity is accompanied by a broadening and red shifting in the peak, which is presented in Table 1. For the data in Table 1, the ratio of the H−Si peak area after each treatment is taken relative to the peak area under the freshly etched H−Si peak *for that sample*. The decrease in peak intensity indicates that H−Si moieties are being consumed through a reaction with CH_3OH; the absence of absorption modes at 2250 cm^{-1} indicates that the oxidation of Si−Si back bonds directly below the H−Si terminated surface is not occurring. Red shifting and broadening of the H−Si peak has previously been attributed to any surface reactions that interferes with dipole coupling between neighboring H−Si groups on a terrace.[87, 129] The red shift and broadening are shown more clearly in the inset of Figure 40 and prove, through the destruction of dipole coupling, that H−Si groups are lost in a random manner from the terraces of the atomically flat H−Si(111) surface.

While there is no evidence that the loss of H−Si corresponds directly with the formation of $Si-O-CH_3$ groups in 100% yield, there is a distinct trend between the increase in Si−O−C stretch intensity and decrease in the H−Si intensity as shown in Table 1. Quantum mechanical modeling experiments have demonstrated that 100% coverage of methoxyl groups on an Si(111) surface has about half the strain per molecule than 100% coverage of a methyl, $Si-CH_3$, overlayer.[5] This suggests that, if given reasonable energy, 100% coverage of the methoxyl surface is feasible. In this case, the presence of Si−O−Si TO modes and the unknown oscillator strengths for the H−Si and Si−O−C stretching frequencies prevent accurate quantification of the $Si-O-CH_3$ coverage. The decrease in the H−Si intensity can only serve as an upper bound.

The right panel of Figure 40 depicts the spectral region where C−H stretching modes are observed. The presence of CH_3 stretching modes at 2838 cm^{-1} and 2940 cm^{-1}

(which is occasionally accompanied by a shoulder at 2970 cm^{-1}) is clearly observed out of the noise only after 6 days of exposure to CH_3OH. These values agree well with the methyl stretching modes of liquid CH_3OH [($\nu_s(CH_3)$ at 2822 cm^{-1} and $\nu_{as}(CH_3)$ at 2934 cm^{-1})[130] and (2845 cm^{-1} and 2978 cm^{-1})[131]], methyl modes of crystalline CH_3OH at −108°C [$\nu_s(CH_3)$ at 2831 cm^{-1} and two asymmetric modes $\nu_{as}(CH_3)$ at 2954 and 2980 cm^{-1}],[130] methoxyl groups absorbed on glass [2857 cm^{-1}, 2959 cm^{-1}, and 2996 cm^{-1}],[132] methoxyl groups on copper [at 2798, 2875, and 2911 cm^{-1}],[133] electrochemically methoxylated porous silicon surfaces [2840 cm^{-1} and 2945 cm^{-1}],[112] and methoxylated abraded silicon [$\nu_s(CH_3)$ at 2843 cm^{-1} and $\nu_{as}(CH_3)$ at 2947 cm^{-1}].[120] The presence of these CH_3 stretching modes, in addition to the absence of a broad OH band, has been previously ascribed to the formation of a surficial $Si{-}O{-}CH_3$ moiety.[112, 120, 121]

Figure 41 shows the low frequency FTIR spectra for freshly etched silicon after exposure to CH_3OH for various times. At low coverage (*i.e.,* for reaction times 24 hours or less that corresponds to, at most, 30% of a monolayer), these spectra all demonstrate a sharp peak centered around 1080 cm^{-1} that has been previously assigned to an Si−O−C stretching mode. However, this is the first time to our knowledge that this peak has been observed to be so sharp which is probably due to the low coverage and structural order imparted by the atomically flat nature of the substrate. At higher coverage, the peak broadens and blue shifts, which indicates that steric and chemical interactions are likely affecting the local geometry. The sharpness of the Si−O−C peak is distinctive and clearly separates it from the LO and TO modes of Si−O−Si groups, which would form much broader peaks even at low coverage amounts.[134]

The presence of a broad Si−O−Si TO peak can be observed at 1050 cm^{-1}, which demonstrates that the insertion of oxygen into the Si−Si back bonds is occurring during room temperature exposure of H−Si(111) to methanol. The magnitude of this oxide peak is not consistent between identically prepared samples and may be the result of handling or contamination errors. For example, the sample exposed to methanol for 3 hours (solid gray line, Figure 41) displays a larger TO peak than the sample exposed to methanol under the same conditions for 24 hours (broken black line, Figure 41). Curiously, the absence of H−Si stretching modes at 2250 cm^{-1} indicates that the formation of the Si−O−Si TO band does not occur through the typical oxygen insertion into Si−Si back bonds below H−Si surface sites. Perhaps the formation of Si−O−Si occurs underneath Si−O−CH_3 sites.

The broad peak at 1190 cm^{-1} in Figure 41 has previously been assigned to the CH_3 rocking mode of surface bound methoxyl species;[112, 120] however presence of the Si−O−Si TO mode at 1050 cm^{-1} suggests that this peak could be due, at least in part, to the Si−O−Si LO optical phonon mode. While the frequency of the TO does not change with oxide coverage, the frequency of the LO phonon mode red shifts as the oxide coverage decreases. If this part of this peak does correspond to an LO mode, it would suggest the presence of very small clusters of Si−O−Si groups.

Figure 42 shows the Si−O−C and H−Si stretching regions for freshly etched H−Si(111) exposed to a variety of ambients as control experiments. Exposure of the H−Si(111) surface to the nitrogen environment of the glove box did not noticeably decrease the H−Si peak area or produce any observable activity within the 800–1300 cm^{-1} region. Immersion of the H−Si(111) surface into nitrogen-purged H_2O in the dark decreased the H−Si peak intensity by about 8%, but no significant activity is observed in the 800–1300 cm^{-1} range. This indicates that trace water impurities in the CH_3OH are not responsible for the sharp peak at 1080 cm^{-1}.

Reaction with a concentrated CH_3OH solution of $CoCp_2^0$ leads to spectral features similar to the reaction of H−Si(111) in neat methanol. Methanol solutions of $CoCp_2^0$ were used to quench any trace oxidants that might be present in the neat methanol. It has previously been shown that alcohol solutions of oxidants, such as $Fc^{+/0}$, I_2, and Br_2, can lead to formation of surficial alkoxyl groups through an oxidative mechanism.[35, 47] The addition of $CoCp_2^0$ to the CH_3OH would reduce any trace oxidants and prevent the formation of methoxyl bonds through the oxidative route. Because the methoxylation reaction still proceeds at an appreciable rate in the presence of $CoCp_2^0$, it is evident that another, albeit slower, mechanism must be responsible for the formation of $Si{-}OCH_3$ bonds. The amount of H−Si loss and Si−O−C gain varied more dramatically in the presence of $CoCp_2^0$ than in neat methanol; no inferences can be made at this time about the relative rates of the methoxylation reaction, only that similar spectral features are observed in the presence and absence of $CoCp_2^0$.

The oxidative methoxylation mechanism could still proceed in the light, where photogenerated holes could react with methanol through the oxidative pathway. The reaction, however, proceeds with equal H−Si loss and Si−O−C gain independent of light intensity. (The only dependence on light that was observed was an occasional increase in the broad peaks within the 900–1300 cm^{-1} spectral range, which may be due to oxidation induced by reaction of photogenerated holes with water impurities.) Due to the lack of light dependence on the reaction it appears that the reaction must be chemical in nature and not an electrochemical reaction that would involve free carriers.

In order to investigate the mechanism by which methanol reacts with the H−Si(111) surface, studies were performed with deuterated methanol species, CH_3OD and CD_3OD. Figure 43 shows the FTIR spectra obtained for H−Si(111) surfaces exposed to **a:** neat anhydrous CH_3OH for 3 hours, **b:** neat anhydrous CH_3OD for 3 hours, and **c:** neat anhydrous CD_3OD for 24 hours. Reaction with CH_3OH results in same vibrational modes discussed above, but the spectral range of Figure 43 includes the H−Si bending mode at 626 cm^{-1}. Reaction of H−Si(111) with CH_3OD shows these same spectral features, indicative of the formation of $Si-O-CH_3$ groups, in addition to two other spectral features at 1513 cm^{-1} and 534 cm^{-1}. The peak at 1513 cm^{-1} has previously been assigned to the D−Si stretching mode,[87, 135] while the peak at 534 cm^{-1} is currently not assigned. It seems too high in energy to be assigned to the D−Si bending mode, which should be observed between 440 cm^{-1} and 450 cm^{-1} based on the change in reduced mass for the deuterium atom. One possibility is that it represents a composite mode of a phonon and the D−Si bending mode. It doesn't seem likely that this peak could be due to SiD_2 or SiHD scissor modes since the D−Si stretch is so sharp. The assignment of the 534 cm^{-1} mode will be the focus of future studies.

After a 3-hour exposure to CH_3OD, the integrated area of the H−Si stretching mode is quite a bit lower than that after the 3-hour exposure to CH_3OH, while the intensities of the Si−O−C peaks remain the same for both cases. The integrated area for a fully D−Si(111) terminated surface has been shown to be 51% of the integrated area of a fully H−Si(111) terminated surface.[87] The contributions of the H−Si and D−Si coverage on the CH_3OD-reacted surface sum to 77 ± 4% of initial H−Si(111) total surface coverage, which is within error the same as the H−Si(111) coverage remaining after reaction with CH_3OH for the same length of time. This strongly suggests that while the same decrease in hydrogen termination occurs, a significant amount of the acidic hydrogen atoms from the methanol molecules end up bonded to the silicon surface.

No CH_3 stretching modes are observed in the 2700–2900 cm^{-1} range after reaction of H−Si(111) with CD_3OD. Instead, CD_3 stretching modes are observed at 2070 cm^{-1} and 2240 cm^{-1}. The inset shows the appearance of the 2070 cm^{-1} mode as a shoulder on the remaining H−Si stretching mode. The D−Si stretching mode at 1513 cm^{-1} as well as the mode at 534 cm^{-1} are observed. The appearance of a strong sharp CD_3 rocking mode is observed at 1120 cm^{-1}, while the Si−O−C peak is red shifted due to the increased mass.

Figure 44 displays the FITR spectra recorded at various angles for freshly etched H−Si(111), **a** and **b**, and for freshly etched H−Si(111) exposed to CD_3OD for 24 hours, **c** and **d**. Since the stretching mode for the H−Si bond is oriented normal to the surface, the absorption disappears as the incident light is oriented roughly normal to the surface. The H−Si bending mode at 626 cm^{-1} can be excited at many angles, and the absorption is observed at both 74 and 10 degrees off normal. The D−Si stretching mode at 1512 cm^{-1} displays similar polarization indicating that formation of D−Si moieties through reaction with CD_3OD are orientated normal to the surface. The mode at 534 cm^{-1} is observed at both angles, which is expected if it is associated with the D−Si bending mode.

Figure 45 presents the FTIR spectra obtained at 74 and 10 degrees off the surface normal for H−Si(111) surfaces exposed to CD_3OD for 24 hours, **a** and **b**, and H−Si(111) surfaces exposed to CH_3OH for 24 hours, **c** and **d**. These spectra show that the sharp Si−O−C stretch is also polarized normal to the surface. Only broad modes around 1050 cm^{-1} can be observed at 10 degrees, which is expected for TO Si−O−Si modes.

IV. DISCUSSION

The FTIR spectra demonstrate that freshly etched, atomically-smooth H−Si(111) surfaces can react with neat anhydrous CH_3OH at room temperature in as short as 10 minutes. The Si−O−C stretch at low coverage is characterized by a sharp absorption peak, which broadens and blue shifts as the intensity increases. These spectral changes with surface coverage are likely due to the increase in steric interactions between neighboring methoxyl groups as the coverage increases. The Si−O−C stretching, CH_3 stretching, and CH_3 rocking modes are all observed to increase with reaction time, which suggests that surficial H−Si bonds are being replaced, at least partially, by Si−O−CH_3 groups.

One possible mechanism for the methoxylation of silicon in neat alcohol, which has been previously proposed by other scientists, [121, 122] is shown in Figure 46. This mechanism is very similar to the first, hydrogen-gas-evolving step of the chemical etching mechanism of silicon by water, as proposed by Allongue and co-workers,[111] except that methanol is used instead of water.

A different methoxylation mechanism has been previously proposed for silicon in the presence of methanolic solutions containing an oxidant such as Fc^+ or I_2.[35] Complete loss of the H−Si stretching band is observed in as short at 10 min with these solutions, while only 9% of the H−Si is lost after 10 min in the presence of neat anhydrous methanol. The studies involving $CoCp_2^0$ solutions of methanol presented in this work demonstrate that methoxylation can also occur through a non-oxidative mechanism as well. While $CoCp_2^0$ is a strong enough reducing agent to reduce any trace oxidants that may be present in solution, and therefore shut off the oxidative methoxylation pathway, the extent of methoxylation and loss of H−Si did not decrease. Furthermore, the reaction of neat anhydrous methanol at room temperature proceeds at roughly the same rate whether in the dark or in the light, which further suggests that free carriers are not involved in this reaction.

While the reaction mechanism displayed in Figure 46 is the most convincing mechanism for the formation of surface-bound $Si{-}OCH_3$ groups, it does not address the formation of the experimentally observed D−Si stretching mode. Another methoxylation mechanism that involves breaking Si−Si back bonds is shown in Figure 47. Similar mechanisms have been proposed for the methoxylation of abraded or porous silicon.[121] Those mechanisms have involved the breaking of two surficial, HSi−SiH, bonds which are not present on the terraces of the H−Si(111) surface; breaking of Si−Si bonds on the Si(111) terraces requires breaking HSi−Si(bulk) bonds. As shown, this mechanism involves the attack of methanol molecules on the HSi−Si(bulk) backbonds, such that the Si−Si and D−O bonds are broken while $Si{-}OCH_3$ and D−Si bonds are formed. Due to the geometry of these products, this mechanism does not appear to be the dominant mechanism for the room temperature reaction of H−Si(111) terraces with methanol since the polarization experiments indicate that both the D−Si and $Si{-}O{-}CH_3$ bonds are oriented normal to the surface; surface species of H−Si, D−Si, and $Si{-}O{-}CH_3$ formed through this reaction would not be oriented normal to the surface. This mechanism would also lead to significant steric strain on the (111) face.

In order to explain the polarized D−Si moieties formed through the reaction with deuterated methanol, an etching mechanism along H−Si(111) step sites is proposed as shown in Figure 48. The depiction of the step edge is left general since the reaction could occur at both monohydride and dihydride step edges. Reaction of methanol with Si−Si back bonds at a step edge would have considerably less steric strain than reaction with Si−Si bonds on a terrace. In this proposed mechanism, one molecule of deuterated methanol, CD_3OD, attacks one of the two Si−Si back bonds labeled with broken gray arrows, cleaving the bond, and forming $Si{-}OCD_3$ and D−Si species. All other remaining back bonds of that edge site silicon atom are cleaved in the same way to liberate a molecule of $SiH_x(OCH_3)_y$, which could further decompose in solution. The removal of this silicon edge site atom leaves the neighboring silicon atoms deuterated. The removal of the next silicon atom occurs in a similar manner with methanolic attack on the Si−Si bond labeled with a broken gray arrow. The removal of edge site silicon atoms continues until an atomically flat terrace of D−Si species results. With the exception of the step edge atoms, all D−Si species formed through this reaction are oriented normal to the surface.

Studies of H−Si(111) surfaces immersed in D_2O solutions KF have been observed to undergo conversion of atomically flat H−Si to atomically flat D−Si through a similar step-flow etching mechanism.[87] The step flow mechanism of Luo *et al.* was proposed based on the sharpness of the H−Si and D−Si stretches, which showed no shifting throughout the conversion, which supports the step edge etching mechanism because new domains of pure H−Si are formed leaving behind unetched terraces of pure D−Si. The occurrence of the terrace methoxylation reaction obscures a similar analysis in this study since coupling of neighboring D−Si terraces would be interrupted by the presence of Si-OCH_3 groups. Indeed the D−Si stretching frequencies are shifted by approximately 4 cm^{-1} relative to the clean D−Si(111) surface reported by Luo *et al.*, but the polarization of the D−Si bond is nevertheless oriented normal to the surface. Luo *et al.*, observed a full conversion of a initial deuterated, D−Si(111) surface to a smooth H−Si(111) surface after only 3 min.[87] The conversion of H−Si to D−Si using deuterated methanol in this study occurs at a much slower rate; this is not unreasonable considering the increased steric bulk of methanol over water. An observable amount of H−Si is present even after 24 hours of exposure of H−Si(111) to CD_3OD.

Another possible mechanism that would result in polarized D−Si species is direct H-to-D exchange on the surface, *e.g.*, $H{-}Si + D^+ \rightarrow D{-}Si + H^+$. In this reaction mechanism the D^+ is supplied by the acid equilibrium reaction: $CH_3OD \rightarrow CH_3O^- + D^+$. However due to the relative strength of the H−Si bond and its bond polarity estimated by the Pauling scale of electronegative which places more electron density on the H atom, the H−Si bond is not expected to be significantly acidic and this direct exchange is not expected to proceed at an appreciable rate.

The presence of polarized Si−OCH_3 and D−Si functional groups can be explained by the occurrence of two reactions: a reaction of terrace H−Si sites with methanol, and an H-to-D reaction possibly involving either a direct exchange mechanism or a step-flow etching of step sites by methanol. The step edge etching of H−Si(111) by methanol, if real, may be responsible for limiting the coverage of methoxyl groups to approximately

50% as observed even after 6 days of reaction. A limiting coverage of methoxyl species could occur if the terrace methoxylation reaction occurs at a similar rate as a step-flow etching reaction; in such a case, the terrace coverage cannot approach 100% since the layer is stripped off to expose a fresh D−Si or H−Si surface below.

V. CONCLUSIONS

FTIR analysis has been used to study the reaction of neat anhydrous methanol with atomically flat H−Si(111) surfaces. The observation of a sharp Si−O−C stretching peak appears within 10 min and polarization dependence spectroscopy identifies that this group is normal to the surface. Two mechanisms are proposed for the reaction of methanol with atomically flat H−Si(111) surfaces. The first involves the reaction of methanol with terrace H−Si sites to form hydrogen gas and Si−O−CH_3 species that are orientated normal to the surface. This reaction has been demonstrated to proceed at about the same rate in the light, in the dark, and in the presence of a reducing agent, which demonstrates that free carriers are not involved in the reaction. The second mechanism involves the step edge etching of silicon atoms, which preserves the atomically smooth surface. The reaction of methanol with Si−Si back bonds on the terraces does appear to proceed at a significant rate.

Table 15: H−Si stretching mode parameters following various treatments.

Surface Treatment	Rel. Peak Area	Peak Center	FWHM
Freshly Etched	1	2083.5 ± 0.1	4.46 ± 0.07
10 min CH_3OH	0.91 ± 0.06	2082.3 ± 0.6	6 ± 1
3 hrs CH_3OH	0.83 ± 0.05	2081.0 ± 0.5	7.5 ± 0.7
24 hrs CH_3OH	0.71 ± 0.08	2080 ± 1	10 ± 2
6 days CH_3OH	0.56 ± 0.12	2077.1 ± 0.4	18.2 ± 0.9
3 hrs under $N_2(g)$	1.03 ± 0.05	2083.5 ± 0.1	4.6 ± 0.1
3 hrs N_2-H_2O	0.92 ± 0.06	2083.3 ± 0.1	4.54 ± 0.06

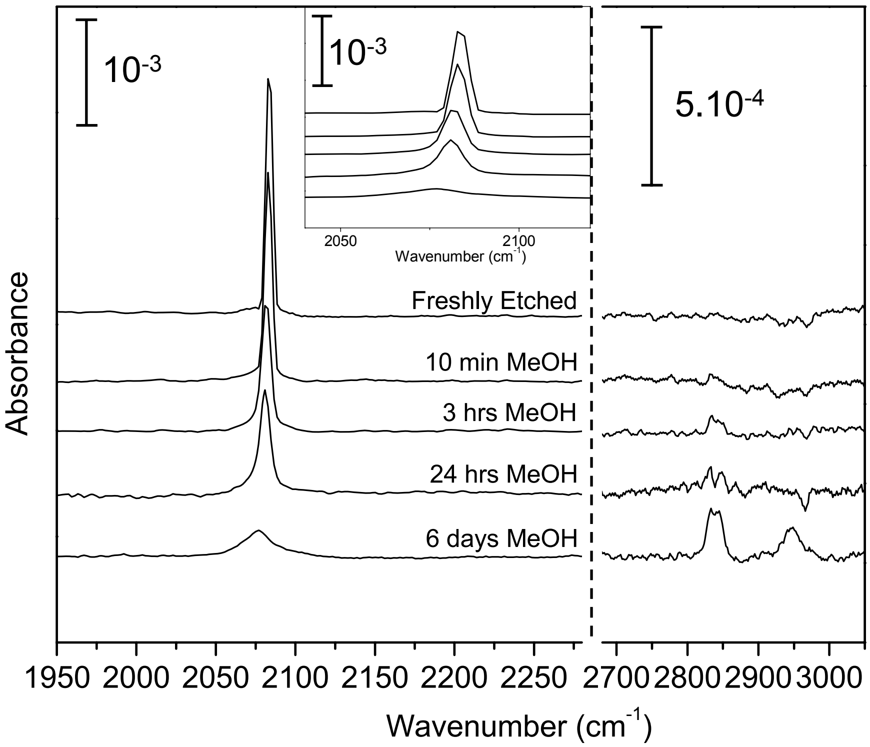

Figure 40: FTIR spectra of H−Si(111) exposed to CH_3OH for various times. Hydrogen-terminated *n*-Si(111) samples were immersed in neat anhydrous CH_3OH for various times at room temperature, and FTIR spectra were obtained under nitrogen gas. The left panel shows the decrease of the H−Si peak with immersion time. The inset shows the red shift of the H−Si stretching frequency as coverage decreases. The right panel shows the increase in C−H stretching with immersion time. All spectra are referenced to the initial native oxide terminated surface.

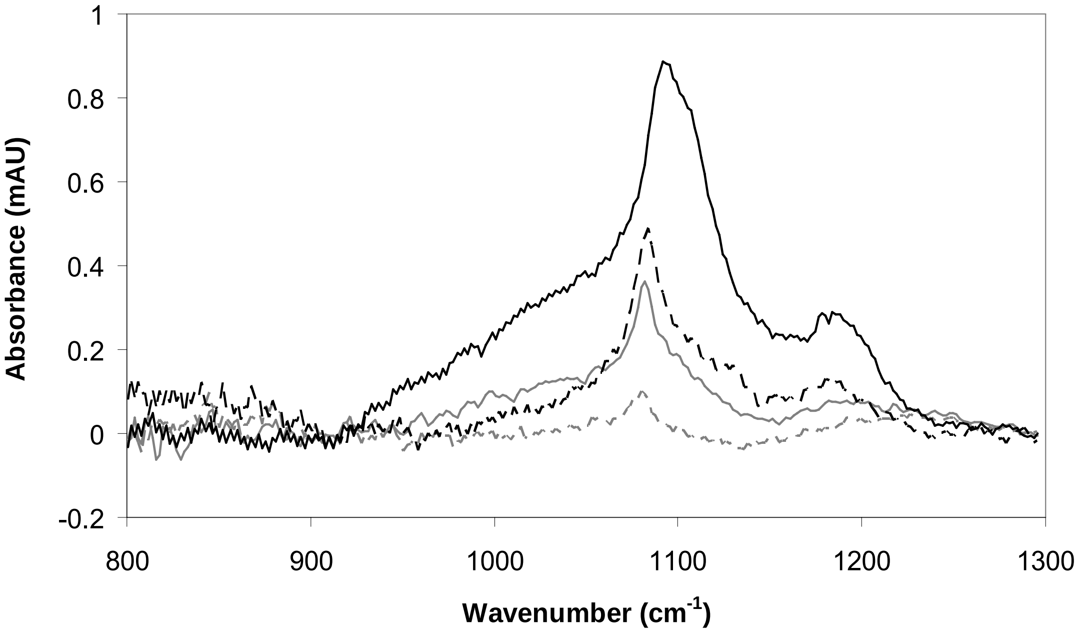

Figure 41: Low frequency FTIR region of H−Si(111) after immersion in CH_3OH for various times.

Hydrogen-terminated *n*-Si(111) samples were immersed in neat anhydrous CH_3OH at room temperature for various times, and FTIR spectra were obtain subsequently under nitrogen: gray broken line, 10 min in CH_3OH; gray solid line, 3 hours in CH_3OH; black broken line, 24 hours in CH_3OH; and solid black line, 6 days in CH_3OH. The sharp Si−O−C stretching mode at 1080 cm^{-1} broadens and blue shifts as the coverage increases. The TO phonon mode for Si−O−Si oxidation can be observed at 1050 cm^{-1}. The peak at 1180 cm^{-1} could be due to the CH_3 rocking mode or the Si−O−Si LO mode or both. All spectra are referenced relative to the freshly etched, hydrogen-terminated surface.

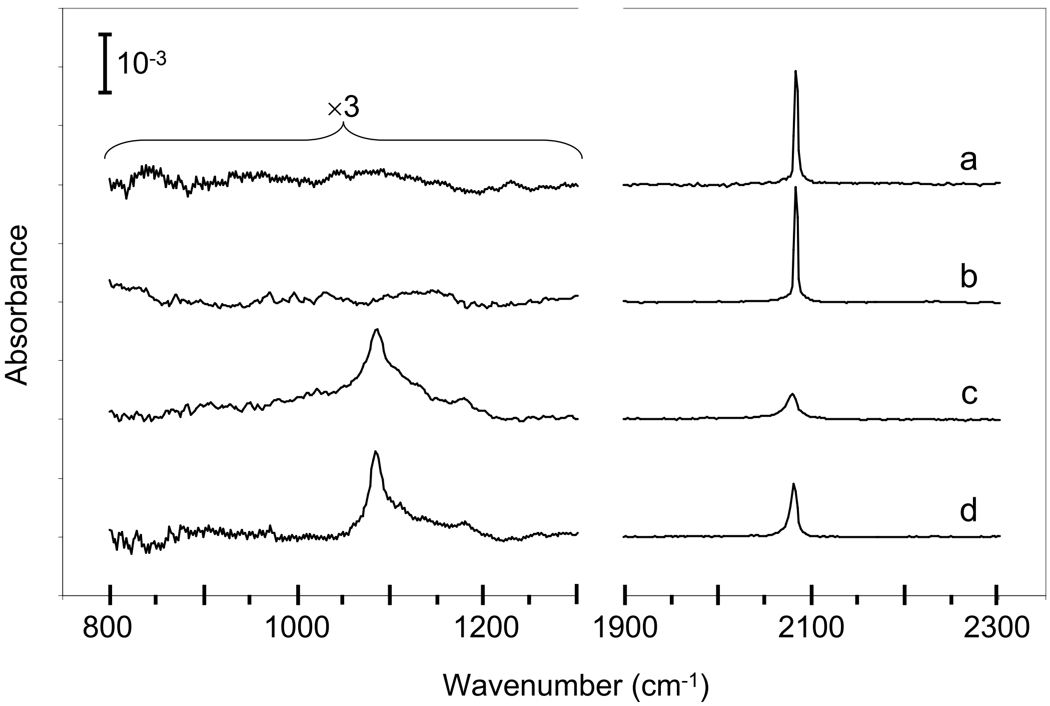

Figure 42: FTIR spectra of H−Si(111) controls experiments.

FTIR spectra of freshly etched H−Si(111) samples were obtained after exposure to **a:** the nitrogen environment of the glove box for 3 hours; **b:** N_2(g)-purged H_2O for 3 hours; **c:** a concentrated solution of $CoCp_2^0$ in anhydrous CH_3OH for 10 min; **d:** neat anhydrous CH_3OH for 3 hours in the dark. All reactions were performed at room temperature in a nitrogen glove box. For all spectra, the absorbance values within the spectral range of 800–1300 cm^{-1} are magnified by a factor of 3 for clarity. All spectra within the 800−1300 cm^{-1} range have been referenced relative to the freshly etched H−Si(111) surface while the same single beam spectra are referenced with respect to the initial native oxide surface for the 1900–2300 cm^{-1} range.

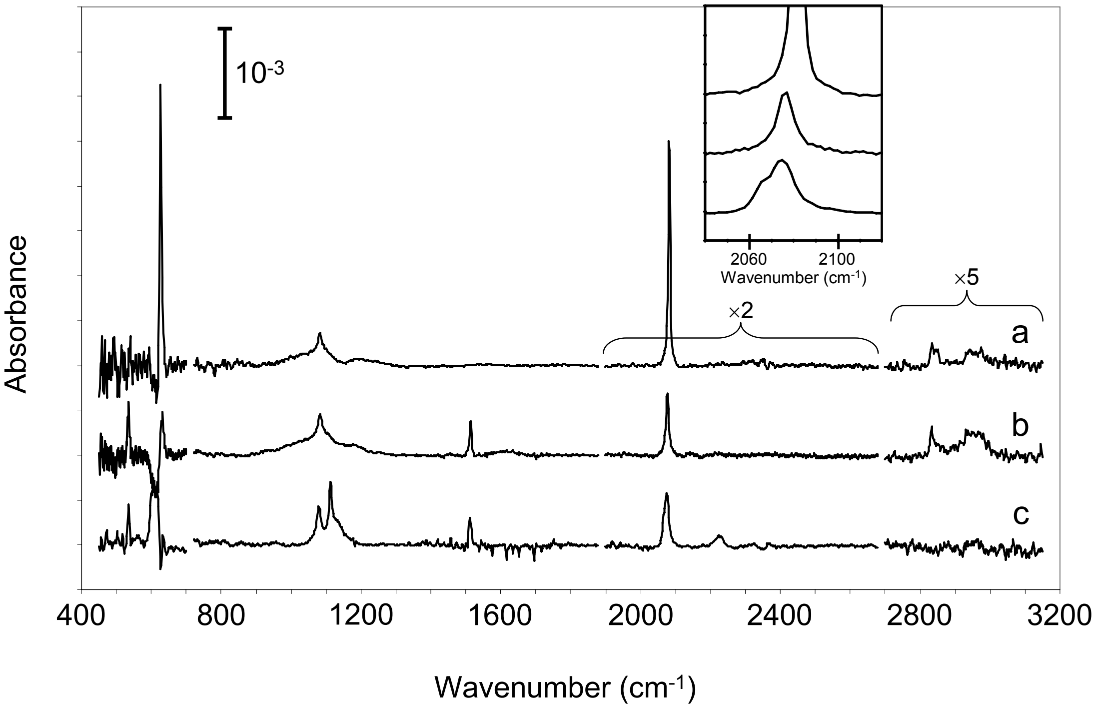

Figure 43: FTIR spectra of H−Si(111) samples exposed to CH_3OH, CH_3OD, or CD_3OD.

FTIR spectra of H−Si(111) samples were obtained after exposure to **a:** neat anhydrous CH_3OH for 3 hours; **b:** neat anhydrous CH_3OD for 3 hours; and **c:** neat anhydrous CD_3OD for 24 hours. All reactions were performed at room temperature in a nitrogen glove box. The original single beam spectra are referenced relative to the freshly etched H−Si(111) surface for the 700–1900 cm^{-1} and 2700–3200 cm^{-1} spectral regions and are referenced to the native oxide surface for the 450–700 cm^{-1} and 1900–2700 cm^{-1} spectral regions. Absorbance values for the spectral region of 1900–2700 cm^{-1} are multiplied by a factor 2 and absorbance values for the region of 2700–3200 cm^{-1} are multiplied by a factor of 5 for clarity.

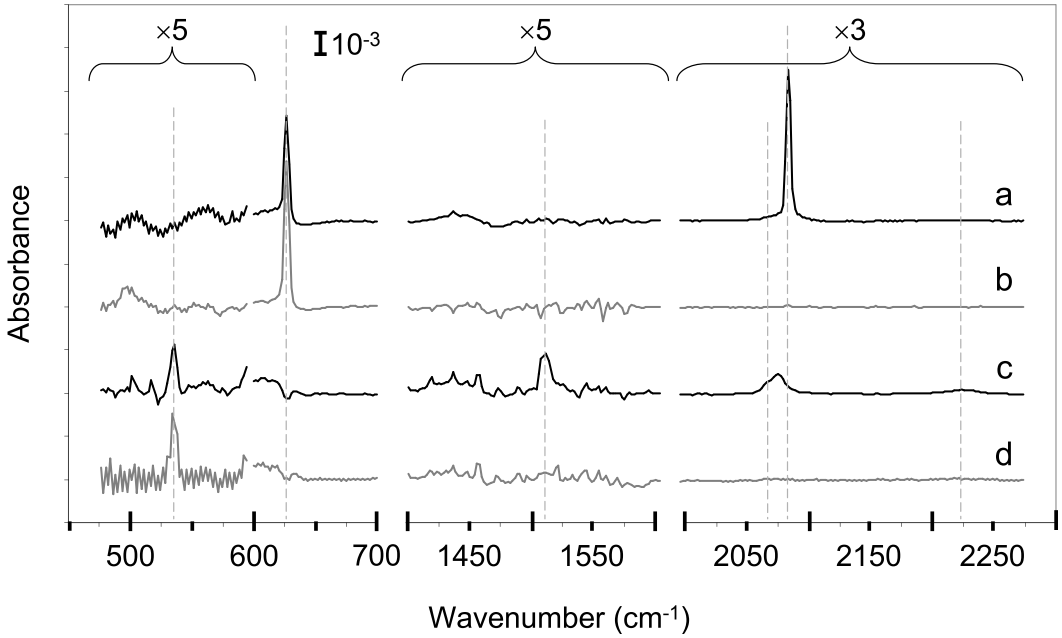

Figure 44: Angle resolved FTIR spectra of H−Si(111) after exposure to CD_3OD. FTIR spectra of freshly etched H−Si(111) samples as prepared and after reaction with CD_3OD. Spectra were recorded for samples situated in the light path at 74 degrees off surface normal for **a:** H−Si(111) and **c:** after a room temperature exposure of H−Si(111) to CD_3OD for 24 hours. Spectra were also recorded with samples situated in the light path at 10 degrees off the surface normal for **b:** H−Si(111) and **d:** after exposure to CD_3OD for 24 hours. All spectra are referenced relative to the initial native oxide surface. For clarity, absorbance values within various spectral regions were multiplied by the scaling factors shown. Polarization experiments on H−Si(111) (spectra **a** and **b**) demonstrate that the H−Si bond is normal to the surface since the peak disappears when the light is oriented nearly normal to the surface. The D−Si peak, formed through the reaction of H−Si(111) with CD_3OD, displays similar polarization indicating that most D−Si bonds are orientated normal to the surface.

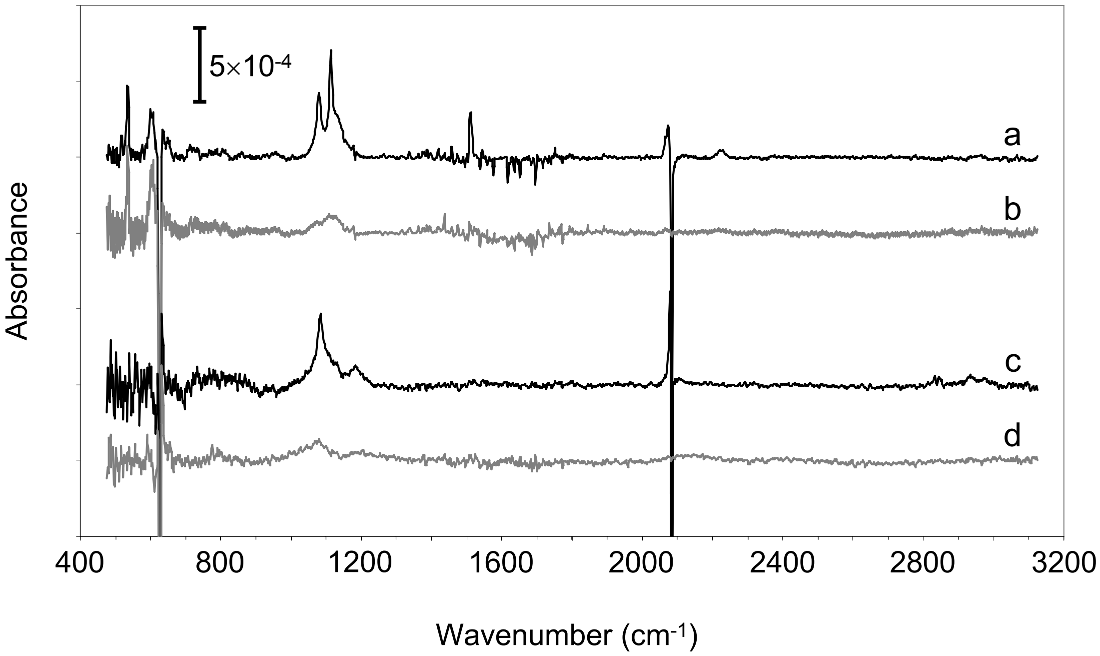

Figure 45: Angle resolved FTIR spectra for H−Si(111) exposed to CH_3OH and CD_3OD for 24 hours.

FTIR spectra were obtained for freshly etched H−Si(111) surfaces exposed to neat anhydrous CH_3OH and CD_3OD for 24 hours. The spectra for H−Si(111) exposed to CD_3OD were measured at 74 and 10 degrees off normal, **a** and **b** respectively. The spectra for H−Si(111) exposed to CH_3OH were measured at 74 and 10 degrees off normal, **c** and **d** respectively. All single beam spectra are referenced relative to the freshly etched H−Si(111) surface. These spectra indicate that the Si−O−CH_3 and Si−O−CD_3 species are orientated normal to the surface since only broad modes around 1100 cm^{-1} can be observed at 10 degrees.

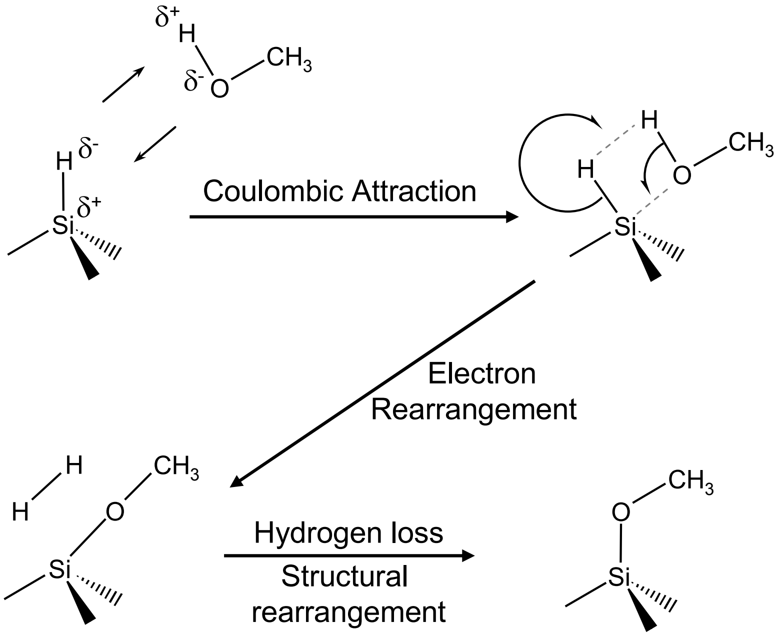

Figure 46: Possible mechanism for the spontaneous methoxylation in neat anhydrous methanol.

This mechanism is proposed since it requires no oxidant. Hydrogen gas is evolved and a methoxyl species is orientated normal to the surface. While this mechanism leads to the formation of Si−O−CH_3 species, it cannot be the only mechanism at work since it doesn't produce D−Si species, which have been observed oriented normal to the surface.

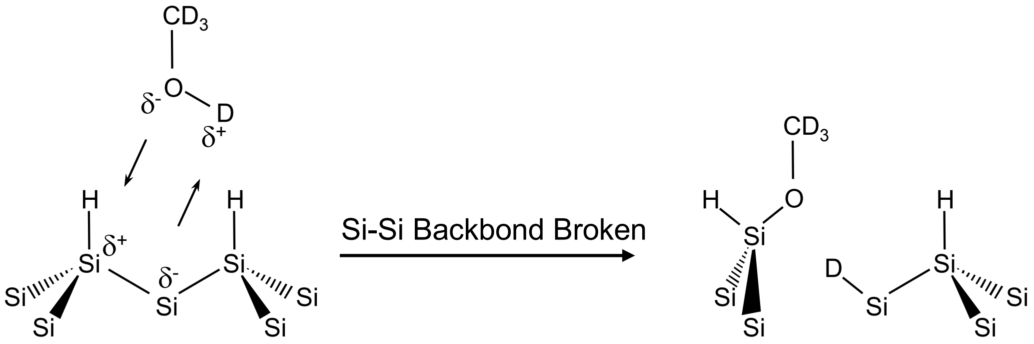

Figure 47: Methoxylation mechanism breaking a Si-Si back bond

A similar mechanism has been proposed by other scientists particularly for porous silicon or the H−Si(100) 2×1 surface. In this mechanism the methanol dissociatively reacts with a Si−Si back bond. This mechanism has two problems: First, there appears to be considerable steric limitations for this reaction to proceed on a (111) surface terrace. Secondly neither the Si−O−C nor the D−Si dipole moments are oriented normal to the surface as has been experimentally observed.

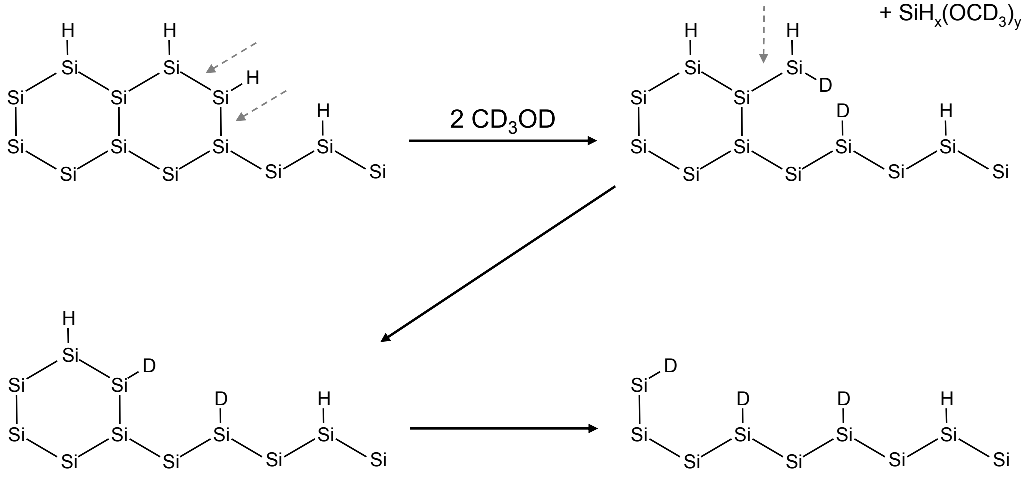

Figure 48: Proposed etching mechanism of H−Si(111) by methanol.

This figure outlines the proposed slow etching mechanism of silicon by methanol at step edges. The depiction of the step edge is left general since this mechanism could occur at both dihydride and monohydride step edge sites. In the first step, Si-Si back bonds (labeled by broken arrows) of an edge silicon atom are broken by dissociative reaction with methanol as shown in Figure 47. It is expected that step edges provide lower steric strain than terrace atoms. Enough back bonds are broken to free a molecule of $SiH_x(OCH_3)_y$, which could further oxidize in solution. The remaining silicon atoms of the crystal lattice are left deuterated. This process of methanol attack on step edge silicon atoms occurs until a terrace of deuterated silicon atoms forms that is orientated normal to the surface. These resulting terraces contribute to most of the observed polarized D−Si signal. A mixed surface of H−Si, D−Si, and Si−O−CH_3 can occur by the parallel occurrence of this mechanism with that depicted in Figure 46.

Appendix A: Derivation of Recombination Mechanisms

Recombination is nature's way to restore the equilibrium concentrations of electrons and holes within a semiconductor device. Perturbations such as light pulses or applied biases generate either an excess or a deficiency of charge carriers. In response to this perturbation it can be desirable to have either fast or slow recombination rates for various device applications. Fast recombination rates are necessary for high speed devices so that biases can be switched on and off quickly. Slow recombination rates are desirable for solar energy devices so that electrons and holes generated by sunlight can last long enough to be collected. Slow recombination rates are also desirable in certain electronic devices for charge storage and for low power devices. Thus a fundamental understanding of the various recombination processes can be desirable.

During the return to equilibrium from a perturbation, the total recombination or generation current is the sum of many individual recombination mechanisms including trap mediated recombination (either at the surface, J_{ss}, in the bulk, J_{br}, or in the depletion region, J_{dr}), radiative recombination, J_{rad}, and auger recombination, J_{aug}, to name a few.

$$J_{tot} = J_{ss} + J_{br} + J_{dr} + J_{rad} + J_{aug} \qquad \text{(A1)}$$

Any of these different mechanisms may dominate the total recombination or generation current under different conditions. Radiative recombination in non-porous silicon devices is not very prevalent because of the indirect band gap of silicon prevents fast direct recombination of electrons and holes. Auger recombination occurs significantly only at very high injection levels that are not realized in this work. Trap mediated recombination mechanisms dominate the recombination-generation currents for silicon devices at low to moderate injection levels and this subtopic derives the equations pertinent to these mechanisms.

Shockley-Read-Hall Equation

Derivation of the General Equation

The Shockley-Read-Hall (SRH) formalism[2, 3] is used to describe the trap-mediated recombination mechanisms that apply to the bulk, depletion region, and surface state recombination pathways. The recombination and generation currents observed for the silicon devices and measurement conditions used in our lab are almost entirely dominated by the trap mediated recombination mechanism, and hence it is the most important mechanism considered in this Appendix. The derivation of the SRH equation is shown below for trap states at a single energy within the bandgap of the semiconductor.

These electrical traps, either in the bulk, in the depletion region, or at surface, act as an intermediate for the recombination. The recombination processes are shown in Figure 49 below. Empty traps can be filled either by electrons in the conduction band, process 1, or by electrons in the valence band, process 4, the latter of which is also known as hole emission. Filled traps can be emptied either by electron emission back into the conduction band, process 2, or by hole capture, process 3.

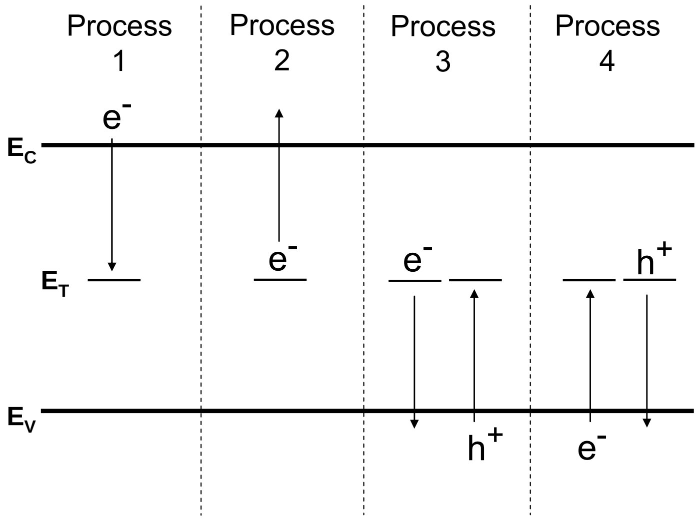

Figure 49: Description of the four trap-mediated recombination processes.

In process 1, an empty trap state is filled with an electron. In process 2, a filled trap state undergoes electron emission into an empty state within the conduction band. In process 3, an electron in a trap state goes to an empty state (hole) within the valence band; this is equivalent to hole capture by a filled trap state. In process 4, an electron from the valence band is captured by the trap state which is equivalent to hole emission from an empty state.

During recombination or generation, the transient concentration of electrons in the conduction band or holes in the valence band can be described by the expressions below.

$$\left.\frac{dn}{dt}\right|_{R-G} = \left.\frac{dn}{dt}\right|_{1} + \left.\frac{dn}{dt}\right|_{2} \tag{A2}$$

$$\left.\frac{dp}{dt}\right|_{R-G} = \left.\frac{dp}{dt}\right|_{3} + \left.\frac{dp}{dt}\right|_{4} \tag{A3}$$

In these equations, *n* is the electron concentration in the conduction band, and its time derivative is the sum of any electron depleting (process 1) or electron enhancing (process

2) rates. Similarly, p is the hole concentration in the valence band, and its time derivative is the sum of any rate process depleting or generating holes in the valence band. Rate expressions for each of these processes (1-4) can be written using kinetic theory. The rate expression for process 1 is:

$$\left.\frac{dn}{dt}\right|_1 = -k_n n(x)(1 - f_T)N_T . \tag{A4}$$

Since process 1 results in a net loss of electrons in the conduction band, the negative sign is used, k_n is the rate constant for electron capture, $n(x)$ is the electron concentration at a position x within the semiconductor, N_T is the trap state density at position x, and $(1 - f_T)$ is the fraction of trap states that are empty. The electron concentration at a given position, $n(x)$, is the sum of two terms, an equilibrium electron concentration at position x, $n_0(x)$, and an injected electron concentration, $\delta n(x,t)$.

$$n(x) = n_0(x) + \delta n(x,t) \tag{A5}$$

The injected electron concentration, $\delta n(x,t)$, and hence $n(x)$, can be a complicated function of position, x, and time, t. For example, immediately upon a light pulse excitation, an exponentially decaying profile of charge carriers is generated into the semiconductor as described below, where $\delta n(x,t_0)$ is the initial distance-dependent injected carrier concentration, $\delta n(x=0,t_0)$ is the initial injected concentration at the surface, and $\alpha(\lambda)$ is the absorption length, which is wavelength dependent.

$$\delta n(x,t_0) = \delta n(x = 0, t_0)\exp\left(-\frac{\alpha(\lambda)}{x}\right) \tag{A6}$$

This carrier profile will quickly change as the carriers move in response to concentration and voltage gradients. Accurately modeling such phenomena must be accomplished using computer programs; however certain approximations can be made under certain conditions to aid in a conceptual understanding.

The function, f_T, in equation A4 is the fraction of trapped states filled with electrons and is obtained by using the Fermi-Dirac expression for the electron concentration versus energy as shown below.

$$f_T = \frac{1}{\exp\left[-\frac{\mathbf{E_F} - \mathbf{E_T}(x)}{kT}\right] + 1} \tag{A7}$$

$$1 - f_T = \frac{\exp\left[-\frac{\mathbf{E_F} - \mathbf{E_T}(x)}{kT}\right]}{\exp\left[-\frac{\mathbf{E_F} - \mathbf{E_T}(x)}{kT}\right] + 1} = \frac{1}{\exp\left[\frac{\mathbf{E_F} - \mathbf{E_T}(x)}{kT}\right] + 1} \tag{A8}$$

The terms $\mathbf{E_F}$ and $\mathbf{E_T}(x)$ are the Fermi-level energy and position-dependent energy of a trap state respectively, k is the Boltzmann constant, and T is the temperature. When the Fermi level is equal to the trap level (or pinned there), the trap states are half filled, $f_T = 1/2$. For $\mathbf{E_F} \neq \mathbf{E_T}$, the ratio of filled states to empty states changes. Since the Fermi-level can be within thermal energy of the trap states, the Maxwell-Boltzmann expression is not a valid simplification and the Fermi-Dirac expression (shown above) must be used.

Rate expressions for the other processes (2-4) are generated in a similar fashion using kinetic theory and are displayed below.

$$\left.\frac{dn}{dt}\right|_2 = k_n' f_T N_T \tag{A9}$$

$$\left.\frac{dp}{dt}\right|_3 = -k_p p(x) f_T N_T \tag{A10}$$

$$\left.\frac{dp}{dt}\right|_4 = k_p' (1 - f_T) N_T \tag{A11}$$

In these equations, $k_n^{'}$, k_p, and $k_p^{'}$ are the rate constants for electron emission, hole capture, and hole emission respectively, $p(x)$ is the hole concentration in the valence band at a given position, x, and f_T is the fraction of traps states that are filled with electrons. Similar to the expression for $n(x)$, the total hole concentration, $p(x)$, is the sum of an equilibrium hole concentration, $p_0(x)$, and a distance- and time-dependent injected hole concentration, $\delta p(x,t)$.

$$p(x) = p_0(x) + \delta p(x,t) \tag{A12}$$

It should be noted that equations A9 and A11 do not contain carrier concentration terms. This is because these rate expressions require the number of empty states in the conduction band, $N_C - n(x) \approx N_C$, or the concentration of filled states in the valence band, $N_V - p(x) \approx N_V$, which are so large that, for non degenerate situations, they are constants that can be incorporated into the rate constants. This is analogous to the inclusion of the solvent concentration into the rate constant of a solvolysis reaction. This means that the k_n and k_p terms have different units, and significantly different values, from the $k_n^{'}$ and $k_p^{'}$ terms.

The total rate expression for electrons, r_n, or holes, r_p, is just the sum of processes that involve that carrier.

$$r_n = -\left.\frac{dn}{dt}\right|_R = k_n n(x)(1 - f_T)N_T - k_n^{'} f_T N_T \tag{A13}$$

$$r_p = -\left.\frac{dp}{dt}\right|_R = k_p p(x) f_T N_T - k_p^{'}(1 - f_T)N_T \tag{A14}$$

In order to simplify these expressions and arrive at the SRH expression, it is necessary to use the principle of detailed balance and steady state approximation. First, the principle of detailed balance will allow us to relate the *k* and *k*' terms for each rate expression. The steady state approximation will then lead to the formation of the Shockley-Read-Hall expression.

The principle of detailed balance specifies that a given process and its inverse process must be equal for a system at equilibrium, *i.e.*, at equilibrium $r_n = r_p = 0$. This allows the total rate equations A13 and A14 to be rearranged so that the *k*' terms can be expressed in terms of *k* terms as follows:

$$k_n^{'} = \frac{(1-f_T)}{f_T} k_n n_0(x) \tag{A15}$$

$$k_p^{'} = \frac{f_T}{(1-f_T)} k_p p_0(x)\,. \tag{A16}$$

In these expressions, $n_0(x)$ and $p_0(x)$ are the *equilibrium* electron and hole concentrations at a given position, *x*. The ratio of filled states to empty states can be evaluated by using expressions A7 and A8 where the terms inside the exponential function are initially replaced by *A* for clarity.

$$\frac{f_T}{1-f_T} = \frac{\dfrac{1}{\exp[-A]+1}}{\dfrac{\exp[-A]}{\exp[-A]+1}} = \frac{1}{\exp[-A]} = \exp[A] = \exp\left[\frac{(\mathbf{E_F} - \mathbf{E_T}(x))}{kT}\right] \tag{A17}$$

This ratio can now be substituted into the previous rate expressions as necessary. One more simplification can be made by using the definitions of the equilibrium electron and hole concentrations.

$$n_0(x) = N_C \exp\left[-\frac{\mathbf{E_C}(x) - \mathbf{E_F}}{kT}\right] \tag{A18}$$

$$p_0(x) = N_V \exp\left[-\frac{\mathbf{E_F} - \mathbf{E}_V(x)}{kT}\right] \qquad \text{(A19)}$$

In these expressions, $\mathbf{E_C}(x)$ and $\mathbf{E_V}(x)$ are the position-dependent energies of the conduction and valence bands, N_C is the density of states in the conduction band, and N_V is the density of states in the valence band. When substituting these expressions for $n_0(x)$ and $p_0(x)$ into the expressions for k', the $\mathbf{E_F}$ terms in the arguments of the exponential terms cancel, and the resulting expressions for the electron and hole emission rate constants are:

$$k_n^{'} = k_n n_1 \qquad \text{(A20)}$$

$$k_p^{'} = k_p p_1 \qquad \text{(A21)}$$

where

$$n_1 \equiv N_C \exp\left[-\frac{\mathbf{E_C}(x) - \mathbf{E_T}(x)}{kT}\right] \qquad \text{(A22)}$$

$$p_1 \equiv N_V \exp\left[-\frac{\mathbf{E_T}(x) - \mathbf{E_V}(x)}{kT}\right]. \qquad \text{(A23)}$$

The terms n_1 and p_1 relate to the energy difference between the trap level and the corresponding band edge, and their definitions serve to illustrate that, for traps states within the semiconductor band gap, the rate constant for carrier capture by traps is always larger than the rate constant for carrier emission from traps. It also shows that the rate constant increases exponentially with the energy difference between the trap state and the majority carrier band. The rate constants for capture and emission from a trap state are equal only for the isoenergetic case that occurs when the trap energy is equal to the respective carrier band energy, *e.g.*, $k_n = k_n^{'}$ for $\mathbf{E_C} = \mathbf{E_T}$, or $k_p = k_p^{'}$ for $\mathbf{E_V} = \mathbf{E_T}$.

(Remember that the expression for $k_n^{'}$ also includes the density of empty states in the conduction band that is approximately N_C.)

Substituting A20 into A13 and substituting A21 into A14 results in the total rate expressions in terms of the capture rate constants, k_n and k_p, only.

$$r_n = -\left.\frac{dn}{dt}\right|_R = k_n n(x)(1 - f_T)N_T - k_n n_1 f_T N_T \tag{A24}$$

$$r_p = -\left.\frac{dp}{dt}\right|_R = k_p p(x) f_T N_T - k_p p_1 (1 - f_T)N_T \tag{A25}$$

Elimination of the f_T terms requires the steady state approximation that is frequently used in many device analyses. This approximation specifies that the status quo is maintained by a balance between rate processes. Specifically in this case, the fraction of filled trap states will be held constant at a value equal to the equilibrium fraction throughout the entire recombination process. In order for this to be the case, the net rate of electrons filling trap states must be equal to the net rate at which holes empty these states so that the fraction of filled states does not change.

$$\frac{df_T}{dt} = 0 = r_n - r_p \tag{A26}$$

This requires that $r_n = r_p \neq 0$. Under the steady state approximation the rate of hole recombination equals the rate of electron recombination. Since these rates are assumed to be equal, a generalized recombination rate U can be defined as:

$$U = -\left.\frac{dn}{dt}\right|_R = -\left.\frac{dp}{dt}\right|_R = r_n = r_p\,. \tag{A27}$$

Because of this, equations A24 and A25 can be set equal to each other and can be rearranged to solve for either f_T or $(1 - f_T)$.

$$f_T = \frac{k_n n(x) + k_p p_1}{k_n n(x) + k_n n_1 + k_p p(x) + k_p p_1} \tag{A28}$$

$$1 - f_T = \frac{k_n p(x) + k_p n_1}{k_n n(x) + k_n n_1 + k_p p(x) + k_p p_1} \tag{A29}$$

It can be seen that the expression for f_T is the sum of trap-electron-filling mechanisms (processes 1 and 4) in the numerator divided by the total number of mechanisms. This is logical because fT, the fraction of filled states, is defined as the number of filled states divided by the total number of trap states. Similarly, the expression for empty states, $(1 - f_T)$, is the sum of electron-emptying mechanisms (processes 2 and 3) divided by the total mechanisms. These expressions can now be substituted into equations A24 and A25 to eliminate the f_T terms. For example, substitution into equation A24 yields:

$$U(x) = N_T \frac{k_n n(x)\left(k_p p(x) + k_n n_1\right) - k_n n_1\left(k_n n(x) + k_p p_1\right)}{k_n\left(n(x) + n_1\right) + k_p\left(p(x) + p_1\right)}. \tag{A30}$$

This equation can be simplified through algebra to:

$$U(x) = N_T \frac{k_n k_p\left(n(x)p(x) - n_1 p_1\right)}{k_n\left(n(x) + n_1\right) + k_p\left(p(x) + p_1\right)}. \tag{A31}$$

By using the expressions for n_1 and p_1, it can be shown that the product, n_1p_1, is equal to the product of the equilibrium electron, $n_0(x)$, and hole, $p_0(x)$, concentrations.

$$n_1 p_1 = N_C N_V \exp\left[-\frac{\mathbf{E}_\mathbf{C}(x) - \mathbf{E}_\mathbf{V}(x)}{kT}\right] = n_i^2 = n_0(x) p_0(x) \tag{A32}$$

Substituting this into the equation for $U(x)$ yields the final Shockley-Read-Hall expression, which is also listed in Chapter 2.

$$U(x) = N_T \frac{k_n k_p \left(n(x)p(x) - n_i^2\right)}{k_n\left(n(x)+n_1\right) + k_p\left(p(x)+p_1\right)} \tag{A33}$$

If excess carriers are injected into the semiconductor, either through a light pulse or through the application of forward bias conditions, then $n(x)p(x) > n_i^2$ and recombination occurs until $n(x)p(x) = n_i^2$. If carriers are depleted from the semiconductor through the application of reverse bias, $n(x)p(x) < n_i^2$, then carrier *generation* occurs until $n(x)p(x) = n_i^2$.

It should be noted that the SRH rate expression derived thus far applies for only *one* trap state at a given energy level within the bandgap defined by n_1 and p_1. In reality there might be many different trap states with different densities, $N_T(\mathbf{E})$, at different energies, **E**. To adequately address the distribution of traps states within the bandgap, an integral over energy and trap density would need to be performed.

Analysis of the SRH Equation

Influence of the Trap Energy

It can be shown that the recombination rate varies depending on the energetic position of the trap state within the band gap. The rate constants for carrier capture relative to carrier emission are proportional by n_1 or p_1 as described in equations A20 and A21. The ratio of carrier capture to carrier emission increases exponentially as the energy difference between the trap and the carrier band edge increases. However trap capture of an electron is in electrically series with trap capture of a hole, so the slower of those two rate processes will dominate to total recombination. Thus, it can be seen that electrical traps with energies right in the middle of the band gap will lead to the fastest recombination rates because the electron and hole capture rates for these two processes will be roughly equal. For trap energies away from the midgap, either the electron or hole capture rates are rate limiting and slower than for traps at midgap energies.

The energy of trap 1, $\mathbf{E_{T,1}}$, (shown in Figure 50) is close to the conduction band so that net hole capture rate is very large (three arrows are drawn to demonstrate a fast rate). The net electron capture rate by this trap, however, is significantly slower than the hole capture rate (one arrow is drawn to demonstrate a slower rate) since the trap energy is not very far away from the conduction band edge. Because recombination requires both electron and hole capture to occur in series, recombination across trap 1 is limited by the slower electron capture step. A similar argument holds for trap 3; its energy is close to the valence band so that the net electron capture rate is fast (3 arrows), but the net hole capture rate is comparatively slow (one arrow) and rate limiting for the net recombination rate. As drawn, traps 1 and 3 would have similar recombination rates. For trap 2, the net hole capture rate is roughly equal to the net electron capture rate. Even though the electron and hole capture rates for trap 2 are slower than both hole capture for trap 1 and electron capture by trap 3, they are both faster than the rate-limiting steps of either trap 1 or trap 3.

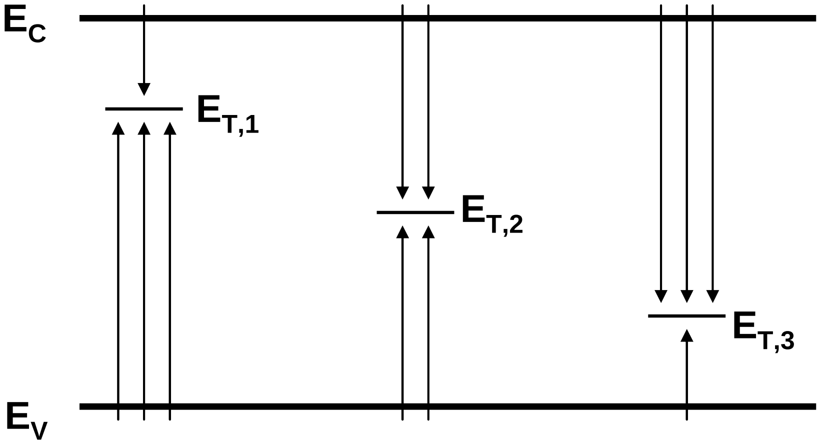

Figure 50: Carrier capture rates for various trap energies. The total recombination rate is fastest for midgap trap (2 arrows), because, while the rate capture for one carrier may be faster (3 arrows) for trap energies away from the midgap, the total recombination rate is limited by the slower carrier capture rate (one arrow).

Mathematically, this is represented in the Shockley-Read-Hall equation by the additive nature of $k_n n_1$ and $k_p p_1$ in the denominator. If either $k_n n_1$ or $k_p p_1$ is large, it dominates the denominator, and makes the recombination rate smaller than if $k_n n_1 = k_p p_1$. The maximum in the recombination rate occurs when $k_n n_1 = k_p p_1$, which is true for traps near the midgap when $k_n = k_p$.

Injection Level Conditions

As mentioned above, $n(x)$ and $p(x)$ are sums of the injected and equilibrium carrier concentrations. They can be complex functions of position and time due to diffusion, migration, and recombination. In order to obtain a fundamental grasp of the recombination rates a couple assumptions can be made. One assumption that is often made is that any position dependence of the carrier concentrations induced by the absorption of light pulse has been eliminated through carrier diffusion before any significant recombination has occurred. This assumption implies that carrier diffusion throughout the sample is much faster than any recombination rate, and if this is true then the carriers can reach a steady state distribution at each point during recombination. This assumption is the same as the assumption that the quasi-Fermi levels remain flat throughout the recombination process.

There are occasions, often observed in the lab, when this assumption clearly breaks down. For a surface with a high electrical defect density, carriers recombine as soon as they reach the surface. This means that the entire recombination process is limited by carrier diffusion toward the defective surfaces and that the surface recombination rate itself is not being measured. (In Chapters 2 and 3 this was often observed for native oxide or copper-contaminated surfaces, and only a lower bound on the surface recombination velocity, S, can be provided for these surfaces since the rate is carrier diffusion limited and not surface recombination limited, *i.e.*, surface recombination is faster than carrier diffusion.) This leads to an uneven quasi-Fermi level with respect to distance. (This is analogous to water flowing down a drain. If the drain opening is very wide, water flow through the drain is limited by water getting to the drain and the water level changes with distance from the drain.)

However for surfaces that are passivated enough to prevent this diffusion-limited recombination, the flat quasi Fermi level assumption holds, and this can provide useful simplifications to the SHR equation. Under these assumptions, the injected carrier concentration is independent of *both* distance and time and can be represented as Δn for electrons and Δp for holes so that the total carrier concentrations can be described as follows.

$$n(x) = n_0(x) + \Delta n \tag{A34}$$

$$p(x) = p_0(x) + \Delta p \tag{A35}$$

Since a light pulse generates equal numbers of electrons and holes, the equilibrated injected electron and hole concentrations are equal: $\Delta n = \Delta p$. Using these new definitions, the Shockley-Read-Hall equation can be written as shown below where U_{fQFL} indicates that the recombination rate is under the assumption of flat quasi-Fermi levels.

$$U_{fQFL}(x) = N_T \frac{k_n k_p \left((n_0(x) + \Delta n)(p_0(x) + \Delta p) - n_i^2 \right)}{k_n \left(n_0(x) + \Delta n + n_1 \right) + k_p \left(p_0(x) + \Delta p + p_1 \right)} \tag{A36}$$

The terms in the numerator can be multiplied through to obtain the following expression where the identity $n_0(x)p_0(x) = n_i^2$ has been used for simplification.

$$U_{fQFL}(x) = N_T \frac{k_n k_p \left(\Delta n p_0(x) + \Delta p n_0(x) + \Delta n \Delta p \right)}{k_n \left(n_0(x) + \Delta n + n_1 \right) + k_p \left(p_0(x) + \Delta p + p_1 \right)} \tag{A37}$$

The expression for the recombination rate can be further simplified into two cases by making some assumptions about the injected carrier concentrations. Low-level injection (LLI) occurs when the injected charge carrier density, $\Delta n = \Delta p$, is less than the majority carrier concentration, but greater than the minority carrier concentration. High-level injection (HLI) occurs when the injected charge carrier density is greater than majority carrier concentration. These two cases are examined in more detail below.

CAUTION: While the following sections low-level and high-level injection conditions apply to a general position, *x*, within the bulk of the semiconductor, they do not apply at the surface as will be discussed in the surface recombination section below.

Low-Level Injection

For the sake of example, consider an *n*-type sample with dopant density, $N_D = 10^{13}\ \text{cm}^{-3}$, which is typical for samples used in photoconductivity decay measurements. Let's also consider a specific position, *x*, where $n_0(x) = 10^{13}\ \text{cm}^{-3}$ and $p_0(x) = n_i^2/n_0(x) = 10^7\ \text{cm}^{-3}$. Low-level injection specifies that $n_0(x) >> \Delta n = \Delta p >> p_0(x)$. An injection level of $\Delta n = \Delta p = 10^{12}\ \text{cm}^{-3}$ serves as a useful example. Given these values, the numerator of $U_{fQFL}(x)$ is dominated by the $n_0(x)\Delta n$ term. For midgap traps, such that $n_1 \approx p_1 \approx n_i \approx 10^{10}\ \text{cm}^{-3}$, those terms are negligible, and the denominator is dominated by $k_n n_0(x)$. The equation simplifies to the expression shown below, using $\tau_p = (N_T k_p)^{-1}$, which is the minority carrier (hole) lifetime in the bulk. (*Caution: this use of the bulk lifetime and subsequent integration does not translate to the case of surface recombination.*)

$$U_{LLI}(x) = N_T \frac{k_n k_p \Delta p n_0(x)}{k_n n_0(x)} = N_T k_p \Delta p = \frac{\Delta p}{\tau_p} \tag{A38}$$

The recombination rate, $U_{LLI}(x)$, is equal to the time derivative of the charge carrier concentration, which can be integrated in order to obtain an expression for the total hole concentration as a function of time.

$$U_{LLI}(x) = -\frac{\delta n(x)}{\delta t} = -\frac{\delta p(x)}{\delta t} = \frac{\Delta p}{\tau_p} \tag{A39}$$

$$-\int \frac{\delta p(x)}{\left(p(x) - p_0(x)\right)} = \int \frac{\delta t}{\tau_p} \tag{A40}$$

$$\ln\left[p(x) - p_o(x)\right] = -\frac{t}{\tau_p} + C \qquad \text{(A41)}$$

$$p(x) - p_0(x) = \exp\left(-\frac{t}{\tau_p}\right)\exp(C) = C'\exp\left(-\frac{t}{\tau_p}\right) \qquad \text{(A42)}$$

In the first step, the identity $\Delta p = p(x) - p_0(x)$ was used. In the second step, the integral relation shown below was used.

$$\int \frac{dx}{a + bx} = \frac{1}{b}\ln\left[a + bx\right] + C \qquad \text{(A43)}$$

The value of C' = Δp can be obtained from the boundary condition that at $t = 0$, $p(x) - p_0(x) = \Delta p$, so that the final time evolution of the total hole concentration $p(x)$ is:

$$p(x) = \Delta p \exp\left(-\frac{t}{\tau_p}\right) + p_0(x) \qquad \text{(A44)}$$

This expression shows that under low-level injection, the injected minority carrier concentration, Δp, decays as a single exponential with a time constant, τ_p. The total electron concentration, on the other hand, remains relatively constant through this whole process since $n_0(x) >> \Delta n$. Since the conductivity, σ, is proportional to the total free carrier concentration by $\sigma = q\mu_p p + q\mu_n n$, this apparatus is sensitive enough to measure the time-dependent profile of the minority carrier concentration which corresponds to fractional changes on the order of 0.1 to 0.001 in the total conductivity of the sample.

High-Level Injection

A similar method can be used to analyze the high-level injection conditions. Using the sample with the same carrier concentrations as before, high-level injection specifies that $\Delta n = \Delta p >> n_0(x) > p_0(x)$. Since $n_0(x) = 10^{13}$ cm^{-3}, and $p_0(x) = 10^{7}$ cm^{-3} for this sample, a photoinjected charge carrier concentration of $\Delta n = \Delta p = 10^{14}$ cm^{-3} would are reasonable for high-level injection conditions. The numerator of $U_{fQFL}(x)$ is now dominated by the $\Delta n\Delta p$ term in the numerator and the Δn and Δp terms in the denominator as shown below. (*Caution: this use of the bulk lifetime and subsequent integration does not translate to the case of surface recombination.*)

$$U_{HLI}(x) = N_T \frac{k_n k_p \Delta n \Delta p}{k_n \Delta n + k_p \Delta p} = N_T \Delta n \frac{k_n k_p}{k_n + k_p} = \Delta n \frac{1}{\tau_p + \tau_n} \tag{A45}$$

If $\tau_n \approx \tau_p$, then $U_{LLI} = 2U_{HLI}$, which means that the recombination rate for low-level injection is about two times faster than the high injection lifetime. This may be surprising since the high-level injection generates *more* carriers; however under low-level injection, the majority carrier concentration is essentially not significantly perturbed, so that the lifetime of holes is the rate-limiting step. Under high-level injection, both the electron and hole concentrations are perturbed and since a recombination even requires both electrons and holes, the amount of time necessary for the entire recombination process is dictated by the series combination of electron and hole lifetimes.

Using a similar integration method, the time-dependent total electron or total hole concentration profiles can be described as shown below.

$$n(x) = \Delta n \exp\left(-\frac{t}{\tau_n + \tau_p}\right) + n_0(x) \tag{A46}$$

$$p(x) = \Delta p \exp\left(-\frac{t}{\tau_n + \tau_p}\right) + p_0(x) \tag{A47}$$

Since the recombination rates for electrons and holes were assumed to be equal by the steady state approximation their time-dependent profiles should indeed be equal.

CAUTION: As written, one might assume that charge carrier recombination profile after a high-level injection should proceed through a single exponential decay back to equilibrium. This is actually not true. The HLI profile *will* adhere to a single exponential for the initial part of the decay as long as $\Delta n = \Delta p >> n_0(x)$; however once $\Delta n \approx n_0(x)$, the semiconductor is no longer under conditions of high-level injection (but instead low-level injection), and the remaining excess minority charge carriers will decay with a single exponential profile with a time constant as derived in the LLI section. The observed lifetime for a high-level injection experiment may however be fit well to a single exponential for reasons regarding the dynamic range of the oscilloscope; the transition to low-level injection may occur well below the noise floor for significantly high high-level injection conditions.

Recombination Rates and Passivation Mechanisms

The trap-mediated recombination rate, $U(x)$, for a given trap energy can be lowered in two ways. First, a reduction in the electrical trap state density, N_T, obviously lowers the recombination rate since the $U(x)$ is proportional to this value. This reduction of electrical traps at the surface, $N_{T,s}$, has been termed *chemical passivation* in this thesis because a reduction in $N_{T,s}$ is usually accomplished through adequate chemical control over the surface.

The recombination rate can also be reduced, locally, through an imbalance of the electron and hole concentrations, $n(x)$ and $p(x)$. This is mathematically similar to the rate reduction due to an imbalance in n_1 and p_1: if either $n(x)$ or $p(x)$ is large, the denominator of the SRH equation is large and the recombination rate is small. Similarly, the maximum recombination rate occurs when $k_n n(x) = k_p p(x)$. Since k_n is usually close to k_p, this occurs when $n(x) \approx p(x)$. Physically, this can be understood because the recombination process involves both electrons and holes, and if one carrier or the other is deficient at a given position, the recombination rate will be smaller than for cases where the electron and hole concentrations are roughly equal.

The equilibrium carrier concentrations, $n_0(x)$ and $p_0(x)$, vary exponentially with distance in the depletion region due to the band bending.

$$n_0(x) = n_{b,0} \exp\left(\frac{qV(x)}{kT}\right) \tag{A48}$$

$$p_0(x) = p_{b,0} \exp\left(-\frac{qV(x)}{kT}\right) \tag{A49}$$

In these equations, $n_{b,0}$ and $p_{b,0}$ are the equilibrium electron and hole concentrations in the bulk respectively, and $V(x)$ is the potential at position, x, relative to the potential in the bulk. For depletion conditions in an *n*-type semiconductor, the bands bend up towards the surface and $V(x) < 0$ because "up" on the energy level diagram moves to more negative voltages. In this case, the electron concentration decreases by one order of magnitude for every 60 mV decrease in voltage; the hole concentration, on the other hand, increases by a factor of 10 for every 60 mV change.

Due to the position-dependent carrier concentrations within the depletion region, the recombination rates at each position are dependent on voltage distribution within the semiconductor.

Recombination Rates at Different Positions

So far the recombination rate expressions have been derived at an arbitrary distance, x, into the semiconductor. These expressions can be made more specific by examining the special cases of surface recombination, $x = 0$, depletion region recombination, $W > x > 0$, and bulk recombination $x > W$, where W is the width of the depletion region. As mentioned in the previous section, the carrier concentrations are dependent on position due to the voltage change with band bending. In this section, the recombination rates as a function of position are examined in more detail.

Differences in recombination with position, x, are due to changes induced by band bending. As the bends bend, the energies of the conduction band, $\mathbf{E_C}(x)$, valence band, $\mathbf{E_V}(x)$, and trap states, $\mathbf{E_T}(x)$, all change, but the Fermi-level, $\mathbf{E_F}$, remains independent of position. Thus, band bending leads to position-dependent values for the equilibrium carrier concentrations, $n_0(x)$ and $p_0(x)$. The occupancy of trap states, f_T, also changes with position because the energy difference between the trap and the Fermi-level, $(\mathbf{E_T}(\boldsymbol{x}) - \mathbf{E_F})$, changes as shown in equation A17. The n_1 and p_1 terms are not affected by position since the energy difference between the trap state and carrier band edge remains constant even though both are position dependent.

Bulk Recombination

The bulk of the semiconductor is defined as the region free of voltage changes induced by the surface. Charge carriers within the bulk do not feel the effect of any surface or external perturbations. For the silicon samples used in this thesis, the dopant density is also uniform throughout the entire sample such that the carrier concentrations are equal everywhere. This simplifies the expression for the bulk recombination rate, U_b, because it simply requires setting $n(x)$ and $p(x)$ equal to the bulk electron and hole concentrations: n_b and p_b respectively.

$$U_b = N_{T,b}\frac{k_{n,b}k_{p,b}\left(n_b p_b - n_i^2\right)}{k_{n,b}\left(n_b + n_1\right) + k_{p,b}\left(p_b + p_1\right)} \tag{A50}$$

Since the Shockley-Read-Hall equation is general for many positions in space, all other terms should have been specified with subscripts to indicate their values in the bulk, which may be different from values in other regions.

The capture of charge carriers by trap states can be modeled after the capture of asteroids by a planet. The rate constants have units of cm^3 sec^{-1}, which can be broken up into a capture cross section, σ, and a speed, v_{th}. In the asteroid and planet analogy, σ is the surface area of the planet in cm^2, and is v_{th} is the velocity of the asteroid. For the capture of charge carriers by trap states, the thermal velocity of an electron (v_{th} = 10^7 cm sec^{-1}) and the cross sectional area of an atom (if r = 3Å, $\sigma \approx 10^{-15}$ cm^2) can be used to yield the right order of magnitude of the rate constant ($k = \sigma v_{th} = 10^{-8}$ cm^3 sec^{-1}).

Dividing the numerator and denominator of the SRH equation by $N_T k_n k_p$ yields:

$$U_b = \frac{n_b p_b - n_i^2}{\frac{1}{N_T k_p}\left(n_b + n_1\right) + \frac{1}{N_T k_n}\left(p_b + p_1\right)}. \tag{A51}$$

The $N_T k_n$ and $N_T k_p$ terms have units of sec^{-1} and therefore represent reciprocal lifetimes so that the SRH can be written as follows where τ_p is the lifetime of holes and τ_n is the lifetime of electrons, since $\tau_n = \frac{1}{N_T k_n}$ and $\tau_p = \frac{1}{N_T k_p}$.

$$U_b = \frac{n_b p_b - n_i^2}{\tau_p\left(n_b + n_1\right) + \tau_n\left(p_b + p_1\right)} \tag{A52}$$

This bulk recombination rate is subject to the same dependencies on low-level and high-level injection conditions as described previously. High-level injection conditions would lead to a recombination lifetime of ($\tau_n + \tau_p$), and a low-level injection lifetime of τ_p for an *n*-type sample or τ_n for a *p*-type sample would be observed.

Surface Recombination

Surface recombination is the next easiest situation to understand since, similar to the bulk case, the recombination rate just requires evaluating the values of each term at the surface as shown below.

$$U_s = N_{T,s}\frac{k_{n,s}k_{p,s}\left(n_s p_s - n_i^2\right)}{k_{n,s}\left(n_s + n_1\right) + k_{p,s}\left(p_s + p_1\right)} \tag{A53}$$

Some of the terms in the surface recombination rate are, however, a bit different from those in the expression for the bulk recombination rate, specifically $N_{T,s}$, and U_s. The units for the bulk trap state density, $N_{T,b}$, are cm^{-3}, because it corresponds to the number of traps within a certain volume of bulk material. For the surface trap state density, $N_{T,s}$, the units are cm^{-2}, because it describes the number of trap states per unit area on the surface. The recombination rates, U_s and U_b, therefore have different units as sensible for the positions where the recombination events occur. The bulk recombination rate has units of cm^{-3} sec^{-1} since it describes the number of recombination events per volume per second. The surface recombination rate has units of cm^{-2} sec^{-1} because it describes the number of recombination events occurring per surface area per second (because of this, the surface recombination rate is basically a flux of carriers to the surface). The units for the carrier capture rate constants (cm^3 sec^{-1}) and the units for the surface electron and hole concentrations (cm^{-3}), however, remain the same in both cases. While it may seem contradictory to for the units of surface electron and hole concentrations to be cm^{-3}, one can consider the surface concentrations as a volume concentration where the third dimension, normal to the surface, is taken to comprise a small finite element, similar to case of electron and hole concentrations evaluated at a given position, x.

During the analysis of bulk recombination, it was shown that a measure of the bulk recombination rate could be described by a carrier lifetime, $\tau_n = (N_{T,b}k_{n,b})^{-1}$ or $\tau_p = (N_{T,b}k_{p,b})^{-1}$. A similar measure of the surface recombination rate can be performed using $S_n = (N_{T,s}k_{n,s})$ or $S_p = (N_{T,s}k_{p,s})$. The units of $(N_{T,s}k_{n,s})$ are not sec^{-1}, as was the case for bulk recombination, but cm sec^{-1}, and thus a different term called the surface recombination velocity, S, is used. The surface recombination velocity, S, can also be abbreviated as SRV. (CAUTION: notice that while τ_n is inversely proportional to $N_{T,b}k_{n,b},$ S_n is directly proportional to $N_{T,s}k_{n,s}$)

The analysis of the SRH equation under different light intensities becomes tricky because $n_{s,0}$ and $p_{s,0}$ can have entirely different values from $n_{b,0}$ and $p_{b,0}$. This means that the definitions for high-level and low-level injection conditions in the bulk are separate from those at the surface. In defining high-level injection and low-level injection for bulk recombination, we specified that the injected carrier concentration was either higher than or lower than the majority carrier concentration respectively. This was done to allow simplification of the SRH equation under these conditions. An analogous approach for surface recombination would dictate that high-level injection conditions occur when the injected carrier concentration, $\Delta n = \Delta p$, is much greater than the larger of $n_{s,0}$, or $p_{s,0}$. Because the different amounts of band banding can lead to a larger $n_{s,0}$ or $p_{s,0}$, this definition of high-level injection is independent of the carrier doping type and only dependent on the surface potential. It should be re-iterated that the definitions of high-level injection and low-level injection for surface recombination can be, and probably are, entirely different from those applicable to bulk recombination.

Using the definitions of high-level injection and low-level injection as pertaining to the surface concentrations, $n_{s,0}$ and $p_{s,0}$, rather than the bulk concentrations, $n_{b,0}$ and $p_{b,0}$, the same mathematical methods for simplifying the SRH equation can be applied to yield the following expressions below.

$$U_{s,HLI} = \Delta n \frac{1}{\frac{1}{S_p} + \frac{1}{S_n}} \qquad \text{(A54)}$$

$$U_{s,LLI} = \Delta p S_p \qquad \text{(A55)}$$

The time-dependent charge carrier profiles for a volume of sample engaging in both surface recombination and bulk recombination can not be calculated as easily as the integration that was performed above in the case of bulk recombination only. Instead, diffusion throughout the sample must be included to allow the carriers to interact with a certain volume of bulk material and with a surface characterized by a given S value. The net result is that an observed photoconductivity decay profile (that is well-fit to a single exponential characterized by a measured lifetime, τ_m) can be related to the surface recombination velocity, S, through the expression below, where, τ_b is the bulk recombination lifetime, d is the sample thickness, and 2 appears because both surfaces are active recombination positions.[32-34]

$$\frac{1}{\tau_m} = \frac{1}{\tau_b} + \frac{2S}{d} \tag{A56}$$

This equation is logical because it demonstrates that the total recombination time is the sum of the bulk recombination time and the surface recombination time. These recombination times represent rates that are not volume normalized (*i.e.*, the bulk recombination time, $1/\tau_b$, has units of sec). The usual volume normalization should not be performed in this case, because the specific dimensions of the particular sample will influence the relative contributions of bulk and surface recombination mechanisms to the total recombination time. The $2S/d$ term then represents the surface recombination time, and this is logical because it includes the sample thickness, through which carriers must diffuse to get to the surface, as well as a factor of 2, to represent that there are 2 surfaces on this wafer (assumed to be infinite in the x and y directions) where recombination can occur.

As discussed in the position dependent recombination section, the surface recombination rate can be significantly lowered by either a large $n_{s,0}$ or $p_{s,0}$ value. An accurate evaluation of the surface trap state density, $N_{T,s}$, can only be performed if the $n_{s,0}$ and $p_{s,0}$ values are well known. At equilibrium, the surface electron and hole concentrations are dependent on the voltage difference between the surface and the bulk, V_s, through Boltzmann statistics as shown in equations below.

$$n_{s,0} = n_{b,0} \exp\left(\frac{qV_s}{kT}\right) \tag{A57}$$

$$p_{s,0} = p_{b,0} \exp\left(-\frac{qV_s}{kT}\right) \tag{A58}$$

In order to facilitate a conceptual understanding, let us first analyze the simple case where the surface electron and hole concentrations are equal. When this is the case, $n_{s,0} = p_{s,0} = n_i$. Furthermore, for trap states with energies poised at the midgap, $n_1 = p_1 = n_i$. The expression for the surface recombination rate significantly simplifies as shown below, considering that $\Delta n = \Delta p$, and assuming that $k_{n,s} = k_{p,s}$.

$$U_s = N_{T,s}\frac{k_{n,s}k_{p,s}\left(\Delta n p_s + \Delta p n_s + \Delta n \Delta p\right)}{k_{n,s}\left(n_s + \Delta n + n_1\right) + k_{p,s}\left(p_s + \Delta p + p_1\right)} \tag{A59}$$

$$U_s\left(n_{s,0} = p_{s,0}\right) = N_{T,s}\frac{k_{n,s}k_{p,s}\left(\Delta n n_i + \Delta n n_i + \Delta n^2\right)}{k_{n,s}\left(2n_i + \Delta n\right) + k_{p,s}\left(2n_i + \Delta p\right)} \tag{A60}$$

$$U_s\left(n_{s,0} = p_{s,0}\right) = N_{T,s}\frac{k_{n,s}^2 \Delta n\left(2n_i + \Delta n\right)}{2k_{n,s}\left(2n_i + \Delta n\right)} = N_{T,s}\frac{k_{n,s}\Delta n}{2} \tag{A61}$$

This expression holds for all light intensities; no assumption about the injection level was needed. It should be pointed out, however, that any modest light intensity (greater than $n_{s,0} \approx p_{s,0} \approx n_i \approx 10^{10}$ cm^{-3}) is formally considered to by high-level injection, since it will be larger than the equilibrium surface concentration of electrons and holes. Considering that this is high-level injection, we can use the expression described above (again using $k_{n,s} = k_{p,s}$, or $S_n = S_p = S$), $U_s = \Delta nS/2$, to relate the surface recombination velocity to the trap state density.

$$U_s\left(n_{s,0} = p_{s,0}\right) = \frac{\Delta n S}{2} = \frac{N_{T,s}k_{n,s}\Delta n}{2} \tag{A62}$$

$$S\left(n_{s,0} = p_{s,0}\right) = N_{T,s}k_{p,s} = N_{T,s}\sigma v_{th} \tag{A63}$$

In the last expression, σ is the cross sectional area of the electric trap and v_{th} is the thermal velocity of the electron as presented previously. This simple relation allows a measured photoconductivity decay lifetime, τ_m, to be related to a surface recombination velocity, S, and hence to an electrical trap state density, $N_{T,s}$. However, this simple relation **only applies when $\boldsymbol{n_{s,0} = p_{s,0}}$**. If $n_{s,0}$ and $p_{s,0}$ have any other value, then the surface recombination rate is reduced due to either a large $n_{s,0}$ or a large $p_{s,0}$ in the denominator, as analogous to the case presented above for general $n(x)$ and $p(x)$ values.

The potential, V_s, necessary for $n_{s,0} = p_{s,0}$ can be redefined as a "surface potential" equal to zero, $V_{surf} = 0$. Using this definition, the surface recombination velocity can be rewritten so that its change with any surface potential away from 0 can be observed.[136] In the expression below, n_i is the intrinsic free carrier concentration and u_s^* is the normalized surface potential under illumination (qV_{surf}^*/kT).[136] For this expression, it is assumed that $k_{n,s} = k_{p,s}$, and that the trap energy is positioned at midgap.

$$S = N_{T,s} \frac{(k_{n,s} k_{p,s})^{\frac{1}{2}} (n_b + p_b)}{2\{n_i + n_i^* \cosh[u_s^*]\}} \tag{A64}$$

$$n_i^* = \sqrt{\frac{n_{b,0} + \Delta n}{p_{b,0} + \Delta n}} \tag{A65}$$

A graphical analysis of this expression is shown in Figure 51. It can be seen clearly that the surface recombination velocity (SRV) decreases significantly for any surface potentials not equal to zero, *i.e.*, where $n_{s,0} \neq p_{s,0}$. **This figure clearly demonstrates that the surface electron and hole concentrations, and hence the surface potential, *must be known* before any experimentally observed *S* values can be used to calculate a surface trap state density, $\boldsymbol{N_{T,s}}$.**

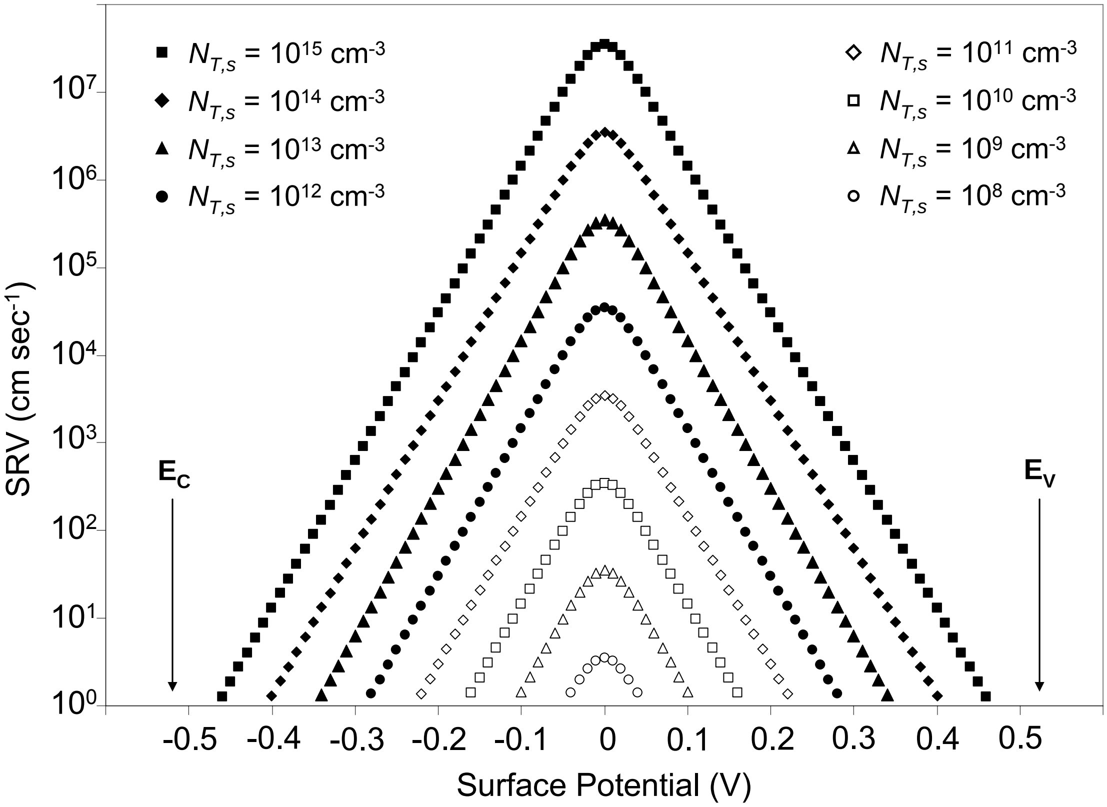

Figure 51: Theoretic plot of surface recombination velocity vs. surface potential. The surface recombination velocity (SRV) can vary dramatically with surface potential, V_{surf}. For $V_{surf} = 0$, the surface electron and hole concentrations are equal ($n_{s,0} = p_{s,0}$). For every 60 mV change in V_{surf}, $n_{s,0}$ and $p_{s,0}$ change by a factor of 10. Many different SRV vs. V_{surf} curves are displayed for surfaces containing different surface trap state densities, $N_{T,s}$. A surface trap state density of 10^{15} cm^{-3} corresponds to an electric defect on every silicon atom of the surface, yet, theoretically, this surface can display a low S value near 10 cm sec^{-1} when the surface is either under inversion, $V_{surf} = 0.4$ V, or accumulation, $V_{surf} = -0.4$ V. V_{surf} values near these have been experimentally observed in this thesis for silicon contacts to Fc$^{+/0}$-MeOH or CoCp$_2^{+/0}$-MeOH respectively. An S value of 10 cm sec^{-1} can also be achieved for a surface with $N_{T,s} = 10^9$ cm^{-3} and $V_{surf} = 0$, clearly demonstrating the need for quantification of V_{surf} in order to reliably obtain $N_{T,s}$ values.

Depletion Region Recombination

Recombination within the depletion region can also occur. So far, only the recombination rates within the bulk or at the surface have been analyzed in detail. Within the depletion region the electron and hole concentrations are a strong function of position as defined by the Boltzmann distribution and by the quadratic dependence of potential on position. Thus the recombination rate will be different at each position, *x*, within the depletion region as defined by the Shockley-Read-Hall expression shown below for clarity.

$$U(x) = N_T \frac{k_n k_p \left(n(x)p(x) - n_i^2\right)}{k_n\left(n(x) + n_1\right) + k_p\left(p(x) + p_1\right)} \tag{A66}$$

Since the recombination rate will change with position, the total recombination occurring within the depletion region can be estimated by integrating the position-dependent SRH equation over the entire depletion width. This integration will not be performed here because it is rather involved and because depletion region recombination is not a significant recombination mechanism for the systems studied in this thesis. Nevertheless, a number of key points can be discussed. Assuming that the trap state density is constant across the depletion region, the maximum recombination rate will occur at the position, if it exists, where $n(x) = p(x)$. This position may not exist, for example, if an *n*-type semiconductor is under accumulation; the band are bent such that the electron concentration is never less than the bulk electron concentration, and hence, can never equal the hole concentration. In this accumulation case, the maximum recombination rate (neglecting surface recombination) occurs within the bulk of the semiconductor because this is the position where the electron concentration is most similar to the hole concentration. For depletion or inversion conditions, however, there will be a position (either within the depletion region or at the surface) where $n(x)$ will equal $p(x)$, and at this position the recombination rate will be at its maximum.

For the silicon samples used within this thesis, the bulk lifetime is so long that even the maximum recombination, occurring at the position where $n(x) = p(x)$, is still very often considerably slower than the surface recombination rate. Even for systems where the surface recombination rate is very low, e.g. accumulation or inversion conditions, only the inverted contact could demonstrate a depletion region recombination rate lower than that in the bulk. Because, however, the trap state density at that position is low (provided it is within the bulk), and because the concentrations of electron and holes after the injection of the photoexcited carriers are not that significantly different from those in bulk other, depletion region recombination is not significantly different from bulk recombination, and not a major concern for the studies presented in this thesis.

Other Mechanisms

Diffusion Limit

For a surface with an extremely high defect density, carriers recombine as soon as they arrive at the surface. Since carrier excitation occurs within the bulk of the semiconductor, the decay profile will be dominated only by carrier transport to the surface. In order to estimate the electronic lifetime associated with carrier diffusion, the ambipolar diffusion constant for carriers, D_{amb}, and the thickness of the wafer, W, must be known. The diffusion time, τ_{diff}, for carriers is shown below.[137]

$$\tau_{diff} = \frac{4\left(\frac{W}{2}\right)^2}{\pi^2 D_{amb}} \tag{A67}$$

$$D_{amb} = \frac{D_n D_p}{D_n + D_p} \tag{A68}$$

The ambipolar diffusion constant is used because recombination at the surface requires diffusion of both carriers to the surface. The electron and hole diffusion constants, D_n and D_p respectively, can be obtained from the Einstein equations shown below.

$$D_n = \mu_n \frac{kT}{q} \tag{A69}$$

$$D_p = \mu_p \frac{kT}{q} \tag{A70}$$

Using the values of 1500 and 450 $\text{cm}^2\ \text{V}^{-1}\ \text{sec}^{-1}$ as the electron and hole mobilities respectively, D_n and D_p can be obtained as 38.8 and 11.6 $\text{cm}^2\ \text{V}^{-1}\ \text{sec}^{-1}$ respectively. The ambipolar diffusion constant, D_{amb}, is then 8.9 $\text{cm}^2\ \text{sec}^{-1}$. For wafers 500 microns thick, the carriers only really have to travel 250 microns before reaching a surface so the diffusion time becomes 18 μs. This is very close to the experimentally observed value of approximately 20 μs for this thickness of silicon.

Factors that Limit the Evaluation of the Surface Electrical Properties

For the work in the Lewis group, we are interested in the electrical perfection of the various chemically modified surfaces. To this end, it is important to be able to reliably measure the surface recombination properties so that an accurate evaluation of $N_{T,s}$ can be performed. In practice, however, the overall recombination rate may not be limited by surface recombination and, hence, an accurate evaluation of the surface electrical properties is obscured such that only upper or lower bounds can be provided.

The overall recombination rate of a particular sample is dominated by the mechanism that has the lowest recombination rate. This is the case because all of the recombination processes are in electrical parallel, and the pathway that can source the most current (has the fastest rate) will dominate the overall recombination process. In many cases the dominant recombination rate need not be surface recombination. For the samples used in this study, only bulk and surface recombination mechanisms need to be considered because auger, radiative, and depletion region recombination is negligible for high purity, float zone wafers measured with reasonable injection levels from a light pulse. Under these conditions, surface recombination will dominate the overall rate only for moderate surface recombination velocities. For very low surface recombination rates, bulk recombination will be the dominant mechanism and only an upper bound on a very low surface recombination velocity will be possible. For very large surface recombination rates, the observed photoconductivity decay is dominated by diffusional transport of electrons and holes to the surface; this is because diffusional transport is in electrical series with surface recombination, and it can limit the overall rate of recombination if it takes longer for the carriers to reach the surface as it does for them to recombine once there. When diffusional transport is rate-limiting, only a lower bound on a very large surface recombination rate can be estimated.

Below is a graph describing the range of surface recombination rates where recombination at the surface will dominate the overall recombination process and allow an assessment of the surface electrical properties (provided that $n_{s,0}$ and $p_{s,0}$ are known). The upper limit of the surface recombination rate is determined by the bulk recombination rate. When designing a system to measure the surface recombination rates, it is desirable to have the samples no thicker than 1/10th of the bulk diffusion length so that the carriers will interact with the surfaces approximately 10 times before they would normally recombine in the bulk. If multi- or poly-crystalline silicon samples are used, the low bulk recombination rates associated with these samples will require samples thinner than may be technologically available; furthermore even if such samples are obtained, samples thinner than 100 microns will present significant signal to noise issues with the rf photoconductivity decay apparatus.

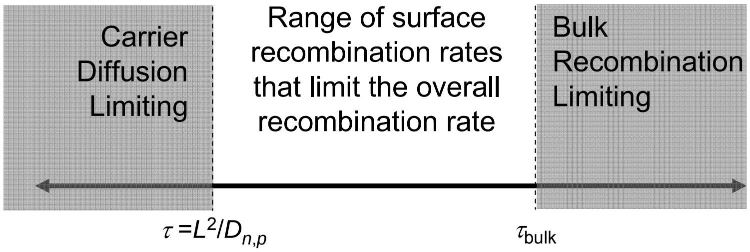

Surface Recombination Rate

The lower limit on the range is dominated by the carrier diffusion time. This limit can be lowered by using samples of smaller thickness, *L*. These limitations on the range of surface recombination rates must be considered when designing any system to measure the surface electrical properties.

Appendix B: Semiconductor Space Charge Equations

Rigorous analysis of the space charge region within the semiconductor is necessary for a full understanding of its electrical properties. This part of the appendix will derive several of the equations pertaining to the space charge region that have been used for data analysis. The derivation begins with the most general, and hence most complex, analysis of the fields generated within a space charge region. Simplifications are described later on when necessary.

Derivation of the Electric Field

The potential, $V(x)$, electric field, $E(x)$, and charge density, $\rho(x)$, are all related through integral equations. The electric field is related to the potential by:

$$E(x) = -\frac{dV(x)}{dx}\,. \tag{A71}$$

The voltage is related to the charge density through the one-dimensional Poisson equation, which states that the second derivative of the potential, $V(x)$, is proportional to the charge density distribution, $\rho(x)$, where $\kappa\varepsilon_0$ is the dielectric of the semiconductor.

$$\frac{d^2V(x)}{dx^2} = -\frac{\rho(x)}{\kappa\varepsilon_0} \tag{A72}$$

The charge density within the space charge region includes the sum of all things charged at a given position: ionized dopant atoms (either donor, N_D^+, or acceptor, N_A^-), and charge carriers such as electrons, $n(x)$, and holes, $p(x)$.

$$\rho(x) = q\left[N_D^+(x) - N_A^-(x) + p(x) - n(x)\right] \tag{A73}$$

Since ionized acceptors and electrons are negatively charged, they are subtracted from the charge density, while ionized donors and holes are positively charged and, hence, added. For most semiconductors used in this thesis there is predominantly only one dopant within the bulk, either N_D^+ for *n*-type or N_A^- for *p*-type. However in some cases, for example at the interface between the n^+- or p^+-regions of a diode, both acceptor and donor atoms may coexist. Certain other semiconductor regions may require the presence of both dopant and acceptor concentrations. For example, it is sometimes desired to have a region within the semiconductor behave intrinsically, and accomplishing through the equal doping of a particular region (such that $N_D^+ = N_A^-$) is easier than removing unwanted impurities and other dopants.

Let us first make the assumption that the dopant densities are uniform throughout the semiconductor so that their *x*-dependence is removed. This assumption is valid for most of the semiconductor devices used in this thesis but may not be acceptable for more complicated semiconductor devices.

Before proceeding it is important to acknowledge one more requirement. Within the bulk, charge neutrality must exist, *i.e.*, $\rho_{\text{bulk}} = 0$. More specifically, the total free carrier concentrations in the bulk, $n_{b,0} + p_{b,0}$, must equal the total ionized dopant concentration as shown below.

$$N_D^+ - N_A^- = n_{b,0} - p_{b,0} \qquad \text{(A74)}$$

Notice, that this equation is completely general and applies for either *n*-type or *p*-type material. The charge density at any position, *x*, can now be written as follows.

$$\rho(x) = q\left[n_{b,0} - p_{b,0} + p(x) - n(x)\right] \qquad \text{(A75)}$$

The electron and hole concentrations have x-dependencies defined by Boltzmann statistics.

$$n(x) = n_{b,0}\exp\left(\frac{qV(x)}{kT}\right) = n_{b,0}\exp(\beta V(x)) \tag{A76}$$

$$p(x) = p_{b,0}\exp\left(-\frac{qV(x)}{kT}\right) = p_{b,0}\exp(-\beta V(x)) \tag{A77}$$

$$\beta \equiv \frac{q}{kT} \tag{A78}$$

The definition of β is used to save space in working with these equations. These expressions can be added into the expression for the charge density.

$$\rho(x) = q\left[p_{b,0}\left(e^{-\beta V(x)} - 1\right) - n_{b,0}\left(e^{\beta V(x)} - 1\right)\right] \tag{A79}$$

Poisson's equation is now as shown below.

$$\frac{d^2V(x)}{dx^2} = -\frac{q}{\kappa\varepsilon_0}\left[p_{b,0}\left(e^{-\beta V(x)} - 1\right) - n_{b,0}\left(e^{\beta V(x)} - 1\right)\right] \tag{A80}$$

Integration of this equation to obtain either the electric field, $E(x)$, or the voltage, $V(x)$, is complicated since the second derivative of the voltage is dependent on the charge density, which itself is exponentially dependent on the voltage. The first integration can be performed relatively easily using a mathematical trick; however the second integration to obtain the voltage cannot be solved analytically.

The first integration is performed from bulk to some position, x.

$$\int_{bulk}^{x}\frac{d^2V(x)}{dx^2}dx = \int_{bulk}^{x} -\frac{q}{\kappa\varepsilon_0}\left[p_{b,0}\left(e^{-\beta V(x)} - 1\right) - n_{b,0}\left(e^{\beta V(x)} - 1\right)\right]dx \tag{A81}$$

The trick is to multiply both sides by $dV(x)/dx$, essentially a change of variables, so that the left hand side (LHS) of the equation becomes:

$$\int \frac{dV(x)}{dx} \cdot \frac{d^2V(x)}{dx^2} dx = \int \frac{dV(x)}{dx} \cdot \frac{d}{dx}\left[\frac{dV(x)}{dx}\right] dx \tag{A82}$$

$$\int \frac{dV(x)}{dx} \cdot d\left[\frac{dV(x)}{dx}\right]. \tag{A83}$$

The integration from bulk to position, *x*, must now be written in terms of the integration variable. The electric field in the bulk is zero since the charge density is zero there. At position *x*, in the space charge region, the field is *dV*(*x*)/*dx* so the integration becomes:

$$= \int_0^{\frac{dV(x)}{dx}} \frac{dV(x)}{dx} \cdot d\left[\frac{dV(x)}{dx}\right] = \frac{1}{2}\left(\frac{dV(x)}{dx}\right)^2. \tag{A84}$$

Similarly treatment of the right hand side (RHS) of the equation leads to:

$$\int -\frac{q}{\kappa\varepsilon_0}\left[p_{b,0}\left(e^{-\beta V(x)} - 1\right) - n_{b,0}\left(e^{\beta V(x)} - 1\right)\right] dx \frac{dV(x)}{dx}. \tag{A85}$$

The same method for change of variables is used. In this case, the potential in the bulk is zero, and the potential within the depletion region is *V*(*x*) so that the integral becomes:

$$-\frac{q}{\kappa\varepsilon_0}\int_0^{V(x)}\left[p_{b,0}\left(e^{-\beta V(x)} - 1\right) - n_{b,0}\left(e^{\beta V(x)} - 1\right)\right] dV(x). \tag{A86}$$

This integration can be performed stepwise on each term.

$$-\frac{q}{\kappa\varepsilon_0}\left[p_{b,0}\left(-\frac{1}{\beta}e^{-\beta V(x)}\Big|_0^{V(x)} - V(x)\Big|_0^{V(x)}\right) - n_{b,0}\left(\frac{1}{\beta}e^{\beta V(x)}\Big|_0^{V(x)} - V(x)\Big|_0^{V(x)}\right)\right] \tag{A87}$$

$$-\frac{q}{\kappa\varepsilon_0}\left[p_{b,0}\left(-\frac{1}{\beta}e^{-\beta V(x)} + \frac{1}{\beta} - V(x)\right) - n_{b,0}\left(\frac{1}{\beta}e^{\beta V(x)} - \frac{1}{\beta} - V(x)\right)\right] \tag{A88}$$

Factoring out a $1/\beta$ and factoring in the minus sign leads to:

$$\frac{q}{\beta\kappa\varepsilon_0}\left[p_{b,0}\left(e^{-\beta V(x)} + \beta V(x) - 1\right) + n_{b,0}\left(e^{\beta V(x)} - \beta V(x) - 1\right)\right]. \tag{A89}$$

The LHS and RHS can be put together to describe the electric field.

$$\frac{1}{2}\left(\frac{dV(x)}{dx}\right)^2 = \frac{q}{\beta\kappa\varepsilon_0}\left[p_{b,0}\left(e^{-\beta V(x)} + \beta V(x) - 1\right) + n_{b,0}\left(e^{\beta V(x)} - \beta V(x) - 1\right)\right] \quad \text{(A90)}$$

$$\left(E(x)\right)^2 = \frac{2q}{\beta\kappa\varepsilon_0}\left[p_{b,0}\left(e^{-\beta V(x)} + \beta V(x) - 1\right) + n_{b,0}\left(e^{\beta V(x)} - \beta V(x) - 1\right)\right] \quad \text{(A91)}$$

$$E(x) = \pm\left\{\frac{2q}{\beta\kappa\varepsilon_0}\left[p_{b,0}\left(e^{-\beta V(x)} + \beta V(x) - 1\right) + n_{b,0}\left(e^{\beta V(x)} - \beta V(x) - 1\right)\right]\right\}^{\frac{1}{2}} \quad \text{(A92)}$$

We now have a rather complicated expression for the electric field as a function of the voltage and equilibrium charge carrier concentrations in the bulk. The positive sign is used for $V(x) > 0$, and the negative sign is used for $V(x) < 0$. It should be noted that the exponential terms and the voltage-independent terms in this expression came from the electron and hole-free carrier concentrations, while the terms linear in voltage came from the ionized dopant concentrations. For a semiconductor sample with a single dopant, one of these linear terms will be zero. For a single dopant that is *n*-type, the term $p_{b,0}\beta V(x) = 0$, or for a singly-doped *p*-type sample, the term $n_{b,0}\beta V(x) = 0$.

This expression is often written another way depending on the specific doping of the semiconductor. If it is *p*-type, then $p_{b,0} = N_A^-$, and it is often factored out of the square bracketed term in the equation above. Doing so allows some terms to be substituted for the extrinsic Debye length for holes, $L_{D,h}$, which is defined below.

$$L_{D,h} \equiv \sqrt{\frac{kT\kappa\varepsilon_0}{p_{b,0}q^2}} \equiv \sqrt{\frac{\kappa\varepsilon_0}{q\beta N_A^-}} \quad \text{(A93)}$$

The equation for the electric field can now be written as below.

$$E_p(x) = \pm\frac{\sqrt{2}kT}{qL_{D,h}} \cdot F_p\left(\beta V(x), \frac{n_{b,0}}{p_{b,0}}\right) \quad \text{(A94)}$$

The function F_p is defined as below.

$$F_p\left(\beta V(x),\frac{n_{b,0}}{p_{b,0}}\right)=\left[\left(e^{-\beta V(x)}+\beta V(x)-1\right)+\frac{n_{b,0}}{p_{b,0}}\left(e^{\beta V(x)}-\beta V(x)-1\right)\right]^{\frac{1}{2}} \qquad \text{(A95)}$$

The text *Physics of Semiconductor Devices* by Sze uses these expressions for a *p*-type semiconductor sample. A similar method can be used to write expressions for an *n*-type semiconductor as shown below.

$$L_{D,n}\equiv\sqrt{\frac{kT\kappa\varepsilon_0}{n_{b,0}q^2}}\equiv\sqrt{\frac{\kappa\varepsilon_0}{q\beta N_D^+}} \qquad \text{(A96)}$$

$$F_n\left(\beta V(x),\frac{p_{b,0}}{n_{b,0}}\right)=\left[\frac{p_{b,0}}{n_{b,0}}\left(e^{-\beta V(x)}+\beta V(x)-1\right)+\left(e^{\beta V(x)}-\beta V(x)-1\right)\right]^{\frac{1}{2}} \qquad \text{(A97)}$$

$$E_n(x)=\pm\frac{\sqrt{2}kT}{qL_{D,n}}\cdot F_p\left(\beta V(x),\frac{p_{b,0}}{n_{b,0}}\right) \qquad \text{(A98)}$$

Since the work in my thesis uses both *n*-type and *p*-type silicon samples, I will continue subsequent derivations with a generalized expression for $F(V)$ and the field shown below.

$$E(x)=\pm\sqrt{\frac{2q}{\beta\kappa\varepsilon_0}}\cdot F(V) \qquad \text{(A99)}$$

$$F(V)=\left[p_{b,0}\left(e^{-\beta V(x)}+\beta V(x)-1\right)+n_{b,0}\left(e^{\beta V(x)}-\beta V(x)-1\right)\right]^{\frac{1}{2}} \qquad \text{(A100)}$$

Electric Field and Charge at the Surface

Equilibrium Conditions

The equilibrium electric field at the surface, $E_{s,0}$, can be obtained by using the voltage difference between the bulk and the surface, V_{bi}, in the equations presented above.

$$E_{s,0} = \pm\sqrt{\frac{2q}{\beta\kappa\varepsilon_0}} \cdot F(V_{bi}) \tag{A101}$$

By Gauss's law, the electric charge in the space charge region per unit area can be calculated.

$$Q_{s,0} = -\kappa\varepsilon_0 E_{s,0} = \mp\sqrt{\frac{2q\kappa\varepsilon_0}{\beta}} \cdot F(V_{bi}) \tag{A102}$$

The equilibrium surface charge, $Q_{s,0}$, is in C cm^{-2} and represents the total charge integrated from the bulk to the surface within a given surface area volume. The positive and negative signs have switched relative to the electric field. For a relatively large positive built-in voltage, $V_{bi} >> 0$, the exponential term representing the electron concentration dominates the equation, and a large electron concentration within the space charge region would lead to a net negative charge. For a large negative built-in voltage, $V_{bi} << 0$, the bands bend up and the exponential term representing the hole concentration dominates the equation. In this case, the large hole concentration within the depletion region leads to a positive total charge.

Non-Equilibrium Conditions

Under illumination or the application of a bias, the voltage difference between the surface and the bulk changes, and V_{bi} is no longer adequate. The voltage, V_s, is defined as the voltage difference between the surface and the bulk away from equilibrium. Interestingly, the type of perturbation, light pulse or bias application, may or may not change the total charge even if the band bending changes. A light pulse generates equal numbers of electrons and holes so that the net total charge does not change. The application of a bias injects more majority carriers into the semiconductor, which changes the net charge. The electric field, E_s, and surface charge, Q_s, away from equilibrium are described in a similar method using V_s instead of V_{bi}.

$$E_s = \pm\sqrt{\frac{2q}{\beta\kappa\varepsilon_0}} \cdot F(V_s) \tag{A103}$$

$$Q_s = -\kappa\varepsilon_0 E_s = \mp\sqrt{\frac{2q\kappa\varepsilon_0}{\beta}} \cdot F(V_s) \tag{A104}$$

Charge Necessary for Inversion

It is possible to calculate the total charge, Q_i, necessary to reach the onset of strong inversion. Strong inversion is defined as the point where the surface minority concentration is equal to the bulk majority concentration, *i.e.*, for *n*-type this is where $p_0(x) = n_{s,0}$. The potential necessary to reach strong inversion, V_i, is:

$$V_i = 2\frac{kT}{q}\ln\left(\frac{N_B}{n_i}\right). \tag{A105}$$

In this expression, n_i is the intrinsic carrier concentration, and N_B represents a generalized dopant density that could be either N_D or N_A. To calculate the total charge necessary to reach the onset of strong inversion, V_i can be substituted into equation A99 for the electric field.

$$Q_i = \mp\sqrt{\frac{2q\kappa\varepsilon_0}{\beta}} \cdot F(V_i) \tag{A106}$$

Differential Capacitance

The differential capacitance at the surface of a semiconductor, C_D, is defined as the differential change in charge at the surface, Q_s, with voltage dropped across the semiconductor surface, V_s. Since the differential capacitance can be measured away from equilibrium it is necessary to use V_s.

$$C_D \equiv \frac{dQ_s}{dV_s} = \frac{d}{dV_s} \cdot \left[\mp\sqrt{\frac{2q\kappa\varepsilon_0}{\beta}} \cdot F(V_s)\right] \tag{A107}$$

C_D is an *area-normalized* capacitance and has units of F cm^{-2}. To obtain an expression for C_D, it is necessary to differentiate the expression for Q_s with respect to V_s. This can be started by first deriving the function F(V_s) vs. V_s.

$$\frac{dF(V_s)}{dV_s} = \frac{d}{dV_s}\left[p_{b,0}\left(e^{-\beta V_s} + \beta V_s - 1\right) + n_{b,0}\left(e^{\beta V_s} - \beta V_s - 1\right)\right]^{\frac{1}{2}} \tag{A108}$$

Using the chain rule this becomes:

$$\frac{dF(V_s)}{dV_s} = \left(-\frac{1}{2}\right)\frac{\frac{d}{dV_s}\left[p_{b,0}\left(e^{-\beta V_s} + \beta V_s - 1\right) + n_{b,0}\left(e^{\beta V_s} - \beta V_s - 1\right)\right]}{F(V_s)} \tag{A109}$$

$$\frac{dF(V_s)}{dV_s} = \left(-\frac{1}{2}\right)\frac{\left[p_{b,0}\left(\beta - \beta e^{-\beta V_s}\right) + n_{b,0}\left(\beta e^{\beta V_s} - \beta\right)\right]}{F(V_s)} \quad . \tag{A110}$$

Plugging this expression into the definition of the differential capacitance gives:

$$C_D \equiv \frac{dQ_s}{dV_s} = \pm\sqrt{\frac{q\beta\kappa\varepsilon_0}{2}} \cdot \frac{\left[p_{b,0}\left(1 - e^{-\beta V_s}\right) + n_{b,0}\left(e^{\beta V_s} - 1\right)\right]}{F(V_s)} \, . \tag{A111}$$

This expression for the differential capacitance holds for a semiconductor in accumulation, depletion, or inversion since its derivation stemmed from the charge density equation that included contributions from electrons, holes, and dopants of either type.

This is a very important equation for the work in this thesis and will be analyzed in more detail in the subsequent sections.

Differential Capacitance for Specific Dopant Types

The expression for the differential capacitance can be made specific for *n*-type and *p*-type electrodes as shown above for the electric field and surface charge equations. For an *n*-type electrode, $n_{b,0}$ is factored out of the numerator, $\sqrt{n_{s,0}}$ is factored out of the denominator, and the equation is simplified to include $L_{D,n}$, the extrinsic Debye length for electrons.

$$C_{D,n} \equiv \frac{dQ_s}{dV_s} = \pm\frac{\kappa\varepsilon_0}{\sqrt{2} \cdot L_{D,n}} \cdot \frac{\left[\frac{p_{b,0}}{n_{b,0}}\left(1 - e^{-\beta V_s}\right) + \left(e^{\beta V_s} - 1\right)\right]}{F_n(V_s)} \tag{A112}$$

$$F_n(V_s) = \frac{F(V_s)}{\sqrt{n_{s,0}}} \tag{A113}$$

A similar technique allows the differential capacitance for *p*-type semiconductors to be written as shown below.

$$C_{D,p} \equiv \frac{dQ_s}{dV_s} = \pm \frac{\kappa\varepsilon_0}{\sqrt{2} \cdot L_{D,p}} \cdot \frac{\left[\left(1 - e^{-\beta V_s}\right) + \frac{n_{b,0}}{p_{b,0}}\left(e^{\beta V_s} - 1\right)\right]}{F_p(V_s)} \tag{A114}$$

$$F_p(V_s) = \frac{F(V_s)}{\sqrt{p_{s,0}}} \tag{A115}$$

The equation for the space charge capacitance for the *p*-type electrode is presented as such in the text *Physics of Semiconductor Devices* by Sze.

From these very important equation, the space charge capacitance over a wide range of potentials can be calculated. Alternatively, from a measured capacitance, a set of potential values can be numerically evaluated using Mathematica, or any other analysis program, that would be consistent with this observed capacitance. This was done in Chapters 2 and 3, where open-circuit frequency analysis was used to obtain a differential capacitance, and the voltage values necessary to obtain this differential capacitance were numerically evaluated using Mathematica. In general there are always at least 2 voltage values that can lead to a given differential capacitance. This is because the differential capacitance is simply the small change in charge (general to positive and negative charge) with a small change in voltage and either electrons or holes can be responsible for this differential charge. The same magnitude of a measured capacitance can be obtained from either a certain electron or a certain hole concentration. Meaning that at low enough frequencies (for reasons discussed later), a capacitance of 100 nF cm^{-2} can be obtained from either an accumulation layer or an inversion layer. As written these equations imply that positive and negative capacitances can be observed, based on the ±

sign in front of the equation. This is of course not the case since an observed capacitance is always positive; the ± sign in these equations are preserved to allow correlation with the ± sign of the surface charge, Q_s. During numerical fitting, the ± sign is *absolutely critical* in correctly calculating the potentials necessary to obtain a given capacitance from either an accumulation condition or an inversion or depletion condition.

Frequency Response of the Differential Capacitance

As written, the equation for the space charge capacitance does not explicitly demonstrate any frequency dependence. This is because the equation for the differential capacitance does not include any time dependence, nor does it describe the mechanisms for changes induced by any perturbations that *may be* time dependent. The mathematical introduction of time-dependent parameters into the expression for C_D is not performed here. Instead, qualitative changes and mechanism are discussed to address the frequency dependence of C_D.

The equation for C_D is included again for the sake of discussion.

$$C_D \equiv \frac{dQ_s}{dV_s} = \pm\sqrt{\frac{q\beta\kappa\varepsilon_0}{2}} \cdot \frac{\left[p_{b,0}\left(1 - e^{-\beta V_s}\right) + n_{b,0}\left(e^{\beta V_s} - 1\right)\right]}{F(V_s)} \tag{A111}$$

The exponential terms in this expression arise from the mobile charge carriers; specifically, the $e^{-\beta V_s}$ terms are due to holes while the $e^{\beta V_s}$ terms are due to electrons. The differential capacitance is defined as the change in charge with surface voltage, which implies that a voltage change must be slow enough for the mobile charge carriers to respond. It's easy to imagine that the majority carriers can respond to the excitation frequency since they carry the current that establishes voltage difference. However, for the minority carriers to be able to adequately contribute to the differential capacitance, they must be able to respond to the excitation frequency. This is more difficult because, while the current is carried by majority carriers, the minority carriers can only respond to a voltage perturbation through indirect mechanisms, such as recombination-generation or bulk-diffusion mechanisms.

For example, consider an *n*-type electrode under inversion at equilibrium, $V_{bi} << 0$. The surface hole concentration is very high, and the differential capacitance is expected to be dominated by the $e^{-\beta V_s}$ term. This is indeed the case for a slow differential change in voltage, *i.e.*, for frequencies less than a few Hertz, because, even though the perturbation current is carried by electrons, the holes can respond through a recombination-generation mechanism on this time scale. For faster perturbation voltages, the holes can no longer respond at that frequency since the recombination-generation rates are slower than the oscillation period of the voltage perturbation. In this case, the hole concentration remains constant throughout the perturbation and does not contribute *at all* to the differential capacitance.

The observed differential capacitance thus depends on frequency. In fact, as written, the equation for C_D only holds at low frequencies. At higher frequencies, the terms involving minority carrier terms should be set to zero.

Further Simplifications: The Mott-Schottky Equation

Under a certain set of conditions, the equation for the differential capacitance, C_D, can be drastically simplified. Mott-Schottky analysis typically involves the application of a high frequency, 100 Hz to 100 kHz, small signal (10 mV) excitation to probe the differential capacitance at different dc biases where the semiconductor is under depletion or inversion conditions. These conditions lead to a drastic simplification of the differential capacitance as outlined below. The full expression for C_D is given below for reference.

$$C_D = \pm\sqrt{\frac{q\beta\kappa\varepsilon_0}{2}} \cdot \frac{\left[p_{b,0}\left(1 - e^{-\beta V_s}\right) + n_{b,0}\left(e^{\beta V_s} - 1\right)\right]}{\left[p_{b,0}\left(e^{-\beta V_s} + \beta V_s - 1\right) + n_{b,0}\left(e^{\beta V_s} - \beta V_s - 1\right)\right]^{\frac{1}{2}}} \tag{A116}$$

Let us consider an *n*-type electrode for example. It has been demonstrated in the previous section that minority carriers will not contribute to C_D at the high frequencies used in Mott-Schottky analysis. (This assumption is, of course, dependent on the fact that the surface and bulk recombination rates are slow enough that the minority carriers can not respond at these frequencies. For the silicon samples and contacts used in this work, this is a good assumption, but for bulk materials or surfaces that exhibit high recombination rates, this may not be the case.) For this reason we can immediately eliminate the terms arising from the hole concentration as shown below.

$$n\text{-type:} \quad C_D = \pm\sqrt{\frac{q\beta\kappa\varepsilon_0}{2}} \cdot \frac{\left[p_{b,0} + n_{b,0}\left(e^{\beta V_s} - 1\right)\right]}{\left[p_{b,0}\left(\beta V_s\right) + n_{b,0}\left(e^{\beta V_s} - \beta V_s - 1\right)\right]^{\frac{1}{2}}} \tag{A117}$$

If our *n*-type sample is only doped with donors and there are no acceptors atoms in the bulk, the terms originating from N_A can be eliminated. The $n_{b,0}$ term can also be replaced by the donor density, N_D, as shown below.

$$n\text{-type:} \quad C_D = \pm\sqrt{\frac{q\beta\kappa\varepsilon_0}{2}} \cdot \frac{\left[N_D^+\left(e^{\beta V_s} - 1\right)\right]}{\left[N_D^+\left(e^{\beta V_s} - \beta V_s - 1\right)\right]^{\frac{1}{2}}} \tag{A118}$$

Finally, since Mott-Schottky analysis is performed under reverse bias or inversion conditions for the *n*-type electrode, $V_s << 0$ and the exponential terms corresponding to the electron concentration are negligible. Since $V_s << 0$, the negative sign in ± term is used, which cancels with the negative sign in the numerator. The expression for C_D now becomes:

$$n\text{-type:} \qquad C_D = \sqrt{\frac{q\beta\kappa\varepsilon_0}{2}} \cdot \frac{N_D^+}{\left[N_D^+(-\beta V_s - 1)\right]^{\frac{1}{2}}} = \sqrt{\frac{q\beta\kappa\varepsilon_0 N_D^+}{2(-\beta V_s - 1)}}\,. \qquad \text{(A119)}$$

This expression can be rearranged as follows.

$$n\text{-type:} \qquad \frac{1}{C_D^2} = \frac{2}{q\kappa\varepsilon_0 N_D^+}\left(-V_s - \frac{1}{\beta}\right) \qquad \text{(A120)}$$

The form of this expression indicates that only the charges due to the ionized donors, and the small contribution of thermalized electrons near the interface of the depletion region and the bulk, account for the differential capacitance.

As mentioned before, V_s is the nonequilibrium voltage difference between the surface and the bulk, which can be described in terms of an equilibrium voltage, V_{bi}, and an applied bias, V_{app}, in the following manner.

$$V_s = V_{bi} - V_{app} \qquad \text{(A121)}$$

The sign convention for these voltages is kind of tricky. For an *n*-type semiconductor under depletion conditions at equilibrium, the built in voltage is negative: $V_{bi} < 0$. And under no applied bias, $V_s = V_{bi}$ as demonstrated in the above equation. Application of a positive bias, $V_{app} > 0$, to the equilibrium condition acts to bend the bands farther so that the potential difference between the surface and bulk is now larger and more negative: $V_s < V_{bi}$ but $|V_s| > |V_{bi}|$. This requires that V_{app} is subtracted from V_{bi} as shown. Substituting this expression for V_s into the rearranged expression for the differential capacitance gives the familiar Mott-Schottky equation for an *n*-type electrode.

$$n\text{-type:} \qquad \frac{1}{C_D^2} = \frac{2}{q\kappa\varepsilon_0 N_D^+}\left(V_{app} - V_{bi} - \frac{kT}{q}\right) \tag{A122}$$

The same analysis can be applied towards the derivation of the Mott-Schottky equation for a *p*-type electrode. In this case, all terms involving $n_{b,0}$ can be neglected, the $e^{-\beta V_s}$ terms can be ignored in depletion, and $p_{b,0}$ can be set equal to N_A.

$$p\text{-type:} \qquad C_D = \pm\sqrt{\frac{q\beta\kappa\varepsilon_0 N_A^-}{2(\beta V_s - 1)}} \tag{A123}$$

A similar rearrangement can be performed and the equation for V_s can be used to obtain the final expression.

$$p\text{-type:} \qquad \frac{1}{C_D^2} = \frac{2}{q\kappa\varepsilon_0 N_A^-}\left(-V_{app} + V_{bi} - \frac{kT}{q}\right) \tag{A124}$$

By plotting C_D^{-2} vs. V_{app}, the built-in voltage, V_{bi}, can be obtained from the *x*-intercept. Analysis of the slope will lead to the dopant density, which should be verified using a four-point probe technique for reasons discussed in the next section.

Complications of Mott-Schottky Analysis

The Mott-Schottky equation, shown in equation 1a for an *n*-type semiconductor and in equation 1b for a *p*-type semiconductor, was used to determine the flatband potential of a given semiconductor/liquid contact.

$$n\text{-type:} \qquad C_{SC}^{-2} = \frac{2}{q\kappa\varepsilon_o A^2 N_D^+}\left(E_{app} - E_{fb} - \frac{kT}{q}\right) \tag{1a}$$

$$p\text{-type:} \qquad C_{SC}^{-2} = \frac{2}{q\kappa\varepsilon_o A^2 N_A^-}\left(-E_{app} + E_{fb} - \frac{kT}{q}\right) \tag{1b}$$

C_{SC} is the space charge capacitance of the silicon near the surface, κ is the relative permittivity of silicon, ε_0 is the permittivity of vacuum, N_D^+ and N_A^- represent the ionized dopant densities of *n*-type and *p*-type silicon respectively, A is the interfacial area, E_{app} is the applied bias, E_{fb} is the flat band voltage, and kT/q represents the thermal energy. Mott-Schottky analysis must be performed under reverse bias conditions so that the space charge capacitance dominates over the Helmholtz capacitance of the solution. As mentioned in the introduction, the reverse bias region for *n*-type silicon could involve etching or oxidation. This changing surface condition may generate electrical states within the band gap and, if those states are charged, they would change the effective total charge in the depletion region. The Mott-Schottky equation in the presence of charged trap states is shown in equations 2a and 2b.

$$n\text{-type:} \qquad C_{SC}^{-2} = \frac{2}{q\kappa\varepsilon_o A^2 \left(N_D^+ + N_T(E_{app})\right)}\left(E_{app} - E_{fb} - \frac{kT}{q}\right) \tag{2a}$$

$$p\text{-type:} \qquad C_{SC}^{-2} = \frac{2}{q\kappa\varepsilon_o A^2 \left(N_A^- + N_T(E_{app})\right)}\left(-E_{app} + E_{fb} - \frac{kT}{q}\right) \tag{2b}$$

$N_T(E_{app})$ is the applied bias-dependent charged trap state density. The trap state density is allowed to be dependent on the applied bias because the electron occupation of a trap state, and hence its charge, may change as the Fermi level is moved. $N_T(E_{app})$ may also be of either sign, for example, positively charged trap states will add to N_D^+, but negatively charged trap states will subtract from N_D^+. Thus, charged trap states can either increase or decrease the slope of a Mott-Schottky plot. Since q, κ, and ε_0 are known constants and the area and dopant density can be measured, a theoretical slope in the absence of trap states can be calculated and compared to the experimental slope to assess the presence or generation of charged surface trap states during the reverse bias measurement. The presence of such trap states could cause Fermi-level pinning, which would obscure the extrapolation to an equilibrium flatband potential.

Surface trap states can also lead to frequency dispersion of the measured space charge capacitance. The capacitance at a certain applied bias may change with frequency if trap states are present that have a resonance within the frequency range. At high frequency, the excitation is too fast to fill and unfill traps, but at lower frequencies the trap can be filled and unfilled, which adds to the measured differential capacitance.

Measuring and Fitting Impedance Data

Impedance spectra, obtained from Mott-Schottky analysis or from open-circuit frequency spectra which are measured over a larger range of frequencies, are typically fit to a simple 3-element model circuit for the space charge region, which consists of a resistor in series with a parallel combination of a resistor and a capacitor. To address the possibility of frequency-dependent trap states, the impedance spectra presented in this thesis were also fit to a similar 3-element equivalent circuit except that the pure capacitor is exchanged for a constant phase element (CPE). The physical nature of the CPE is still not well understood, but it is often ascribed to a distribution of time constants that can arise from surface roughness, a distribution of reaction rates, a distribution of surface adsorbed charge, or the presence of electrical traps states. The CPE is nevertheless used since it allows for a frequency dependence of the parallel capacitance. The equations for the impedance of a pure capacitor, Z_C, and CPE, Z_{CPE}, are given in equation 3.

$$Z_C = \frac{1}{Cj\omega}, \qquad Z_{CPE} = \frac{1}{CPE_T\left(j\omega\right)^{CPE_P}} \tag{3}$$

When the CPE_P value is equal to unity, the equation for the impedance of a CPE equals that for a pure capacitor, and, in this case only, $CPE_T = C$. When the CPE_P value is anything but unity, the CPE_P term must also include fractional units of time, specifically sec$^{(1\text{-CPE-P})}$, to make up for the fractional time units that the $j\omega$ term lacks, and thus this term no longer represents a real capacitance. Due to this, the impedance data were always fit to the pure capacitor-containing 3-element circuit to extract the parallel capacitance, while the 3-element CPE-containing circuit was used only to assess the ideality of the previous fit by examining the CPE_P value.

The capacitance values obtained from this 3-element fit correspond to either the Helmholtz capacitance, the space charge capacitance of the semiconductor, or the capacitance of a grown oxide layer. (The measured capacitance might also be convoluted with a trap state capacitance; the CPE_P value will identify the extent of frequency dispersion that might be the result of trap states.) Helmholtz layer capacitances are typically on the order of μF cm^{-2}, oxide capacitances will vary depending on the thickness of the oxide, and semiconductor space charge capacitance values, for depletion conditions or inversion conditions measured at high frequencies, are on the order of 10 nF cm^{-2}. The thickness of the oxide or space charge region can be calculated by using the equation for a capacitor, where A is the area, κ is the relative dielectric, ε_0 is the permittivity of free space, and d is the thickness.

$$C = \frac{\kappa \varepsilon_0 A}{d} \tag{4}$$

Appendix C: Description of RF Contactless Photoconductivity Apparatus

The rf photoconductivity apparatus is comprised of two separate systems: a pulsed laser system necessary to generate the excess carriers within the silicon sample, and a radio frequency magnetic induction system necessary to transiently measure the conductivity of the sample as these excess carriers recombine.

A. The Laser System

A Nd:YAG laser (Spectra-Physics INDI-30, 1064 nm) is used to generate 10 ns optical pulses operating at a repetition rate of 10 Hz. (Considering that the bulk lifetime of the silicon, and hence the maximum observable recombination lifetime, is on the order of 3-6 ms, the 10 Hz repetition rate is more than sufficient to ensure that the carrier concentration has completely returned to its equilibrium dark values before the next laser pulse arrives.) The power density of the beam is attenuated using three beam splitters, and the desired optical intensity is fine tuned using various neutral density filters, the transmittance of which have been measured at 1064 nm using a UV-vis spectrometer for calibration. Laser pulses were further manipulated by expansion to approximately 2 cm^2 in diameter using a Galilean beam expander, and a spatially uniform beam profile was produced on the silicon substrates by placing a holographic diffuser (Coherent, 1^o) directly above the sample. The incident beam power, in the absence of the neutral density filters was determined directly above the Si samples using a power meter

(Coherent Fieldmaster GS) that was equipped with a pyroelectric sensor (Coherent LM-P10i). The neutral density filters were then used to attenuate the measured light power to either 7×10^{-4} mJ cm^{-2} pulse^{-1} for high-level injection conditions or to 1.3×10^{-6} mJ cm^{-2} pulse^{-1} for low-level injection conditions. In calculating the injected charge carrier densities from these light intensities, corrections for the reflectivity of silicon at 1064 nm, as well as the total optical absorption over the thickness of the sample based on the optical absorption length at 1064 nm were considered. In the case of solution contacts, UV-vis absorption at 1064 nm was also considered, however the unknown absorption length of the solution on top of the silicon presented some errors in an accurate calculation. After the injected carriers had spread throughout the 190–500 μm thick Si samples, these power densities produced photogenerated carrier concentrations around 2×10^{14} carriers cm^{-3} pulse^{-1} at high-level injection conditions or 5×10^{11} carriers cm^{-3} pulse^{-1} at low-level injection conditions.

B. The Radio-Frequency System

General Description and Basic Principles

The electromagnetic principles of the contactless rf photoconductivity system are similar to those used in eddy current detection techniques, such as metal detectors or in the non-destructive evaluation of metal parts. In these systems, detection occurs because a magnetic field, emanating from a coil positioned close to the sample, interacts with the mobile charge carriers (electron and holes) and forces them to move in circular “eddy” currents. These circular eddy currents generate their own magnetic field that opposes that generated by the coil, and the net result is a back electromotive force (EMF) generated in the coil. In the absence of a conductive sample, the back EMF of the coil is determined only by its self inductance. In the presence of a conductive sample, mobile charge carriers can generate a significantly stronger back EMF, and the magnitude of this EMF is proportional to the conductivity of the sample. The detection of the transient conductivity of a semiconductor sample after a light pulse is then based on the transient change in back EMF that is generated in the coil. (*In this manner the coil and the sample act as the primary and secondary circuits of a transformer, except in this case the magnetic flux connecting the two circuits occurs through free space, rather than through the magnetic core of a transformer.*)

Mobile charge carriers within a sample are theoretically able to move in circular eddy currents at any frequency up to their drift velocity (hence this is a non-resonance process), but radio frequencies are used in this system for various optimization reasons. First, the very low oscillation period (~ 2 ns) of the radio frequencies in the 400–500 MHz range prevents the carriers from being significant displaced before the magnetic field switches direction. If significantly lower frequencies were used, carrier polarization over the macroscopic size of the sample could occur and lead to signal saturation. Secondly, for detection reasons, the period of the rf oscillation must be significantly shorter than both the transient decay lifetime of the silicon sample and the resonant discharge time of the tank circuit.

The penetration of the oscillating magnetic field within the sample is also of interest. As opposed to eddy current detection in metallic samples, where the magnetic field is entirely absorbed within the thickness of the metallic samples, a linear response with conductivity, as desired for the transient detection of semiconductor conductivity, requires that only a small fraction of the magnetic field is absorbed by the entire sample. The screening length, δ, of an oscillation frequency, f, for a sample characterized by a permeability, μ, and conductivity, σ, is described below.

$$\delta = \frac{1}{\sqrt{\pi f \mu \sigma}} \tag{A125}$$

For a 450 MHz oscillation frequency, a screening length for lightly doped silicon ($N_D = 10^{13}$ cm^{-3}), such as those used in the photoconductivity decay studies, is approximately 50 mm in the dark. Even under a high-level injection condition of $\Delta n = \Delta p = 10^{15}$ cm^{-3}, the screening length is 5 mm. In all cases, the screening length is significantly longer than the sample thickness (200 – 500 μm) so that a linear response is still assumed. While these calculations suggest that a linear correlation between the magnetic response and the conductivity will apply, linearity of the signal with conductivity can be checked by observing the peak signal voltage over a range of known injection levels attenuated by the addition of various neutral density filters in the beam path.

RF Components

The electrical schematic for the rf system is described in Figure 52. Radio frequency signals between 400–500 MHz are generated by either Wavetek 2500A or Rohde & Schwarz SMY01 signal generator. The output of the frequency generator is connected to a power splitter (Mini-Circuits ZSC2-1W), with one output of the power splitter connected through an amplifier (ANZAC AM-147, +17 dB gain) and a phase-shifter (General Radio 847-LTL) to the local oscillator (LO) input of a double-balanced frequency mixer (Mini Circuits ZAY-2). The other output of the power splitter is connected through an amplifier (Mini-Circuits ZHL-1A, +20 dB gain) to the coupled port

(CPL) of a directional coupler (Merrimac CR-20-500, 20 dB isolation). Radio frequencies entering the CPL port are attenuated significantly and emerge from the IN port of the directional coupler and propagate towards the front end, which is composed of a tunable LC circuit consisting of a variable matching capacitor (1-11 pF, quartz) in electrical parallel with a series combination of a variable coupling capacitor (1-11 pF, air gap) and a 1- to 3-turn coil (Cu wire, 1.1 mm diameter) placed in close proximity to the sample. The other end of each leg of this parallel network is connected to instrument ground through the coax cable shielding. The matching capacitor is separated by the coupling capacitor, the coil, and the sample by a λ/2 (22 cm) length of 50 Ohm cabling. This specific length of cable (λ/2) does not affect the circuit properties of the front end (as demonstrated by transmission line analysis), but provides a physical separation between the circuit elements so that the capacitance of a user's hand does not significantly interfere with tuning of the circuit elements. The frequency of the rf generator and the matching capacitor are subsequently tuned so that the front end, when in the presence of a semiconductor sample in the dark, is in resonance. At the resonant frequency all power is delivered to instrument ground and no rf radiation is reflected back to the IN port of the directional coupler. (Tuning is performed by minimizing the voltage emerging from the OUT port of the directional coupler as monitored using a separate high-frequency digital oscilloscope, Tektronix TDS-680c.) The increase in conductivity of the silicon sample directly after a light pulse changes the impedance of the front end, through a change in the induced EMF of the coil, and a significant fraction of the rf radiation is reflected from the front end, enters the IN port of the directional coupler, and emerges from the OUT port. As the conductivity of the silicon decreases during the decay, the amplitude of the reflected signal also decays. When the conductivity of the silicon sample returns to its equilibrium dark value, the front end regains tune and no reflected power is observed. The transient reflected signal, emerging from the OUT port of the directional coupler, is connected through an attenuator (Kay 0/400A, 0 to –13 dB) to the radio frequency (RF) port of the double-balanced frequency mixer. The attenuator is used to ensure that the amplitude of the LO input remains larger than the amplitude of the RF input as required for proper functionality of the mixer. Because the RF and LO ports of the mixer see the same frequency, one output from the mixer is a dc signal that is proportional to the amplitude and phase difference between the reference signal and the signal reflected from the front end. This dc output is then displayed on a digital oscilloscope (Tektronix TDS-210) for measurement of the photoconductivity decay profiles.

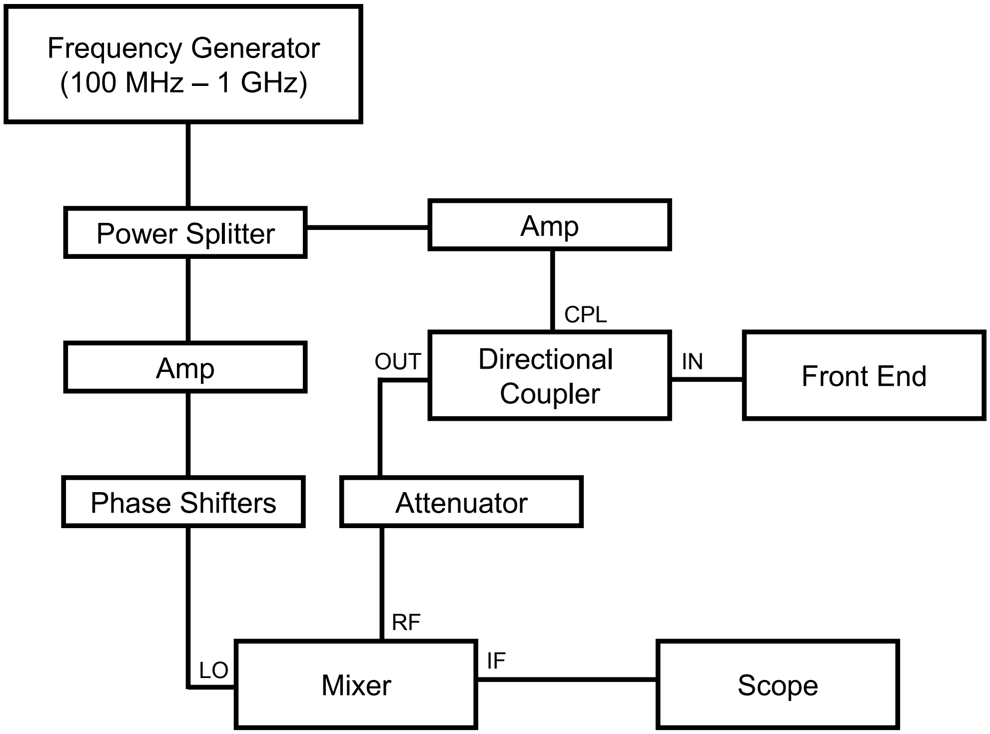

Figure 52: Electronic schematic for the rf system.

Sample Measurement

Samples are typically placed into sealed glass vessels or are encased between polystyrene petridishes that enable collection of rf conductivity decay measurements for that sample in contact with either N_2(g), air, or various liquid solutions. Data are recorded within 20 min of exposure to the ambient of interest, and the photoconductivity decays are typically stable over at least a 30 min period of data collection. Both sides of the semiconductor sample are exposed during etching and during contact with the electrolyte solutions, and both sides are therefore active surfaces for recombination during the lifetime measurements. Lifetimes for individual samples are obtained by averaging 128 signal decays for each experiment. Most rf decay signals are well-fitted by single exponential decays.

Factors Complicating Measurement

Since the rf photoconductivity technique is based on magnetic induction between the coil and any conductive material, the signal strength can be significantly decreased for silicon samples in the presence of any other conductive material. Ideally the dark conductivity of the entire system is very low so that the light pulse generates a significant change in the conductivity. This requires that the silicon samples used for this technique are low doped (typically with $N_D = 10^{13}$ cm^{-3}) so that reasonable injection levels $\Delta n = \Delta p = 10^{12}$–$10^{15}$ cm^{-3} can be employed without the possibility of Auger recombination dominating the decay kinetics. Higher doped silicon samples start with a higher dark conductivity and require a higher light pulse intensity to achieve the same relative change in photoconductivity. Even if low doped silicon samples are used, the dark conductivity of the entire system my be considerably higher if, for example, there exists any of the following within the magnetic field lines of the coil: thin metallic overlayers, patterned metallic regions, regions of higher doping within the sample, or conductive electrolyte solutions. The use of conductive electrolyte liquid contacts in the thesis presented a significant signal to noise problem. The conductivities of the 40% NH_4F, buffered HF, and 48% HF solutions were particularly high and relatively noisy decay profiles were obtained that required substantial signal averaging techniques. In the case of these etching solutions, UV-vis analysis demonstrated that the solutions were not absorbing a significant amount of the laser power. Instead the loss in signal most comes from an increased dark conductivity of silicon/liquid system as probed by the coil. To test this, the signal strength was measured for silicon in contact with solutions of various NaCl concentration. In this study, the lifetimes of the decay were not important, but the voltage amplitude of the decay profile was recorded. The data in Figure 53 demonstrate that the loss in signal correlates well with the conductivity of the solution contact and is relatively independent of the excitation frequency used. Because the signal strength for each silicon/liquid contact is relatively independent of excitation frequency, the loss mechanism is non-resonant and consistent with a loss due to solution conductivity.

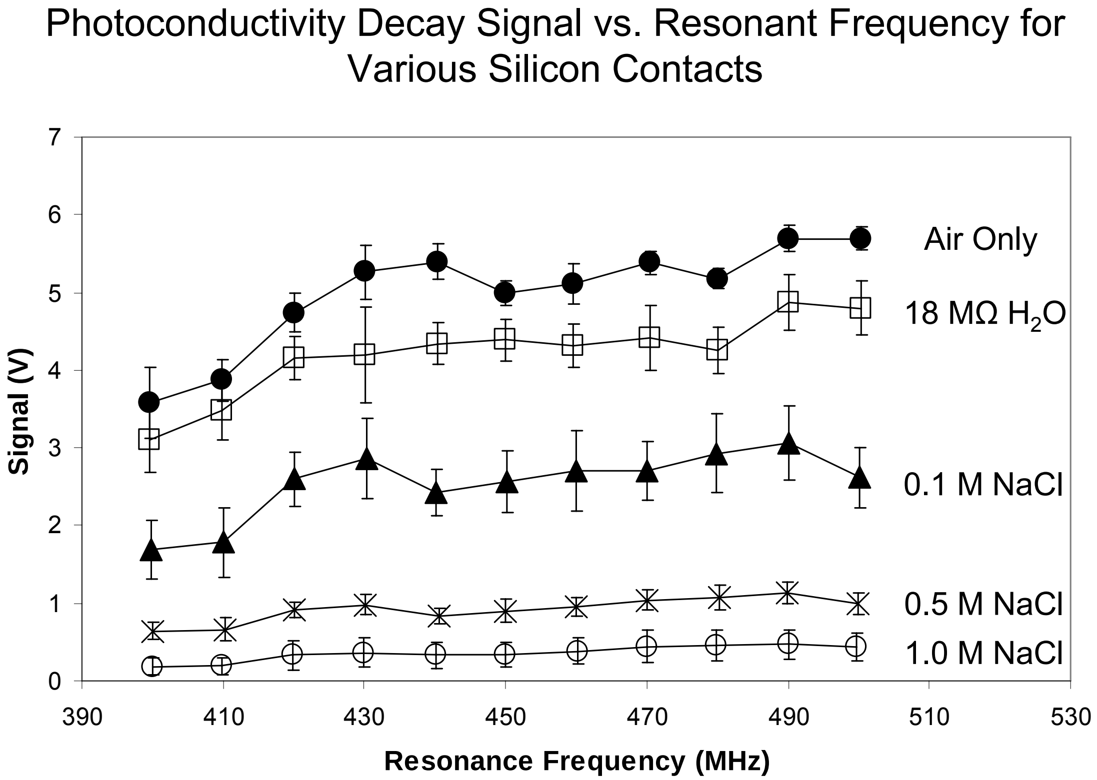

Figure 53: The amplitude of the photoconductivity decay vs. excitation frequency for various silicon/liquid contacts.

The photoconductivity decay amplitude (signal) is also plotted versus NaCl concentration over a wider range of concentrations in Figure 54. The data are presented for two different excitation frequencies, which display the same results within the experimental error. There is a clear screening of the signal due to the conductivity of the NaCl solution.

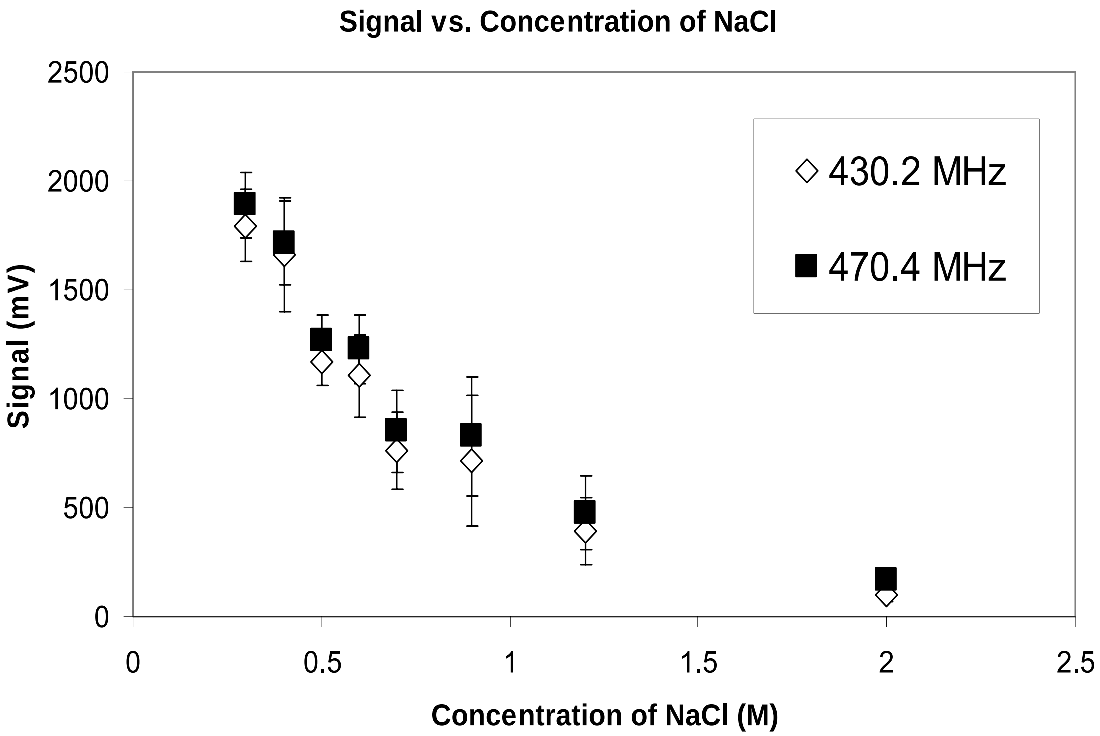

Figure 54: The amplitude of the photoconductivity decay is plotted vs. NaCl concentration.

These results highlight the importance of the entire system being studied; any conductive material will add to the dark conductivity and decrease the photoconductivity decay amplitude. For the NaCl concentrations used in this study, high-level injection conditions were used as no detectable signal from low-level injection conditions could be obtained. For the measurement of many conductive solution contacts performed in this thesis, such as the 40% NH_4F, buffered HF, and 48% HF contacts, a specially-designed cell was needed to simultaneously place the silicon sample as close to the coil as possible and also minimize, but not exclude, the amount of liquid contained on either side of the sample. Because the rf radiation penetrates entirely through the Si sample, as necessary for a linear response as defined above, a significant reservoir of liquid on the opposite of the sample with respect to the rf coil can still significantly reduce the photoconductivity decay amplitude.

Appendix D: Detailed Description of the FTIR Procedures

Transmission mode experiments on functionalized silicon surfaces are quite difficult because the number of optical absorbers on a surface is very small (less than 2×10^{15} cm^{-2}). Because of this, several tricks must be employed to successfully implement transmission mode FTIR as a surface analysis technique.

For the most flexibility in terms of references, single beam spectra are recorded, and a desired absorbance spectrum is obtained by reprocessing a single beam spectrum with the desired reference spectrum, such as the native oxide surface or freshly etched hydrogen-terminated sample. Often it is necessary to reference a the single beam spectrum of a surface-functionalized sample to both the oxide and H-term surfaces, separately, so that the absorption modes associated with these reference spectra do not interfere with those of the sample spectrum.

While spectral manipulation can fix a lot of problems, it should be approached cautiously. It is far better to get the best raw spectra possible and make only minor changes thereafter, if needed.

Obtaining the Best Single Beam Spectra

While spectral subtractions of contaminants such as H_2O and CO_2 can be very handy, one should not rely on them solely. The best, lowest noise, spectral subtractions are obtained for those spectra that already have the smallest H_2O and CO_2 bands. To that end, it is important to generate the best and most reproducible original single beam spectra possible. Here are a few tips:

First, make sure that the nitrogen flow rate is as *constant* as possible. This won't solve all of your problems because if the humidity changes appreciably between single beam collections you'll still get changes. I used flow rates of $N_2(g)$ between 25 and 40 scfh. Remember that it is the difference in H_2O and CO_2 that matters, not the absolute values. This means that even if a reference spectrum was obtained with a low $N_2(g)$ purge rate, it is *not* better to obtain the sample spectrum with a higher purge rate; in fact it is better (for the sake of H_2O absorption) to use the same low flow rate of $N_2(g)$. Large differences in the purge rates will lead to large differences in the steady state concentrations of H_2O and CO_2 within the spectrometer bench and it is these differences that matter. In general, however, it is easier to obtain similar and low steady state values of these impurities at higher flow rates.

Second, use the best DTGS detector you can find. For whatever reason, the LN_2 cooled detectors (MCT-A or MCT-B) seem to perform inferior spectral subtractions. This is not just limited to the water region, I've noticed significant baseline shifting and wobbling across the whole spectral region.

Third, all regions of the sample holder must be *stable and immobile*. Small changes in the angle, tilt, and position of your sample can introduce non-negligible differences in phonon absorption bands, which will hamper attempts at understanding the low frequency region.

Fourth, I typically let samples purge in the closed sample compartment for 10 min after placement before the scans were obtained. This leads to slightly better resulting spectra.

Performing the H_2O and CO_2 Spectral Subtractions

Traces of water vapor and CO_2 become introduced into the sample chamber whenever samples are placed inside for measurement. While the bench is purged with nitrogen to remove both H_2O and CO_2, differences in the purge rate of nitrogen or amount of air introduced to the bench during sample placement can lead to differences in the total absorption of H_2O or CO_2 in the sample and background single beam spectra, which will show up as either positive or negative bands in the resulting absorption spectrum.

Ideally the best case is to have the changes in water and CO_2 be negligible between the two single beam spectra, but this can pose quite a problem for reactions as long as 24 hours to 6 days where the humidity or nitrogen flow rate can change. Even for two single beam spectra collected close in time, complete elimination of H_2O and CO_2 bands rarely occurs, and spectral subtractions may be necessary to observe peaks in this region.

Generating the H_2O and CO_2 Reference Spectra

First, appropriate spectra of H_2O only and CO_2 only must be generated that can be separately subtracted from the desired absorbance spectrum. In order to do this, 5 consecutive single beam spectra were obtained as usual but in the absence of a silicon sample in the beam path. The first spectrum is reprocessed with the fifth spectrum as a reference yielding an absorbance spectrum with positive water and CO_2 peaks. To generate the water spectrum, all regions except the water bands are replaced with a straight line that is then straightened and set to zero absorbance using the baseline correcting procedure in Ohmic. In generating this spectrum it is important to zoom in on the baseline to crop the water region at a value that is close to zero so no strange peaks appear at the end of the water region after subtraction. The CO_2 spectrum is generated in exactly the same way except that only the CO_2 stretching modes and bending modes are retained; all other regions are set equal to zero. The water and CO_2 regions are not baseline corrected, but are taken as is or fit to a linear baseline fit.

In some cases, a better water spectrum was obtained by placing a few drops of water were added to a small Petri dish to present a small vapor pressure of water within the sample holder region. This should be approached with caution because many of the components within the bench are sensitive to water and may fail if water contamination occurs. Addition of water to the sample holder should only be performed if the bench of the spectrometer is purged in parallel and separately from the sample holder region. The water vapor spectrum was then reprocessed with respect an $N_2(g)$ only purged spectrum to yield the H_2O vapor spectrum. This water spectrum can then be subtracted from the H_2O and CO_2 containing spectrum generated above. This is in fact better, because there are 4 small CO_2 modes around 3600 that can be seen if the water spectrum used for subtraction is good.

Performing the Spectral Subtraction

A raw absorption spectrum is improved first by subtracting the water and CO_2 bands. This is done in Ohmic by selecting both spectra (Ctrl+mouse click) and then selecting the *Spectral Math…* option under the *Process* menu. The spectrum first selected is named *A*, and the second spectrum selected, by pressing Ctrl+click, is spectrum *B*. The function $A - k*B$ was used to do the spectral subtraction and *k*, the multiplication factor, was adequately chosen in real time by observing the *Spectral Math Result* window.

It is very important that separate H_2O and CO_2 spectra be generated for each specific detector and that the H_2O, CO_2, and sample spectra are all obtained *with the exact same detector*. Each detector has small differences that can interfere with spectral subtractions.

Appendix E: Detailed Fabrication of the Channel Conductance Devices

The channel impedance devices were manufactured by Florian Gstrein using standard lithographic techniques. Both of us made the electrical connections and insulation necessary for device use and together we collected the data in various solutions. This Appendix details the fabrication technique Florian used (the details have been obtained from his thesis, personal communication, and examination of his notebook). In addition, the methods of data acquisition are discussed. The goal of this section is to describe the process in enough detail so that the manufacture of such devices can be reproduced if necessary. Recommendations for the conditions for doping were supplied by the Saint Gobain website and were used as a guide for the fabrication process.

Figure 9 depicts schematically the process used to fabricate the n^+-p-Si(111)-n^+ and p^+-n-Si(100)-p^+ devices. Test grade boron-doped p-Si(111) ± 4° wafers (University Wafer, Inc.) with a dopant density of 2×10^{15} cm^{-3}, and phosphorus doped n-Si(100) ± 0.5° wafers of dopant density of 1×10^{14} cm^{-3} were cleaned by sequential immersion in “RCA solutions” consisting of 4:1:1 H_2O:NH_4OH:H_2O_2 at 75 °C for 5 min, de-ionized water for 1 min, 50:1 H_2O:HF for 20 s, 4:1:1 H_2O:HCl:H_2O_2 at 75 °C for 5 min, and de-ionized water (1 min). The wafers were then blown dry with N_2(g). A thick oxide layer

(10 kÅ) was then grown on all wafers by a commercial foundry (Silicon Quest International Inc.) to provide an effective mask for phosphorous or boron doping.

To generate the desired oxide mask, the wafers were cut into 2 cm × 2 cm pieces and were baked on a digital hotplate or in a vacuum oven at 180 °C for 30 min to dry the wafers and improve adhesion of the photoresist. Wafers piece were allowed to cool for 5 min after baking before applying a thin layer of AZ 5214 E photoresist (Clariant) by spin coating at 4000 rpm for 60 sec. The pieces were subsequently pre-baked for 90 s at 95 °C on a hot plate. The photoresist-coated chips were exposed for 8 s to a UV light source (Karl Süss KSM mask aligner, 200 W Hg light bulb) through a glass mask (Microchrome Technology Inc., High Resolution UF Plate, Type 180B; patterns were defined using standard black and white photography), baked for 75 s at 105 °C, and subsequently flooded with UV light for 20 s. After the last exposure step, the samples were immersed in AZ 327 MIF developer (Clariant) for 30 s and were immersed in water for 2 min. The structure was then etched in buffered HF solution (Transene Co) for 10 min to remove the oxide layer. The photoresist was removed by sequential immersion in acetone (10 min), isopropanol (1 min), and RCA solutions, and the wafers were blown dry with N_2(g).

The exposed regions of the *p*-Si(111) were doped n^+-type for 60 min at 1000 °C under flowing N_2(g) (flow rate 1 liter per minute) in a tube furnace equipped with a quartz tube solely dedicated for this purpose. The polished side of the patterned Si wafers was situated 5 mm from the phosphorous diffusion source (Saint Gobain, Phosphorous planar diffusion source, Source type PH-1000N, lot#3082), which had been activated prior to the actual doping for at least 8 h at 1000 °C under flowing N_2(g) (flow rate:1 liter per minute) using Si dummy wafers to establish constant boundary conditions. After the doping process, the wafers were immersed sequentially in a phosphorous glass etch (10:1 H_2O:48% HF for 2 min) and in H_2O (2 min), and were then blown dry with N_2(g). Due to the high diffusion constant of phosphorous in Si, subsequent drive-in was not performed.

The exposed regions of the *n*-Si(100) were doped p^+-type for 60 min at 1100 °C under flowing N_2(g) in a separate tube from the one used for phosphorus diffusion. Again the polished front side of the wafer was held 5 mm from the boron nitride planar diffusion source (Carborundum, Source type BN-HT, lot # X59005), which had been activated by annealing at 400 °C for 1 hour in N_2(g), oxidizing at 950 °C in O_2(g) for 30 min, and finally stabilizing the source wafers at 1100 °C in N_2(g) for 6 hours. Samples were pushed in at 750 °C within 5 min to the center of the furnace, allowed to stabilize at 800 °C for 10 min, ramped up to 1100 °C at a rate of 10 °C min^{-1}, and soaked for 60 min at 1100 °C. The samples were then ramped down at a rate of 5 °C min^{-1} and recovered at 400 °C. After boron diffusion, the unreacted dopant glass was removed by a 2 min 10:1 H_2O:48% HF etch. The resulting insoluable silicon-boron (Si-B skin) phase was oxidized at 800 °C for 20 min in O_2(g) to form B_2O_3 and SiO_2 layers, which were subsequently etched off in a 10:1 H_2O:48% HF solution for 2 min.

The fabrication process was continued by photolithographically defining metal Ohmic contacts on the doped regions. To prevent leaking of the metal pads into the base material it was necessary to create the n^+ and p^+ source and channel regions wide enough so that the whole metal contact pad could be inside the source and drain. This was a modification on Laibinis' method. The metal contacts were 200 nm of Al alloyed with 1 wt% Si, and were deposited by means of a home-built rf-sputtering system. The photoresist was lifted off by sequential immersion in hot acetone (30 min; ultrasonic cleaning for 5 min) and isopropanol (5 min). The contacts were not annealed.

The wafers were glued to polycarbonate plates, and Ohmic contact to the Al metal pad was electrically contacted through very stiff, V-shaped pieces of piano wire (McMaster, 0.2 mm diameter). The piano wire clips were in electrical contact with brass screws, which were soldered to tinned copper wires. To avoid electrostatic discharge, the electrical assembly was performed on a grounded metal surface. The wafers and the 4 contacts were subsequently encapsulated in white epoxy (Loctite 1C Hysol Epoxi-Patch Adhesive) exposing the center channel and exposing only very small regions of the n^+- or p^+-doped source and drain regions adjacent to each side of the center channel. This exposure of a small part of the n^+- or p^+-doped regions was necessary to ensure complete liquid contact over the entire channel region. Measurements in contact with 18 M H_2SO_4(aq) required insulation with paraffin wax (Paxter household wax) instead of epoxy.

Working devices had a < 4 Ω resistance across a common phosphorous- or boron-doped contact (A to C or B to D in Figure 9) and showed a symmetrical double-diode behavior, with large (> 1 MΩ) low bias resistances, across the central channel (A+B to C+D in Figure 9). Impedance spectra were recorded with a Schlumberger Model 1260 frequency response analyzer (FRA), which was GBIB-controlled using the ZPlot Impedance Analyzer Software (Scribner Associates, Inc.). All contacts were grounded during the initialization sequence of the FRA. All experiments reported in this work were carried out inside a metal-mesh Faraday cage, in the dark, in unstirred solutions, and with minimal exposure to light while in solution.

To acquire an impedance spectrum, the contacts on a common junction were shorted together (A+C and B+D, Figure 9), and a sinusoidal 10 mV amplitude AC signal, with zero DC offset, ranging in frequency from 10^{-2}–10^{6} Hz was applied across the central channel of interest. Scans comprised of 10 steps per frequency decade, and 10-20 cycles at each frequency were collected to obtain a high confidence level for the measured impedance at each frequency.

Bibliography:

1. Sze, S. M., *Physics of Semiconductor Devices*. 2nd ed.; John Wiley & Sons: New York, 1981.
2. Shockley, W.; Read, W. T., *Physical Review* **1952,** 87, (5), 835-842.
3. Hall, R. N., *Physical Review* **1952,** 87, (2), 387.
4. Gstrein, F.; Michalak, D. J.; Royea, W. J.; Lewis, N. S., *J. Phys. Chem. B* **2002,** 106, (11), 2950-2961.
5. Solares, S. D.; Michalak, D. J.; Goddard, W. A.; Lewis, N. S., *J. Phys. Chem. B* **2006**, ASAP Web Release Date: 01-Apr-2006 (DOI: 10.1021/jp056796b).
6. Fonash, S. J., *Solar Cell Device Physics*. Academic: New York, 1981.
7. Green, M. A., *Appl. Phys. Lett.* **1978,** 33, (2), 178-180.
8. Lewis, N. S.; Rosenbluth, M. L., In *Photocatalysis: Fundamentals and Applications*, Serpone, N.; Pelizzetti, E., Eds. John Wiley & Sons: New York, 1989.
9. Yablonovitch, E.; Gmitter, T., *Appl. Phys. Lett.* **1986,** 49, (10), 587-589.
10. Royea, W. J.; Juang, A.; Lewis, N. S., *Appl. Phys. Lett.* **2000,** 77, (13), 1988-1990.
11. Forbes, M. D. E.; Lewis, N. S., *J. Am. Chem. Soc.* **1990,** 112, (9), 3682-3683.
12. Tan, M. X.; Kenyon, C. N.; Kruger, O.; Lewis, N. S., *J. Phys. Chem. B* **1997,** 101, (15), 2830-2839.
13. Tan, M. X.; Kenyon, C. N.; Lewis, N. S., *J. Phys. Chem.* **1994,** 98, (19), 4959-4962.
14. Reddy, A. J.; Burr, T. A.; Chan, J. K.; Norga, G. J.; Michel, J.; Kimerling, L. C., Silicon surface defects: The roles of passivation and surface contamination. In *Defects in Semiconductors - Icds-19, Pts 1-3*, Transtec Publications Ltd: Zurich-Uetikon, 1997; Vol. 258-2, pp 1719-1724.
15. Horanyi, T. S.; Pavelka, T.; Tutto, P., *Appl. Surf. Sci.* **1993,** 63, (1-4), 306-311.
16. Msaad, H.; Michel, J.; Lappe, J. J.; Kimerling, L. C., *J. Electron. Mater.* **1994,** 23, (5), 487-491.
17. Stephens, A. W.; Green, M. A., *J. Appl. Phys.* **1996,** 80, (7), 3897-3903.
18. Stephens, A. W.; Green, M. A., *Sol. Energy Mater. Sol. Cells* **1997,** 45, (3), 255-265.
19. Sekar, K.; Kuri, G.; Satyam, P. V.; Sundaravel, B.; Mahapatra, D. P.; Dev, B. N., *Surf. Sci.* **1995,** 339, (1-2), 96-104.
20. Sekar, K.; Kuri, G.; Satyam, P. V.; Sundaravel, B.; Mahapatra, D. P.; Dev, B. N., *Phys. Rev. B* **1995,** 51, (20), 14330-14336.
21. Sekar, K.; Satyam, P. V.; Kuri, G.; Mahapatra, D. P.; Dev, B. N., *Nucl. Instrum. Methods Phys. Res. Sect. B-Beam Interact. Mater. Atoms* **1992,** 71, (3), 308-313.
22. Sekar, K.; Satyam, P. V.; Kuri, G.; Mahapatra, D. P.; Dev, B. N., *Nucl. Instrum. Methods Phys. Res. Sect. B-Beam Interact. Mater. Atoms* **1993,** 73, (1), 63-70.

23. Laibinis, P. E.; Stanton, C. E.; Lewis, N. S., *J. Phys. Chem.* **1994,** 98, (35), 8765-8774.

24. Pomykal, K. E.; Fajardo, A. M.; Lewis, N. S., *J. Phys. Chem.* **1996,** 100, (9), 3652-3664.

25. Royea, W. J.; Michalak, D. J.; Lewis, N. S., *Appl. Phys. Lett.* **2000,** 77, (16), 2566-2568.

26. Shreve, G. A.; Karp, C. D.; Pomykal, K. E.; Lewis, N. S., *J. Phys. Chem.* **1995,** 99, (15), 5575-5580.

27. Fajardo, A. M.; Lewis, N. S., *Science* **1996,** 274, (5289), 969-972.

28. Fajardo, A. M.; Lewis, N. S., *J. Phys. Chem. B* **1997,** 101, (51), 11136-11151.

29. Kobayashi, H.; Takeda, N.; Sugahara, H.; Tsubomura, H., *J. Phys. Chem.* **1991,** 95, (2), 813-818.

30. Tomkiewicz, M., *Electrochim. Acta* **1990,** 35, (10), 1631-1635.

31. Hendrickson, D. H.; Sohn, Y. S.; Gray, H. B., *Inorg. Chem.* **1971,** 10, (8), 1550.

32. Kunst, M.; Sanders, A., *Semicond. Sci. Technol.* **1992,** 7, (1), 51-59.

33. Yablonovitch, E.; Allara, D. L.; Chang, C. C.; Gmitter, T.; Bright, T. B., *Phys. Rev. Lett.* **1986,** 57, (2), 249-252.

34. Yablonovitch, E.; Swanson, R. M.; Eades, W. D.; Weinberger, B. R., *Appl. Phys. Lett.* **1986,** 48, (3), 245-247.

35. Haber, J. A.; Lauermann, I.; Michalak, D.; Vaid, T. P.; Lewis, N. S., *J. Phys. Chem. B* **2000,** 104, (43), 9947-9950.

36. Rosenbluth, M. L.; Lewis, N. S., *J. Am. Chem. Soc.* **1986,** 108, (16), 4689-4695.

37. Schroder, D. K., *Semiconductor Material and Device Characterization*. John Wiley & Sons: New York, 1990.

38. Pierret, R. F., Advanced Semiconductor Fundamentals. In *Modular Series on Solid State Devices*, Neudeck, G. W.; Pierret, R. F., Eds. Reading, MA, 1987; Vol. VI.

39. Aberle, A. G.; Glunz, S.; Warta, W., *J. Appl. Phys.* **1992,** 71, (9), 4422-4431.

40. Chabal, Y. J.; Harris, A. L.; Raghavachari, K.; Tully, J. C., *Int. J. Mod. Phys. B* **1993,** 7, (4), 1031-1078.

41. Higashi, G. S.; Becker, R. S.; Chabal, Y. J.; Becker, A. J., *Appl. Phys. Lett.* **1991,** 58, (15), 1656-1658.

42. Higashi, G. S.; Chabal, Y. J.; Trucks, G. W.; Raghavachari, K., *Appl. Phys. Lett.* **1990,** 56, (7), 656-658.

43. Burrows, V. A.; Chabal, Y. J.; Higashi, G. S.; Raghavachari, K.; Christman, S. B., *Appl. Phys. Lett.* **1988,** 53, (11), 998-1000.

44. Chabal, Y. J.; Higashi, G. S.; Raghavachari, K.; Burrows, V. A., *J. Vac. Sci. Technol. A-Vac. Surf. Films* **1989,** 7, (3), 2104-2109.

45. Pourbaix, M., *Atlas d'équilibres électrochemiques*. Pergamon: Oxford: New York, 1966.

46. Allongue, P.; Kieling, V.; Gerischer, H., *Electrochim. Acta* **1995,** 40, (10), 1353-1360.

47. Haber, J. A.; Lewis, N. S., *J. Phys. Chem. B* **2002,** 106, (14), 3639-3656.

48. Msaad, H.; Michel, J.; Reddy, A.; Kimerling, L. C., *J. Electrochem. Soc.* **1995,** 142, (8), 2833-2835.

49. Weaver, M. J., In *Comprehensive Chemical Kinetics*, Compton, R. G., Ed. Elsevier: New York, 1987; Vol. 27, p 1.

50. Kruger, O.; Kenyon, C. N.; Tan, M. X.; Lewis, N. S., *J. Phys. Chem. B* **1997,** 101, (15), 2840-2849.

51. Lehmann, V., *The electrochemistry of silicon : instrumentation, science, materials and applications*. Wiley-VCH: 2002.

52. Weldon, M. K.; Queeney, K. T.; Eng, J.; Raghavachari, K.; Chabal, Y. J., *Surf. Sci.* **2002,** 500, (1-3), 859-878.

53. Chazalviel, J. N.; Etman, M.; Ozanam, F., *J. Electroanal. Chem.* **1991,** 297, (2), 533-540.

54. Turner, D. R., *J. Electrochem. Soc.* **1958,** 105, (7), 402-408.

55. Seo, Y. H.; Yun, M. H.; Nahm, K. S.; Lee, K. B., *J. Vac. Sci. Technol. B* **1993,** 11, (1), 70-77.

56. Matsumura, M.; Morrison, S. R., *J. Electroanal. Chem.* **1983,** 144, (1-2), 113-120.

57. Matsumura, M.; Morrison, S. R., *J. Electroanal. Chem.* **1983,** 147, (1-2), 157-166.

58. Gerischer, H.; Lubke, M., *Ber. Bunsen-Ges. Phys. Chem. Chem. Phys.* **1987,** 91, (4), 394-398.

59. Lewerenz, H. J.; Stumper, J.; Peter, L. M., *Phys. Rev. Lett.* **1988,** 61, (17), 1989-1992.

60. Peter, L. M.; Li, J.; Peat, R.; Lewerenz, H. J.; Stumper, J., *Electrochim. Acta* **1990,** 35, (10), 1657-1664.

61. Stumper, J.; Lewerenz, H. J.; Pettenkofer, C., *Phys. Rev. B* **1990,** 41, (3), 1592-1597.

62. Gerischer, H.; Allongue, P.; Kieling, V. C., *Ber. Bunsen-Ges. Phys. Chem. Chem. Phys.* **1993,** 97, (6), 753-756.

63. Yahyaoui, F.; Dittrich, T.; Burke, T.; Aggour, M.; Lust, S.; Levy-Clement, C.; Rappich, J., *J. Electrochem. Soc.* **2002,** 149, (11), E472-E478.

64. Hoffmann, P. M.; Vermeir, I. E.; Searson, P. C., *J. Electrochem. Soc.* **2000,** 147, (8), 2999-3002.

65. Kolasinski, K. W., *Phys. Chem. Chem. Phys.* **2003,** 5, (6), 1270-1278.

66. Memming, R.; Schwandt, G., *Surf. Sci.* **1966,** 4, (2), 109.

67. Turner, D. R., *J. Electrochem. Soc.* **1960,** 107, (10), 810-816.

68. Vanmaekelbergh, D.; Searson, P. C., *J. Electrochem. Soc.* **1994,** 141, (3), 697-702.

69. Gerischer, H.; Lubke, M., *J. Electrochem. Soc.* **1988,** 135, (11), 2782-2786.

70. Hu, S. M.; Kerr, D. R., *J. Electrochem. Soc.* **1967,** 114, (4), 414.

71. Eddowes, M. J., *J. Electroanal. Chem.* **1990,** 280, (2), 297-311.

72. Ottow, S.; Popkirov, G. S.; Foll, H., *J. Electroanal. Chem.* **1998,** 455, (1-2), 29-37.

73. Gerischer, H.; Lubke, M., *Ber. Bunsen-Ges. Phys. Chem. Chem. Phys.* **1988,** 92, (5), 573-577.

74. Michalak, D. J.; Lewis, N. S., *Appl. Phys. Lett.* **2002,** 80, (23), 4458-4460.

75. Soppa, W. M.; Wagemann, H. G., *IEEE Trans. Electron Devices* **1988,** 35, (7), 970-977.

76. Sharma, U.; Booth, R. V. H.; White, M. H., *IEEE Trans. Electron Devices* **1989,** 36, (5), 954-962.

77. Amm, D. T.; Mingam, H.; Delpech, P.; Douville, T. T., *IEEE Trans. Electron Devices* **1989,** 36, (5), 963-968.

78. Morrison, S. R., *Electrochemistry at Semiconductor and Oxidized Metal Electrodes*. Plenum Press: New York, 1980.

79. Sadkowski, A., *J. Electroanal. Chem.* **2000,** 481, (2), 222-226.

80. Zoltowski, P., *J. Electroanal. Chem.* **1998,** 443, (1), 149-154.

81. Bard, A. J.; Faulkner, L. R., *Electrochemical Methods: Fundamentals and Applications*. 2nd ed.; John Wiley & Sons: New York, 2001.

82. Kim, C. H.; Pyun, S.; Kim, J. H., *Electrochim. Acta* **2003,** 48, (23), 3455-3463.

83. Bidoia, E. D.; Bulhoes, L. O. S.; Rochafilho, R. C., *Electrochim. Acta* **1994,** 39, (5), 763-769.

84. Bai, L.; Gao, L.; Conway, B. E., *J. Chem. Soc.-Faraday Trans.* **1993,** 89, (2), 235-242.

85. Brews, J. R., *Solid-State Electron.* **1978,** 21, (2), 345-355.

86. Wade, C. P.; Chidsey, C. E. D., *Appl. Phys. Lett.* **1997,** 71, (12), 1679-1681.

87. Luo, H. H.; Chidsey, C. E. D., *Appl. Phys. Lett.* **1998,** 72, (4), 477-479.

88. Wayner, D. D. M.; Wolkow, R. A., *J. Chem. Soc.-Perkin Trans. 2* **2002**, (1), 23-34.

89. Oskam, G.; Hoffmann, P. M.; Schmidt, J. C.; Searson, P. C., *J. Phys. Chem.* **1996,** 100, (5), 1801-1806.

90. Oskam, G.; Hoffmann, P. M.; Searson, P. C., *Phys. Rev. Lett.* **1996,** 76, (9), 1521-1524.

91. Zhong, L.; Shimura, F., *Appl. Phys. Lett.* **1992,** 61, (9), 1078-1080.

92. Watanabe, K.; Munakata, C., *Semicond. Sci. Technol.* **1993,** 8, (2), 230-235.

93. Abbas, C. C., *IEEE Trans. Electron Devices* **1984,** 31, (10), 1428-1432.

94. Schmid, W.; Reiner, J., *J. Appl. Phys.* **1982,** 53, (9), 6250-6252.

95. Norga, G. J.; Black, M. R.; Black, K. A.; Msaad, H.; Michel, J.; Kimerling, L. C., High sensitivity detection of silicon surface reactions by photoconductance decay. In *Icds-18 - Proceedings of the 18th International Conference on Defects in Semiconductors, Pts 1-4*, Transtec Publications Ltd: Zurich-Uetikon, 1995; Vol. 196, pp 1531-1536.

96. Oskam, G.; Long, J. G.; Natarajan, A.; Searson, P. C., *J. Phys. D-Appl. Phys.* **1998,** 31, (16), 1927-1949.

97. Cheng, X.; Li, G.; Kneer, E. A.; Vermeire, B.; Parks, H. G.; Raghavan, S.; Jeon, J. S., *J. Electrochem. Soc.* **1998,** 145, (1), 352-357.

98. Zambelli, T.; Munford, M. L.; Pillier, F.; Bernard, M. C.; Allongue, P., *J. Electrochem. Soc.* **2001,** 148, (9), C614-C619.

99. Bertagna, V.; Rouelle, F.; Revel, G.; Chemla, M., *J. Electrochem. Soc.* **1997,** 144, (12), 4175-4182.

100. Bertagna, V.; Rouelle, F.; Erre, R.; Chemla, M., *Semicond. Sci. Technol.* **2000,** 15, (2), 121-125.

101. Homma, T.; Wade, C. P.; Chidsey, C. E. D., *J. Phys. Chem. B* **1998,** 102, (41), 7919-7923.

102. Ye, S.; Ichihara, T.; Uosaki, K., *J. Electrochem. Soc.* **2001,** 148, (6), C421-C426.

103. Lee, I. C.; Bae, S. E.; Song, M. B.; Lee, J. S.; Paek, S. H.; Lee, C. W. J., *Bull. Korean Chem. Soc.* **2004,** 25, (2), 167-171.

104. Li, G. M.; Jiao, J.; Seraphin, S.; Raghavan, S.; Jeon, J. S., *J. Appl. Phys.* **1999,** 85, (3), 1857-1863.

105. Rossi, R. C.; Lewis, N. S., *J. Phys. Chem. B* **2001,** 105, (49), 12303-12318.

106. Rossi, R. C.; Tan, M. X.; Lewis, N. S., *Appl. Phys. Lett.* **2000,** 77, (17), 2698-2700.

107. Grujicic, D.; Pesic, B., *Electrochim. Acta* **2005,** 50, (22), 4426-4443.

108. Allongue, P.; Costakieling, V.; Gerischer, H., *J. Electrochem. Soc.* **1993,** 140, (4), 1009-1018.

109. Reddy, A. J.; Chan, J. V.; Burr, T. A.; Mo, R.; Wade, C. P.; Chidsey, C. E. D.; Michel, J.; Kimerling, L. C., *Physica B* **1999,** 274, 468-472.

110. Greenwood, N. N.; Earnshaw, A., *Chemistry of the Elements*. Pergamon: New York, 1984.

111. Allongue, P.; Costakieling, V.; Gerischer, H., *J. Electrochem. Soc.* **1993,** 140, (4), 1018-1026.

112. Warntjes, M.; Vieillard, C.; Ozanam, F.; Chazalviel, J. N., *J. Electrochem. Soc.* **1995,** 142, (12), 4138-4142.

113. Chazalviel, J. N., *J. Electroanal. Chem.* **1987,** 233, (1-2), 37-48.

114. Mao, D.; Kim, K. J.; Frank, A. J., *J. Electrochem. Soc.* **1994,** 141, (5), 1231-1236.

115. Buriak, J. M., *Chem. Commun.* **1999**, (12), 1051-1060.

116. Buriak, J. M., *Chem. Rev.* **2002,** 102, (5), 1271-1308.

117. Sailor, M. J.; Heinrich, J. L.; Lauerhaas, J. M., Luminescent porous silicon: Synthesis, chemistry, and applications. In *Semiconductor Nanoclusters- Physical, Chemical, and Catalytic Aspects*, Elsevier Science Publ B V: Amsterdam, 1997; Vol. 103, pp 209-235.

118. Sailor, M. J.; Lee, E. J., *Adv. Mater.* **1997,** 9, (10), 783.

119. Cleland, G.; Horrocks, B. R.; Houlton, A., *J. Chem. Soc.-Faraday Trans.* **1995,** 91, (21), 4001-4003.

120. Bateman, J. E.; Horrocks, B. R.; Houlton, A., *J. Chem. Soc.-Faraday Trans.* **1997,** 93, (14), 2427-2431.

121. Bateman, J. E.; Eagling, R. D.; Horrocks, B. R.; Houlton, A., *J. Phys. Chem. B* **2000,** 104, (23), 5557-5565.

122. Boukherroub, R.; Morin, S.; Sharpe, P.; Wayner, D. D. M.; Allongue, P., *Langmuir* **2000,** 16, (19), 7429-7434.

123. Ozanam, F.; Djebri, A.; Chazalviel, J. N., *Electrochim. Acta* **1996,** 41, (5), 687-692.

124. Collins, R. J.; Fan, H. Y., *Physical Review* **1954,** 93, (4), 674-678.

125. Queeney, K. T.; Fukidome, H.; Chaban, E. E.; Chabal, Y. J., *J. Phys. Chem. B* **2001,** 105, (18), 3903-3907.

126. Glass, J. A.; Wovchko, E. A.; Yates, J. T., *Surf. Sci.* **1995,** 338, (1-3), 125-137.

127. Rivillon, S.; Amy, F.; Chabal, Y. J.; Frank, M. M., *Appl. Phys. Lett.* **2004,** 85, (13), 2583-2585.

128. Rivillon, S.; Chabal, Y. J.; Webb, L. J.; Michalak, D. J.; Lewis, N. S.; Halls, M. D.; Raghavachari, K., *J. Vac. Sci. Technol. A* **2005,** 23, (4), 1100-1106.

129. Jakob, P.; Chabal, Y. J.; Raghavachari, K.; Christman, S. B., *Phys. Rev. B* **1993,** 47, (11), 6839-6842.

130. Falk, M.; Whalley, E., *J. Chem. Phys.* **1961,** 34, (5), 1554-1568.

131. Noether, H. D., *J. Chem. Phys.* **1942,** 10, (12), 693-699.

132. Pelmenschikov, A. G.; Morosi, G.; Gamba, A.; Zecchina, A.; Bordiga, S.; Paukshtis, E. A., *J. Phys. Chem.* **1993,** 97, (46), 11979-11986.
133. Mudalige, K.; Warren, S.; Trenary, M., *J. Phys. Chem. B* **2000,** 104, (11), 2448-2459.
134. Queeney, K. T.; Chabal, Y. J.; Weldon, M. K.; Raghavachari, K., *Phys. Status Solidi A-Appl. Res.* **1999,** 175, (1), 77-88.
135. Chabal, Y. J., *Surf. Sci. Rep.* **1988,** 8, (5-7), 211-357.
136. Many, A.; Goldstein, Y.; Grover, N. B., *Semiconductor surfaces*. Interscience Publishers: New York, 1965.
137. Orton, J. W.; Blood, P., *The Electrical Characterization of Semiconductors: Measurement of Minority Carrier Properties*. Academic Press, Inc.: San Diego, CA, 1990.